MODELLING OF SUBCOOLED FLOW BOILING IN A RECTANGULAR MICRO-CHANNEL HEAT SINK

Chong Jen Haw

THESIS SUBMITTED TO THE UNIVERSITY OF NOTTINGHAM FOR THE DEGREE OF DOCTOR PHILOSOPHY
AUGUST 2018

Abstract

Attaching micro-channel heat sinks operating under flow boiling conditions on heat sources of electronic components is an efficient cooling technique which still requires further improvements of designs. When developing this system, the efficient heat transfer performance is essential, however, this development often entangles with difficulties. The difficulties arise as existing prediction approaches are underdeveloped and inadequate to perform the accurate prediction in wide ranges of operating conditions. This inadequacy persists due to incomplete discoveries of involved mechanisms that involve fluid and dynamics for the heat transfer during the flow boiling. Also, the mechanisms involved in the flow boiling process are complicated, hindering the development of more reliable approaches. By addressing this issue, this study explores and investigates the relating mechanisms.

The mechanisms of fluids during the flow boiling of subcooled liquids in micro-channel heat sinks immediately before and during the nucleation of first bubbles were explored in this study. This study then addressed the mechanisms of heat transfer enhancement of flow boiling. Later, this study repeated with different substrate materials of micro-channel heat sinks and working fluids. This study serves the purpose to better understand the involved mechanisms during the flow boiling of subcooled liquids in micro-channel heat sinks for the development of more reliable approaches to predict the heat transfer.

This study regarding the mechanisms during the flow boiling in micro-channel heat sinks implemented the numerical model associated with the Volume of Fluid (VOF) in which corresponding governing equations were solved using a computational fluid dynamics (CFD). In this model, computational domains of micro-channel heat sinks in three dimensions that include the sub-domains of solids and fluid were created to consider the conjugate heat transfer for better estimation of data. The data collected in this study were from operating parameters of heat flux, mass flux, and inlet temperature of the micro-channel at 500-3197 kW/m^2, 115-389 kg/m^2 s, and 23-53°C, respectively. The micro-channel heat sinks operated at the atmospheric pressure, and the corresponding substrate materials chosen were steel, silicon, aluminium and copper, and working fluids selected were water and ethanol. The numerical results agree well with the experimental data from the previous study.

The results show that although the bubble nucleation is absent, the heat transfer mechanisms in micro-channels possesses the nucleate boiling characteristic involving the transient conduction with the existence of the phase change process. The heat transfer mechanisms from the phase change process with the incomplete

evaporation induce the ascending and descending flows and liquid-vapour mixture on the heating surfaces. From the results, four different modes of heat transfer mechanisms from the phase change process associated with ascending and descending flows and liquid vapour mixture become apparent. The ascending and descending flows on the heating surfaces appear with local increases of pressure gradients near to the heating surfaces facilitating the heat transfer enhancement due to phase change. On the other hand, the liquid-vapour mixture produced from the phase change process impeding the heat transfer. In overall, the heat transfer enhancement due to the phase change at the side surfaces in the micro-channel is more extensive as compared to the bottom surface for each condition tested in this study. Meanwhile, the amount of the liquid-vapour mixture accumulating on the bottom surface is more massive as compared to the side surfaces, leading to the impedance of the heat transfer. These heat transfer mechanisms also persist during flow boiling in micro-channels. The heat transfer enhancement due to phase change from the side and bottom surfaces also varies when employing different operating conditions before and during flow boiling.

This study provides better insights for researchers and designers in industries regarding the local mechanisms for the heat transfer during the flow boiling in micro-channel heat sinks. These understandings assist the researchers to develop the more reliable prediction methods to design new and better heat transfer performance of micro-channel heat sinks and avoid repeating experiments which are costly and tedious in procedures.

Contents

Abstract iii
Contents v
List of Figures vii
List of Tables xiv
Nomenclature xv
Abbreviations xxi
Chapter 1 Introduction 1
1.1 Background of Research 1
1.2 Objective 10
1.3 Outline of Thesis 10
Chapter 2 Literature Review 11
2.1 Experimental Studies of Heat Transfer Trends and Mechanisms of Flow Boiling of Subcooled Liquids in Rectangular Micro-Channels 11
2.2 Empirical Correlations of Heat Transfer during Flow Boiling in Micro-Channels 25
2.3 Flow Regimes of Flow Boiling in Rectangular Micro-Channels 26
2.4 Experimental Studies of Characteristics and Mechanisms of Nucleate Boiling during Flow Boiling of Subcooled Liquids in Rectangular Micro-Channels .. 37
2.5 Numerical Studies of Characteristics and Mechanisms of Nucleate Boiling during Flow Boiling of Subcooled Liquids in Rectangular Micro-Channels .. 45
2.6 Mechanistic Prediction Methods of Nucleate Boiling during Flow Boiling in Rectangular Micro-Channels 56
Chapter 3 Methodology 67
3.1 Operating Parameters 67
3.2 Numerical Model 69
3.2.1 Computational Domain 70
3.2.2 Governing Equations 73
3.2.3 Boundary Conditions 78
3.2.4 Initial Conditions 79
3.2.5 Discretisation Methods 79

3.2.6 Under-relaxation Factors 80
3.2.7 Convergence Criteria 80
3.2.8 Validation of Numerical Model 80
Chapter 4 Effects of Mass Fluxes, Heat Fluxes, and Inlet Temperatures 85
4.1 Transient Heat Transfer for Different Mass Fluxes, Heat Fluxes and Inlet Temperatures before Flow Boiling 85
4.2 Heat Transfer Mechanisms before Flow Boiling 89
4.3 Effects of Mass Fluxes before Flow Boiling 108
4.4 Effects of Mass Fluxes during Flow Boiling 117
4.5 Location of Bubble Nucleation for Different Mass Fluxes 122
4.6 Effects of Heat Fluxes before Flow Boiling 123
4.7 Effects of Heat Fluxes during Flow Boiling 132
4.8 Location of Bubble Nucleation for Different Heat Fluxes 136
4.9 Effects of Inlet Temperatures before Flow Boiling 137
4.10 Effects of Inlet Temperatures during Flow Boiling 143
4.11 Location of Bubble Nucleation for Different Inlet Temperatures 146
Chapter 5 Effects of Substrate Materials 149
5.1 Transient Heat Transfer for Different Substrate Materials before Flow Boiling 149
5.2 Effects of Substrate Materials before Flow Boiling 152
5.3 Effects of Substrate Materials during Flow Boiling 164
5.4 Location of Bubble Nucleation and Bubble Growth for Different Substrate Materials 170
Chapter 6 Effects of Working Fluids 173
6.1 Transient Heat Transfer for Different Working Fluids before Flow Boiling 173
6.2 Effects of Working Fluids before Flow Boiling 174
6.3 Effects of Working Fluids during Flow Boiling 179
6.4 Location of Bubble Nucleation and Bubble Growth for Different Working Fluids 182
Chapter 7 Conclusions 185
References 189
Appendix A Flow Chart of Numerical Algorithm 199

List of Figures

Figure 1.1: International Technology Roadmap for Semiconductors (ITRS) [1] 1

Figure 1.2: Attainable range of heat transfer coefficients h of water under the conditions of forced convection of single-phase flow and flow boiling [5] 2

Figure 1.3: Cross-sectional views for (a) triangular (b) rectangular, and (c) trapezoidal micro-channel heat sinks, and the corresponding number of corners with the sites of the nucleation of bubbles 4

Figure 1.4: A typical example of the schematic diagram of rectangular micro-channel heat sink 4

Figure 1.5: Schematic diagram of flow regimes and heat transfer coefficients along a mini- or micro-channel with a uniform circumferential heat flux for (a) nucleate boiling and (b) convective boiling dominant heat transfer [22] 6

Figure 2.1: Boiling curve of flow boiling in channels [19] 12

Figure 2.2: Boiling curves for different $\dot{m}''$ for (a) W_c = 400 μm and (b) W_c = 2200 μm 19

Figure 2.3: h_{local} against $q''_{total,fin}$ for each mass flux m'' in 400 μm wide and 400 μm deep of micro-channels [20, 32, 51] 20

Figure 2.4: h_{local} against $q''_{total,fin}$ of the micro-channels for each width [49] $\dot{m}''$ = 630 kg/m^2 s 20

Figure 2.5: h_{local} against base heat flux q''_b of the micro-channels for each width [20] 21

Figure 2.6: Boiling curves (ΔT_{sub} of 50°C) of micro-channel with channel width, height, and length of 241 × 198 × 21900 μm^3 [22] 22

Figure 2.7: Boiling curves (ΔT_{sub} of 50°C) of micro-channel with channel width, height, and length of 471 × 378 × 21900 μm^3 [22] 23

Figure 2.8: Local h_{tp} against X of micro-channel with channel width, height, and length of 241 × 198 × 21900 μm^3 [22] 23

Figure 2.9: Local h_{tp} against X of micro-channel with channel width, height, and length of 471 × 378 × 21900 μm^3 [22] 24

Figure 2.10: Local h_{tp} against $q''_{total,fin}$ of micro-channel with channel width, height, and length of 241 × 198 × 21900 μm^3 [22] 24

Figure 2.11: Local h_{tp} against $q''_{total,fin}$ of micro-channel channel width, height, and length of 471 × 378 × 21900 μm^3 [22] 25

Figure 2.12: Flow regime map of Re against Bo of nucleate boiling, convective boiling, and dry-out of Koşar [55] 28

Figure 2.13: Flow regime map of $q''_{total,fin}$ against x/L_c of single phase, subcooled boiling, and saturated flow boiling ($\dot{m}''$ of 330 kg/m^2 s and ΔT_{sub} of 7.9°C) from Liu and Garimella [19] 29

Figure 2.14: Actual images (left) and sketched images (right) of flow patterns in a shape of square of micro-channels (400 × 400 μm^2 and 12.7 mm long) made of silicon at the horizontal position under the condition of flow boiling (ΔT_{sub} of 5°C) [32] 31

Figure 2.15: Flow regime map of $\dot{m}''$ against $q''_{total,fin}$ of W_c of 100-5850 μm and H_c of 100-400 μm for bubble, slug, churn, wispy-annular, annular, alternating bubbly/slug flow, alternating churn/wispy-annular flow, and single-phase flow from Harirchian and Garimella [57] 32

Figure 2.16: Flow regime map of (a) $\dot{m}''$ against X and (b) J_l against J_v of W_c of 100-5850 μm for the transition from bubbly or slug flow to intermittent churn/wispy-annular or churn/annular flow from Harirchian and Garimella [32] 33

Figure 2.17: Flow regime map of Re against Bo of unconfined flow and confined flow Harirchian and Garimella [57] 34

Figure 2.18: Flow regime map of $Bo \times Re$ against $Bn^{0.5} \times Re$ of confined flug, churn/confined annular, bubbly, churn/wispy-annular, and churn/annular from Harirchian and Garimella [57] 35

Figure 2.19: Actual images (left) and enhanced with Matlab image processing tool (right) of flow regimes of (a) bubbly flow, (b) slug flow, (c) churn flow, (d) annular flow, (e) wavy annular flow, and (f) inverted annular flow [22] 36

Figure 2.20: Flow regime map of $\dot{m}''$ against q''_b of single-phase flow (SP), slug flow (S), slug-annular flow (S-A), and inverted annular flow (I) from Galvis and Culham [22] 37

Figure 2.21: Visualisation of bubble at ONB [61] 39

Figure 2.22: Visualisation of bubble at ONB at p_{out} of 104469 Pa of, T_{in} of 70.9°C of, u_{in} of 0.55 m/s, and q''_{hs} of 28.87 W/cm^2 from Liu et al. [47] 40

Figure 2.23: Visualisation of bubble at ONB from Mosyak et al. [46] 40

Figure 2.24: (a) Bottom surface bubble and (b) side surface bubble growth curves in subcooled flow boiling for q''_b of 445 kW/m^2 and $\dot{m}''$ of 153 kg/m^2 s 44

Figure 2.25: (a) Axial view of nucleated bubbles at the bottom and side surfaces, and corner, and (b) side view of nucleated bubble [6] 52

Figure 2.26: Characteristics of the nucleation of bubble (a) change of radius of curvature of bubble in a cavity, (b) a chopped spherical bubble, and (c) criterion for the nucleation of bubble [106] 58

Figure 2.27: Active cavity range for (a) different thermal boundary layer thickness of saturated water and (b) different ΔT_{sub} and constant thermal boundary layer thickness of 0.5 mm [100] 60

Figure 2.28: Distribution of the temperature of fluid at the cross section of the location of ONB (a) $T_{f,ONB} < T_{sat}$ and (b) $T_{f,ONB} \approx T_{sat}$ [46] 63

Figure 2.29: Free body diagram of the forces acting on a liquid-vapour interface in a channel [108] 64

Figure 2.30: Schematic diagram of forces acting on a bubble during flow boiling in a micro-channel θ_{rec} 66

Figure 3.1: Schematic diagram of the computational domain of micro-channel heat sink with the inlet extension and outlet extension 72

Figure 3.2: Mesh of the computational domain in cross-sectional view (y-z plane) 73

Figure 3.3: $q''_{total,fin}$ against T_{bottom} from the present numerical model and experimental data of Koşar et al. [116] 81

Figure 3.4: H_{bub} at the centre along the length of channel against t_{bub} for the present numerical model and experimental data of Bogojevic et al. [65] 82

Figure 3.5: ΔT_{sup} against q''_{ONB} for the present numerical results and existing models of ONB from researchers [47, 100, 101, 103, 104] 83

Figure 4.1: Transient heat transfer data of $q''_{total,fin}$ against $T_{avg,surf}$ of water flowing in silicon micro-channels for different m'' at T_{in} = 23°C and q''_b = 1561 kW/m^2 before flow boiling $\Delta t_{fb} < 0$ (first and second marks at Δt_{fb} about -5.8 and -2.9 ms, respectively, of each curve) 86

Figure 4.2: Transient heat transfer data of $q''_{total,fin}$ against $T_{avg,surf}$ of water flowing in silicon micro-channels for different q''_b at $\dot{m}''$ = 389 kg/m^2 s and T_{in} = 23°C before flow boiling $\Delta t_{fb} < 0$ (first and second marks at Δt_{fb} about -5.8 and -2.9 ms, respectively, of each curve) 87

Figure 4.3: Transient heat transfer data of $q''_{total,fin}$ against $T_{avg,surf}$ of water flowing in silicon the micro-channels for different T_{in} at $\dot{m}''$ = 389 kg/m^2 s and q''_b = 1691 kW/m^2 before flow boiling $\Delta t_{fb} < 0$ (first and second marks at Δt_{fb} about -5.8 and -2.9 ms, respectively, of each curve) 87

Figure 4.4: Velocity vector, pressure (Pa), and density (kg/m^3) distributions at x-y plane and q''^*_{local} and ΔT_{sup} against x^* at $y = 0$ at $z = 0.08$ mm when $\Delta t_{fb} = -5.8$ ms for q''^*_b = 1561 kW/m^2, $\dot{m}''$ = 165 kg/m^2 s, and T_{in} = 23°C in silicon micro-channel 97

Figure 4.5: Velocity vector, pressure (Pa), and density (kg/m^3) distributions at x-y plane and q''^*_{local} and ΔT_{sup} against x^* at $y = 0$ at $z = -0.08$ mm when $\Delta t_{fb} = -5.787$ ms for q''^*_b = 1561 kW/m^2, $\dot{m}''$ = 389 kg/m^2 s, and T_{in} = 23°C in silicon micro-channel 107

Figure 4.6: q''^*_{local} along x^* for $\dot{m}''$ of 165 kg/m^2 s at q''^*_b of 1561 kW/m^2 and T_{in} of 23°C at Δt_{fb} about (a) −5.8 and (b) −2.9 ms 110

Figure 4.7: q''^*_{local} along x^* for $\dot{m}''$ of 265 kg/m^2 s at q''^*_b of 1561 kW/m^2 and T_{in} of 23°C at Δt_{fb} about (a) −5.8 and (b) −2.9 ms 111

Figure 4.8: q''^*_{local} along x^* for $\dot{m}''$ of 389 kg/m^2 s at q''^*_b of 1561 kW/m^2 and T_{in} of 23°C at Δt_{fb} about (a) −5.8 and (b) −2.9 ms 112

Figure 4.9: q''^* against $\dot{m}''$ at q''^*_b 1561 kW/m^2 and T_{in} of 23°C at Δt_{fb} about (a) −5.8 and (b) −2.9 ms 116

Figure 4.10: $h*$ against $\dot{m}''$ at q''^*_b 1561 kW/m^2 and T_{in} of 23°C at Δt_{fb} about −5.8 and −2.9 ms 117

Figure 4.11: q''^*_{local} along x^* for $\dot{m}''$ of (a) 165, (b) 265, and (c) 389 kg/m^2 s at q''^*_b of 1561 kW/m^2 and T_{in} of 23°C at Δt_{fb} about 10 ms 120

Figure 4.12: q''_{local} against $\dot{m}''$ at q''^*_b of 1561 kW/m^2 and T_{in} of 23°C at Δt_{fb} about 10 ms 121

Figure 4.13: $h*$ against $\dot{m}''$ at q''^*_b of 1561 kW/m^2 and T_{in} of 23°C at Δt_{fb} about 10 ms 122

Figure 4.14: Location of bubble nucleation against $\dot{m}''$ at q''^*_b of 1561 kW/m^2 and T_{in} of 23°C at Δt_{fb} within 0 and 10 ms 123

Figure 4.15: q''^*_{local} along x^* for q''^*_b of 1691 kW/m^2 at $\dot{m}''$ of 389 kg/m^2 s and T_{in} of 23°C at Δt_{fb} about (a) −5.8 and (b) −2.9 ms 124

Figure 4.16: q''^*_{local} along x^* for q''^*_b of 2030 kW/m^2 at $\dot{m}''$ of 389 kg/m^2 s and T_{in} of 23°C at Δt_{fb} about (a) −5.8 and (b) −2.9 ms 125

Figure 4.17: q''^*_{local} along x^* for q''^*_b of 2706 kW/m^2 at $\dot{m}''$ of 389 kg/m^2 s and T_{in} of 23°C at Δt_{fb} about (a) −5.8 and (b) −2.9 ms 126

Figure 4.18: q''_{local} along x^* for q''^*_b of 3197 kW/m^2 at $\dot{m}''$ of 389 kg/m^2 s and T_{in} of 23°C at Δt_{fb} about (a) −5.8 and (b) −2.9 ms 127

Figure 4.19: Ascending and descending flows formed from side surfaces 128

Figure 4.20: q''^* against $q_b''^*$ at $\dot{m}''$ of 389 kg/m^2 s and T_{in} of 23°C at Δt_{fb} about (a) −5.8 and (b) −2.9 ms 130

Figure 4.21: h^* against $q_b''^*$ at $\dot{m}''$ of 389 kg/m^2 s and T_{in} of 23°C at Δt_{fb} about −5.8 and −2.9 ms 131

Figure 4.22: $q_{local}''^*$ along x^* for $q_b''^*$ of (a) 1691, (b) 2030, (c) 2706, and (d) 3197 kW/m^2 at $\dot{m}''$ of 389 kg/m^2 s and T_{in} of 23°C at Δt_{fb} about 10 ms 134

Figure 4.23: q''^* against $q_b''^*$ at $\dot{m}''$ of 389 kg/m^2 s and T_{in} of 23°C at Δt_{fb} about 10 ms 135

Figure 4.24: h^* against $q_b''^*$ at $\dot{m}''$ of 389 kg/m^2 s and T_{in} of 23°C at Δt_{fb} about 10 ms 136

Figure 4.25: Location of bubble nucleation against $q_b''^*$ at $\dot{m}''$ of 389 kg/m^2 s and T_{in} of 23°C at Δt_{fb} within 0 and 10 ms 137

Figure 4.26: $q_{local}''^*$ along x^* for T_{in} of 38°C at $\dot{m}''$ of 389 kg/m^2 s and $q_b''^*$ of 1691 kW/m^2 at Δtfb about (a) −5.8 and (b) −2.9 ms..... 138

Figure 4.27: $q_{local}''^*$ along x^* for T_{in} of 53°C at $\dot{m}''$ of 389 kg/m^2 s and $q_b''^*$ of 1691 kW/m^2 at Δt_{fb} about (a) −5.8 and (b) −2.9 ms 139

Figure 4.28: q_{local}'' against T_{in} at $\dot{m}''$ of 389 kg/m^2 s and $q_b''^*$ of 1691 kW/m^2 at Δt_{fb} about (a) −5.8 and (b) −2.9 ms..... 142

Figure 4.29: h^* against T_{in} at $\dot{m}''$ of 389 kg/m^2 s and $q_b''^*$ of 1691 kW/m^2 at Δt_{fb} about −5.8 and −2.9 ms 143

Figure 4.30: $q_{local}''^*$ along x^* for T_{in} of (a) 38 and (b) 53°C at $\dot{m}''$ of 389 kg/m^2 s and qb'' of 1691 kW/m^2 at Δt_{fb} about 10 ms 144

Figure 4.31: q''^* against T_{in} at $\dot{m}''$ of 389 kg/m^2 s and $q_b''^*$ of 1691 kW/m^2 at Δt_{fb} about 10 ms..... 145

Figure 4.32: h^* against T_{in} at $\dot{m}''$ of 389 kg/m^2 s and $q_b''^*$ of 1691 kW/m^2 at Δt_{fb} about 10 ms..... 146

Figure 4.33: Location of bubble nucleation against T_{in} at $\dot{m}''$ of 389 kg/m^2 s and $q_b''^*$ of 1691 kW/m^2 at Δt_{fb} within 0 and 10 ms 147

Figure 5.1: Transient heat transfer data of $q_{total,fin}''^*$ against $T_{avg,surf}$ for the substrates of micro-channel heat sinks made of different materials before flow boiling $\Delta t_{fb} < 0$ (the first and second marks at each curve are at Δt_{fb} about −5.8 and −2.9 ms, respectively, and the marks at each curve from the substrate materials of silicon, aluminium, stainless steel, and copper are oval, square, triangle, and cross, respectively) 149

Figure 5.2: q''^{*}_{local} along x^{*} for aluminium micro-channel at Δt_{fb} about (a) −5.8 and (b) −2.9 ms 153

Figure 5.3: q''^{*}_{local} along x^{*} for copper micro-channel at Δt_{fb} about (a) −5.8 and (b) −2.9 ms 154

Figure 5.4: q''^{*}_{local} along x^{*} for stainless steel micro-channel at Δt_{fb} about (a) −5.8 and (b) −2.9 ms 155

Figure 5.5: A thermal boundary layer in the micro-channel heat sink made of stainless steel at a cross-section with the liquid-vapour mixture before flow boiling 159

Figure 5.6: q''^{*} for micro-channels made of different substrate materials at Δt_{fb} about (a) −5.8 and (b) −2.9 ms 162

Figure 5.7: h^{*} for micro-channels made of different substrate materials at Δt_{fb} about −5.8 and −2.9 ms 163

Figure 5.8: q''^{*}_{local} along x^{*} for (a) aluminium, (b) copper, and (c) stainless steel micro-channels at Δt_{fb} about 10 ms 166

Figure 5.9: q''^{*} for micro-channels made of different substrate materials at Δtfb about 10 ms 169

Figure 5.10: h^{*} for micro-channels made of different substrate materials at Δtfb about 10 ms 169

Figure 5.11: Location of bubble nucleation against substrate material at Δt_{fb} within 0 and 10 ms 171

Figure 6.1: Transient heat transfer data of $q''_{total,fin}$ against $T_{avg,surf}$ of different working fluids flowing in micro-channels made at $\dot{m}''$ = 389 kg/m^2 s, $\Delta T_{avg,surf}$ about 16°C at Δt_{fb} of 10 ms, and T_{in} = 23°C before flow boiling $\Delta t_{fb} < 0$ (first and second marks at Δt_{fb} about −5.8 and −2.9 ms, respectively) 174

Figure 6.2: q''^{*}_{local} along x^{*} for ethanol flowing in silicon micro-channel at $\dot{m}''$ of 389 kg/m^2 s, $\Delta T_{avg,sup}$ of 16°C at Δt_{fb} about 10 ms, and T_{in} of 23°C at Δt_{fb} about (a) −5.8 and (b) −2.9 ms 175

Figure 6.3: q''^{*} for different working fluids flowing in silicon micro-channel at $\dot{m}''$ of 389 kg/m^2 s, $\Delta T_{avg,sup}$ of 16°C at Δt_{fb} about 10 ms, and T_{in} of 23°C at Δt_{fb} about (a) −5.8 and (b) −2.9 ms 178

Figure 6.4: h^{*} for different working fluids at $\dot{m}''$ of 389 kg/m^2 s, $\Delta T_{avg,sup}$ of 16°C at Δt_{fb} about 10 ms, and T_{in} of 23°C at Δt_{fb} about −5.8 and −2.9 ms 179

Figure 6.5: q''^{*}_{local} along x^{*} for ethanol at Δt_{fb} about 10 ms 180

Figure 6.6: q''^{*} for micro-channels made of different working fluids at Δt_{fb} about 10 ms 181

Figure 6.7: h^{*} for micro-channels made of different working fluids at Δt_{fb} about 10 ms 182

Figure 6.8: Location of bubble nucleation against working fluid at Δt_{fb} within 0 and 10 ms..... 183

Figure A.1: PISO pressure velocity coupling scheme associated with explicit time discretisation scheme of mass equation of vapour phase..... 200

List of Tables

Table 1.1: Classification of Channels from Mehendele et al. [7] 2

Table 1.2: Classification of Channels from Kandlikar and Grande [8] 3

Table 1.3: Classification of Channels from Kandlikar et al. [9] 3

Table 2.1: Operating parameters of selected experimental studies of heat transfer trends during ONB in rectangular micro-channels in the literature 13

Table 2.2: Operating parameters of selected experimental studies of heat transfer trends and mechanisms of flow boiling of subcooled liquids in rectangular micro-channels in the literature 14

Table 2.3: Operating parameters of selected experimental studies of flow regimes of flow boiling in rectangular micro-channels in the literature 27

Table 2.4: Operating parameters of selected experimental studies relating to the location of ONB in rectangular micro-channels in the literature 39

Table 2.5: Operating parameters of selected experimental studies with the findings of characteristics and mechanisms of nucleate boiling during flow boiling of subcooled liquids in rectangular micro-channels in the literature 41

Table 2.6: Operating parameters of selected numerical studies of characteristics and mechanisms of nucleate boiling during flow boiling of subcooled liquids in rectangular micro-channels in the literature 49

Table 3.1: Thermo-physical properties of substrate materials 68

Table 3.2: Thermo-physical properties of the working fluid of water in the liquid and vapour phases 68

Table 3.3: Thermo-physical properties of the working fluid of ethanol in the liquid and vapour phases 69

Table 3.4: Discretisation methods of each term in governing equations 80

Nomenclature

Symbol	Description	SI unit
Roman		
A	Area	[m^2]
A'''	Interfacial area density	[1/m]
a	Thermal diffusivity	[m^2/s]
Bn	Bond number	-
Bo	Boiling number	-
b	Ratio of the height of superheated layer to bubble	-
$\boldsymbol{C}$	Colour function	-
C	Coefficient or constant	-
Ca	Capillary number	-
Co	Courant number	-
c	Specific heat capacity	[J/kg K]
D	Constant	-
d	Diameter	[m]
E	Specific internal (thermal) energy	[J/kg]
e	Percentage error	[%]
F	Force	[N]
F'	Force per unit length	[N/m]
F''	Force per unit area	[N/m^2]
F'''	Force per unit volume	[N/m^3]
$\mathcal{F}$	Factor	-
f	Function	-
f	Frequency	[Hz]
Fo	Fourier number	-
G	Mass flux	[kg m^2/s]
$\bar{G}$	Net mass flux	[m/s^2]
g	Gravitational acceleration	[m/s^2]
H	Height	[m]
$\mathcal{H}$	Prancle number	-
$\boldsymbol{h}$	Static specific enthalpy	[J/kg]
$\widetilde{\boldsymbol{h}}$	Standard state enthalpy	[J/mol]
h	Heat transfer coefficient	[W/m^2 K]

J	Superficial velocity	[m/s]
Ja	Jacob number	-
$\boldsymbol{k}$	Constant of Boltzmann	[m^2 kg/s^2 K]
k	Thermal conductivity	[W/m K]
Kn	Knudsen number	-
L	Length	[m]
m	Mass	[kg]
$\dot{m}$	Mass flow rate	[kg/s]
$\dot{m}'''$	Mass flow rate per unit volume	[kg/m^3s]
$\widetilde{m}$	Molar mass or molecular weight	[kg/mol]
Ma	Marangoni number	-
N_a	Density of active nucleation	[$1/m^2$]
N_0	Number of molecule per unit volume	[$1/m^3$]
$N_{a,hom}$	Homogeneous nucleation	[$1/m^3$ s]
$N_{a,het}$	Heterogeneous nucleation	[$1/m^2$ s]
Nu	Nusselt number	-
n	Normal	-
$\hat{n}$	Unit normal	-
Pr	Prandtl number	-
Nu	Nusselt number	-
P	Power	[W]
p	Pressure	[Pa]
p'	Modified pressure	[Pa]
Q	Volumetric rate of flow	[m^3/s]
q	Rate of heat transfer	[W]
q''	Heat flux	[W/m^2]
q'''	Rate of the generation of heat or the rate of interfacial heat transfer	[W/m^3]
R	Universal constant of gas	[J/kg K]
Ra	Ratio	-
Re	Reynolds number	-
r	Radius	[m]
S	Volumetric source	[W/m^3]
T	Temperature	[K]
t	Time	[s]
U	Mean velocity	[m/s]
u	Velocity in x-direction	[m/s]

$\bar{u}$	Mean velocity in x-direction	[m/s]
V	Volume	[m^3]
v	Velocity in y-direction	[m/s]
$\bar{v}$	Mean velocity in y-direction	[m/s]
V	Volume	[m^3]
W	Width	[m]
We	Weber number	-
w	Velocity in z-direction	[m/s]
$\bar{w}$	Mean velocity in z-direction	[m/s]
X	Quality	-
$\boldsymbol{x}$	Distance	-
x	Distance in x-direction	[m]
y	Distance in y-direction	[m]
z	Distance in z-direction	[m]

Greek

Δ	Difference	-
Θ	Non-dimensional temperature	-
α	Volume fraction	-
β	Half angle of a corner	-
γ	Phase change or accommodation coefficient	-
δ	Thickness	[m]
ζ	Damping factor	-
η	Efficiency	-
θ	Contact angle	[°]
κ	Curvature	-
λ	Mean free path	[m]
μ	Dynamic viscosity	[kg/m s] or [Pa s]
ρ	Density	[kg/m^3]
σ	Surface tension	[N/m]
τ	Shear stress	[N/m^2]
υ	Specific volume	[m^3/kg]
ϕ	Orientation angle	[°]
ϕ_{base}	Factor of base	-
ϕ_c	Factor of curvature	-
ϕ_s	Factor of surface	-

ϕ_v	Factor of volume	-
χ	Shear flow parameter	-
ψ	Surface available for the heterogeneous nucleation per unit volume of liquid	-
ω	Geometric correction factor for the minimum work required to a critical nucleus	-

Subscripts

a	Activation
ac	Accommodation
adv	Advancing
app	Applied
asp	Aspect
avg	Average
B	Buoyancy
b	Base
$bottom$	Bottom
bub	Bubble
c	Channel
cav	Cavity
$char$	Characteristic
$cond$	Conduction
$conv$	Convection
cp	Contact pressure
$crit$	Critical
cs	Cross-section
$channel$	Channel
D	Drag
d	Dimension
eff	Effective
$enh\ cond$	Enhanced conduction
eq	Equivalent
ev	Evaporation
$excess$	Excess
exp	Experimental
f	Fluid
fb	Flow boiling

fc	Forced convection
fin	Fin
fr	Friction
G	Due to gravity
g	Growth of bubble
h	Hydraulic
I	Due to inertia
i	To be assigned to x-, y-, or z-direction, or number, or phase type
ie	Inlet extension
ifb	Incipient flow boiling
inc	Inclination
int	Interface
j	To be assigned to x-, y-, or z-direction, or number
in	Inlet
inf	Influence
$init$	Initial
k	To be assigned to x-, y-, or z-direction, or number
l	Liquid
le	Leave
$local$	Local
M	Due to mass
m	To be assigned to number
$mconv$	Convection of Marangoni
max	Maximum
$mean$	Mean
n	To be assigned to number
nc	Natural convection
nl	Nucleation
num	Numerical
oe	Outlet extension
ONB	Onset of nucleate boiling
out	Outlet
P	Due to pressure
p	At constant pressure

pc	Phase change
qsd	Quasi-steady drag
r	Reduction
rec	Receding
ref	Reference
rel	Relative
s	Solid
sm	Sauter mean
st	Due to surface tension
$surf$	Surface
sat	Saturation
sl	Shear lift
sp	Single phase
sub	Sub-cooled
T	Turbulent
t	Top
tc	Transient conduction due to stationary bubble
$tcsl$	Transient conduction due to sliding bubble
th	Thermal
tot	Total
tc	Transient conduction
ud	Unsteady drag
V	At constant volume
v	Vapour
vd	Due to viscous dissipation
w	Waiting
x	$x-$direction
y	$y-$direction
z	$z-$direction

Abbreviations

Symbol	Description
3D	Three-dimensional or three dimensions
CAC	Critical aggregation concentration
CFD	Computational fluid dynamics
CHF	Critical heat flux
EDM	Electrical discharge milling
FDB	Fully developed boiling
LHS	Left hand side
MAE	Mean absolute error
MEMS	Micro-electro-mechanical systems
NVG	Net vapour generation
ONB	Onset of nucleate boiling
RHS	Right hand side
SVF	Significant void flow

Chapter 1 Introduction

1.1 Background of Research

Effective cooling techniques are essential for heat sources such as electronic components and optical components, and equipment systems of nuclear and microwave with high frequencies to dissipate the heat. The heat generated from the heat sources is expected to increase in the future as can be seen in Figure 1.1 [1]. Figure 1.1 shows that thermal design powers (TDP) for high performances of semiconductors (ITRS 2004 Update High Perf.) rise linearly in 2009-2010. In following years, the TDP of the semiconductors remains constant associated with smaller sizes of the electronic components, causing increments of dissipated heat. The higher dissipated heat lead to higher tendencies to form local hot spots in the heat sources. By preventing the local hot spots, better designs of cooling devices to dissipate the heat as high as 500-3000 W/cm^2 or 5-30 MW/m^2 are necessary [2]. Such large amounts of heat dissipation are often beyond the capability of conventional cooling technique.

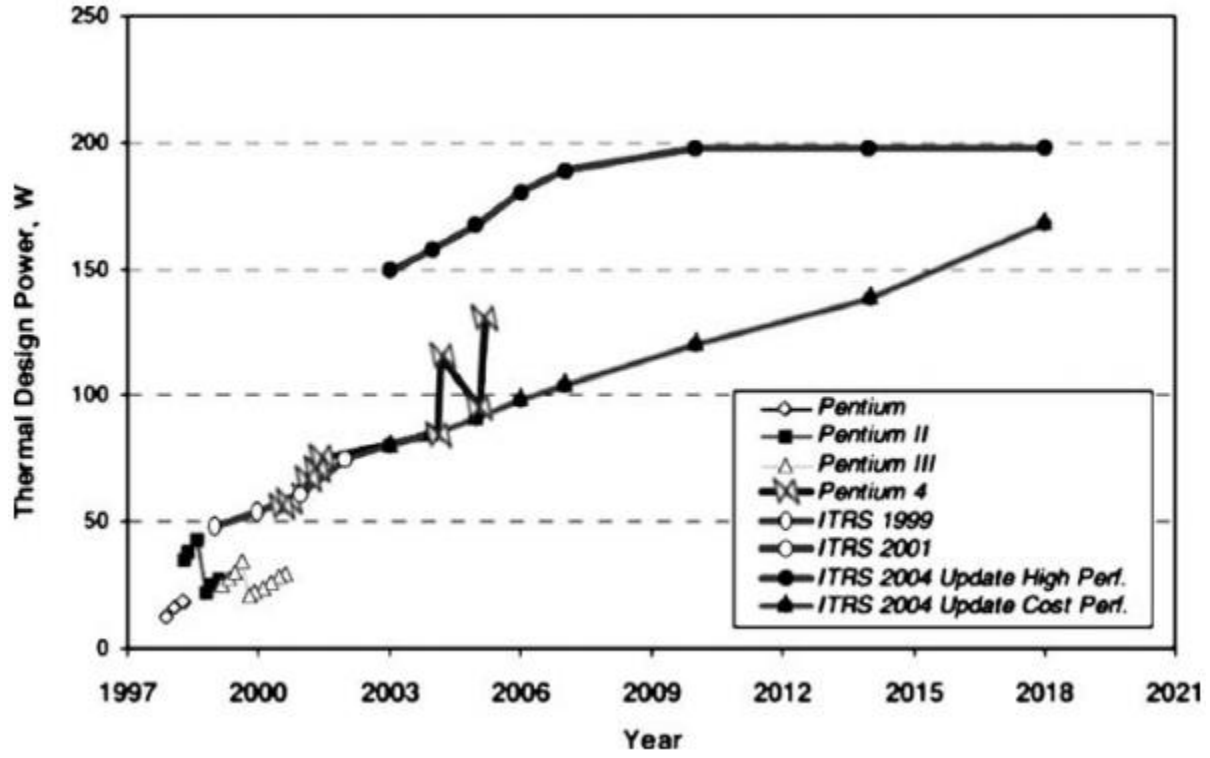


Figure 1.1: International Technology Roadmap for Semiconductors (ITRS) [1]

There are several recent technologies of cooling methods for the heat dissipation from heat sources [3]. One of the efficient liquid cooling methods as found by

Tuckerman and Pease [4] is to attach the micro-channel heat sinks (as high as 790 W/cm^2) made of the materials with high thermal conductivities associated with the flow of liquid to the heat sources. This technique comprises of high surface-area-to-volume ratios that facilitates higher heat dissipation than the conventional-sized channels. For this reason, several studies relating to the micro-channel heat sinks become available. In micro-channels, the heat transfer during flow boiling is higher than single-phase flow of liquid [5] as can be observed in Figure 1.2. In Figure 1.2, the range of heat transfer coefficient h of water which is attainable during the single-phase flow and flow boiling are 8×10^2-7×10^4 W/m^2 K and 6×10^3-2×10^6 W/m^2 K, respectively. The range of h during the flow boiling is higher due to the existence of the bubble interfaces that absorbs more dissipated heat in the form of latent heat at the lower rates of flow [6].

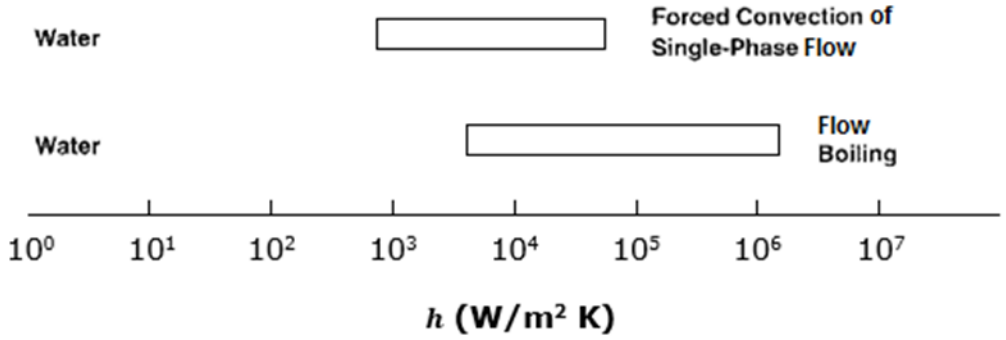


Figure 1.2: Attainable range of heat transfer coefficients h of water under the conditions of forced convection of single-phase flow and flow boiling [5]

By differentiating micro-channels from conventional channels, some of the criteria for classifications have been proposed by researchers. Mehendale et al. [7], Kandlikar and Grande [8], and Kandlikar et al. [9] classified the channels based on hydraulic diameters as listed in Table 1.1, Table 1.2, and Table 1.3, respectively. This study adopts 3 mm as the threshold diameter d_h between macro- and micro-channels, as classified by Kandlikar et al. [9] as a well-established theory for the classification, is unavailable. Nevertheless, this threshold d_h allows more relevant studies to include in the literature review in Chapter 2.

Table 1.1: Classification of Channels from Mehendele et al. [7]

Class of channel	Range of hydraulic diameter d_h
Conventional channels	$d_h \geq 6$ mm
Compact channels	1 mm $\leq d_h \leq$ 6 mm
Meso-channels	100 μm $\leq d_h \leq$ 1 mm
Micro-channels	1 μm $\leq d_h \leq$ 100 μm

Table 1.2: Classification of Channels from Kandlikar and Grande [8]

Class of channel	Range of hydraulic diameter d_h
Conventional channels	$d_h \geq 3$ mm
Mini-channels	200 μm $\leq d_h \leq$ 3 mm
Micro-channels	10 μm $\leq d_h \leq$ 200 μm
Transitional micro-channels	1 μm $\leq d_h \leq$ 10 μm
Transitional nano-channels	0.1 μm $\leq d_h \leq$ 1 μm
Molecular nano-channels	$d_h \leq$ 0.1 μm

Table 1.3: Classification of Channels from Kandlikar et al. [9]

Class of channel	Range of hydraulic diameter d_h
Conventional channels	$d_h \geq 3$ mm
Macro- or mini-channels	200 μm $\leq d_h \leq$ 3 mm
Micro-channels	10 μm $\leq d_h \leq$ 200 μm

There are different cross-sectional shapes of micro-channel heat sinks such as circular, rectangular, square, triangular, and trapezoidal micro-channels that produce different heat transfer performance. The heat transfer performance for different square and circular micro-channels is available in [10, 11]. Based on the literature, the non-circular micro-channels with corners provide the feature as active nucleation sites, serving better heat transfer than the circular micro-channel. On the other hand, the triangular micro-channel (Figure 1.3a) as in [12] has one corner, whereas rectangular (Figure 1.3b) and trapezoidal (Figure 1.3c) micro-channels have two. Therefore, they provide more active nucleation sites and higher heat transfer than the triangular micro-channels. On the other hand, the performance of the heat transfer of the rectangular micro-channels is better than the trapezoidal micro-channel with the lower temperature of the nucleation of bubbles [10, 11]. Therefore, in this study, the rectangular micro-channels are employed. The corresponding schematic diagram depicts in Figure 1.4 associated with the features as follows:

- A fin is between two channels (with channel width W_c, channel height H_c, channel length L_c, total finned surface areas $A_{total,fin}$ in channels or the sum of the surface areas of all fins A_{fin} or $2H_cL_c$, and unfinned portion areas A_{unfin} or W_cL_c, and width W_{fin}). The number of channels changes with W_C and W_{fin}.
- The micro-channels are on the top part of a substrate (with the dimension of $W_b \times H_b \times L_b$, and L_b is equivalent to L_c, and the base area A_b is $W_b \times L_b$) associated with the surface roughness.

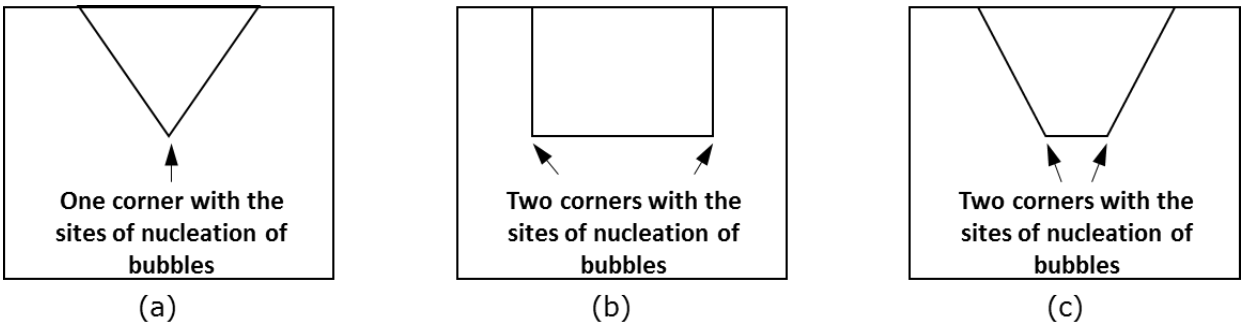


Figure 1.3: Cross-sectional views for (a) triangular (b) rectangular, and (c) trapezoidal micro-channel heat sinks, and the corresponding number of corners with the sites of the nucleation of bubbles

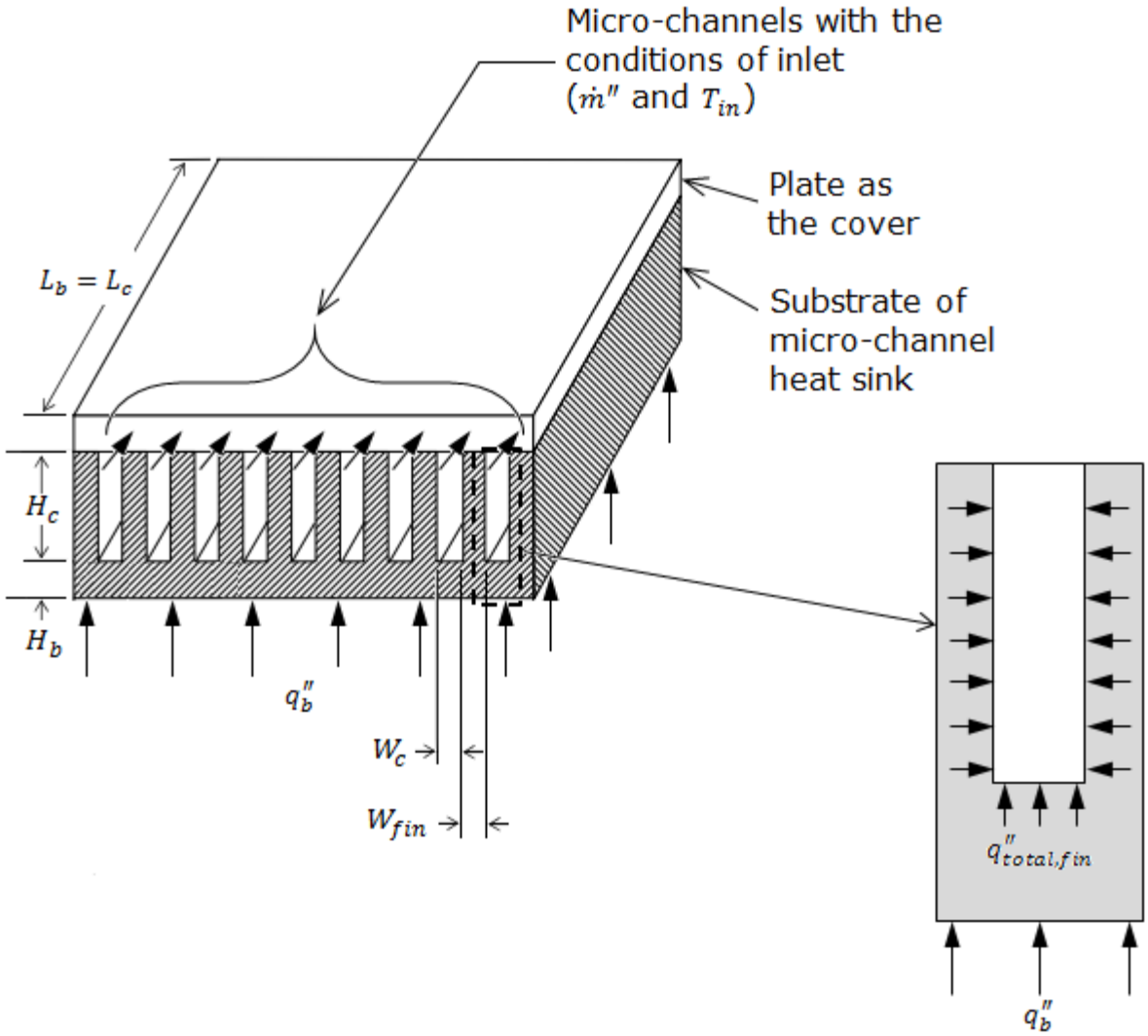


Figure 1.4: A typical example of the schematic diagram of rectangular micro-channel heat sink

- An insulated plate covers the top part of the micro-channels and fins to prevent the leakage of flow, whereas the base of substrate attaches to the top part of the heat sources to allow the heat dissipation.
- Liquid enters the channels from inlets with mass fluxes $\dot{m}''$ (the multiplied product of the density of liquid ρ_l and inlet velocity u_{in}) and temperatures T_{in}.
- The heat input to the channels involves heat fluxes q_b'' at the base and heat fluxes $q_{total,fin}''$ ($= q_b'' A_b / A_{total,fin}$) at the finned surfaces in the channels.

The micro-channel heat sinks can be designed to allow gases (e.g., air) enter into the channels together with liquids to form gas bubbles in which the properties are dissimilar to vapour bubbles nucleating in the channels. Also, the micro-channel heat sinks designed under different levels of gravitation are also available.

Since flow boiling in rectangular micro-channel heat sinks is a promising cooling technique, researchers have performed several related studies as highlighted in the literature [3, 13-15] for better designs. When designing this cooling technology, prediction of the corresponding heat transfer performance is essential by employing prediction methods developed from the heat transfer trends and mechanisms. The available prediction methods are empirical correlations and mechanistic prediction methods. The empirical relationships of the heat transfer during flow boiling in rectangular micro-channels are according to curve fittings to specific heat transfer trends of experimental data. The mechanistic prediction methods of the heat transfer during flow boiling in micro-channels are from understandings of the corresponding heat transfer mechanisms [15]. Hence, the heat transfer trends and mechanisms are necessary, and the related studies have been carried out by researchers [16-21] to propose the prediction methods.

The heat transfer trends of flow boiling in micro-channels are strongly dependent on the heat transfer mechanisms [15]. The heat transfer mechanisms commonly appear in micro-channels are the nucleate boiling and convective boiling as shown in the schematic diagram [22] in Figure 1.5. In Figure 1.5, both the nucleate boiling and convective boiling dominant heat transfer consist of the bubbly, slug, annular, and mist flow regimes. During the nucleate boiling, bubbly and slug regions are more massive. Meanwhile, the annular flow is more extensive during the convective boiling. During the nucleate boiling dominant heat transfer, the heat transfer is strongly dependent on heat fluxes and less reliant on mass fluxes and vapour qualities. On the other hand, the heat transfer is less dependent on heat fluxes and strongly dependent on mass fluxes and vapour qualities for the convective boiling dominant heat transfer. These two mechanisms can also coexist in the micro-channels with complex mechanisms. Hence, the heat transfer mechanisms are affected by both heat fluxes and mass fluxes, nevertheless, depending on channel sizes and shapes, fluid types, etc. The substrate materials

also can change the flow boiling process as a result of different axial heat conduction with different thermal conductivities of substrate materials as evidence in the studies of single-phase flow [23-25]. Although some studies propose the two heat transfer mechanisms during the flow boiling in micro-channels, the actual heat transfer mechanisms are more complicated than these mechanisms. Other mechanisms are also significant [26] such as:

- Enhanced mixing of fluid away from the bubble due to rapid bubble growth and collapse.
- Liquid flow modification at downstream of an attached or detached bubble.
- The heating of a thin liquid layer sandwiched between a big bubble and the heat transfer surface.

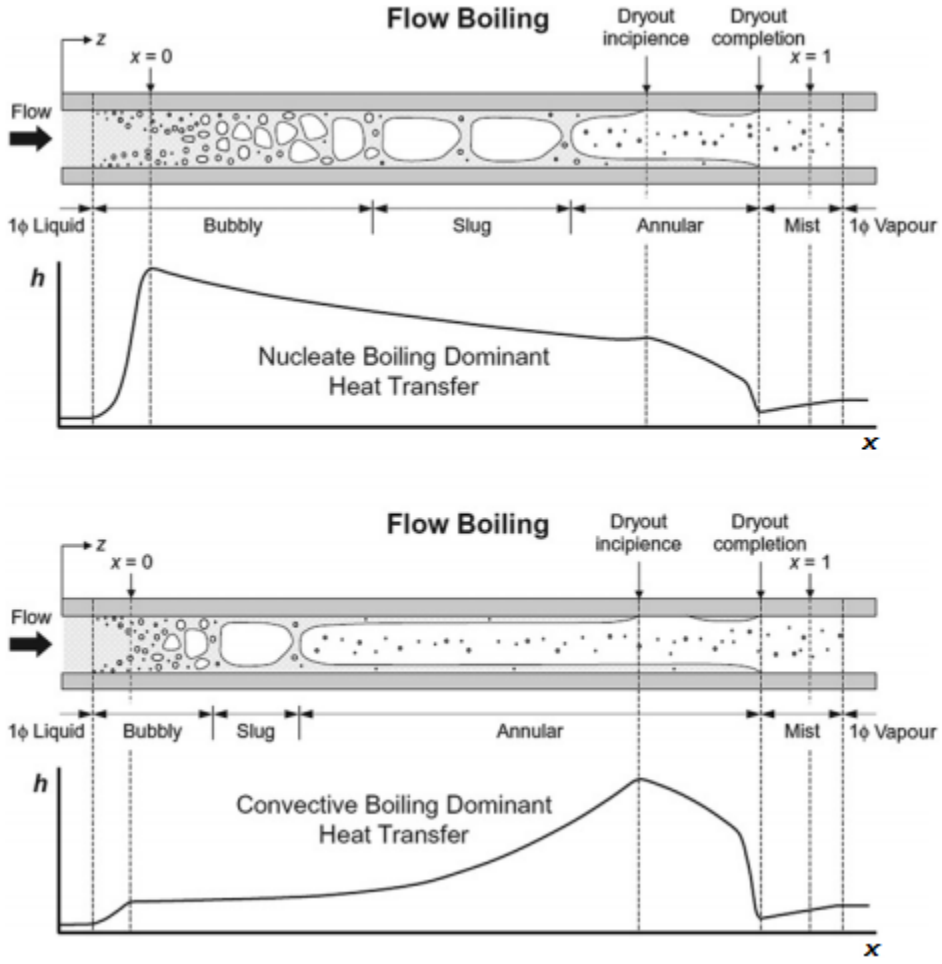


Figure 1.5: Schematic diagram of flow regimes and heat transfer coefficients along a mini- or micro-channel with a uniform circumferential heat flux for (a) nucleate boiling and (b) convective boiling dominant heat transfer [22]

When investigating the heat transfer during the flow boiling in micro-channels through experiments, contradictions between experimental results with similar conditions are possible [15]. These occurrences are likely due to:

- The improper data collection methods, designed test facility, test sections, and experiments, and flow instabilities [27] contributing to the discrepancies.
- Difficulties in taking measurements. For instance, measuring devices such as sensors are hardly setup at solid-fluid interfaces due to small length scales of test sections and short time scales of flow activities [28]. These disadvantages produce drastic errors in the measurements when the experimental procedure is inappropriate [14, 15, 29].
- Failure to control some significant operating conditions such as surface roughness, channel dimension uncertainties, etc. [15] also causing the discrepancies.

These limitations of the experimental studies warrant the need of alternating approaches for the investigation of the heat transfer.

Since the experimental data of flow boiling in micro-channels differ from each study, nearly all the existing prediction methods of empirical correlations proposed from these data are inadequate to predict the heat transfer [9, 15, 30]. In other words, these empirical relationships provide limited tested fluids and conditions [15]. Also, the empirical correlations are inaccurate due to:

- Employing or extrapolating them to different operating conditions, including surface roughness, channel dimension uncertainties, etc. that are hardly controlled [15]. For instance, the accuracy of most correlations deviated with the changes of diameter from macro- to micro-scale and the heated length of channels due to the variation of the heat transfer mechanisms of flow boiling. Moreover, the transition from conventional-scale to micro-scale gives significant effect on flow boiling associated with unfamiliar aspects, especially for the nucleation and bubble dynamics as stated by Peng [31].
- Referring to data read from the different setup of the test section (e.g., various heating methods) and different data reduction methods (e.g., measuring either local or average heat transfer coefficients).
- Collecting heat transfer data from unreasonable test facility, measurement system, and improper data reduction methods.
- Neglecting or lacking of understandings of the heat transfer mechanisms that produce local phenomena of heat transfer through flow patterns associated with bubble dynamics that influence the heat transfer [15].
- Disregarding variables that are significant on the heat transfer such as properties of substrate materials, fluids, etc. also produce the inaccuracies.

With these inadequacies of the empirical correlations, the more reliable mechanistic prediction methods that consider the flow regimes associated with bubbles dynamics are essential to understanding the corresponding heat transfer mechanisms [15].

This development of mechanistic prediction methods requires the investigation of the flow regimes associated with bubble dynamics relating to the heat transfer and mechanisms [14, 15] to understand the heat transfer trends and mechanisms [32]. The flow regimes are classified as bubbly, slug, annular, and mist as depicted in Figure 1.5 [22] and sometimes they are categorised into subcooled flow boiling and saturated flow boiling regimes [19]. These flow regimes emerge and vary with different operating conditions and are accessible in flow regime maps, which are x-y plots that show the variation of the flow regimes with variables. The investigation of flow regimes serves essential details for better understanding of the complication of the heat transfer mechanisms [9, 33, 34]. These details aid to focus on each particular flow regime for more accurate mechanistic prediction methods of the heat transfer coefficient. The details of flow regimes and heat transfer behaviours also facilitate the exploration of new heat transfer mechanisms since the actual mechanisms are more complicated than nucleate boiling and convective boiling as already mentioned.

The flow regime of bubbly flow involving bubble dynamics and liquid flow is evident in some studies, however, absent in other studies [15]. The bubbly flow is unobtainable due to the short lifespan of bubbles in which they either coalesce or grow to the channel size quickly [35]. Nevertheless, the bubbly flow in micro-channels serves the advantage for high heat dissipation associated with low mass quality corresponding to the nucleate boiling as stated by Houshmand and Peles [26]. On the other hand, Kandlikar [36] also attempted to obtain the condition of flow boiling with bubble nucleation while the bulk stream is still subcooled to avoid elongated bubble flow pattern which is a limiting factor in the heat transfer. The bubbly flow is dominant during the subcooled flow boiling regime as evident in the study of Lee and Mudawar [37]. They [37] also mentioned that higher heat transfer coefficients are possible with subcooled flow boiling as compared to saturated. Therefore, studies relating to the bubbly flow during the subcooled flow boiling in micro-channels are crucial.

Flow boiling begins when first bubble nucleates, however, unlike the conventional-size channels, the characteristics of flow boiling emerge in the micro-channels before the nucleation of the first bubble [31]. Also, the heat transfer at this instant is higher as compared to flow boiling in conventional-sized channels. This phenomenon is evident in the experimental studies of Peng and Wang [38-41] and Peng et al. [42]. Peng and Wang [38-41] and Peng et al. [42] observed that the heat transfer exhibited the characteristics of flow boiling in rectangular micro-

channels at extremely low superheat about 2°C. Peng et al. [42] found that heat fluxes higher than 10^6 W/m^2 or superheats above 100°C at atmospheric pressure produce flow without bubble nucleation in micro-channels if employing a good seal between the glass cover plate and micro-channels. This occurrence is possibly due to the strong influence of the size scale of the liquid geometry on the phase-change transition and corresponding flow boiling [42]. With this hypothesis, two concepts of evaporating space and fictitious boiling are proposed [40]. The evaporating space is the required space for the evaporation whereas fictitious boiling occurs when the heat transfer performance possesses nucleate boiling characteristics even though the bubbles are absent in the channels. If the micro-channel size is smaller than the evaporating space, fictitious boiling occurs. On the other hand, if the setup is improper in which some narrow gaps between the glass cover and the plate exist, small bubbles nucleate at low superheats and heat fluxes. These holes that are smaller than the channel size become the active nucleation sites. The fictitious boiling involves extraordinary phase-change transport phenomena of hydrodynamics and thermodynamics conditions, and the study regarding this aspect is incomplete without the exploration of the corresponding mechanisms. Also, the fictitious boiling is unavailable in the existing studies employing numerical methods that facilitate the local investigation.

Nevertheless, the exploration of the liquid flow and bubble dynamics are incomplete in which measurement of local values is arduous and the limitation to visualise the bubble dynamics through experiments persist [14]. The hurdle to observe the bubble dynamics is evident in the study of Barber et al. [43]. With these limitations, researchers usually sceptically speculate the heat transfer mechanisms rather than understand them through proven principles, indicating that the knowledge of the mechanisms is insufficient from the experiments. With this limitation of experimental tests, numerical methods are paramount importance to explore the regional mechanisms. The numerical methods are the reliable approach to examine the local mechanisms of heat transfer, especially those details which are inaccessible from the experiments for the development of more reliable mechanistic prediction methods [14]. Nevertheless, the numerical techniques still require validation from experimental data.

By exploring and understanding these heat transfer mechanisms from liquid flow and bubble dynamics just before and during the flow boiling in micro-channel heat sinks, researchers and designers can incorporate the knowledge to develop more reliable prediction methods. More reliable prediction methods assist in designing new micro-channel heat sinks and avoiding repeating experiments which are costly and tedious in procedure.

1.2 Objective

The primary objective (or aim) of this study is to investigate the mechanisms of the flow boiling of subcooled liquid with the low mass qualities of vapour in rectangular micro-channel heat sinks numerically. The sub-objectives of this study are listed as follows:

- To explore the mechanisms during flow boiling of subcooled liquid with the bubbly flow in micro-channel heat sinks from the effects of mass fluxes, heat fluxes and inlet temperatures.
- To address the variations of mechanisms during flow boiling of the subcooled liquid with the bubbly flow in micro-channel heat sinks due to the impacts of substrate materials.
- To identify the changes of mechanisms during the flow boiling of subcooled liquid with the bubbly flow in micro-channel heat sinks due to of the effects of working fluids.

1.3 Outline of Thesis

After the introduction of research in this chapter, or Chapter 1, the following chapters of this thesis comprise of:

- Chapter 2 Literature Review: presents the past and current state regarding findings and understandings from literature related to this study. This chapter also summarised the corresponding gaps based on the evaluated research about this study.
- Chapter 3 Methodology: describes the operating parameters and numerical models for the investigation of the dominance of mechanisms during the flow boiling of subcooled liquids with the low mass qualities of vapour in micro-channel heat sinks in this study.
- Chapter 4 Effects of Mass Fluxes, Heat Fluxes, and Inlet Temperatures: discusses the results of the changes of mechanisms due to the effects of mass fluxes, heat fluxes, and inlet temperatures.
- Chapter 5 Effects of Substrate Materials: discusses the results of the changes of mechanisms due to the effects of substrate materials.
- Chapter 6 Effects of Working Fluids: presents the results and discussion of the changes of mechanisms when employing different working fluids.
- Chapter 7 Conclusion: concludes the discussion of results.

Chapter 2 Literature Review

This literature review describes the past and current state regarding significant findings including understandings from the literature of existing studies related to this study which are:

- Experimental studies of heat transfer trends and mechanisms of flow boiling of subcooled liquids in rectangular micro-channels.
- Empirical correlations of heat transfer during flow boiling in micro-channels.
- Flow regimes of flow boiling in rectangular micro-channels.
- Experimental studies of characteristics and mechanisms of nucleate boiling during flow boiling of subcooled liquids in rectangular micro-channels.
- Numerical studies of characteristics and mechanisms of nucleate boiling during flow boiling of subcooled liquids in rectangular micro-channels.
- Mechanistic prediction methods of nucleate boiling during flow boiling in rectangular micro-channels.

The sufficient literature employed in this review serves the purpose of the presentation without making attempts to cite all literature. Based on the reviewed literature, each section of this chapter also summarises the corresponding gaps based on the evaluated research about this study to justify the objectives of this work as listed in Section 1.2. This review also provides useful information when conducting the investigation.

2.1 Experimental Studies of Heat Transfer Trends and Mechanisms of Flow Boiling of Subcooled Liquids in Rectangular Micro-Channels

For the sake of designing better cooling systems of flow boiling in rectangular micro-channels, the identification of the corresponding heat transfer trends and mechanisms are essential. For this purpose, researchers have carried out experimental studies to investigate heat transfer of flow boiling of subcooled liquids in micro-channels as cited in the recent review articles [13, 14]. By conducting the experimental studies, researchers commonly employ:

- Microscopes and high-speed cameras to visualise the flow patterns in the micro-channels.
- Flow meters to measure the flow rate of the working fluids from reservoir tank or syringe pumps.
- Cartridge heaters connected to the power supply to heat up the micro-channels.

- Thermocouples or thermistors attaching at the base of the micro-channel heat sink to measure the temperature.

The heat transfer trends during the flow boiling in micro-channel are according to boiling curves. A typical example of the boiling curve of heat flux against heated surface temperature in channels under different stages of flow boiling condition is shown in Figure 2.1 [19]. At point A, the fluid enters the channel as a subcooled single-phase liquid undergoing a heat transfer mode of single-phase convective heat transfer. In the single-phase regime, the wall temperature increases linearly with the heat flux and exceeding saturation temperature at point B. From point B, when further increases q_b'' until the stage C, the wall temperature exceeds the threshold value for the occurrence of the onset of nucleate boiling (ONB). Beyond point C, the boiling curve becomes steeper, and the total heat transfer involves the single-phase convection and the nucleate boiling in the channel. When the heat flux exceeds the stage D, the fluid experiences a fully developed boiling (FDB) and the regime between point C and D is the partial boiling regime. As the fluid continues to absorb heat, saturated boiling initiates at point E in which the bulk temperature reaches local saturation temperatures. Above point E, the channel dry-out occurs as the amount of the vapour increases.

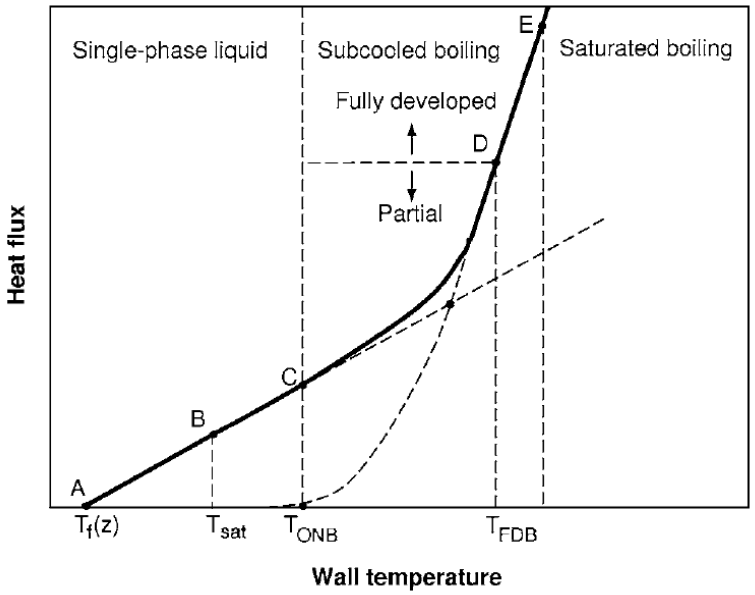


Figure 2.1: Boiling curve of flow boiling in channels [19]

The ONB refers to the location of the nucleation of the first bubble from the inlet of channels at the state of subcooled boiling as mentioned in the literature [44, 45]. The ONB in micro-channels has attracted the attention of researchers for few reasons [6]:

- Determining the upper limit of design for heat sinks intended for the single phase cooling only, and the lower limit for two-phase heat sinks planned for the maximum heat dissipation with the prediction.
- Identifying the abrupt transition from the liquid flow to two-phase slug flow in micro-channel from the calculation in which the change is unlikely to emerge from the conventional channels.
- Providing the understanding of the phenomena of ONB to design the micro-channel heat sinks from the prediction.

By identifying the ONB, researchers commonly employ two approaches. The first method is determining the first set of bubbles appear on the surface of the channels after the temperature on the surface of the channels exceeds the saturation temperature [45, 46]. The first set of bubbles often appears near the outlet of the channels. The second approach is identifying a sudden change of the slope of the temperature and pressure drop against the heat flux.

Researchers have examined the trend of ONB through experimental studies, and Table 2.1 summaries the operating parameters of selected experimental studies in the literature. Qu and Mudawar [6] studied the ONB in channels with the small increment of $q''_{total,fin}$ from low values for all tested conditions until observing the first set of bubbles. Then, $q''_{total,fin}$ that produces the ONB refers to q''_{ONB}. They [6] found that q''_{ONB}, $\Delta T_{sub,out}$, and channel bottom surface superheat (3-21°C which is insignificant) increase when increasing u_{in} and reduce of T_{in}. Liu et al. [47] have collected the q''_{ONB} reading with the similar procedure as Qu and Mudawar [6] and observed that when increasing $\dot{m}''$, p_{out}, or H_c, or decreasing T_{in} or W_c, q''_{ONB} increases.

Table 2.1: Operating parameters of selected experimental studies of heat transfer trends during ONB in rectangular micro-channels in the literature

Literature	Operating parameter
Qu and Mudawar [6]	Working fluid of deionised water; substrate of copper; p_{out} of 1.2 bar; T_{in} of 30-90°C; u_{in} of 0.13-1.44 m/s; twenty-one 231 μm wide, 713 μm high, and 4.48 cm long micro-channels.
Liu et al. [47]	Working fluid of deionised water; substrate of copper; q''_b of 9.88-68.81 W/cm^2; u_{in} of 0.32-0.92 m/s; T_{in} of 41.2-92.0°C; p_{out} of 97844-107523 Pa; twenty-five 275 μm wide, 636 μm high, and 54.4 mm long micro-channels, W_s of 118 μm H_b of 2464 μm, and W_s of 542 μm.

Other than the ONB, researchers have also studied the heat transfer trends and mechanisms during flow boiling in rectangular micro-channels, and Table 2.2 summaries the operating parameters of selected experimental studies in the literature.

Table 2.2: Operating parameters of selected experimental studies of heat transfer trends and mechanisms of flow boiling of subcooled liquids in rectangular micro-channels in the literature

Literature	Operating parameter
Qu and Mudawar [16]	Working fluid of water; substrate of copper; q_b'' of 20-135 W/cm^2; $\dot{m}''$ of 135-402 kg/m^2 s; T_{in} of 30-60°C; p_{out} of 1.17 bar; X_e up to 0.2; twenty-one 231 μm wide, 713 μm high, and 4.48 cm long micro-channels, and W_{fin} of 118 μm on 1 cm × 4.48 cm with a thickness of 2462 μm of the substrate.
Chen and Garimella [18]	Working fluid of dielectric liquid FC-77; substrate of silicon; q_b'' of 80-730 kW/m^2; $\dot{Q}$ of 35-60 ml/min; T_{in} of 71°C; p_{out} of 1 atm; and twenty-four 389 μm wide, 389 μm high, and 12.7 mm long micro-channels on 12.7 × 12.7 mm^2 of the substrate.
Chen and Garimella [34]	Working fluid of dielectric liquid FC-77; substrate of copper; q_b'' of 0.9-1.61 W/cm^2; $\dot{Q}$ of 30-50 ml/min; subcooling ΔT_{sub} or $T_{sat} - T_{in}$ of 17 K; p_{out} of 1 atm; and ten 504 μm wide, 2.5 mm high, and 25.4 mm long mico-channels on 25.4 mm × 25.4 mm × 7 mm of the substrate.
Liu and Garimella [19]	Working fluid of water; substrate of copper; maximum q_b'' of 129 W/cm^2; $\dot{m}''$ of 221-1283 kg/m^2 s; T_{in} of 67-95°C; maximum X_e of 0.2; micro-channel heat sink I is 275 μm wide, 636 μm high, and 25.4 mm long, and W_{fin} of 542 μm; micro-channel heat sink II is 406 μm wide, 1063 μm tall, and 25.4 mm long; 25.4 × 25.4 mm^2 substrate; W_{fin} of 597 μm; and 7.5 μm wide re-entrant cavities.
Lee and Mudawar [37, 48]	Working fluid of HFE 7100 (T_{sat} of 60°C); substrate of copper; q_b'' of 0-750 W/cm^2; $\dot{m}''$ of 670-6730 kg/m^2 s; T_{in} of -30-0°C; p_{out} of 1.138 bar; 11-24 of 123.4-259.9 μm wide, 304-1041.3 μm high, and 25.27 mm long micro-channels, and W_{fin} of 84.2-205.0 μm on 25.3 × 25.3 mm^2 of the substrate.
Harirchian and Garimella [20, 32, 49]	Working fluid of dielectric liquid FC-77; substrate of silicon; maximum q_b'' of 640 kW/m^2; $\dot{m}''$ of 250-1600 kg/m^2 s; ΔT_{sub} of 5°C; p_{out} of 1 atm; 2-60 of 100-5850 μm wide, 400 μm high, and 12.7 mm long micro-channels and W_{fin} of 100-300 μm on 12.7 × 12.7 mm^2 of the substrate with a thickness of 650 μm.
Bertsch et al. [50]	Working fluid of refrigerant R-134a and R-245a; substrate of copper; $q''_{total,fin}$ of 0-22 W/cm^2; $\dot{m}''$ of 20-350 kg/m^2 s; T_{sat} of 8-30°C; p_{sat} of 125-750 kPa; X of 0.2-0.9; 17-33 of 381-762.0 μm wide, 953-1905 μm high, and 9.53 mm long micro-channels, and W_{fin} of 381-762.0 μm on 25.3 × 25.3 mm^2 of the substrate.

Table 2.2: (Continued)

Literature	Operating parameter
Galvis and Culham [22]	Working fluid of water; substrate of copper; $q''_{total,fin}$ within 4000 kW/m^2; $\dot{m}''$ of 340-1296 kg/m^2 s; ΔT_{sub} of 50.7-54.2°C; and p_{out} of 1 atm; ΔT_{sub} of 99°C; two micro-channel heat sinks; Each micro-channel heat sink has one channel with different size of $W_c \times H_c \times L_c$ of 241 × 198 × 21900 μm^3 and 471 × 378 × 21900 μm^3 on 44 × 10 × 13 mm^3 of the substrate.

Qu and Mudawar [16] found that h strongly dependent on $\dot{m}''$ but weakly dependent on q''_b , indicating that the dominant heat transfer mechanism is convective boiling. The convective boiling in the study corresponds to the annular flow. Therefore, the annular flow becomes apparent with a sudden transition when thermodynamic equilibrium quality X_e near 0. The annular flow regime is dominant at moderate and high heat fluxes. On the other hand, an unexpected trend becomes apparent in which h decreases with X_e due to droplet entrainment at the onset of annular flow regime near the outlet. The thermodynamic quality or vapour quality at the exit, or exit quality X_e is the mass fraction of vapour in which the relationship is [21]:

$$X_e = \frac{1}{\boldsymbol{h}_{lg}}\left[\frac{Q_l}{\dot{m}} - c_{p,l}(T_{sat} - T_{in})\right] \tag{2.1}$$

where $\boldsymbol{h}_{lg}$ is the enthalpy of vaporisation, Q_l is the volumetric flow rate of liquid, $\dot{m}$ is the mass flow rate, $c_{p,l}$ is the liquid specific heat at constant pressure, T_{sat} is the saturation temperature, and T_{in} is the inlet temperature. Some researchers, for instance, Liu and Garimella, define local vapour quality X as:

$$X = \frac{\boldsymbol{h}_l - \boldsymbol{h}_{sat}}{\boldsymbol{h}_{lg}} \tag{2.2}$$

where $\boldsymbol{h}_l$ is the enthalpy of liquid and h_{sat} is the enthalpy at saturation conditions. In the equation of X_e (2.1) or X (2.2), the enthalpy term, which is directly proportional to the mass of vapour produced, is often employed instead of the mass of vapour term for the ease of calculation.

Chen and Garimella [18] observed that h increases with q''_b, and independent on $\dot{Q}$ in fully developed boiling at lower q''_b. At higher q''_b (exceeding 542, 673, and 730 kW/m^2 for 35, 47, and 60 ml/min, respectively), the reversed trend begins in which h decreases with the increase of q''_b due to partial dry-out in some micro-channels and forming stronger fluctuation of surface temperatures. In the later study, they [34] discovered that the dependent of q''_b on surface temperature $T_{total,fin}$ becomes weaker when flow boiling begins. Also, h increases with $\dot{Q}$, and surface dry-out first

occurs near the outlet according to surface temperature measurements at three locations (near the inlet, middle, and outlet of the channels).

Liu and Garimella [19] found that $\dot{m}''$ and T_{in} affect the ONB whereas insignificant on the boiling curve once the ONB has occurred. Notwithstanding, the inlet temperature or inlet subcooling is possible to modify the heat transfer mechanisms as mentioned by Saha [15], and there is less investigation in this aspect.

Both Chen and Garimella [34] and Liu and Garimella [19] showed that the boiling curves overlap after the ONB for all measured flow rates. When increasing q_b'' further, the curves diverge and become dependent on mass flux.

Lee and Mudawar [37, 48] have employed the low fluid temperatures producing subcooled flow boiling conditions in which the outlet fluid temperatures never reach saturation for the study of the heat transfer. This situation is dissimilar to most of the two-phase micro-channel heat sink studies in which the annular film evaporation is the dominant mechanism for heat removal. They discovered that [37, 48] decreasing fluid temperature delays the onset of boiling and enhances the cooling performance. Also, the heat flux along the micro-channel surfaces decreases when implementing small d_h of channels with larger total wetted areas, and therefore the void fraction reduces along the micro-channels. Also, lowering the micro-channel width to a limit will cause bubbles to span the entire width and provide the early transition to slug flow and reduce the cooling effectiveness. These complex effects warrant the need for a comprehensive model for subcooled flow boiling in micro-channel heat sinks. On the other hand, premature critical heat flux (CHF) can occur at low mass fluxes. This incidence is due to the reverse flow of vapour towards the inlet followed by the development of a large vapour mass in the upstream plenum that prevents liquid from flowing into the channels. Nevertheless, the premature CHF diminishes when decreasing fluid temperature or increasing flow rate or both. During the premature CHF, the transitory dry-out occurs in the channels associated with rising of surface temperatures, and the vapour build-up causes an increase of the upstream pressure to remove the vapour mass to the outlet. This process repeats in a cyclical manner associated with the gradual increment of surface temperatures with each new cycle.

Harirchian and Garimella [20, 32, 49] have evaluated the heat transfer during the flow boiling in seven horizontal rectangular micro-channel heat sinks. They [49] stated that cross-sectional area of micro-channels is a more appropriate parameter to determine the heat transfer performance, instead of the width, depth, or aspect ratio of micro-channels, individually. They [32, 49] observed that:

- The ONB occurs with a sharp drop of surface temperature as illustrated in the boiling curve in Figure 2.2. The temperature then overshoots with a sufficiently small increment of $q''_{total,fin}$ for all tested conditions. In general,

the ONB occurs at a low temperature and heat flux for lower $\dot{m}''$. The boiling curves are also independent on $\dot{m}''$ in the nucleate boiling regimes for a fixed channel size but dependent on $\dot{m}''$ at sufficiently high $q''_{total,fin}$. This trend also shows up in [19, 34]. The nucleate boiling is dominant up to high heat $q''_{total,fin}$ for W_c of 400 μm and more substantial. Nevertheless, the trend for small W_c of 100 μm in Figure 2.2b is different from larger W_c in which T_{surf} is smaller at a fixed $q''_{total,fin}$ as compared to larger W_c below $q''_{total,fin}$ of 125 kW/m^2. This occurrence is due to the rapid increase of vapour quality and early formation of annular flow with such small W_c.

- When increasing W_c for a fixed $\dot{m}''$, the boiling curves converge into a single curve after the ONB associated with a weak dependence of $T_{total,fin}$ on $q''_{total,fin}$ regardless of the flow pattern. This occurrence shows that W_c is independent on the boiling curves, showing the characteristic of nucleate boiling dominance. At higher $q''_{total,fin}$, T_{surf} becomes more dependent on $q''_{total,fin}$ and the boiling curves diverge for different W_c.
- Local h (measured near the outlet) is independent on $\dot{m}''$ in the nucleate boiling regimes for a fixed channel size. However, local h is dependent on $\dot{m}''$ in the dominant region of convective boiling at higher $q''_{total,fin}$ and more heat dissipation as $\dot{m}''$ increases as shown in Figure 2.3.
- Local h is independent of channel size for W_c of 400 μm and broader.
- At a fixed $q''_{total,fin}$ and cross-sectional areas A_c greater than 0.089 mm^2 (250 mm wide and 400 mm high), nucleate boiling is dominant up to extremely high $q''_{total,fin}$ as illustrated in Figure 2.4, and local h is independent on channel size.
- In Figure 2.4, local h is higher for A_c smaller than 0.089 mm^2 at $q''_{total,fin}$ below 150 kW/m^2. When $q''_{total,fin}$ above 150 kW/m^2, the curve crosses over and is lower than larger micro-channels due to high X_e. For this reason, slug flow begins immediately at the incipience of boiling since these studies employ extremely low subcooling (ΔT_{sub} of 5°C), and churn/annular flow also forms at low $q''_{total,fin}$. The churn/annular flow that possesses the feature of vapour confinement provide larger local h as the heat transfer consists of both nucleate boiling and liquid film evaporation mechanisms. Also, $q''_{total,fin}$ allows smaller variation of $T_{total,fin}$ due to the dominance of nucleate boiling when A_c smaller than 0.089 mm^2.
- The flow becomes asymmetric when implementing larger W_c of channels, or larger aspect ratio in which two different flow patterns distribute at each side across the channels.

- Also, in Figure 2.3 and Figure 2.4, at higher $q''_{total,fin}$, a decrease of the local h decreases due to partial drying of the heated surfaces.
- On the other hand, at a fixed q''_b as displayed in Figure 2.5, local h increases with W_c (dissimilar to Figure 2.4) and also $T_{total,fin}$. However, increasing W_c decreases the maximum allowable q''_b (from q''_b of 640 to 300 kW/m^2 when W_c decreases from 5850 μm to 100 μm) due to smaller surface enhancement with larger micro-channels. In the study, the micro-channels with large W_c has less number of channels and therefore providing low surface areas in the channels to dissipate heat from the base, and the maximum allowable q''_b is low.

Bertsch et al. [50] have studied the heat transfer during the flow boiling in horizontal rectangular micro-channel heat sinks. They [50] found that h increases significantly with $q''_{total,fin}$ and X, but only slightly with $\dot{m}''$ and p_{sat} within the tested conditions, indicating the nucleate boiling dominates the heat transfer. When X is above 0.5, h decreases rapidly. Hence, the maximum h occurs at X between 0.1 and 0.5 depending on the tested conditions. R-134a is superior in the heat transfer in the flow boiling regime as compared to R-245fa due to the higher molecular mass and surface tension. The heat fluxes for ONB becomes higher when increasing $\dot{m}''$ for both fluids in the tested condition. On the other hand, h weakly increases when increasing $\dot{m}''$ and almost constant with T_{sat} in this study. When d_h is smaller, h becomes higher.

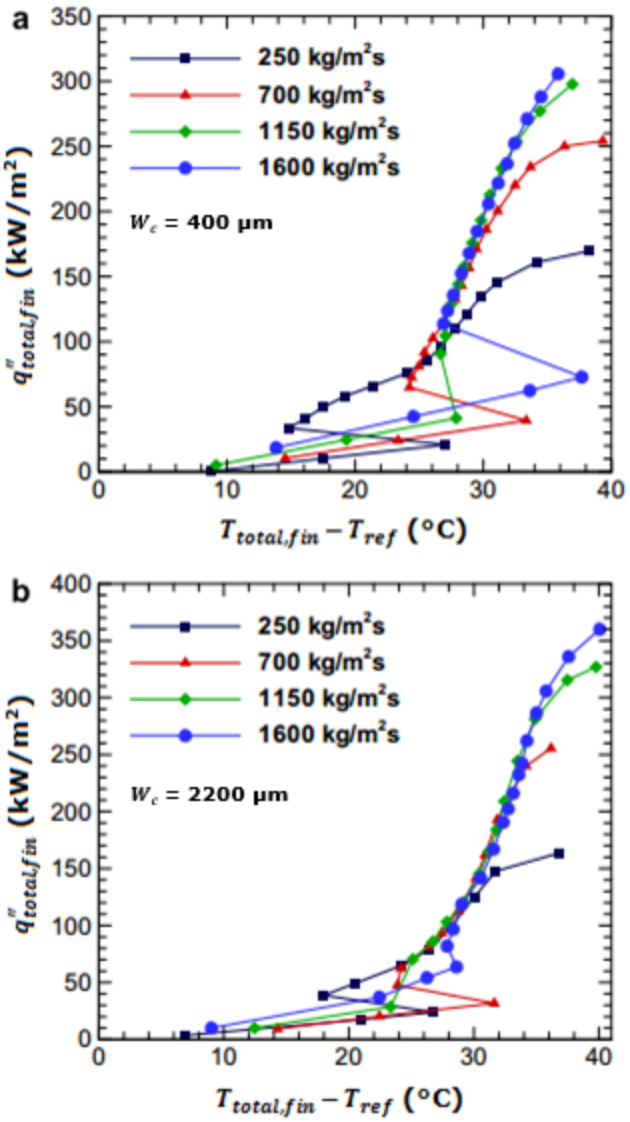


Figure 2.2: Boiling curves for different $\dot{m}''$ for (a) W_c = 400 μm and (b) W_c = 2200 μm

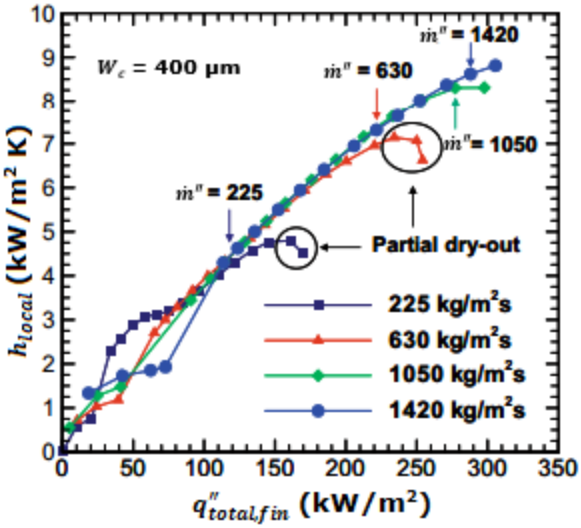


Figure 2.3: h_{local} against $q''_{total,fin}$ for each mass flux $\dot{m}''$ in 400 μm wide and 400 μm deep of micro-channels [20, 32, 51]

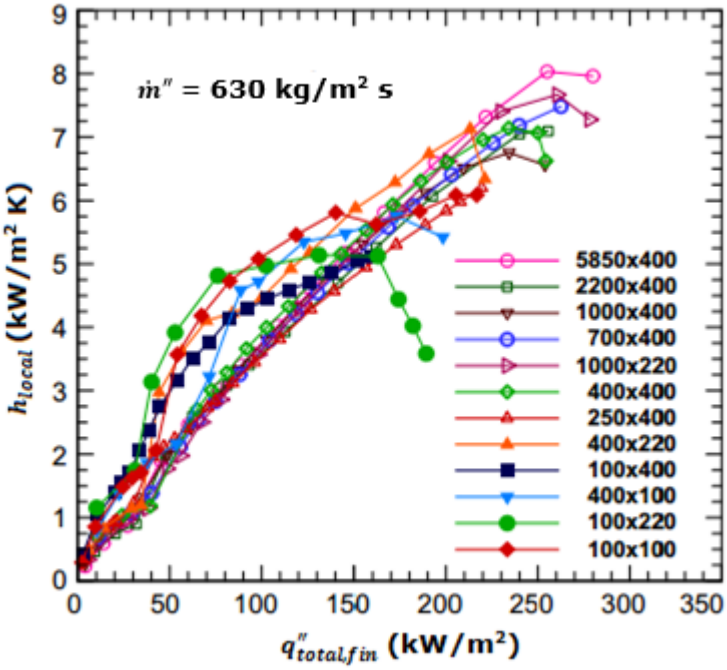


Figure 2.4: h_{local} against $q''_{total,fin}$ of the micro-channels for each width [49] $\dot{m}''$ = 630 kg/m² s

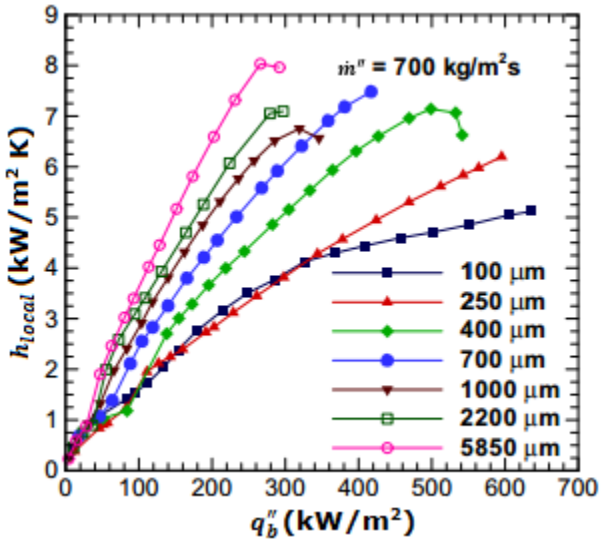


Figure 2.5: h_{local} against base heat flux q_b'' of the micro-channels for each width [20]

Galvis and Culham [22] have investigated the heat transfer during the flow boiling in two horizontal rectangular micro-channel heat sinks. They [22] found that $q''_{total,fin}$ for the ONB increases when increasing $\dot{m}''$ for 241 × 198 µm² channel as shown in the boiling curves in Figure 2.6. This occurrence is due to the reduction of thermal boundary layer thickness that suppresses the ONB until the superheat becomes sufficiently high. After the ONB, the nucleate boiling in which the slopes of boiling curves of all $\dot{m}''$ all become steeper before the dry-out and converge into a single curve above 7 K of superheat. In other words, the boiling curves are unlikely to vary with the change of $\dot{m}''$, showing that the boiling mechanism is nucleate boiling dominance in 241 × 198 µm² channel. This trend is also similar to Harirchian and Garimella. For 471 × 378 µm² as depicted in Figure 2.7, the convergence of the boiling curves into a single curve is absent, implying that the convective boiling dominates over nucleate boiling.

On the other hand, Galvis and Culham [22] also found that two-phase heat transfer coefficient h_{tp} decreases when increasing X as depicted in Figure 2.8 and Figure 2.9 for the micro-channels with dimension of 241 × 198 × 21900 µm³ and for 471 × 378 × 21900 µm³, respectively. In Figure 2.10 for 241 × 198 × 21900 µm³ and Figure 2.11 for 471 × 378 × 21900 µm³ of micro-channel, h_{tp} also reduces when increasing q'' as also reported in the study of Steinke and Kandlikar [33]. When h_{tp} decreases down to about 1000 kW/m² of $q''_{total,fin}$ for 241 × 198 × 21900 µm³, h_{tp} remains unchanged with X before the dry-out for all $\dot{m}''$ as shown in Figure 2.10. This h_{tp} trend converges into single boiling curve after 1000 kW/m² of $q''_{total,fin}$ in Figure 2.6 and associates with the slug flow from the flow visualisation. This outcome indicates that the flow boiling is nucleate boiling dominance.

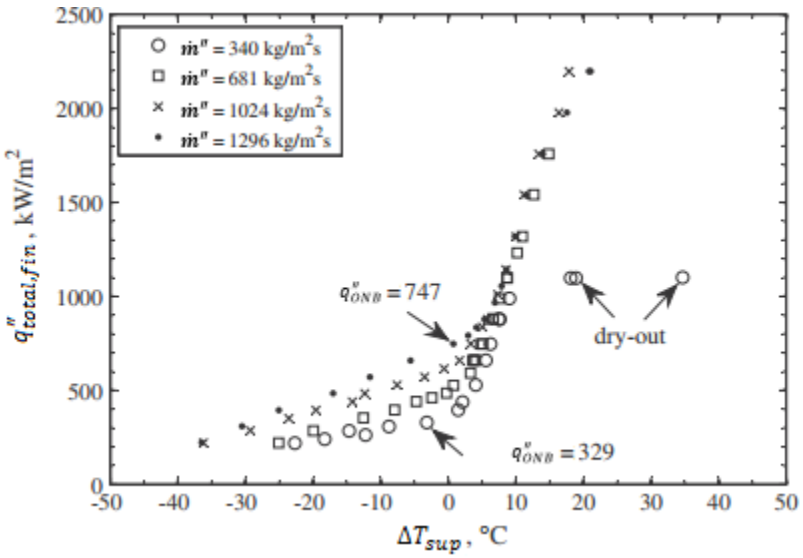


Figure 2.6: Boiling curves (ΔT_{sub} of 50°C) of micro-channel with channel width, height, and length of 241 × 198 × 21900 μm³ [22]

From the investigation of Galvis and Culham [22], h_{tp} for $\dot{m}''$ of 340 kg/m^2 s then decreases abruptly until dry-out at X of 0.42 as shown in Figure 2.10. On the other hand, h_{tp} varies with X (Figure 2.9) and $q''_{total,fin}$ (Figure 2.10) for all tested $\dot{m}''$ without converging boiling curve into a single curve as depicted in Figure 2.7, and associated with a re-wetting flow. This result shows that the nucleate and convective boiling are both of equal importance. On the other hand, reversed flow emerges in the single channel due to the expansion of confined bubbles at the upstream. The development of confined bubbles at the upstream also becomes the reason for the occurrence of the reversed flow in multiple channels associated with a non-uniform distribution of fluid in the channels. Also, the boiling curve shifts upstream when increasing ΔT_{sub}.

There are none of the investigations regarding the effects of different types of substrate materials on the heat transfer during the flow boiling in micro-channels. The investigation of the effects of different substrates is only available in the studies of single-phase flow [23-25]. In these studies [23-25], various substrate materials with different thermal conductivities affect the axial heat conduction (heat conduction along the length of the channel). The axial heat conduction is also in turn affecting the heat transfer during the flow boiling; however, the investigation regarding this aspect is unavailable. On the other hand, the studies regarding effects of fluid types on flow boiling in micro-channels are only available in the studies of Wang et al. [52, 53] and Wang and Sefiane [52, 53]. With the inadequacy of the investigation, this numerical study attempts to address the effect of substrate materials and working fluids on the heat transfer mechanisms during flow boiling of subcooled liquids in micro-channels.

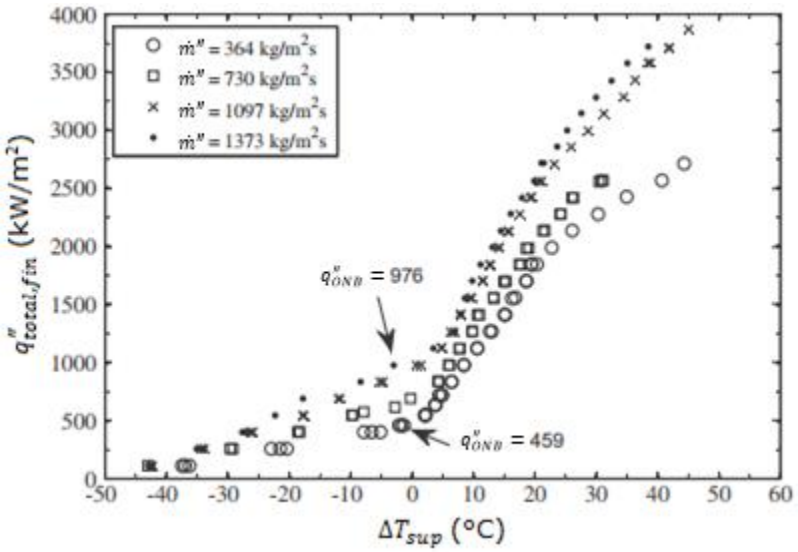


Figure 2.7: Boiling curves (ΔT_{sub} of 50°C) of micro-channel with channel width, height, and length of 471 × 378 × 21900 μm³ [22]

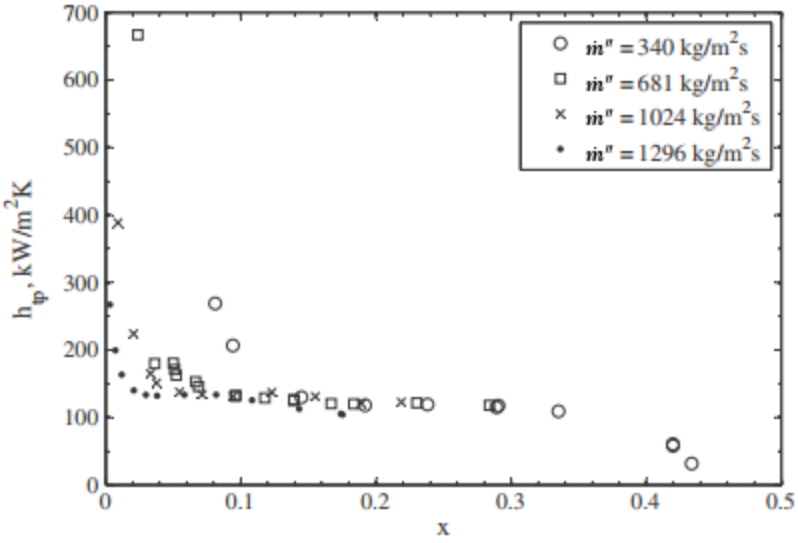


Figure 2.8: Local h_{tp} against X of micro-channel with channel width, height, and length of 241 × 198 × 21900 μm³ [22]

As stated in Section 1.1, the contradiction between experimental results with similar conditions of flow boiling in micro-channels is possible [15] due to the reasons mainly from the experimental errors. By eliminating these faults, alternating approaches of reliable prediction methods for the investigation of the heat transfer are necessary. This study is favourable to subcooled flow boiling with characteristics of nucleate boiling due to higher average heat transfer coefficients as compared to saturated flow boiling according to Lee and Mudawar [37].

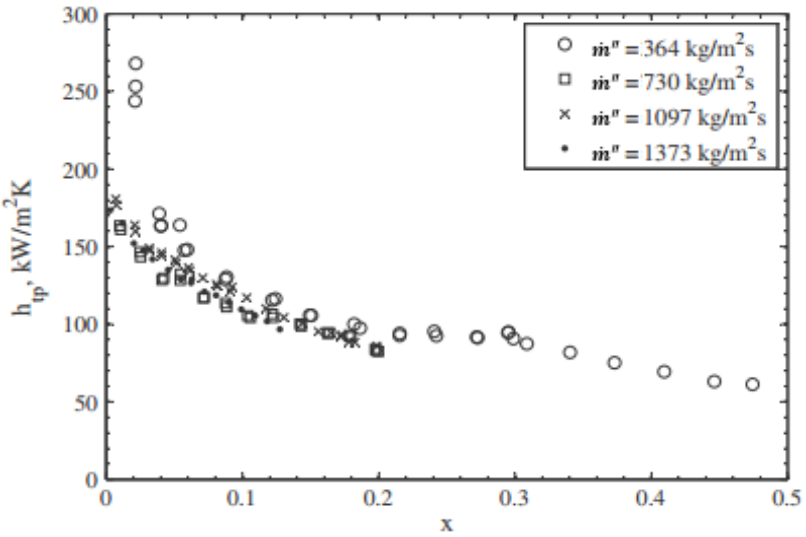


Figure 2.9: Local h_{tp} against X of micro-channel with channel width, height, and length of 471 × 378 × 21900 μm³ [22]

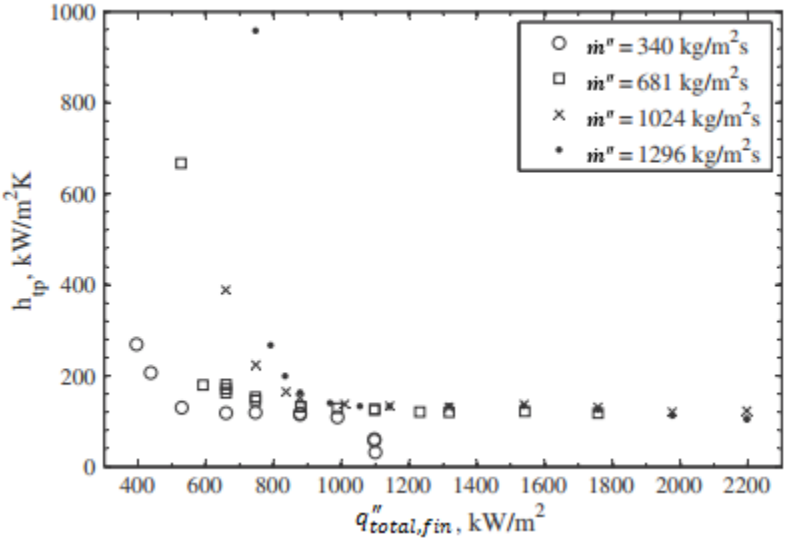


Figure 2.10: Local h_{tp} against $q''_{total,fin}$ of micro-channel with channel width, height, and length of 241 × 198 × 21900 μm³ [22]

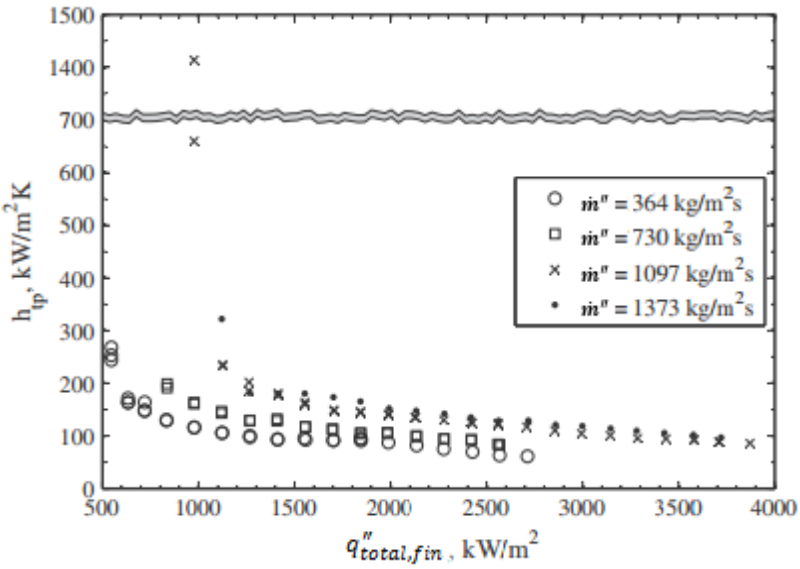


Figure 2.11: Local h_{tp} against $q''_{total,fin}$ of micro-channel channel width, height, and length of 471 × 378 × 21900 μm³ [22]

2.2 Empirical Correlations of Heat Transfer during Flow Boiling in Micro-Channels

Based on the existing experimental results of flow boiling in micro-channels, researchers have proposed several empirical correlations as cited in the recent literature [15, 54]. These empirical relationships neglecting the mechanisms are highly dependent on the measuring ranges of operating conditions for the accuracy.

Mahmoud and Karayiannis [54] observed that all the tested correlations (nineteen correlations) are insufficiently general to predict their experimental data of flow boiling in small to microtubes with acceptable accuracy from local and average (global) h. The accuracy of most empirical relationships deviated with the changes of diameter and the heated length of the channel due to the variation of the modes or mechanisms of flow boiling in channels. When the tubes employed are extremely short in length, it has the high tendency to undergo the domination of the mechanisms of nucleate boiling (occurs when bubbles start growing) whereas convective boiling (takes place when forming a thin film of liquid) for the more extended channels. Also, the applied heat flux must be much higher at a similar exit quality for the short channel as compared to the long channel. For these reasons, the prediction becomes inaccurate when the unsuitable empirical correlations are employed. They [54] have also proposed an empirical relationship from 5152 data points predicting 92% of all data within ±30% error bands at an MAE of 14.3%. Nevertheless, further work is still necessary to evaluate the effect of heated length.

Saha [15] have also analysed the accuracy of twelve existing empirical relationships derived from different approaches on 2336 data points from eleven sets of experimental data in a wide range of test fluids and experimental ranges. These relationships predict within $\pm 30\%$ error bands. The correlations for flow boiling in conventional channels are unable to work for the micro-channel flow boiling associated with inconsistent heat transfer trends and mechanisms. Also, none of the existing correlations can become general prediction method for flow boiling in micro-channels. Furthermore, flow boiling in micro-channels involves complicated mechanisms, and therefore the modification of the relationships for conventional channels is unable to represent the actual mechanisms in micro-scale.

From previous studies, in general, the proposed empirical relationships are inaccurate due to the reasons as stated in Section 1.1. With these inadequacies of the empirical correlations, proper test facilities, instruments, sensors, data reduction methods, designs of test sections, calibration and validation are necessary before commencing experiments to produce reliable data [15]. Also, the more reliable mechanistic prediction methods that consider the flow regimes associated with bubble dynamics are highly necessary by understanding the local heat transfer mechanisms [15], which are the target direction this study.

2.3 Flow Regimes of Flow Boiling in Rectangular Micro-Channels

During flow boiling, different flow regimes with varying patterns of flow become apparent during flow boiling in micro-channels. The distinct flow regimes facilitate the development of more accurate models of heat transfer coefficient to each flow regime [22]. For this reason, the review regarding the experimental studies of flow regimes of flow boiling in rectangular micro-channels is necessary for this study. For this investigation, the flow regime selected is subcooled flow boiling with the bubbly flow in rectangular micro-channels. Therefore, this review first introduces the flow patterns and bubble dynamics during flow boiling of subcooled liquid in a channel and then describes the existing flow regime maps of rectangular micro-channels from the literature. The review of flow regime maps also serves the purpose to determine which operating parameters produce the desired flow regimes in this study.

The chosen experimental studies of flow regimes during flow boiling in rectangular micro-channels associated with the operating parameters in the literature are available in Table 2.3.

Koşar [55] has plotted a map of nucleate boiling and convective boiling with Reynolds number Re against Boiling number Bo for flow boiling in horizontal rectangular micro-channels. The Re against Bo serves the purpose to determine the regime of the different boiling mechanism as illustrated in Figure 2.12. Re and Bo are:

$$Re = \frac{\dot{m}'' d_h}{\mu_l} \tag{2.3}$$

and

$$Bo = \frac{q''_{hs}}{\dot{m}'' \boldsymbol{h}_{lv}} \tag{2.4}$$

Table 2.3: Operating parameters of selected experimental studies of flow regimes of flow boiling in rectangular micro-channels in the literature

Literature	Operating parameter
Koşar [55]	Working fluid of water; substrate of silicon; $q''_{total,fin}$ of 28-445 kW/m^2; $\dot{m}''$ of 41-302 kg/m^2 s; Δp of 0.4-3.0 kPa; five 200 μm wide, 264 μm high, and 1 mm long micro-channels; W_{fin} of 200 μm; and 7.5 μm wide re-entrant cavities.
Lee and Mudawar [17]	Working fluid of water; substrate of copper; q''_b of 15.9-93.8 W/cm^2; $\dot{m}''$ of 127-654 kg/m^2 s; p_{in} of 1.44-6.60 bar; exit quality X_e of 0.26-0.87; and fifty-three 231 μm wide, 713 μm high, and 25.27 mm long micro-channels on 25.3 × 25.3 mm^2 of the substrate.
Zhang et al. [56]	Working fluid of subcooled FC-72; substrate of silicon; $\dot{Q}$ of 0.038-0.092 l/min; P of 20-60 W; ΔT_{sub} around 31°C; and twenty-one 200 μm wide, 2 mm high, and 15 mm long micro-channels.
Chen and Garimella [18]	Working fluid of dielectric liquid FC-77; substrate of silicon; q''_b of 80-730 kW/m^2; $\dot{Q}$ of 35-60 ml/min; T_{in} of 71°C; p_{out} of 1 atm; twenty-four 389 μm wide, 389 μm high, and 12.7 mm long micro-channels on 12.7 × 12.7 mm^2 of the substrate.
Liu and Garimella [19]	Working fluid of water; substrate of copper; maximum q''_b of 129 W/cm^2; $\dot{m}''$ of 221-1283 kg/m^2 s; T_{in} of 78.8-95.4°C; maximum X_e of 0.2; five 406 μm wide, 1063 μm high, and 25.4 mm long micro-channels on 25.4 × 25.4 mm^2 substrate; W_{fin} of 597 μm; and 7.5 μm wide re-entrant cavities.
Harirchian and Garimella [20, 32, 49, 57]	Working fluid of dielectric liquid FC-77; substrate of silicon; maximum q''_{surf} of 640 kW/m^2; $\dot{m}''$ of 225-1420 kg/m^2 s; ΔT_{sub} of 5°C; p_{out} of 1 atm; 2-60 of 400 μm wide, 100-400 μm high, and 12.7 mm long micro-channels on 12.7 × 12.7 mm^2 of the substrate with a thickness of 650 μm; and W_{fin} of 100-300 μm.
Galvis and Culham [22]	Working fluid of water; substrate of copper; q''_b within 4000 kW/m^2; $\dot{m}''$ of 340-1296 kg/m^2 s; ΔT_{sub} of 50.7-54.2°C; p_{out} of 1 atm; single channel of $W_c \times H_c \times L_c$ of 241 × 198 × 21900 μm^3 and 471 × 378 × 21900 μm^3 of on 44 × 10 × 13 mm^3 of the substrate.

respectively, where d_h is the hydraulic diameter. The curve of transition is:

$$Re_{crit} = 163.59 - 2.73 \times 10^4 Bo \quad (2.5)$$

where Re_{crit} is the critical Reynolds number. Figure 2.12 shows that the convective boiling dominates at the high Re and Bo regime whereas nucleate boiling dominates at the low Re and Bo regime. Nucleate boiling occurs when the heat flux increases up to a specific value and causing the change of the temperature is weakly dependent on heat flux in the micro-channels [58]. Besides, the nucleate boiling dominates when applying a low mass flux to the micro-channels and a consistent trend of the increase of the two-phase heat transfer coefficient with heat flux is evident in Koşar [55]. Convective boiling is dominant when applying higher heat fluxes and mass fluxes to the micro-channel. When raised the heat flux, the heat transfer coefficient may decrease as the surface of the micro-channel dries out and consequently reaches a constant value.

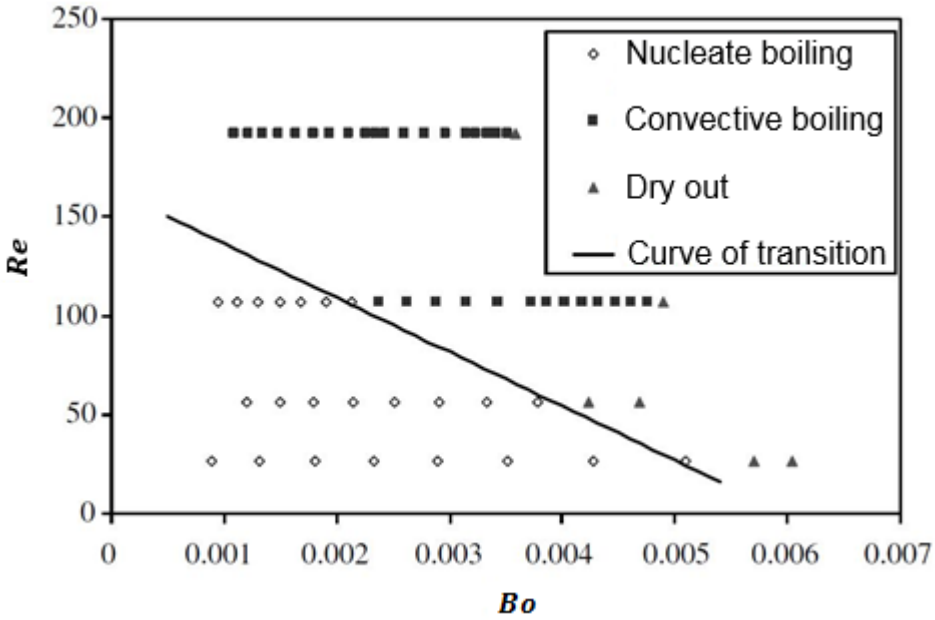


Figure 2.12: Flow regime map of Re against Bo of nucleate boiling, convective boiling, and dry-out of Koşar [55]

Lee and Mudawar [17] have studied the flow regimes during the flow boiling in a horizontal rectangular micro-channel heat sink. They [17] discovered that nucleate boiling with bubbly flow occur only at low X_e ($X_e < 0.05$) with low q_b'', and high q_b'' produce medium X_e ($0.05 < X_e < 0.55$) or high X_e ($X_e > 0.55$) flows dominated by annular film evaporation.

Zhang et al. [56] have investigated the flow regimes during the flow boiling in a micro-channel heat sink. They [56] observed that flow boiling begins at $X < 0$, showing that the subcooled boiling is significant, and becomes unstable at $X \geq 0.2$ associated with the two large-scale flow regimes of bubbly and slug flows in the

channels. However, the annular flow was absent due to the small value of L_c/d_h, which is common in the electronic cooling.

Chen and Garimella [18] have investigated the heat transfer during the flow boiling in a horizontal square micro-channel heat sink. They [18] found four different flow patterns which are bubbly, slug, churn, and wispy-annular flow. The bubbly flow dominates at low q_b'' while the bubbles coalesce to form vapour slugs when increasing q_b''. At high q_b'' or when further rising q_b'', the flow regime of alternating wispy-annular and churn flow appear in the downstream portion and flow reversal becomes apparent near the inlet. q_b'' to form fully developed boiling regime is depending on $\dot{Q}_l$.

Liu and Garimella [19] have plotted a map for the single phase of liquid and subcooled and saturated flow boiling in a rectangular micro-channel heat sink as shown in Figure 2.13. When increasing the heat flux from single-phase flow in the micro-channels, subcooled boiling appears at the outlet, and shifts upstream to a certain length with a slight increase of the heat flux. Further increasing the heat flux induces in the saturated boiling in the micro-channels. The existence of different regimes under different channel conditions shows that the flow boiling is a complicated process. The understanding regarding the characteristics of various regions of flow boiling is still insufficient under the extensive range of geometrical and boundary conditions.

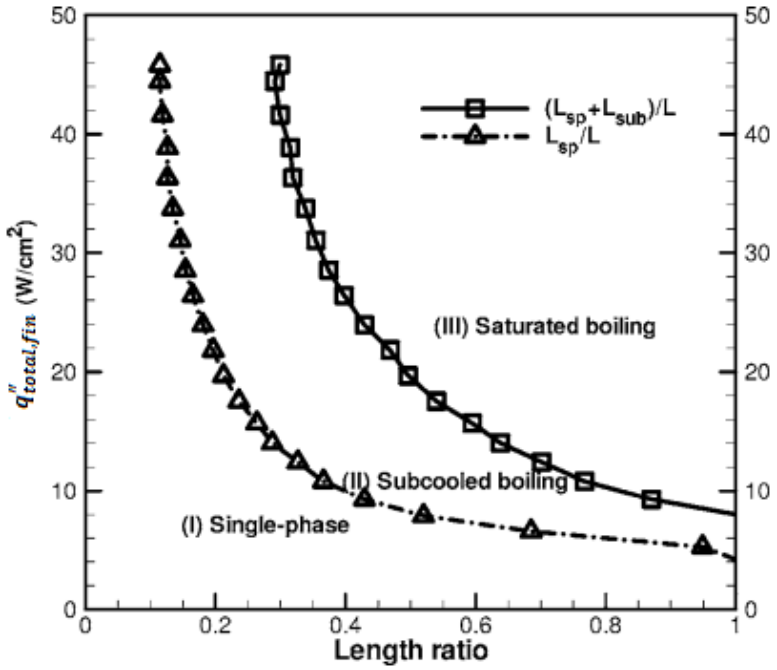


Figure 2.13: Flow regime map of $q''_{total,fin}$ against x/L_c of single phase, subcooled boiling, and saturated flow boiling ($\dot{m}''$ of 330 kg/m^2 s and ΔT_{sub} of 7.9°C) from Liu and Garimella [19]

Harirchian and Garimella [20, 32, 49] have evaluated the flow regimes during the flow boiling in a horizontal square micro-channel heat sink. The flow regimes visualised in the study are at a location near the exit and along the centreline of the length of micro-channel. They [32] discovered the five flow regimes which are bubbly, slug, churn, wispy-annular, and annular flows in the channel as displayed in Figure 2.14:

- In the bubbly flow (Figure 2.14a), the bubbles are isolated round and smaller than the cross-sectional areas of the channel. Bubbles are formed on heated surfaces and detached from the surfaces after growing. The shape and size of the bubbles are varied with the mass fluxes and heat fluxes. The bubbles become smaller and more elongated when the mass flux increases in the bubbly regime.
- In the slug flow (Figure 2.14b), the broad and elongated bubbles form as a result of the coalescence of small bubbles until occupying the entire cross-section of the channel. Meanwhile, tiny bubbles still exist in the liquid between the elongated bubbles.
- In the churn flow (Figure 2.14c), the chunks of vapour form due to the breakdown of the large bubbles from the slug flow and move downstream in this regime. The rate of the formation of bubbles is higher and forming large bubbles on the heating surface in the channel.
- In the wispy-annular flow (Figure 2.14d), the micro-channels experience the suppression of bubble nucleation, and the core of vapour present at the centre of the channel with a thick and unstable film of liquid on the heating surface. Moreover, broad and irregular shapes of the droplets of liquid entrained into the core of vapour, while small bubbles exist in the film of liquid. The thickness of the liquid layer decreases as the mass flux increases.
- In the annular flow (Figure 2.14e), the film of liquid is thinner as compared to the wispy-annular flow, with the formation of a wavy interface between the film of liquid and core of vapour. Also, small and round droplets of liquid enter into the vapour core, but the nucleation of bubbles in the film of liquid is absent. The thickness of the liquid layer decreases as the mass flux increases.
- In the inverted annular flow (Figure 2.14f), the dry-out of the heating surface occurs, and the channel reaches CHF. The core of liquid exists at the centre of the current while the blanket of vapour is present on the heating surface.

Harirchian and Garimella [32, 57] have also created a flow regime map with $\dot{m}''$ against $q''_{total,fin}$ when varying W_c and H_c for horizontal flow boiling in a rectangular micro-channel heat sink as displayed in Figure 2.15. The flow regime map is created based on the flow regimes discovered as shown in Figure 2.14. The multiple regions are also often present along the channel and superimposed by complex mechanisms when employing the sufficiently long channel. When employing smaller

sizes of channels (e.g., $A_{cs} < 0.144$ mm^2) and lower $\dot{m}''$ (e.g. $\dot{m}'' = 225$ kg/m^2 s), the slug and intermittent churn and annular flows appear immediately, however, the bubbly flow is absent. The bubbly flow is only apparent at low q''_{surf} when A_{cs} or $\dot{m}''$ increases. When W_c is more than 400 μm, the patterns of flow of the bubbly and intermittent churn/annular flow emerge, and the nucleate boiling is dominant up to high q''_{surf}. In general, the transition of flow regimes occurs at higher q''_{surf} when increasing $\dot{m}''$. Nevertheless, the nucleate boiling diminishes at relatively low q''_{surf} for 100 and 250 μm of W_c.

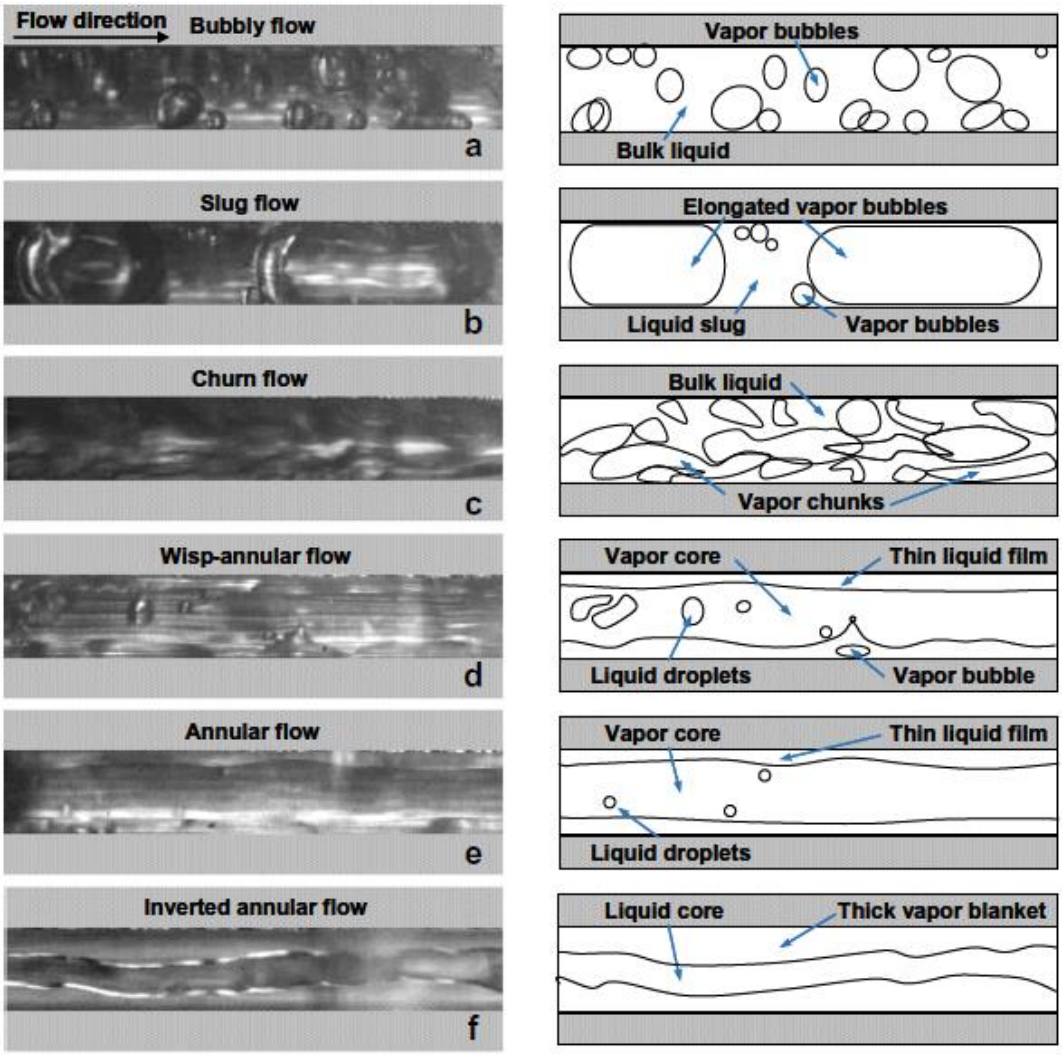


Figure 2.14: Actual images (left) and sketched images (right) of flow patterns in a shape of square of micro-channels (400 × 400 μm^2 and 12.7 mm long) made of silicon at the horizontal position under the condition of flow boiling (ΔT_{sub} of 5°C) [32]

Harirchian and Garimella [35] have also developed the flow regime maps for the transition from bubbly or slug flow to intermittent churn/wispy-annular or

churn/annular flow of $\dot{m}''$ against quality X_v of vapour and superficial velocity of liquid J_l against vapour J_v as shown in Figure 2.14a and Figure 2.14b, respectively.

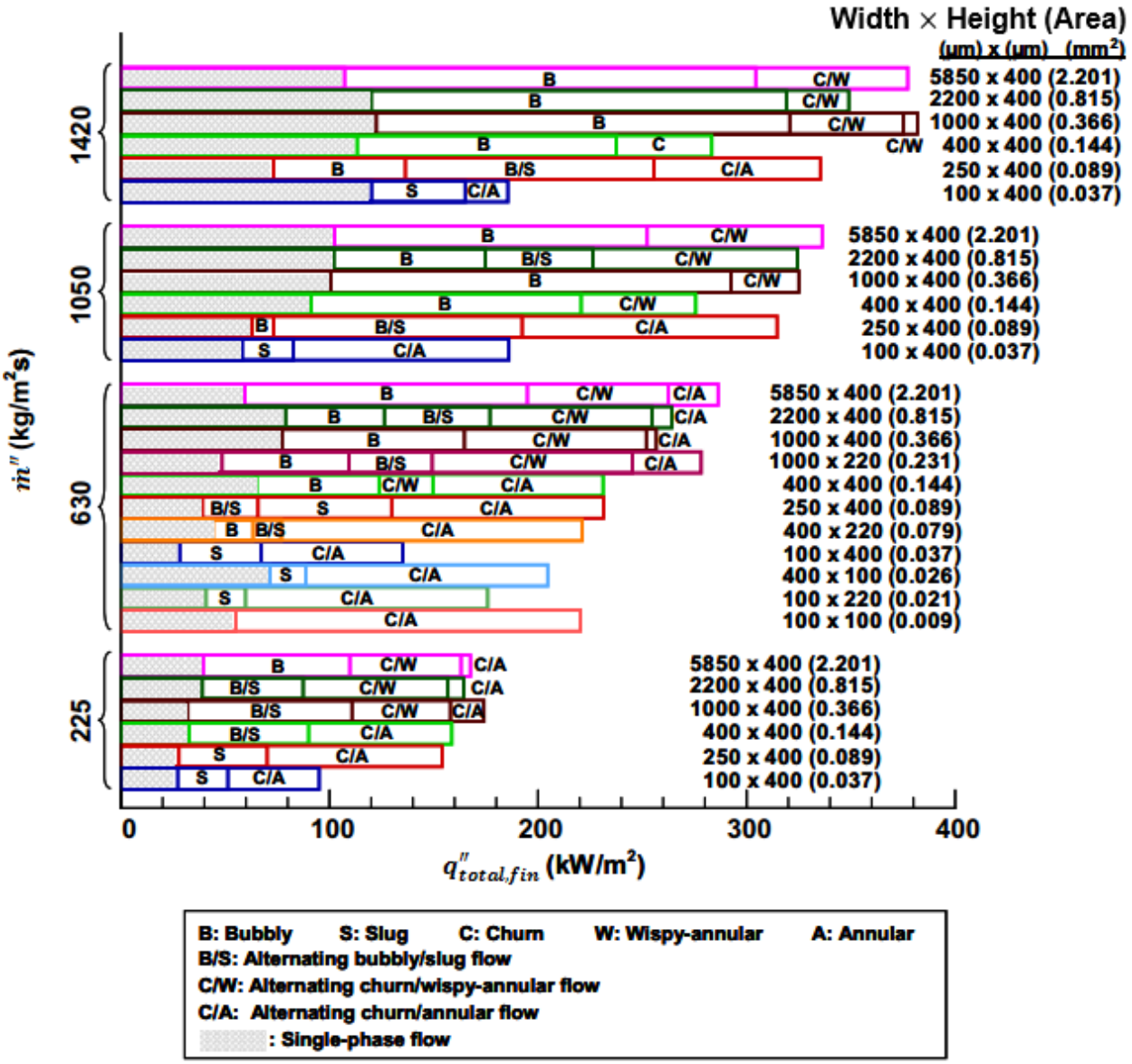


Figure 2.15: Flow regime map of $\dot{m}''$ against $q''_{total,fin}$ of W_c of 100-5850 μm and H_c of 100-400 μm for bubble, slug, churn, wispy-annular, annular, alternating bubbly/slug flow, alternating churn/wispy-annular flow, and single-phase flow from Harirchian and Garimella [57]

When increasing $q''_{total,fin}$ (in Figure 2.13) or X (in Figure 2.14a), the patterns of flow change from bubbly and slug flow to the intermittent churn/wispy-annular and churn/annular occur. In Figure 2.14a, the transition occurs at lower X_v when rising $\dot{m}''$ for each tested W_c. When employing smaller W_c, changes of flow patterns place at larger X_v. In Figure 2.14b, for W_c lesser than 1000 μm, the transition takes place at higher J_v when J_l increases. In contrast, the change occurs at lower J_v when J_l

increases W_c broader than 1000 μm. Also, the transition takes place at larger J_v when employing smaller W_c. Harirchian and Garimella [35] also stated that the developed map from the condensation, large channel and adiabatic two-phase flow are inappropriate to predict the flow boiling in micro-channels.

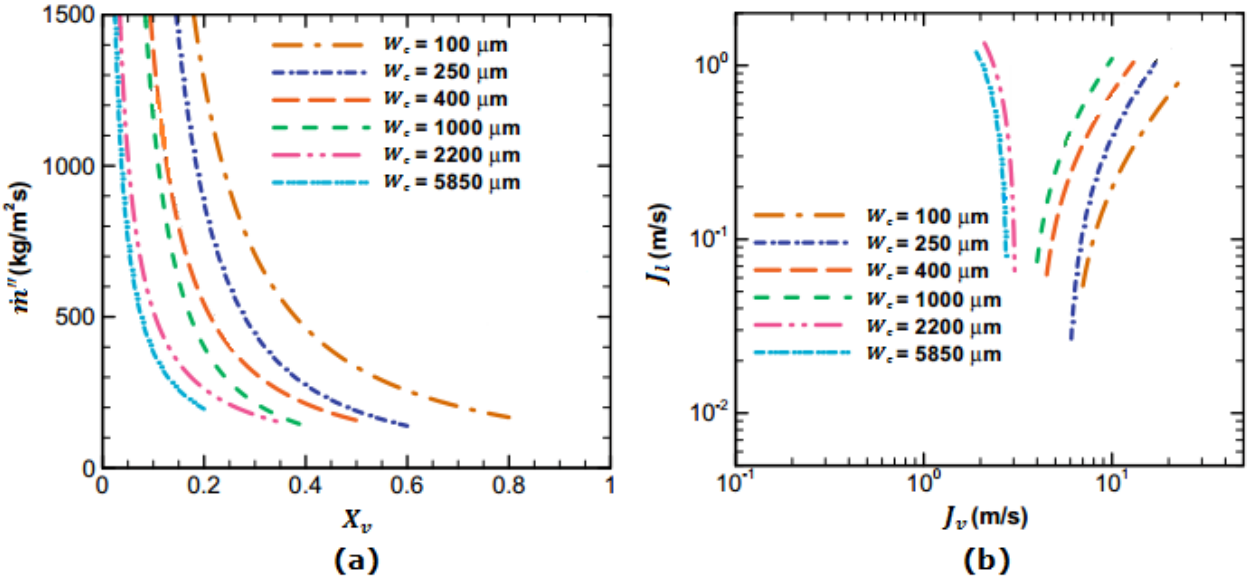


Figure 2.16: Flow regime map of (a) $\dot{m}''$ against X and (b) J_l against J_v of W_c of 100-5850 μm for the transition from bubbly or slug flow to intermittent churn/wispy-annular or churn/annular flow from Harirchian and Garimella [32]

Harirchian and Garimella [57] have distinguished the dominant regimes of unconfined and confined flows in a map with Reynolds number Re against Bond number Bo for horizontal flow boiling in a rectangular micro-channels. The confined flow indicates the flow with a thin film of liquid on the fin surfaces while the vapour flows within the film such as slug and confined annular flow. On the other hand, the bubbly flow is the unconfined flow since the sizes of bubbles that are smaller than the cross-section of the channel. The wispy-annular and annular flows are out of the entity of confined flow as the wispy-annular, and annular flows are unnecessary to occupy the entire cross-section of the channel. These regimes are distinguished using the convective confinement number $Bo^{0.5} \times Re$ as the criterion of transition in the maps of Reynolds number Re against the Bond number Bn as shown in Figure 2.17. $Bn^{0.5} \times Re$ depends on the dimensions of the channel, properties of the fluid, and $\dot{m}''$ as:

$$Bn^{0.5} \times Re = \frac{1}{\mu_l}\left[\frac{g(\rho_l - \rho_g)}{\sigma}\right]^{0.5} \dot{m}'' A_{cs} = 160 \tag{2.6}$$

where A_{cs} is the cross-sectional area ($W_c \times H_c$). $Bo^{0.5} \times Re$ is set arbitrarily as 160 to represent the transition between the unconfined and confined flows. The value of $Bn^{0.5} \times Re$ for flow boiling of FC-77 is 160. When $Bo^{0.5} \times Re < 160$, the confined flow

is observed associated with the evaporation of thin film that contributes to the additional heat transfer and produces higher heat transfer coefficients. Contrasting with $Bn^{0.5} \times Re > 160$, the nucleate boiling is dominant in the unconfined flow that produces lower heat transfer coefficients.

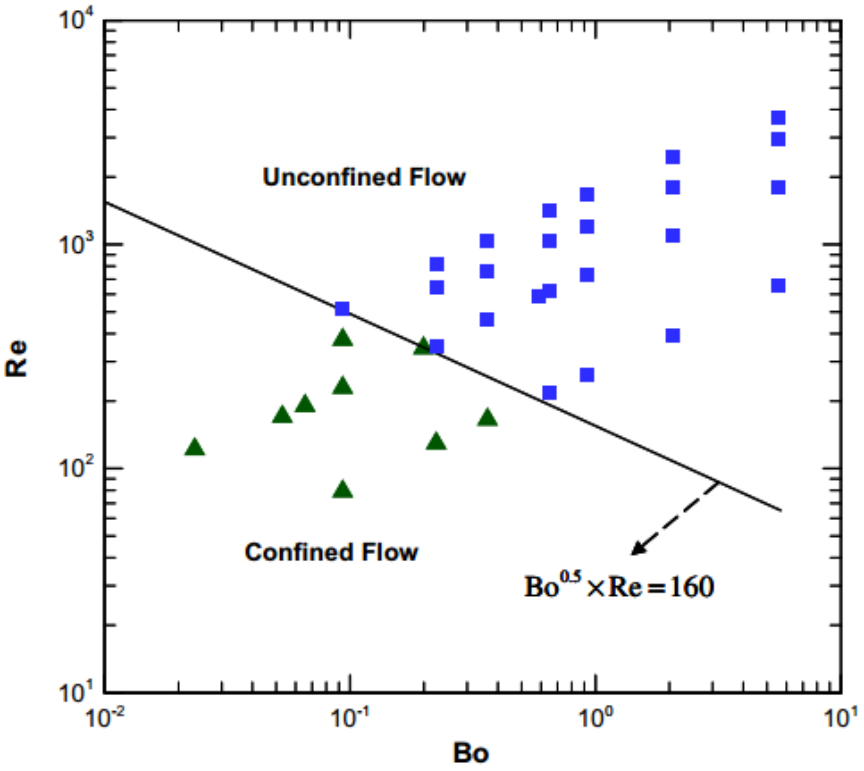


Figure 2.17: Flow regime map of Re against Bo of unconfined flow and confined flow Harirchian and Garimella [57]

Harirchian and Garimella [57] have created a flow regime map with $Bo \times Re$ against $Bn^{0.5} \times Re$ for horizontal flow boiling in rectangular micro-channel heat sinks, as depicted in Figure 2.18. There are two lines to differentiate each pattern of flow, which are:

- The vertical line of $Bn^{0.5} \times Re = 160$ for the transition from the confined to unconfined flow.
- The line of $Bo = 0.017(Bn^{0.4} \times Re^{-0.3})$ for the transition from bubbly and slug (or confined slug) flows to churn/confined annular, churn/wispy-annular and churn/annular flows.

For $Bn^{0.5} \times Re > 160$ (unconfined flow), the heat transfer coefficient is independent of the size of the channel, and the correlations of nucleate boiling in pool boiling are applicable for the prediction of heat transfer. For $Bn^{0.5} \times Re < 160$ (confined flow), the empirical relationships or regime based models require modification for the more accurate prediction of heat transfer. This developed flow regime map also

agrees well with the existing experimental data with the working fluids of water and fluorocarbon liquids.

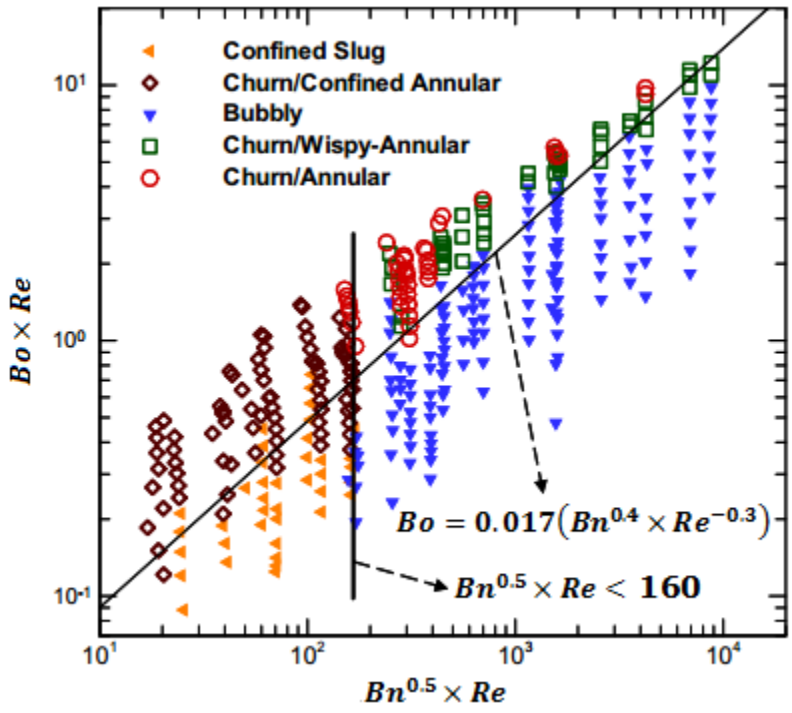


Figure 2.18: Flow regime map of $Bo \times Re$ against $Bn^{0.5} \times Re$ of confined flug, churn/confined annular, bubbly, churn/wispy-annular, and churn/annular from Harirchian and Garimella [57]

Galvis and Culham [22] have investigated the flow regimes during the flow boiling in single horizontal rectangular micro-channel heat sinks. They [22] captured the flow patterns at the midpoint of the length of the channel and observed six different flow patterns which are bubbly, slug, churn, annular, wavy-annular, and inverted annular flow as illustrated in Figure 2.19. The flow patterns are depending on $\dot{m}''$, q'', and channel sizes. The bubbly flow begins at low q'' and progressively develops to slug, churn, and annular flow when increasing q'' for each tested $\dot{m}''$ and channel sizes. However, the flow patterns are unlikely to all appear in a channel for all tested conditions as evident in Figure 2.20. In Figure 2.20, the bubbly flow is absent in 198 × 241 μm micro-channel as the bubble confines from the channel surface, and slug flow begins immediately after the ONB, and develop to annular, and inverted at higher q''. Also, the intermittent stream or multiple flow patterns present in the channel due to re-wetting of the channel surface and the re-wetting becomes the significant role for the development of flow patterns.

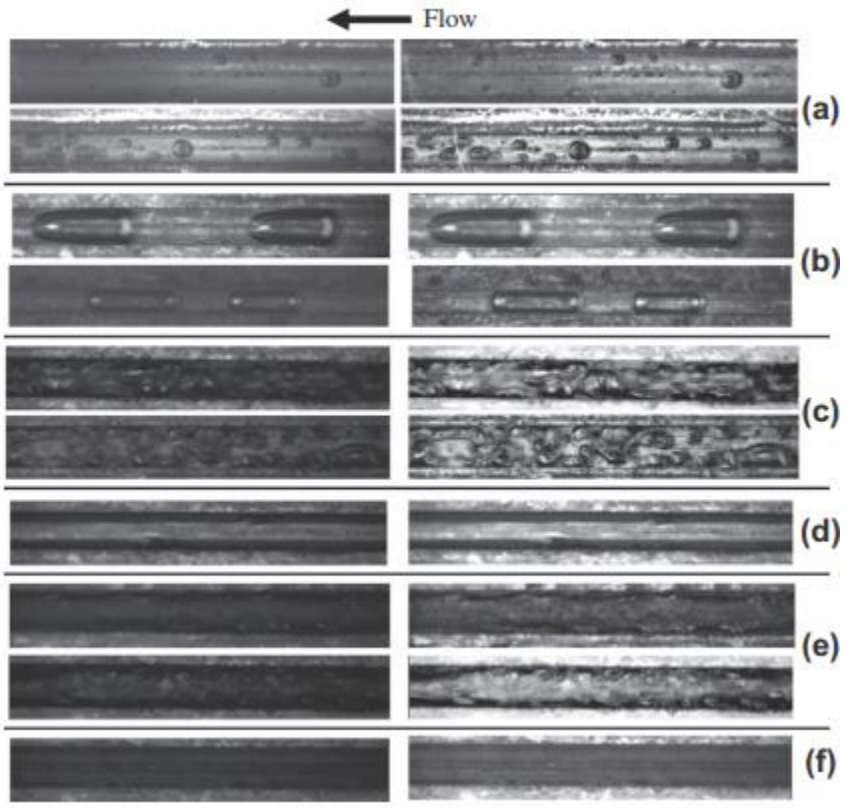


Figure 2.19: Actual images (left) and enhanced with Matlab image processing tool (right) of flow regimes of (a) bubbly flow, (b) slug flow, (c) churn flow, (d) annular flow, (e) wavy annular flow, and (f) inverted annular flow [22]

The existing flow regime maps of flow boiling in rectangular micro-channels proposed are with the parameters of heat fluxes and mass fluxes. However, the flow regime maps with the inlet temperatures (or degrees of subcooling), substrate materials, and working fluids are unavailable. The inlet temperatures indeed have little impact on the boiling curve according to Liu and Garimella [19] after the ONB as stated in Section 2.1. On the other hand, Saha [15] mentioned that the inlet temperature has some effects on the heat transfer coefficients. However, the knowledge in this aspect is limited in the literature. Therefore, from the existing flow regime maps, this study selects the operating parameters which are capable of generating nucleate boiling during flow boiling of subcooled liquids in a micro-channel heat sink. The operating parameters of heat flux and mass flux of the micro-channel selected from the flow regime maps are at 500-3197 kW/m^2 and 115-389 kg/m^2 s, respectively. Without referring to the flow region maps, the range of inlet temperature proposed in this investigation is 23-53°C. Furthermore, the micro-channel heat sink in this study adopts the pressure of 1 atm, the substrate materials of steel, silicon, aluminium and copper, and working fluids of water and ethanol.

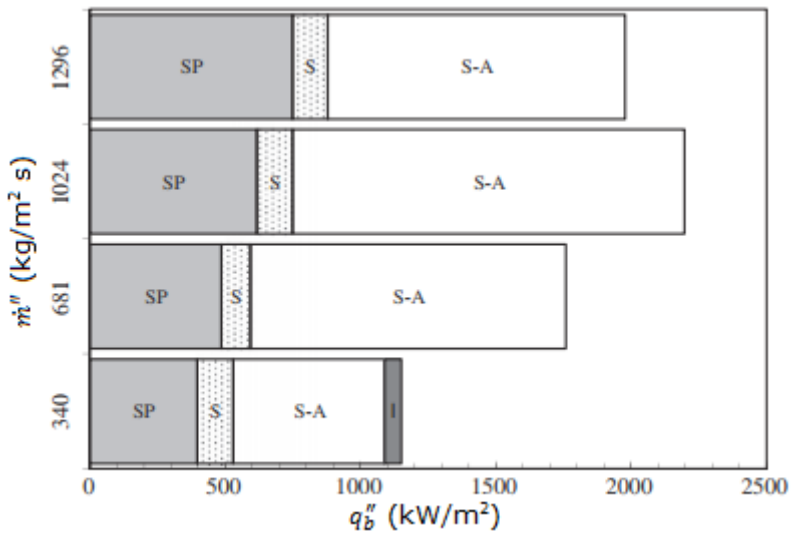


Figure 2.20: Flow regime map of $\dot{m}''$ against q_b'' of single-phase flow (SP), slug flow (S), slug-annular flow (S-A), and inverted annular flow (I) from Galvis and Culham [22]

2.4 Experimental Studies of Characteristics and Mechanisms of Nucleate Boiling during Flow Boiling of Subcooled Liquids in Rectangular Micro-Channels

When flow boiling occurs, the fluid flow involves liquid flow and bubble dynamics associated with heat transfer in channels. The bubble dynamics consist of bubble nucleation, collapse (or condensation), growth, departure, sliding dynamics, lift-off, coalescence, etc. There are current findings of fluid flow and heat transfer from experimental studies to understand the characteristics and mechanisms nucleate boiling during flow boiling of subcooled liquids in rectangular micro-channels. These studies are worthwhile to improve the heat transfer prediction methods, and therefore the review regarding the findings of flow boiling behaviours from the experimental studies at the current stage is necessary.

Peng and Wang [38-41] have observed an unfamiliar aspect of flow boiling in rectangular micro-channels in which as the characteristics of flow boiling are possible before bubble nucleation indicated in Section 1.1. In the investigation of Peng and Wang [40], the bubbles only nucleate in the inlet plenum at extremely high heat fluxes, causing the fluctuation of the liquid in the channels and rapid deterioration of the heat transfer. On the other hand, if the setup is improper in which some too narrow gaps between the glass cover and the plate exists, small bubbles nucleate at low superheats and heat fluxes. The holes that are smaller than the channel size become the active nucleation sites. This phenomenon refers to the single-phase convection named fictitious boiling as also stated by Peng [31]. The fictitious flow boiling has two main aspects:

- The liquid has reached nucleate boiling conditions, however, the internal evaporation and bubble growth are absent or many unseen microbubbles that are unstable exist within the liquid.
- The bubble evaporation and generation occur as soon as the flow enters a space ample enough for evaporating.

For fictitious boiling, the liquid is apparently in an unstable thermodynamic non-equilibrium state. Peng [31] postulates that the fictitious boiling occurs as a result of:

- The physical properties of the liquid in a non-equilibrium state are different from any equilibrium states. For instance, the specific heat in a non-equilibrium state is higher as compared to equilibrium conditions, allowing the liquid to absorb or store more heat with high heat transfer rates without undergoing the phase change.
- The liquid reaches conventional nucleate boiling conditions although the internal evaporation and bubble growth are absent.
- The existence of unstable micro embryo bubbles within the non-equilibrium liquid particularly on heating surfaces which are invisible. These bubbles are too small to be stable and are likely to collapse according to the classical theory of nucleation [59]. The unstable micro embryo bubbles nucleating and collapsing intermittently and frequently cause the liquid to be in a high non-equilibrium state associated and require a significant amount of energy to maintain these bubbles. Therefore, the non-equilibrium liquid from the fictitious boiling facilitates considerably the ability to absorb the heat as compared to the standard nucleate boiling.

Investigators have captured the location of ONB in rectangular micro-channels experimentally, and Table 2.4 lists down the selected experimental studies relating to the spot of ONB. During the ONB, the size of nucleated bubbles is capable of reaching as small as 10-20 μm in the micro-channel as indicated by Kandlikar [60].

Qu and Mudawar [6] have visualised the location of ONB in a rectangular micro-channel heat sink. They [6] stated that the ONB is a local phenomenon that strongly depends on both hydrodynamics and thermal conditions and requires a detailed understanding of the velocity and temperature distributions. In their [6] study, a small number (5-8) of bubbles nucleate near the outlet of channels during the incipient flow boiling with one or two bubbles per channel. Majority of the bubbles nucleate at the bottom surface in the channels, while a few of bubbles nucleate at the side surfaces. Also, the size of the nucleated bubble is comparable to the micro-channel for small u_{in} and decreases with the increase of u_{in}. Bubble departure size is almost similar to the micro-channel size for small u_{in} and progressively increasing u_{in}.

Table 2.4: Operating parameters of selected experimental studies relating to the location of ONB in rectangular micro-channels in the literature

Literature	Operating parameter
Qu and Mudawar [6]	As stated in Table 2.1.
Zhang et al. [61]	Working fluid of deionised water; substrate of silicon; $\dot{m}''$ of 256 kg/m^2 s; 200 μm wide, 130 μm high, and 20 mm long micro-channels; W_b of 200 μm; and H_b of 670 μm.
Liu et al. [47]	As stated in Table 2.1.
Mosyak et al. [46]	Working fluid of water; substrate of aluminium; T_{in} of 20°C; $\dot{m}''$ of 15.4-77.1 kg/m^2 s; twenty-five 200 μm wide, 580 μm high, and 20 mm long micro-channels; W_b of 200 μm; and H_b of 670 μm.

Zhang et al. [61] have found that the bubble nucleates at the corner of a rectangular micro-channel heat sink as shown in Figure 2.21.



Figure 2.21: Visualisation of bubble at ONB [61]

Liu et al. [47] have captured the location of ONB in a rectangular micro-channel heat sink. They [47] found that the bubbles were usually observed to form at the bottom surface near to the vicinity of the corner and to the outlet of the channel as illustrated in Figure 2.22 based on one of the conditions. This observation is similar to Qu and Mudawar [6]. They [47] found that contact angle θ of bubble decreases when increasing the bubble radius. The incipient radius of bubble slightly decreases when increasing the fluid velocity.

Mosyak et al. [46] have observed the location of ONB in a rectangular micro-channel heat sink. The bubble was spotted to nucleate at the corner of the channel as depicted in Figure 2.23.

There is a contradiction of the observation of ONB from the selected experimental studies. Qu and Mudawar [6] and Liu et al. [47] discovered the bubbles nucleate at the bottom surface near the corner and few bubbles nucleate on side surfaces. On the other hand, Zhang et al. [61], and Mosyak et al. [46] found that the bubbles frequently nucleate at corner surfaces as compared to the bottom surface. This difference is possibly due to the different $\dot{m}''$ employed in each

study. From Qu and Mudawar [6] and Liu et al. [47], $\dot{m}''$ are larger than the rest of the selected experimental studies causing the difference of the ONB location within a cross-section.

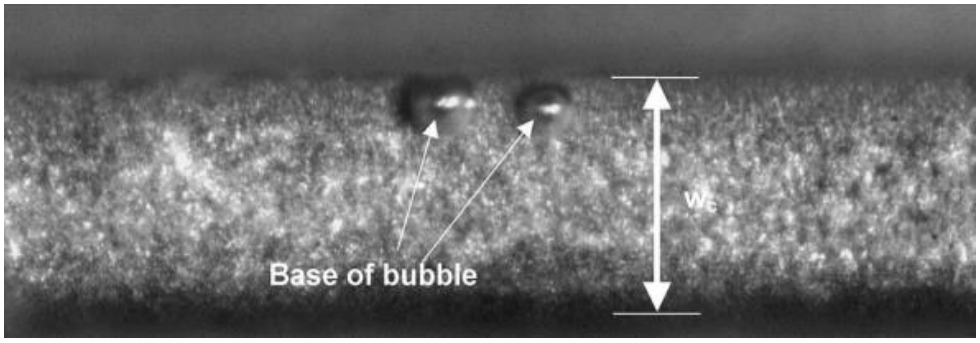


Figure 2.22: Visualisation of bubble at ONB at p_{out} of 104469 Pa of, T_{in} of 70.9°C of, u_{in} of 0.55 m/s, and q''_{hs} of 28.87 W/cm^2 from Liu et al. [47]

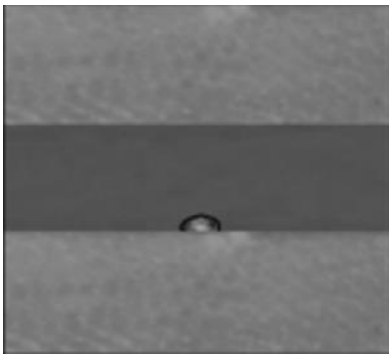


Figure 2.23: Visualisation of bubble at ONB from Mosyak et al. [46]

Table 2.5 summarised the operating parameters of selected experimental studies with the findings of liquid flow and bubble dynamics associated with heat transfer of nucleate boiling during subcooled flow boiling in rectangular micro-channels.

Balasubramanian and Kandlikar [62] have evaluated the bubble dynamics during the flow boiling in a horizontal rectangular micro-channel heat sink. They [62] found that nucleation occurs in the bulk liquid and the thin film at a higher frequency as compared to a single nucleating bubble in the channel, indicating the nucleate boiling dominant heat transfer. The bubble experiences a sudden reduction of growth rate when the bubble nucleates and remains confined to the surface. After the bubble confines to the surface, the bubble grows at an extremely high velocity towards the sides. The velocity of the bubble growth in their channel is capable of reaching as high as 3.5 m/s. Also, the bubble grows and develops to slug with a thin liquid film on the fin surfaces in the channel. The slug flow is dominant for higher surface temperatures; however, a backflow toward the inlet can occur in some cases, leading to severe flow maldistribution.

Table 2.5: Operating parameters of selected experimental studies with the findings of characteristics and mechanisms of nucleate boiling during flow boiling of subcooled liquids in rectangular micro-channels in the literature

Literature	Operating parameter
Balasubramanian and Kandlikar [62]	Working fluid of water; substrate of copper; q_b'' of 208-316 kW/m^2; $\dot{m}''$ of 112-120 kg/m^2 s; T_{sat} of 121°C (by adjusting p_{in}); six 990 μm wide, 207 μm high, and 63.5 mm long micro-channels.
Lee and Mudawar [37, 48]	As stated in Table 2.2.
Lee et al. [63]	Working fluid of water; substrate of silicon; $\dot{m}''$ within 138.9 kg/m^2 s; T_{in} of 24°C; absolute pressure p_{abs} of 100.8-101.5 kPa; one 50-100 μm wide, 46-100 μm high, and 64 mm long micro-channel; and an artificial cavity 24 mm from the inlet with radius of 12.5-16.4 μm at bottom surface in the micro-channel.
Lagus and Kulacki [64]	Working fluid of water; substrate of copper; $\dot{m}''$ of 221-466 kg/m^2 s; q_b'' of 250-1780 kW/m^2; T_{in} of 297.3-316.3 K; thirteen 406 μm wide, 508 μm high, and 1 cm long micro-channels over an area of 1 cm^2 on a substrate of 9.2 × 2.8 × 0.36 cm^3; W_f of 330 μm; and 2.761 cm wide and 508 μm high inlet and outlet plenums.
Bogojevic et al. [65]	Working fluid of water; substrate of silicon; q_b'' of 138-537 kW/m^2; $\dot{m}''$ of 71-204 kg/m^2 s; T_{in} of 71°C; fourty 150 μm wide, 273 μm high, and 15 mm long micro-channels; W_{fin} of 100 μm; and H_b of 112 μm.

Lee and Mudawar [37, 48] have visualised the flow in horizontal rectangular micro-channel heat sinks during flow boiling. They [37, 48] found that the ratio of bubble separation distance to bubble diameter decreases, the likelihood of bubble coalescence increases, and the number of nucleation sites increase when increasing heat fluxes. In the micro-channels, both small discrete bubbles and slug flow bubbles emerge at outlet regions in the same axial location. This occurrence is due to the temperature gradient along the height of the micro-channels. The bubbles are more likely to coalesce into large bubbles near the bottom heating surface whereas near the top part of the channel has less superheat to grow and fuse the small discrete bubbles. On the other hand, lower inlet temperatures facilitate the intense condensation at the bubble interface with the reduction of the bubble growth and coalescence.

Lee et al. [63] have carried out an experimental study of the bubble dynamics during the flow boiling in single horizontal rectangular micro-channel heat sinks.

They [63] observed that two distinct behaviours during the flow regime development, depending on the superheat. The first bubble flow pattern noted is that the earliest or first nucleating bubble detaches from the surface, sweeps downstream and coalesces with subsequent bubbles in order of milliseconds. The second bubble flow type found is that a single bubble explosively grows and expands at the nucleating location in order of microseconds. Both behaviours depict that the first nucleating bubble plays a vital role in changing the flow regime. When the bubble grows in milliseconds, the bubble growth is in under heat-transfer-controlled growth condition. The heat-transfer-controlled growth is the process of bubble growth in which the heat from the surrounding liquid diffuses to the bubble interface to cause the evaporation. However, the growth rate increases when the bubble radius increases. On the other hand, a growing bubble is strongly dependent on the thermal transport from the surrounding heated surfaces. When the bubble grows in microseconds, the bubble growth rate is linear before increasing to the size of the micro-channel, implying that the explosive growing bubble is under inertia-controlled condition.

Lagus and Kulacki [64] have examined the bubble dynamics during flow boiling in a micro-channel heat sink. They [64] discovered that the bubbly flow is the precursors to the bubble nucleation of expanding vapour slug flow. From the bubble dynamics, $r \sim t^{1/3}$ for the bubble growth and then the bubble suddenly expands when reaching the width of the channel. Also, the reversals in bubbles and vapour slug flow become apparent with slug movement and upstream interface evaporation.

Bogojevic et al. [65] have evaluated the bubble dynamics during the flow boiling in a horizontal rectangular micro-channel heat sink. They [65] found that the bubble growth rate in the micro-channels is different from pool boiling and flow boiling in macroscale channels due to confinement of micro-channel and interaction between channels cause extraordinary bubble dynamics in micro-channels. Three stages of bubble growth from the bottom and side surfaces emerge in the channels as observed in one of the condition (q_b'' of 245 kW/m^2 and $\dot{m}''$ of 153 kg/m^2 s) at the centre along the length of the channel as illustrated in Figure 2.24. In Figure 2.24, The first stage (I) is rapid bubble growth in a linear trend, indicating that inertia forces (or inertia-controlled growth) are dominant when the small bubble in a highly superheated liquid layer. The inertia-controlled growth is the process of bubble growth in which the interface of the bubble pushing the surrounding liquid, allowing the inertia of the surrounding liquid to exist. Then, in the second stage (II), the bubble growth stagnates when the bubble interacting more with a lower superheat that slows down the evaporation rate on the bubble contact surface. This process occurs due to the thermal diffusion controlling the heat transfer (or heat-transfer-controlled growth) through the liquid with lower superheat. Consequently, in the third stage (III), the bubble interface accelerates and reaches closer to the next channel surfaces due to bubble growth in confined space of the micro-channel. This

process arises due to the high superheated liquid layer near the surfaces that enhances the evaporation and increasing the bubble growth rate. The first two stages are similar to the bubble growth in the pool boiling and flow boiling in conventional-sized channels whereas phase three is an exclusive behaviour in micro-channels.

In the similar study, Bogojevic et al. [65] also observed that the period between bubble nucleation and explosion, or bubble lifetime and departure diameter and height change with q_b'' and $\dot{m}''$, and decreases with increasing Reynolds number Re. The bubble lifetime decreases exponentially with $q_b''/\dot{m}''$. When the bubble lifetime is shorter, the fluctuation frequency during higher flow boiling instabilities whereas the frequency fluctuation is lower for longer bubble lifetime associated with more moderate growth rate and high amplitudes in pressure and temperature. The bubble grows in the axial direction in the micro-channel and susceptible to flow instabilities and flow reversal that affect the bubble growth. When the liquid film exists, evaporation is the dominant heat transfer mechanisms determining the liquid film thickness which decreases when increasing q_b''.

Bogojevic et al. [65] and Wang and Sefiane [53] have attempted to distinguish transition point between inertia-controlled and heat-transfer-controlled growth in the study. In the investigation of Bogojevic et al. [65], the data points collected are limited, especially near the transition instant. This insufficiency causes the estimation of the transition point to be imprecise from the curve line imposed from few data points. Wang and Sefiane [53] have addressed the transition point of bubble growth stage in a micro-channel heat sink for different heat fluxes and mass fluxes. The mass fluxes that Wang and Sefiane [53] employed are much lower than Bogojevic et al. [65]. Wang and Sefiane [53] found that the transition point is earlier with higher heat fluxes whereas mass fluxes have negligible effects on the transition point. When reducing ranges of heat fluxes employed by Bogojevic et al. [65] to Wang and Sefiane [53], the trend of the transition point of bubble growth only becomes readable from the experimental studies. In other words, the experimental studies are only capable of studying the transition point of bubble growth stage at low mass fluxes. By distinguishing the transition point more precisely in broader ranges of mass fluxes, numerical methods which are capable of providing more data points with the local variation of the phenomenon are necessary. Nevertheless, these studies are unavailable at the moment. Also, the evaluation of the bubble growth is inadequate with the comparison of the bubble growth including the transition point of bubbles in different locations. Furthermore, the transition point between the two bubble growth processes for different T_{in}, substrate materials, and types of fluids is unavailable.

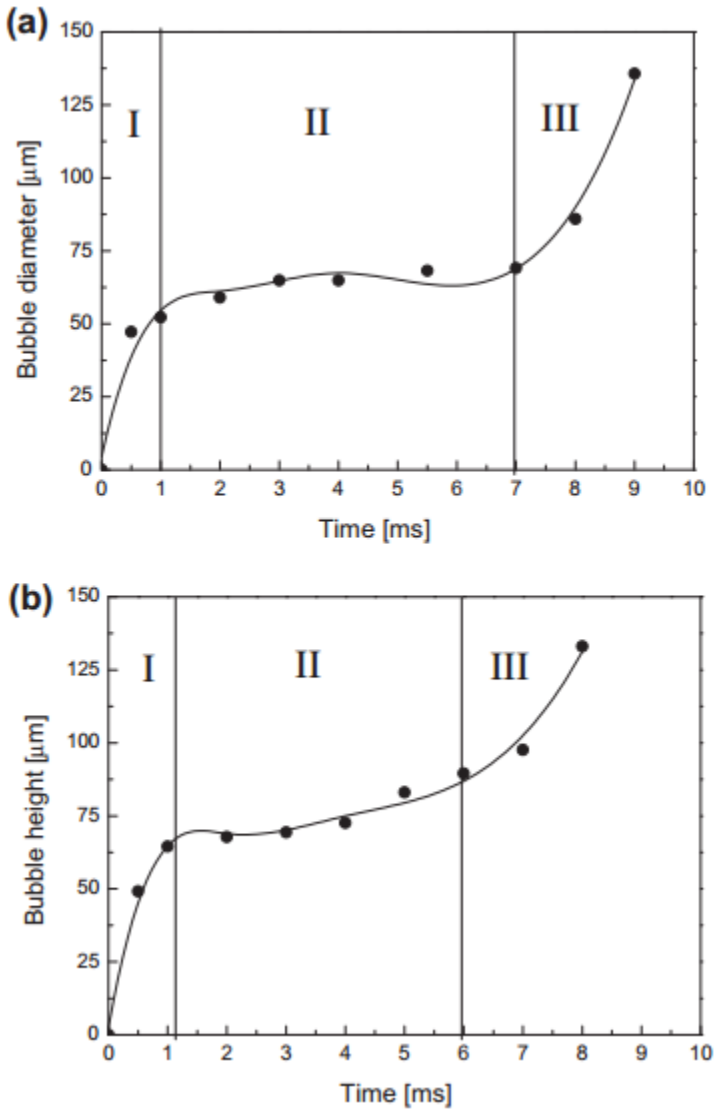


Figure 2.24: (a) Bottom surface bubble and (b) side surface bubble growth curves in subcooled flow boiling for q_b'' of 445 kW/m² and $\dot{m}''$ of 153 kg/m² s

Kandlikar [36, 66] has compared the flow boiling in micro-channels with nucleate pool boiling and discovered significant similarities of bubble growth associated with the heat transfer mechanisms. In both boiling processes, vapour bubbles nucleated grow through the evaporation at the liquid-vapour interface, and the heating surface with the vapour is adjacent to a microlayer. During flow boiling, the front and back of an elongated bubble are similar to the interfaces during growth and departure phases of a nucleating bubble in pool boiling, respectively. In pool boiling, the transient conduction mechanism due to re-wetting of the heating surface during the bubble departure is equivalent to the transient conduction mechanism at the liquid between two elongated bubbles during flow boiling. Also, when flow boiling occurs, the micro-convection mechanism occurs and provides a

pathway for the heat transfer from the superheated layer experiencing the transient conduction to the bubble surface at the upstream. This micro-convection indeed induces flow circulation within the liquid and causes evaporation at the bubble surface at the upstream. Consequently, the liquid accelerates due to the evaporation of the elongated bubble behind the liquid. With the evaporation, the liquid mass decreases at the liquid-vapour interface between the liquid and the elongated bubble.

As mentioned in Section 1.1, the findings through the exploration from experimental studies regarding the characteristics and mechanisms of nucleate boiling during flow boiling of subcooled liquids in rectangular micro-channels are incomplete. The features and mechanisms insufficiently explored involves:

- The local hydrodynamics and thermodynamic of fictitious boiling.
- The liquid flow patterns.
- The movements of bubbles from the side surfaces top through a microscope as also stated by Barber et al. [67].

On the other hand, Kandlikar [68] observed many times that the bubbles are just visible through the record from a high-speed camera with the speed of 1000-6000 fps, and replaying the frames at a slow rate of 30 fps. When further increasing the superheat, the frequency of the nucleation of bubbles becomes exceptionally rapid and problematic for the camera to capture the bubbles even at the speed of 6000 fps. With this limitation of experimental tests, numerical methods are paramount importance to explore the regional mechanisms. The numerical methods are the reliable approach to examine the local mechanisms of heat transfer, especially those details which are inaccessible from the experiments for the development of more reliable mechanistic prediction methods [14]. For this reason, this study employs a numerical technique to explore the local heat transfer mechanisms.

2.5 Numerical Studies of Characteristics and Mechanisms of Nucleate Boiling during Flow Boiling of Subcooled Liquids in Rectangular Micro-Channels

Researchers have employed numerical techniques to investigate characteristics and mechanisms of flow boiling of subcooled liquids in rectangular micro-channels, and this section presents the review of findings of these studies.

The numerical models employed for the investigation of flow boiling in rectangular micro-channels by researchers involve [69]:

- Navier-Stokes governing equations (consist of continuity, momentum, and energy equations) including additional source terms associated with appropriate assumption.

- The definition of the source terms of interphase mass transfer. Both momentum and energy equations in equation exclude the source terms of interfacial momentum transfer and heat transfer as the phase change cancels out in the summed momentum and energy equations. This exclusion is legit as the summed momentum and energy sources are zero to maintain conservation of momentum and energy in the system.
- The definition of the corresponding boundary conditions (e.g., inlet velocities, temperatures, and volume fraction, heat fluxes, outlet pressures, surface conditions – slip or no-slip, etc.).
- The interface capturing methods (out of other two methods which are boundary integral methods and finite element methods). The interface capturing (and tracking) methods are numerical methods for multiphase flows, including flow boiling, by explicitly capturing the interface when the interface is larger than the grid size. The interface capturing methods involve only a single set of conservation equations with an additional advection equation to track the interface [69]. The methods also consider a single homogeneous flow of the two phases of liquid and vapour in which all the phases of fluids have similar velocity, pressure, and temperature fields.
- The phase change model.
- The surface tension model.

The governing equations of the numerical models are available in [69].

The interface capturing methods consist of many types [69]. The two types of the methods commonly implemented in the existing numerical study of flow boiling in rectangular micro-channel heat sinks are the volume of fluid (VOF) [63, 70-72] and level-set methods [29, 73-79]. The VOF method proposed by Hirt and Nuchols [80] is an interface capturing approach by tracking the presence of the two phases or liquid-vapour interface. The liquid-vapour interface is traceable by applying numerical schemes such as geometrical reconstruction [81, 82], higher order difference schemes [83], etc. Another interface capturing method of the level-set proposed by Osher and Sethian [84] and further improved by Sussman et al. [43] implements a level-set function as the colour function to define the interface. The level-set function assumes positive values in one phase and negative values in another phase, and the value at the interface is zero. The absolute value of the level-set function determines the shortest distance from the given location to the interface. In the interface capturing methods, the governing equations require the selection of phase change model and surface tension model. The available phase change models are according to experimental data and theoretical models, heat conduction, and kinetic theory.

Comparing to VOF method, the level-set method possesses a disadvantage that the level-set function advection equation produces more mathematical errors when the interface experiences severe stretching or tearing as stated by Rider and Kothe [81]. The incidence causes the loss of mass conservation. Then, Nourgaliev et al. [85] suggested a way to improve the mass conservation equation in the level-set method applying higher order discretisation to solve the advection equations. On the other hand, the VOF method is computationally cheaper as compared to the level-set method and conserves mass [69]. However, the VOF method excludes explicit distance function and therefore harder to determine the interface curvature accurately. The level-set method has a distance function present for the interface curvature calculation and is more computationally expensive. This incidence is due to an additional step of re-distance the interface location which uncertainty produces a better estimation of curvature. Nevertheless, a strategy is available to couple the level-set and VOF methods together in the calculation to combine their advantageous parts [86].

The available phase change model of the numerical techniques comprise of three classes [69]:

- Phase change models based on experimental data and theoretical models.
- Phase change models based on heat conduction.
- Kinetic-based phase change models.

The numerical studies adopting the phase change model based on experimental data and theoretical models are Zu et al. [87] and Zhuan and Wang [70-72], respectively. Zu et al. [87] inject a vapour mass flow into the micro-channel with the same rate as the bubble growth of the experiment of Gedupudi et al. [88]. On the other hand, Zhuan and Wang [70-72] implement the theoretical model of bubble growth of Plesset and Zwick [89] while applying a heat flux at the liquid-vapour interface with a calculated mass flux. With these settings, both the applied heat flux and vapour mass flow rate are attainable through back-calculation from the bubble growth rate. When the bubble diameter is about to reach the tube diameter, the bubble growth rate becomes stagnant while a liquid film appears between the interface and tube surface. The bubble then experiences the heat conduction, and the phase change continues. Also, the bubble growth in the simulation is identical to the experimental observations or theoretical calculations, allowing the simulation to concentrate on the modelling of following processes (such as film evaporation).

The phase change model based on heat conduction assumes the phase change at the liquid-vapour interface occurs as a result of the difference of the energy conducted to and from the liquid-vapour interface. This model is available in the numerical studies of flow boiling in rectangular micro-channels [29, 73-79]. In the model, the energy of heat available for the phase change is proportional to the

difference of heat conduction between the liquid to the interface and the interface to the vapour. The phase change also causes the mass flux at the interface with a relationship as:

$$\dot{m}'' = \frac{n \cdot (k_l \nabla T_l - k_v \nabla T_v)}{h_{lv}} \tag{2.7}$$

where $\dot{m}''$ is positive for evaporation or boiling process and negative for condensation process.

The kinetic-based phase change models are according to the kinetic theories of liquid and vapour, and the development begins from Schrage [90]. Schrage [90] firstly studied the mass transfer process at the liquid-vapour interface, followed by the review of the work of Schrage [90] and also Rohsenow [91] from Tanasawa [92]. Tanasawa [92] then provides an interphase mass transfer model for interphase condensation as:

$$\dot{m}''_{interface} = \frac{2\gamma}{2-\gamma}\left(\frac{1}{2\pi R}\right)^{1/2} \frac{\rho_v \boldsymbol{h}_{lv}}{T_v^{3/2}} (T_{int} - T_v) \tag{2.8}$$

where $\dot{m}''_{interface}$ is interphase mass transfer per unit area, γ is phase change or accommodation coefficient, R is gas constant, and $\boldsymbol{h}_{lv}$ is latent heat. Equation (2.8) assumes the temperature jump across the liquid and vapour interface is small relative to absolute vapour temperature and includes Clausius-Clapeyron relation to change the pressure difference term into a temperature difference term. Tanasawa [92] also stated that the measurement of γ is complicated and the range of γ is from 0.04 to 1 depending on the fluid. This phase change model has been applied in the simulation of flow boiling in micro-channels from Zhou et al. [93]. Equation (2.8) can also be expressed as:

$$\dot{m}''_{interface} = \frac{2\gamma}{2-\gamma} \frac{p_v - p_{sat}}{\sqrt{2\pi R T_v}} \tag{2.9}$$

Comparing to phase change model based on heat conduction and kinetic theory, the utility of phase change model based on experimental data and theoretical models is limited [69]. This incidence is due to each experimental data, and the analytical model is only available for certain specific cases. The phase change model based on heat conduction is more simple and easy to apply; however, this model is inaccurate as the phase change rate is only according to the heat conduction in the phase without capturing the interface kinetic limitations of an interface. Among the three types of phase change models, the kinetic-based models are the most accurate. The kinetic-based models are accurate due to the consideration of phase change flux based on the physics at the interface and therefore capturing the kinetic limitation.

The surface tension model commonly employed to evaluate the surface tension effect at the phase interphase is the Continuum Surface Force (CSF) model proposed by Brackhill et al. [94]. The CSF model estimates the surface tension induced stress change by a body force acting on a small but finite fluid region surrounding the interface and is available in Brackhill et al. [94].

The researchers have adopted different operating parameters for the numerical investigation relating to the location of ONB in rectangular micro-channels as listed in Table 2.6.

Table 2.6: Operating parameters of selected numerical studies of characteristics and mechanisms of nucleate boiling during flow boiling of subcooled liquids in rectangular micro-channels in the literature

Literature	Operating parameter
Qu and Mudawar [6]	As stated in Table 2.1, θ of 30° and 80°, and neglecting g.
Lee and Son [75]	Working fluid of water (properties at 1 atm); u_{in} of 0.12 m/s, p_{amb} of 1 atm; ΔT_{sup} of 5-20 K; reference length l_0 of 1 mm; $H = W$ in most with H = 0.4; L = 10-22.5; a bubble with $r_{bub,init}$ of 5 x 10-3 mm on the bottom heating surface in the microchannel; θ of 30-50°; and considering g.
Mukherjee and Kandlikar [29]	Working fluid of water (properties at 100°C); u_{in} of 0.146 m/s; T_{in} of 100-107°C; T_{surf} of 100-107°C; T_f = 100°C; one 200 μm wide, 200 μm high, and 1 mm long micro-channel; a bubble with $r_{bub,init}$ of 20 μm at 0.2 mm along the length at the centre of bottom surface of the micro-channel; θ of 50°; and neglecting g.
Mukherjee and Kandlikar [73]	Working fluid of water (properties at 100°C); u_{in} of 0.146 m/s; T_{in} of 102°C; T_{surf} of 108°C; T_f = 102°C; one 200 μm wide, 200 μm high, and 800 μm long micro-channel; a bubble with $r_{bub,init}$ of 20 μm at 0.2 mm along the length at the centre of bottom surface of the micro-channel; θ of 20-80°; and considering g.
Mukherjee and Kandlikar [74]	Working fluid of water (properties at 100°C except varying σ of 0.03-0.0589 N/m^2); u_{in} of 0.146 m/s; T_{in} of 102°C; T_{surf} of 108°C; T_f of 102°C; one 200 μm wide, 200 μm high, and 800 μm long micro-channel; a bubble with $r_{bub,init}$ of 20 μm at 0.2 mm along the length at the centre of bottom surface of the micro-channel; θ of 40°; and considering g.

Table 2.6: (Continued)

Literature	Operating parameter
Suh et al. [76]	Working fluid of water (properties at 1 atm); substrate of silicon ($\rho_s c_{p,s} = 0.43\rho_l c_{p,l}$ and $k_s = 230k_l$); u_{in} of 0.1 m/s; $T_{in} = T_{sat} = 100$°C; ΔT_{sup} of 5-15 K; one to three $H_c = 0.2$ mm, $W_c = 0.4$ mm, $L_c = 10$ mm micro-channels; a bubble with $r_{bub,init}$ of 5×10^{-3} mm on the heated bottom wall of each microchannel; W_{fin} of 0.125 mm; length before inlet of 0.1 mm; θ of 30°-50°; and considering g.
Mukherjee [77]	Working fluid of water (properties at 100°C); Re of 100; ΔT_{sup} of 8 K; T_f of 100°C; one 200 μm wide, 200 μm high, and 800 μm long micro-channel; θ_{rec} of 20°-40°; θ_{adv} of 40°-80°; and neglecting g.
Mukherjee and Kandlikar [78]	Working fluid of water (properties at 100°C); u_{in} of 0.12 m/s; T_{in} of 103°C; T_{surf} of 112°C; T_f of 103°C; one 200 μm wide, 200 μm high, and 800 μm long micro-channel; a bubble with $r_{bub,init}$ of 20 μm at 0.2 mm along the length at the centre of bottom surface of the micro-channel; θ of 40°; and neglecting g.
Zhuan and Wang [71]	Working fluid of water (properties at 1 atm); u_{in} of 0.65 m/s; T_{in} of 30-100°C; $q''_{total,fin}$ of 16.16-70 W/cm^2; p_{in} of 1 atm; $\dot{m}$ of vapour of 2.35×10^{-8} kg/s through a circular inlet with a diameter of 0.2 mm at the side heating surface at x of 10 mm; one 275 μm wide, 636 μm high, and 25.4 mm long micro-channel; and considering g.
Lee et al. [95]	Working fluid of water; substrate of Pyrex glass, silicon, aluminium and copper; 200×200 μm^2, 500×500 μm^2, and 1×1 mm^2 smooth thin Pt heater of located between the working fluid and the substrate; rate of heat generation q'''_{hs} of 10^{13}-5×10^{13} W/m^3; Re of 500-3500; T_{in} of 20°C; one 200 μm-1 mm wide and 200 μm-1 mm micro-channel, W_s of 118 μm H_b of 2464 μm; W_s of 542 μm; and θ of 90°.
Mukherjee et al. [79]	Working fluid of water (properties at 100°C); Re of 50-200; T_{in} of 102°C; ΔT_{sup} of 5-10 K; T_f of 102°C; one 200 μm wide, 200 μm high, and 800 μm long micro-channel; a bubble with $r_{bub,init}$ of 20 μm at 0.2 mm along the length at the centre of bottom surface of the micro-channel; σ of 0.03-0.0589 N/m^2; θ of 20°-80°; and considering g.
Zhuan et al. [72]	Working fluid of HFE 7100 (properties at T_{sat} of 60°C); q''_b of 0-750 W/cm^2; $\dot{m}''$ of 670-6730 kg/m^2 s; T_{in} of -30-0°C; p_{out} of 1.138 bar; 11-24 of 123.4-259.9 μm wide, 304-1041.3 μm high, and 25.27 mm long micro-channels, and considering g.

Qu and Mudawar [6] have developed a numerical model to study the location of ONB during the incipient flow boiling in a rectangular micro-channel heat sink. The numerical model developed is according to a criterion of bubble departure that

considers the force balance on a bubble, superheating of the entire surface of the bubble, axial heat conduction, conjugate heat transfer, and fully developed laminar flow. The locations of the bubble that nucleate at the bottom and side surfaces and corner are also considered in the model as displayed in Figure 2.25. Figure 2.25 shows that the bubble more easily expands into the channel corner when increasing the contact angle from 0° to more than 45°. Also, when the contact angle exceeds 45°, the liquid layer between the bubble and the channel corner is impossible to exist. The nucleation of the first bubble is absent at the corner, although the location provides the hottest spot. Instead, the first bubble that satisfies the criterion of superheat for the nucleation was predicted to nucleate at the bottom surface, which is close to the corner. This occurrence is due to the smallest gradient of temperature that causes the weak heat transfer at the corner. Nevertheless, the location of the bubble nucleation contradicts with the outcome from Yin et al. [96] as mentioned in Section 2.4 in which Yin et al. [96] observed majority of bubbles nucleate at the corners. This difference is possibly due to the different $\dot{m}''$ between the study of Qu and Mudawar [6] and Yin et al. [96] in which Yin et al. [96] applied lower values of $\dot{m}''$ than Qu and Mudawar [6].

Lee and Son [75] have investigated the bubble dynamics and heat transfer associated with nucleate boiling in a rectangular microchannel through the numerical model. In the numerical model, they solve the governing equations of conservation of mass, momentum, and energy in the liquid and vapour phases and track the liquid-vapour interface by a level set method. They [75] discovered that the channel size which is smaller than the bubble departure diameter and smaller contact angle cause the bubble growth rate coupling with the heat transfer rate to significantly increase. Also, when increasing the contact angle from 0° to more than 45°, the bubble more easily expand into the channel corner similar to the observation of Qu and Mudawar [6] as depicted in Figure 2.25. This incidence causes the decrease of the surface heat flux in the micro-channel with more vapour region direct contact with the surfaces. On the other hand, when decreasing the contact angle, the heat transfer rate increases.

Mukherjee and Kandlikar [29] have numerically examined the vapour bubble growth during flow boiling in a micro-channel by employing SIMPLER method [97] to solve the Navier-Stokes equations associated with the level set approach. The SIMPLER method refers to the semi-implicit method for pressure-linked equations revised. The level set method serves the purpose to capture the liquid-vapour interface. The numerical model also includes a bubble with initial radius located at a location along the length and the centre within the cross-section of the micro-channel. They [29] observed that the first bubble grows steadily followed by a rapid axial growth when the bubble is almost occupying the cross-section of the micro-channel. During the fast axial growth, the vapour patch or region with vapour directly contact with the heating surface appears. Meanwhile, within the cross-

section, a thin liquid layer retains between the bubble and the channel surfaces. This thin layer causes the rapid axial growth of the bubble with a high evaporation rate. The rate of bubble growth bubble is also higher with more substantial liquid superheat while the bubble growth rate is lower with larger Re. Also, during the bubble growth, the upstream interface of the bubble tends to move forward and backwards. Furthermore, the bubble growth rate changes insignificantly with the effect of gravity.

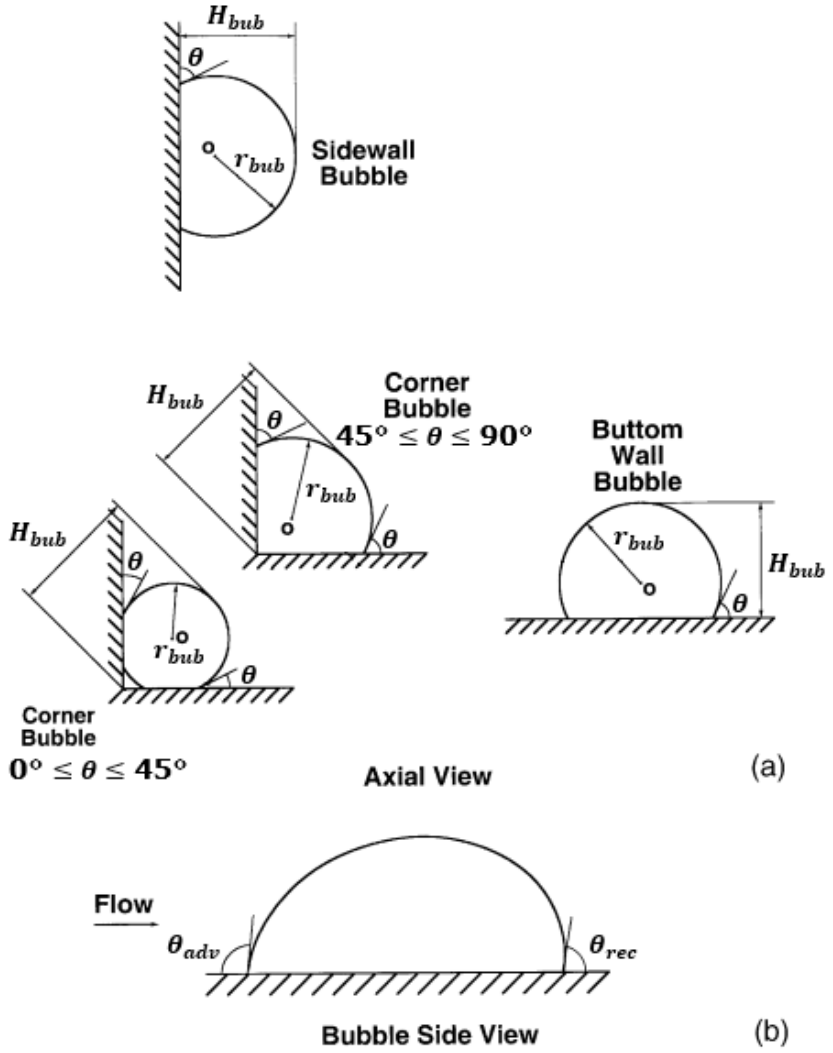


Figure 2.25: (a) Axial view of nucleated bubbles at the bottom and side surfaces, and corner, and (b) side view of nucleated bubble [6]

Mukherjee and Kandlikar [73] have also evaluated the effect of arbitrary contact angles on the growing vapour bubble and area-averaged surface heat transfer on a surface in a micro-channel. They employed the similar approach as their previous study [29]. In this numerical study, they [73] found that the lower the contact angle causes higher surface heat transfer and bubble growth rate with the formation of a liquid layer. The liquid layer is between the downstream bubble

interface and the channel surface. On the other hand, smaller contact angles provide smaller surface tension force and evaporation momentum force.

Mukherjee and Kandlikar [74] at the same time have also studied the effect of surface tension on vapour bubble growth and surface heat transfer during flow boiling in micro-channels with the similar approach [29]. They [74] found that the surface tension is insignificant to the bubble growth and surface heat transfer. Nevertheless, with the low surface tension, the bubble shape varies in which the bubbles become longer and thinner, causing higher surface heat transfer.

Suh et al. [76] have examined the bubble dynamics, flow, and heat transfer during flow boiling in parallel micro-channels by employing the numerical model of Lee and Son [75]. They [76] also consider the axial heat conduction and conjugate heat transfer by including a physical wall in their computational domain of micro-channel. They [76] observed that the backward bubble expansion leads to the reverse flow in the multiple micro-channels and the bubble formation is unsymmetrical in the micro-channels. The reverse flow becomes more significant when decreasing the contact angle and increasing the heating surface superheat. Also, the backward bubble causes the boiling heat transfer rate to fall in the multiple micro-channels as compared to the single micro-channel. The bubble growth occurs in a micro-channel, the area and time-averaged heat flux reduced is about 9-30% whereas 27-34% for all the micro-channels.

Mukherjee [78] employed the similar numerical technique of Mukherjee and Kandlikar [29] to examine the heat transfer mechanism exists on the surfaces in the micro-channel during flow boiling. He [78] discovered that the smaller contact angles improve the heating surface heat transfer during flow boiling which is dissimilar to nucleate pool boiling in which the heat transfer increases with contact angles. Also, the heat transfer at the receding bubble interface is higher than the advancing bubble interface. Furthermore, the primary heat transfer mechanism is the thin-film evaporation that forms the apparent nucleate boiling characteristic in the micro-channel. With their numerical technique, the liquid circulation associated with the transient heat conduction is absent on the heating surface in the micro-channel.

Zhuan and Wang [71] implements the VOF multiphase flow model to study the nucleate boiling water in micro-channels. They categorised the bubble growth in the micro-channel into two stages. At the first stage, the bubble growth through the control of the surface tension whereas the incipient heat transfer dominant at the second stage of the boiling process. Also, they summarised from their analysis that Marangoni heat transfer is significant during the ONB in the micro-channels. On the other hand, in the micro-channels, two stages of nucleate boiling emerge. During the first stage, the suppression of bubble from surface tension while Marangoni convection dominating the interface heat transfer. In the second stage, the surface

superheat is larger than the transitional point, causing sufficiently large heat flux of the ONB to overcome the surface tension. With the more substantial heat flux, the bubbles expand rapidly and lift-off from the surface. Furthermore, higher heat fluxes produce larger volume fractions of vapour at the outlet of the micro-channel. Moreover, the bubbles experience the pressure spike at the nucleation sites as a result of the surface tension on the interface which produces the possibility of the disruption in the flow.

Lee et al. [95] have investigated ONB of water in rectangular micro-channels under the pulsed heating with the numerical model of VOF. They [95] observed that the instant for the appearance of the location of ONB was determined when the void fraction first appears on the surface of micro-heater. The simulated temperature of heater over-estimates the experimental data due to the imperfect insulation of experimental devices and multiple layers of metal underneath the Pt micro-heater. The ONB occurs faster when increasing the power of micro-heater. Also, the substrate materials of copper, aluminium, silicon, and Pyrex with thermal diffusivities $k_s/\rho_s c_{p,s}$ of 11.33, 8.55, 8.03, and 0.078 μm^2/s in the descending order produce shorter transient time.

With the numerical model of Mukherjee and Kandlikar [29], Mukherjee et al. [79] have analysed the heat transfer mechanisms on the heating surface during the vapour bubble growth in a micro-channel. They [75] found that the heated surface heat transfer increased with the superheat of heating surface and bubble growth rate in the micro-channel. However, the heat transfer is almost unaffected by the liquid flow rate. The surface heat transfer raises mainly as a result of the movement of the evaporating liquid-vapour interface. The bubble growth tends to push the liquid towards the micro-channel surfaces, suppressing the growth of the thermal boundary layers.

Zhuan and Wang [71] later extended their numerical study to evaluate the mechanism of bubble dynamics and heat transfer of subcooled flow boiling in a micro-channel. For the bubble dynamics, Zhuan and Wang [71] discovered that the coalescence seldom occurs during the nucleation which is consistent with the observation from Lee and Mudawar [37, 48]. During subcooled flow boiling, the ONB commonly occurs on the heating surfaces while the departure of bubbles or bubbles that lift-off from the surfaces seldom occur upstream. Furthermore, the ONB occurs at the later time, and the bubbles slowly grow with high aspect ratios. Also, the bubble expands at the lower rates and in smaller sizes in the superheated liquid layer near the heating surfaces when increasing the degrees of subcooling and decreasing heat fluxes. Moreover, with the higher degrees of subcooling, the bubble departure sizes are smaller with lesser coalescence effects and the occurrence of slug flow delays. Furthermore, the temperature of lift-off bubbles decreases when the condensation of bubble interfaces becomes more frequent. For

the bubbles with lift-off diameter larger than the thickness of the superheated layer during higher heat fluxes, the bubble reaches unstable state, and the interface oscillates with rapid condensation beyond the superheated layer. This occurrence causes some bubbles to shrink and break or collapse. Therefore, the condensation of bubble interface as a result of the effect of the subcooled liquid suppresses the bubble growth and coalescence, delaying the appearance of annular flow. At high degrees of subcooling, the Marangoni heat flux at the initial time of nucleation controls the interface in which the surface tension suppressing the bubble is substantial, causing low bubble growth rates. The Marangoni heat flux reduces when increasing surface heat fluxes with higher bubble growth rates and lifts-off, and consequently forming the developed subcooled flow boiling.

Zhuan and Wang [72] have also compared the difference of the bubble behaviours between subcooled and saturated flow boiling. During subcooled flow boiling, the bubbles disperse within the micro-channels whereas the bubbles rapidly grow and form slugs during saturated flow boiling. During the saturated flow boiling, the flow regime frequently encountered in the micro-channel is either slug or annular flow whereas bubbly flow dominates at higher degrees of subcooling and heat fluxes. The annular flow seldom occurs in the broad range of mass and heat fluxes during the subcooled flow boiling. The high degree of subcooling delays the ONB during subcooled flow boiling as compared to saturated flow boiling. Also, during the subcooled flow boiling, the fluid is at the thermal-developing region in which the thermal boundary layer becomes thicker along the flow direction while the heat transfer coefficient decreases rapidly. In the thermal-developing region, the heterogeneous temperature is significant, causing non-uniformity of the interfacial evaporation and condensation during subcooled flow boiling. The thermal boundary layer during flow boiling of subcooled liquids also possesses high gradients of temperature, leading to non-uniform temperature distribution along the interface of the growing bubbles.

Although researchers have conducted the numerical studies of nucleate boiling during flow boiling of subcooled liquids in rectangular micro-channels and observed various complex processes, the investigation is inadequate. In most of the existing numerical studies, as found and reviewed in this section, the researchers arbitrarily impose a bubble at the initial time of the numerical simulation opposing to the real condition. By assuming the arbitrary bubble at the initial time, the bubble nucleation process associated with the fictitious boiling encountered in the experimental studies of Peng and Wang [38-41] as reviewed in Section 2.4 remains unexplored. Moreover, from the literature, the studies regarding the effect of substrate materials and working fluids on the characteristics and mechanisms of nucleate boiling are inadequate. Therefore, this investigation evaluates the impacts of substrate materials, and working fluids as well as mass fluxes, heat fluxes, inlet temperatures on the changes of the regional characteristics and mechanisms. The

features and mechanisms explored and studied at the different operating parameters provide useful information for the development of the prediction methods to design better micro-channel heat sinks.

2.6 Mechanistic Prediction Methods of Nucleate Boiling during Flow Boiling in Rectangular Micro-Channels

Since conducting numerical studies are computationally expensive and time-consuming, the reliable mechanistic prediction methods of nucleate boiling of flow boiling in rectangular micro-channels are highly necessary.

There are mechanistic prediction methods of nucleate boiling in the literature to predict the ONB during flow boiling in rectangular micro-channels.

Peng et al. [42, 98] have proposed a non-dimensional parameter N_{mb} and related criteria of the bubble nucleation during the liquid flow in micro-channels. They derived [42, 98] N_{mb} based on the thermodynamic aspects of phase transformations of liquid and interaction of the bubble growth process and the micro-channel geometry in micro-channels as derived in (2.10):

$$N_{mb} = \frac{\boldsymbol{h}_{lv}\alpha_v}{C\pi(\nu_v - \nu_l)q''_{total,fin}d_h} \tag{2.10}$$

where N_{mb} is the dimensionless parameter, α_v is the thermal diffusivity of vapour, and C is an empirical constant which is obtainable from the experiment. The nucleation occurs when $N_{mb} \leq 1$. N_{mb} also considers the effect of liquid thermophysical properties. This model depicts that the liquid in small micro-channels is capable of absorbing the large sensible heat with high heat transfer rates which are possible to exceed the nucleate boiling in micro-channels. This condition resembles the fictitious boiling requiring further investigation.

Liu et al. [47] have developed an analytical model of ONB in rectangular micro-channels. The model incorporates the effects of fluid inlet conditions, contact angle, and geometry of the micro-channel as depicted in (2.11):

$$\sqrt{T_{in} + \frac{q''_b W_b L_b}{\rho_l c_{p,l} u_{in}(NW_c H_c)} + \frac{\left(\frac{\beta}{1+2\eta\beta}\frac{W_c+W_w}{H_c}\right)q''_b}{\left(Nu_{fd,3}k_l\right)/d_h}} - \sqrt{T_{sat}} = \sqrt{\frac{2\sigma C}{\rho_v \boldsymbol{h}_{lv} k_l}\left(\frac{\beta}{1+2\eta\beta}\frac{W_c+W_w}{H_c}\right)q''_b} \tag{2.11}$$

$$T_{surf} - T_{sat} = 2\sqrt{T_{sat}}\sqrt{\frac{2\sigma C}{\rho_v \boldsymbol{h}_{lv} k_l}\left(\frac{\beta}{1+2\eta\beta}\frac{W_c+W_{fin}}{H_c}\right)q''_b}$$

$$Nu_{fb,3} = 8.235(1 - 1.883/\beta + 3.767/\beta^2 - 5.814/\beta^3 + 5.361/\beta^4 - 2/\beta^5)$$

where q_b'' is heat flux at the channel base; W_b is width of channel base; L_b is length of channel base; $c_{p,l}$ is specific heat of liquid at constant pressure; u_{in} is velocity at inlet; N is number of channels; η is efficiency of fin; W_c is channel width; W_{fin} is fin width; H_c is the channel height; β is aspect ratio H_c/W_c; $Nu_{fd,3}$ is Nusselt number for fully developed in a three sides heated rectangular channel; and D_h is hydraulic diameter. $Nu_{fd,3}$ is available in Shah and London [99]. These analytical models assume uniform heat fluxes along the three-sided heating surfaces (bottom and side surfaces) in the micro-channel and produce the readings with 20% higher as compared to the experimental data. This discrepancy is due to the assumption of uniform heat fluxes.

Liu et al. [47] have also compared their analytical model with other prediction models of ONB in subcooled flow boiling in conventional-sized channels from the literature. From the literature employing conventional sized channels, Liu et al. have selected the analytical models of ONB of Hsu [100], Sato and Matsumura [101], Bergles and Rohsenow [102], Davis and Anderson [103], Kandlikar et al. [104], and Celata et al. [105].

Hsu [100] has first created the criterion of the nucleation of a bubble for flow boiling and pool boiling (at pressure equals to or less than atmospheric pressure of water on the heating surface made of stainless steel with 20-170°C of temperature). When developing the model, he [100] considers the size range of active cavities as a function of temperature or heat flux. When the temperature of the liquid exceeds the temperature at the equilibrium of bubble in a cavity, the bubble nucleates and the radius of the bubble r_{bub} changes as shown in Figure 2.26a. Also, in Figure 2.26a, the hemispherical bubble with $r_{bub} = r_{cav}$ that grows out from the cavity has the smaller radius of curvature. When $r_{bub} > r_{cav}$, the bubble possesses the shape of the truncated sphere with the height of bubble y_{bub}, contact angle θ and the limiting thickness of thermal boundary layer δ as depicted in Figure 2.26b. On the other hand, Figure 2.26c illustrates the criterion of bubble nucleation when interception between the curves of the liquid temperature and equilibrium of bubble exists with sufficient development of the thermal layer. Moreover, the thermal layer near the nucleation site is slightly thinner as compared to the bulk liquid during the bubble nucleation without experiencing any distortions. Therefore, the nucleation site possesses the shorter length of between the heating surface and the isotherm line at the temperature at the top part of the bubble than the bulk liquid.

When developing the criterion of the nucleation of a bubble for flow boiling and pool boiling, Hsu [100] assumes θ as 53.1°, $y_{bub} = 1.6r_{bub}$ and critical radius $r_{crit} = 2r_{cav}$. When both curves of liquid temperature and equilibrium of bubble intercept each other at a tangent point with $y_{bub} = r_{crit}$, the bubble nucleation is normally absence. The bubble nucleation takes place when further increasing the superheat of the heating surface until the interception occurs at two points from both curves

with $y = r_{min}$ and $y = r_{max}$. The bubble nucleation occurs when increasing q'' until the liquid temperature reaches or exceeds the temperature of the equilibrium of bubble with $r_{cav,min}$ and $r_{cav,max}$ as:

$$\{r_{cav,min}, r_{cav,min}\} = \frac{\delta(T_{surf} - T_{sat})}{2C_1(T_{surf} - T_\infty)}\left[1 \pm \sqrt{1 - \frac{8C_1}{C_2}\frac{(T_{surf} - T_\infty)T_{sat}\sigma}{(T_{surf} - T_{sat})^2 \delta \rho_v h_{lv}}}\right] \quad (2.12)$$

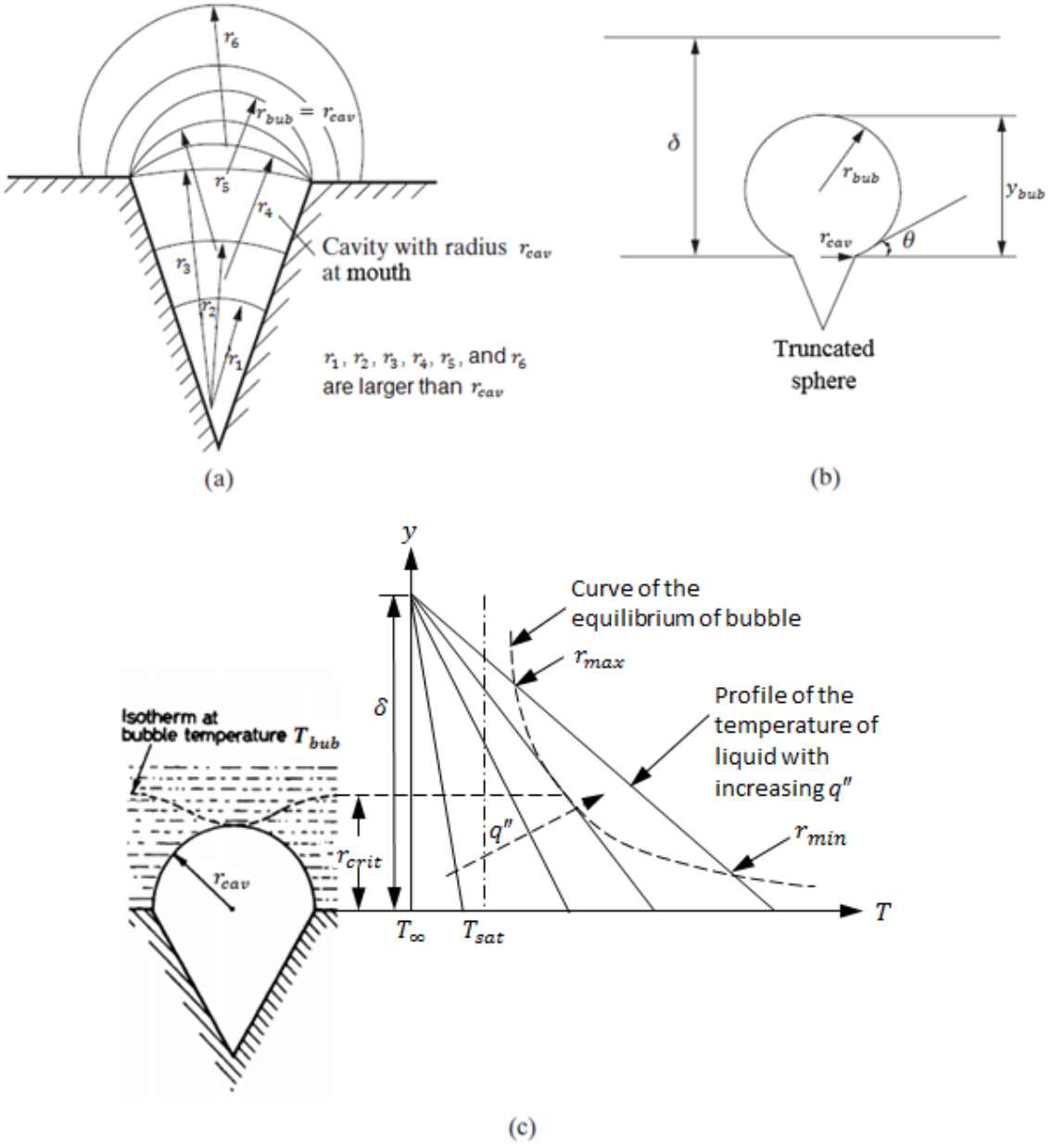


Figure 2.26: Characteristics of the nucleation of bubble (a) change of radius of curvature of bubble in a cavity, (b) a chopped spherical bubble, and (c) criterion for the nucleation of bubble [106]

From equation (2.12), Hsu [100] plotted the active cavity range for different thermal boundary layer thickness of saturated water as shown in Figure 2.27a. Meanwhile, Figure 2.27b depicts the active cavity range for different subcooling ΔT_{sub} with a constant thermal boundary layer thickness of 0.5 mm at atmospheric pressure. The plots in Figure 2.27 indicate that superheat is prerequisite for any cavities in a finite range of r_{cav}. The bubble nucleation becomes difficult with smaller active cavity ranges when thermal boundary layer thickness reduces. The criterion of nucleation of Hsu [100] with the term of incipient heat flux q''_{ONB} (the heat flux during the threshold of incipience of flow boiling) with the assumption of θ of 53.1° is also obtainable as expressed in (2.13):

$$q''_{ONB} = \frac{k_f \boldsymbol{h}_{lv} \rho_v \left(T_{surf} - T_{sat}\right)^2}{12.8 \sigma T_{sat}} \tag{2.13}$$

Sato and Matsumura [101] have derived an analytical relationship from the criterion of nucleation of Hsu [100] for the incipient heat flux q''_{ONB} with the term of wall superheat for the study of incipient subcooled flow boiling. They [101] created the analytical model created considers the bubble shape of the hemispherical sphere in which $r_{bub} = r_{crit}$ and $\theta = 90°$. The model of q''_{ONB} of Sato and Matsumura [101] is:

$$q''_{ONB} = \frac{k_f \boldsymbol{h}_{lv} \rho_v \left(T_{surf} - T_{sat}\right)^2}{8 \sigma T_{sat}} \tag{2.14}$$

Bergles and Rohsenow [102] have proposed a graphical solution according to the experimental studies of the heat transfer of flow boiling of distilled water in a circular tube made of stainless steel. The circular tube is at d_c of 0.094 in and L_c of 5.48 operated at p of 15-2000 lb_F/in^2 and 11-57 m/s. The circular tube attaches to 29 and 48 of L_c/d_c of a heated segment with an annulus with the inner surface (0.0645 in of d_{inner}) made of stainless steel and the outer surface made of Pyrex glass (5 mm of d_{outer}). The analytical model postulates that the hemispherical bubble nucleus grows when satisfying the superheat criterion at length between bubble radius and the heating surface as derived in (2.15) and (2.16).

$$\Delta T_{sup} = 0.555 \left(\frac{q''_{ONB}}{1082 p^{1.156}} \right)^{p^{0.0234}/2.16} \tag{2.15}$$

where p in bar, ΔT_{sup} in K, and q''_{ONB} in MW/m^2, and

$$q''_{ONB} = 15.6 p^{1.156} \left(T_{surf} - T_{sat}\right)^{2.30/p^{0.0234}} \tag{2.16}$$

where q''_{ONB} in Btu/hr-ft², p in psia, and all T (or T_{surf} and T_{sat}) in °F, respectively.

Davis and Anderson [103] have created a prediction technique of ONB by retaining the contact angle as a variable. With the variable contact angle, the hemispherical bubble nucleus grows when satisfying the superheat criterion

between the heating surface and the bubble radius. The prediction model of Davis and Anderson [103] is:

$$q''_{ONB} = \frac{k_f \boldsymbol{h}_{lv} \rho_v \left(T_{surf} - T_{sat}\right)^2}{8(1+\cos\theta)\sigma T_{sat}} \tag{2.17}$$

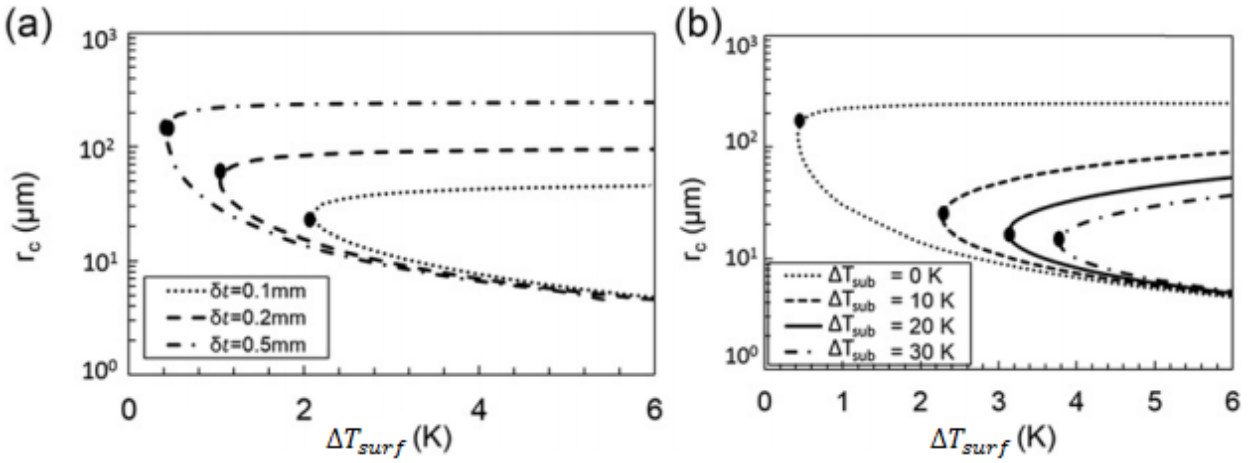


Figure 2.27: Active cavity range for (a) different thermal boundary layer thickness of saturated water and (b) different ΔT_{sub} and constant thermal boundary layer thickness of 0.5 mm [100]

Kandlikar et al. [104] have also proposed a mechanistic model of ONB by assuming the liquid temperature at the bubble top equals to the stagnation point in the thermal boundary layer. The mechanistic model of Kandlikar et al. [104] is:

$$q''_{ONB} = \frac{k_f \boldsymbol{h}_{lv} \rho_v \left(T_{surf} - T_{sat}\right)^2}{8.8\sigma T_{sat}} \tag{2.18}$$

Celata et al. [105] have defined an analytical approach of ONB from experimental study of sub-cooled deionised water in a circular channel made of stainless steel. The channel is at d_c of 8 mm and L_c of 100 mm with p_{out} of 1.0-2.5 MPa, T_{in} of 30-60°C, and u_{in} of 5-10 m/s. They assume that ONB occurs when the experimental data diverge from the theoretical prediction in the pressure against heat flux plot. The prediction approach of Celata et al. [105] is:

$$q''_{ONB} = 0.00195\left(T_{surf} - T_{sat}\right)^2 \exp(0.023p) \tag{2.19}$$

The analytical model of Liu et al. [47] agrees well with other models developed from the conventional sized channels from the literature [100-103] as reviewed above except the prediction models of Hsu [104] and Celata et al. [105]. On the other hand, the mechanistic model of Liu et al. [47] matches the best with the model of Davis and Anderson [103].

Li and Cheng [11] have employed the model of classical nucleation kinetic theory to examine the nucleation temperature of the fluid at the ONB in a micro-

channel. The micro-channel is 60 μm wide, 60 μm long, and 1 cm long at q''_{hs} of 300 W/cm^2 at the bottom surface, T_{in} of 25°C, $\dot{m}$ of 0-6 mg/s. They [11] examined effects of the angles of a corner on the bubble nucleation in the micro-channel with a model defined as:

$$T_{bub} - T_{sat} = \frac{T_{sat}}{\boldsymbol{h}_{lv}\rho_v}\sqrt{\frac{16\pi\sigma^3\omega}{3\boldsymbol{k}T_{bub}\ln\left(\frac{N_0^C\boldsymbol{k}T_{bub}\psi}{N_a\cdot\mathcal{H}}\right)}} \tag{2.20}$$

where T_{bub} is the temperature of bubble; T_{sat} is the saturation temperature; ω is the geometric correction factor for the minimum work required to a critical nucleus; N_0 is the number of molecule per unit volume; C is a constant; $\boldsymbol{k}$ is the constant of Boltzmann (1.3806488 × 10^{-23} kg m²/s² K); ψ is the surface available for the heterogeneous nucleation per unit volume of liquid; N_a is the density of the active site of nucleation; and $\mathcal{H}$ is the Prancle number. This model is applicable for both homogeneous and heterogeneous nucleation. The homogeneous nucleation is the nucleation that occurs in the bulk of superheated liquid whereas the heterogeneous nucleation is the nucleation that initiates in a cavity of a surface. For homogeneous nucleation, $\omega = \psi = C = 1$. For heterogeneous nucleation, $C = 2/3$, and ω and ψ are:

$$\omega = \frac{\beta}{2\pi}(1+\cos\theta)^2(2-\cos\theta) \tag{2.21}$$

and

$$\psi = \frac{1}{2}(1+\cos\theta) \tag{2.22}$$

respectively, where β is the half angle of a corner and θ is the contact angle of a bubble. N_a is equivalent to $N_{a,hom}$ and $N_{a,het}$ for the homogeneous and heterogeneous nucleation in superheated liquids, respectively. $N_{a,hom}$ and $N_{a,het}$ are governed as:

$$N_{a,hom} = N_0\left(\frac{kT_{bub}}{\mathcal{H}}\right)\exp\left[-\frac{16\pi\sigma^3}{3\boldsymbol{k}T_{bub}(p_{bub}-p_l)^2}\right] \tag{2.23}$$

and

$$N_{a,het} = N_0^{2/3}\psi\left(\frac{kT_{bub}}{\mathcal{H}}\right)\exp\left[-\frac{16\pi\sigma^3\omega}{3\boldsymbol{k}T_{bub}(p_{bub}-p_l)^2}\right] \tag{2.24}$$

respectively. From equation (2.23) and (2.24), k is the thermal conductivity, p_{bub} is the pressure of bubble, and p_l is the pressure of the liquid. $\mathcal{H}$ from equation (2.20), (2.23), and (2.24) possesses an expression as:

$$\mathcal{H} = \frac{\boldsymbol{k}T_{bub}}{(3\sigma/\pi m)^{0.5}} \tag{2.25}$$

where m is the mass of a molecule. The corners of a micro-channel act as pseudo-micro-cavities due to their sizes in micro-scale size, which will decrease the nucleation temperature for the heterogeneous nucleation of a bubble. The tested angles are 60°, 90° and 120° for triangular, rectangular and trapezoidal micro-channels, respectively. The measurement is according to the heat transfer from one side of corners. The temperatures of the nucleation of bubbles become lower with the lower angles of corners. In other words, the triangular micro-channel gives the lowest temperature of the nucleation of bubbles, while the trapezoidal micro-channel provides the highest temperature of the nucleation of bubbles. The temperature of the nucleation in rectangular micro-channel is between the values of triangular and trapezoidal micro-channels. Moreover, the predicted temperature of nucleation is relatively higher than the experimental data due to the assumption of the smooth surface in the micro-channel.

Mosyak et al. [46] have developed a mechanistic relationship based on the difference between wall excess temperature and bulk fluid temperature at ONB to the difference between in saturation temperature and fluid temperature to analyse the condition of ONB. The relation is according to the equations of continuity and energy as derived in (2.26):

$$\frac{q''_{ONB}L_{ONB}(2H_c + W_c)}{\rho u_{in}(T_{f,ONB} - T_{in})H_c W_c} = 1 \tag{2.26}$$

If $T_{f,ONB} \approx T_{sat}$, equation (2.26) becomes:

$$\frac{q''_{ONB}L_{ONB}(2H_c + W_c)}{\rho u_{in}(T_{sat} - T_{in})H_c W_c} = 1 \tag{2.27}$$

This mechanistic model provides the estimation of $T_{f,ONB}$ at ONB and the dependence of $T_{f,ONB}$ on ONB cross-section on inlet flow temperature as illustrated in Figure 2.28. In Figure 2.28, $\Delta T_{sub,ONB} = T_{sat} - T_{f,ONB}$ and $\Delta T_{sup,ONB} = T_{surf,ONB} - T_{sat}$, and the dark region indicates the location where the temperature T exceeds T_{sat}. At this vicinity, the maximum probability of the formation of bubble embryo takes place. The nucleation criteria proposed from the conventional sized channel predict well the parameters such as cavity radius and wall excess temperature by implementing experimental data collected.

The investigation of subcooled ONB in a micro-channel under the pulsed heating has been conducted by Lee et al. [95]. The theoretical superheat for the nucleation [100-102, 104, 107] disagrees with the transient ONB of convective flow, but higher than both the simulated and experimental data. This difference is due to the condition of the simulated result is dissimilar with the theoretical superheat, which is according to the criterion of nucleation as shown in Figure 2.26c. In Figure 2.26c, the temperature gradient of liquid is linear and overlapping with the curve of the temperature of the bubble when reaching the state of steady. On the other hand,

the temperature gradient of transient ONB is relatively higher, and therefore higher superheat is required to satisfy the criterion of nucleation with the sensible heat flux at the instant. In other words, the temperature of liquid decreased exponentially with the distance away from the surface during the transient ONB, while overlapping with the curve of the temperature of the bubble. Consequently, when substituting the applied sensible heat flux into the equation of theoretical superheat, the obtained value of theoretical superheat will be much greater than the simulated result and the experimental data.

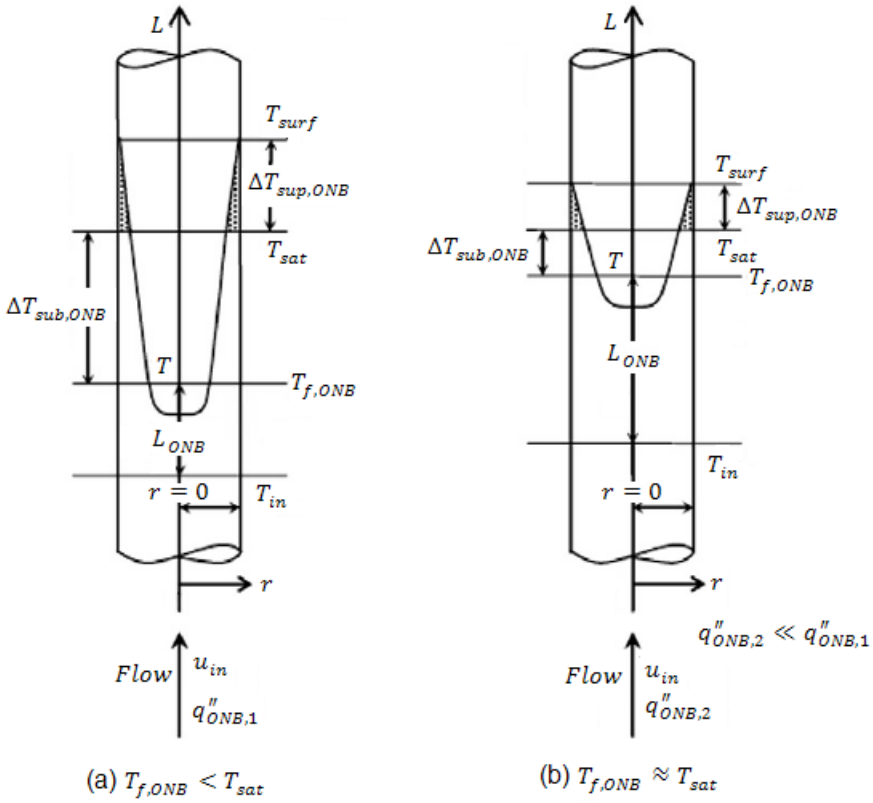


Figure 2.28: Distribution of the temperature of fluid at the cross section of the location of ONB (a) $T_{f,ONB} < T_{sat}$ and (b) $T_{f,ONB} \approx T_{sat}$ [46]

Other than the mechanistic approaches of ONB, researchers have also proposed the mechanistic models of nucleate boiling to analyse forces on the liquid-vapour interface during flow boiling in rectangular micro-channels.

Kandlikar [36, 108] has analysed the forces on a bubble during flow boiling in a micro-channel as depicted in Figure 2.29. In Figure 2.29, the bubble interface involves the forces due to the change of the momentum F'_M, surface tension at the base, $F'_{st,b}$ and $F'_{st,t}$ of the bubble and gravitational force F'_G per unit length. Each force per unit length owns a derivation as indicated in the literature [36, 108]. The change of momentum between the liquid and vapour phases occurs due to higher velocities of the vapour phase as compared to the liquid phase. With the change of momentum, a force exists on the liquid-vapour interface with a higher evaporation

rate at the vapour patch on the heated surfaces in the micro-channel. This occurrence causes the bubble grew rapidly and moved along the flow direction. The bubble moves against the flow direction of the fluid when the pressure inside the bubble increases. The gravitational force in the micro-channel is relatively insignificant as compared to the forces due to the inertia per unit length F_I' and change of the momentum. The forces due to the variation of the momentum overcome the forces holding the bubble which are the surface tension and gravitational force. These forces form a relationship as:

$$F_M' = F_{st,b}' + F_{st,t}' + F_G' \tag{2.28}$$

Kandlikar [36, 108] also observed that the evaporation momentum force acting on the evaporating interface plays a significant role is larger than the inertia and shear forces and depends on applied heat fluxes. The large evaporation momentum force with high evaporation rates at the onset of bubble nucleation is taking the role to facilitate the rapid interface movement, sometimes leading to reversed flow in micro-channels. Apart from the evaporation momentum force, both the viscous force and surface tension force are also significant in the micro-channel. Nevertheless, the viscous force is more important than surface tension with a smaller hydraulic diameter when flow boiling occurs. The smaller hydraulic diameter reduces the Reynolds number, which is the ratio of the inertia force to the viscous force, and therefore the viscous force is vital in a micro-channel. However, the surface tension is still significant in micro-channels, and thus the consideration of the surface tension is still necessary.

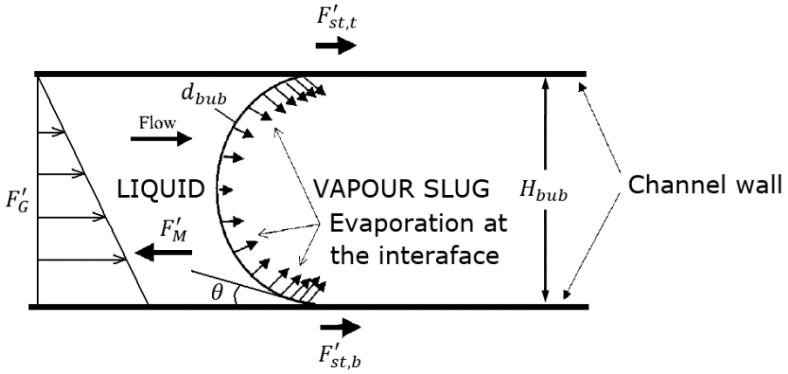


Figure 2.29: Free body diagram of the forces acting on a liquid-vapour interface in a channel [108]

Later Yin et al. [109] have analysed the importance of the forces acting on the meniscus of an evaporating and elongating bubble during flow in micro-channels theoretically. They [109] compared the evaporating momentum force and shear force to other forces such as surface tension force and gravity force. According to their [109] theoretical analysis, the evaporating momentum force is always negligible in micro-channels during flow boiling, unlike the outcome from Kandlikar

[36, 108]. On the other hand, the shear force depends on the particular operating conditions such as channel dimension. When the channel dimension of hydraulic diameter is 10-100 μm, the consideration of the shear force is necessary whereas negligible for the hydraulic diameter of 100 μm-1 mm.

Researchers have also proposed the mechanistic techniques of nucleate boiling to evaluate the motion of growing bubbles during flow boiling in rectangular micro-channels. During flow boiling in micro-channels, the movement of expanding bubbles including bubble departure, sliding dynamics, and lift-off is obtainable through analysing various forces acting on a bubble as depicted in Figure 2.30 from Yin [110]. These forces are in the directions parallel and normal to horizontal heating surfaces and according to the studies of Klausner et al. [111] and Kandlikar [112] as:

$$\sum F_x = F_{st,x} + F_{ud,x} + F_{qsd} + F_{ev,x} \tag{2.29}$$

$$\sum F_y = F_{st,y} + F_{ud,y} + F_{sl} + F_h + F_{cp} + F_{ev,y} \tag{2.30}$$

where F_{st} is surface tension force; F_{ud} is unsteady drag force from the asymmetrical growth of bubble and dynamic effect of the unsteady liquid; F_{sl} is shear lift force; F_h is hydraulic force; F_{cp} is force due to contact pressure; F_{ev} is force due to the evaporation near heated surfaces in micro-channels; and F_{qsd} is quasi steady-drag force in the flow direction. Each force possesses an expression which is available in the literature [111, 112]. When the forces are equivalent to 0 in x- and y-direction, the growing bubble stagnates on the nucleation site. When $F_y > 0$, the bubble lifts-off to the main flow in the direction vertical to the bottom heating surface. Meanwhile, the bubble slides on the channel surfaces without detaching from the heating surfaces.

Indeed, the unsteady drag force F_{ud} in the flow direction is negligible [113] for the nearly constant bubble size during flow boiling in micro-channels as observed in the experimental study of Yin et al. [110] as indicated in Section 2.4. Also, in the theoretical study of Yin et al. [109], the evaporation momentum force is negligible, and therefore F_{ev} is insignificant. By omitting $F_{ud,x}$ and $F_{ev,x}$ from equation (2.29), bubble sliding occurs when the sum of $F_{st,x}$ and F_{qsd} exceeding zero, indicating the breaking of force balance. Since the bubble growth rate is small with the initial immobility in highly subcooled liquid, F_{qsd} is almost constant, and the breaking of force balance is mainly due to the change of $F_{st,x}$. During the evaporation, the bubble contact diameter and contact angles change while reassuring the balance of F_{qsd} and $F_{st,x}$ is possible before a specific time. When the bubble contact diameter and contact angles suddenly change associated with the instantaneous change of $F_{st,x}$, the breaking of force balance occurs, and the bubble starts sliding along the heating surface. The breaking of force balance becomes easier when increasing

mass fluxes and for large heat fluxes. The breaking of force balance is capable of recovering by the adaptive surface tension force caused by the flexibility of the bubble interface that occurs during the slow sliding of the bubble in the earlier stage. When bubbles continue to slide in the flow direction, strong disturbance with serious destabilisation due to the severe disruption to the force balance of the sliding bubble suddenly becomes apparent in the mainstream. This occurrence usually emerges at the downstream of the micro-channel, during the confinement of the bubble in the slow sliding stage, and during the coalescence and discharge of the confined/elongated bubble.

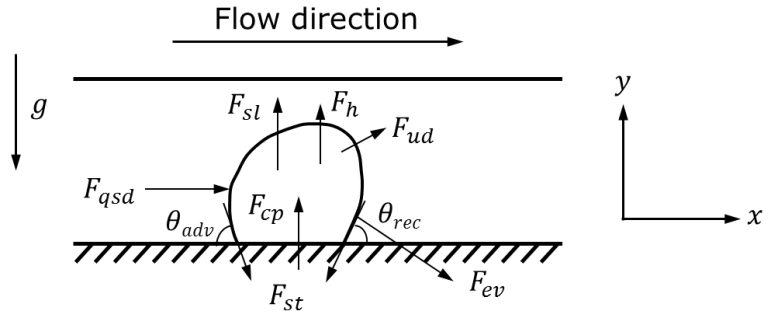


Figure 2.30: Schematic diagram of forces acting on a bubble during flow boiling in a micro-channel θ_{rec}

The existing mechanistic models of nucleate boiling during flow boiling in rectangular micro-channels are merely capable of predicting the ONB, analysing the forces on a bubble, and motion of growing bubbles. Nevertheless, the mechanistic models still insufficient to accurately predicting nucleate boiling during flow boiling in rectangular micro-channels in broad ranges. This inadequacy is probably due to the overlook of some of the mechanisms of the complicated process of flow boiling while proposing the mechanistic models. The mechanisms commonly neglected in the models are axial heat conduction and conjugate heat transfer between the heating surfaces and fluids in the micro-channels which are significant. Also, the mechanisms of liquid flow patterns that might involve fictitious flow boiling in the micro-channels are unexplored in the numerical studies. Therefore, the insufficient studies of the liquid flow patterns lead to the shallow understanding of the mechanisms to generate the more reliable mechanistic models. As a result, the existing models are more dependent on empirical parameters instead of the theory, including the semi-empirical models [15]. For this reason, this numerical study attempts to explore the mechanisms associated with the consideration of axial heat conduction and conjugate heat transfer with different mass fluxes, heat fluxes, and inlet temperatures. Also, this study also continues with the investigation of the impacts of changing substrate materials and working fluids on the mechanisms in which the information is limited at the current stage.

Chapter 3 Methodology

This study employs the numerical method to investigate the mechanisms of nucleate boiling during the flow boiling of subcooled liquid with the bubbly flow in rectangular micro-channel heat sinks. By addressing this study, defining operating parameters and employing a suitable numerical model are essential.

3.1 Operating Parameters

The operating parameters of p, q_b'', $\dot{m}''$, T_{in}, W_c, H_c, W_s, and H_b set in this study are 1 atm, 500-3197 kW/m^2, 115-389 kg/m^2 s, 23-53°C, 200 μm, 264 μm, 200 μm, and 264 μm, respectively. These selected ranges of parameters manage to produce the subcooled flow boiling with the bubbly flow in the rectangular micro-channel heat sinks based on the literature review as presented in Section 2.3. Therefore, this study employs these values for the investigation of the mechanisms. When employing q_b'' around 30 MW/m^2, larger $\dot{m}''$ are necessary to produce this flow boiling condition which complicates the numerical simulation process and are beyond the capability of the existing resources. Also, this study has limited ability to implement as stated in Section 1.1. Also, this study intends to explore the mechanisms to develop better heat transfer prediction methods aiding to design better heat transfer performance of the micro-channel heat sinks. This intention is achievable from the operating parameters employed in this study without the necessity to implement such high values of q_b'' which are more computationally expensive. Other than these parameters, settings of thermo-physical properties of substrate materials and working fluids are needed. The substrate materials selected in this study are stainless steel, silicon, aluminium and copper, whereas the working fluids chosen are water and ethanol. The thermo-physical properties of these materials are available in Table 3.1. In Table 3.1, the thermal diffusivity is equivalent to $k_s/\rho_s c_{p,s}$ whereas volumetric heat capacity equals to $\rho_s c_{p,s}$. For the working fluids of water and ethanol, the thermo-physical properties are available in Table 3.2 and Table 3.4 list down the of water and ethanol, respectively.

Table 3.1: Thermo-physical properties of substrate materials

Thermo-physical property	Substrate material			
	Silicon	**Aluminium**	**Stainless steel**	**Copper**
Density (kg/m^3)	2330	2702	7900	8950
Specific heat at constant pressure (J/kg K)	700	903	477	395
Thermal conductivity (W/m K)	141.2	237	14.9	401
Thermal diffusivity ($\times 10^{-5}$ m^2/s)	8.657	9.713	0.395	11.340
Volumetric heat capacity ($\times 10^3$ J/m^3 K)	1631	2440	3768	3535

Table 3.2: Thermo-physical properties of the working fluid of water in the liquid and vapour phases

Thermo-physical Property	Working fluid	
	Water in the liquid phase (at the reference temperature T_{ref} of 298 K)	**Water in the vapour phase (at the reference temperature T_{ref} of 298.15 K)**
Density (kg/m^3)	958.4	0.59837
Specific heat at constant pressure (J/kg K)	4182	1890
Thermal conductivity (W/m K)	0.6	0.0261
Viscosity (Pa s)	0.001003	1.34×10^{-5}
Molecular weight (kg/kmol)	18.0152	18.01534
Standard state enthalpy (J/kmol)	-2.858412×10^8	-2.418379×10^8

Table 3.3: Thermo-physical properties of the working fluid of ethanol in the liquid and vapour phases

Thermo-physical Property	Working fluid	
	Ethanol in the liquid phase (at the reference temperature T_{ref} of 298 K)	**Ethanol in the vapour phase (at the reference temperature T_{ref} of 298.15 K)**
Density (kg/m^3)	758.105	1.37203
Specific heat at constant pressure (J/kg K)	3255.8	1668.1
Thermal conductivity (W/m K)	0.16917	0.01973
Viscosity (Pa s)	0.000450	1.01×10^{-5}
Molecular weight (kg/kmol)	46	46
Standard state enthalpy (J/kmol)	-2.770×10^{8}	-2.353×10^{8}

3.2 Numerical Model

By setting up the numerical model, the necessary procedures are:

- Defining computational domain.
- Applying governing equations.
- Determining boundary conditions.
- Defining initial conditions.
- Applying discretisation methods.
- Defining under-relaxation factors.
- Setting convergence criteria.
- Validating numerical model.

Also, selecting the suitable numerical model in this study requires reasonable assumptions, and this numerical investigation assumes:

- Fluids are in the continuous flow.
- Thermo-physical properties are constant, except for the viscosity of liquid and vapour (due to the more substantial variation of the temperature at the region of high gradient of temperature).
- The axial heat conduction of substrate and fluid and conjugate heat transfer exist.
- Dispersed and immiscible flows of fluids occur between the liquid and vapour phases.

- The flow is steady.
- The interface of the bubbles is in thermal equilibrium.
- Viscous dissipation presents in the fluid.
- The flow and the heat transfer are in the quasi-steady state.
- Heat radiation is negligible.

The assumption of continuous flow is valid when satisfying a criterion in which Knudsen number $Kn < 10^{-3}$ from the measurement of rarefaction of fluid [114]. Kn is the ratio of molecular mean free path λ and hydraulic diameter d_h. λ is equivalent to $1/NA_{csc}$ according to kinetic theory where N is the number of molecule per unit volume, and A_{csc} is the cross-sectional area of the collision of molecule. Kn is 3.5×10^{-5}-3.5×10^{-4} for water with d_h of 10-100 μm, and Kn is even lower at higher d_h of the micro-channel in this study, which is 227.5 μm. Therefore, the assumption of the fluids in the continuous flow is valid. With this assumption, the continuum model (with the equations of Navier-Stokes) is applicable in this numerical study. Also, with the assumption of constant densities of fluids, the flow is incompressible. Furthermore, by accounting the axial heat conduction of substrate and conjugate heat transfer in the numerical model, the inclusion of a physical wall of micro-channel in the computational domains is necessary. Furthermore, with the assumption of stable flow, the computational domain generated is only a single micro-channel instead of multi-channel. With the interface of bubbles, the suitable model for the evaluation of the position of the interface between the immiscible fluids is Volume of Fluid (VOF) model from the approach of Euler-Euler as mentioned in [115]. Hence, the VOF model combines with the Navier-Stokes equations to evaluate the mechanisms of nucleate boiling during the flow boiling of subcooled liquids in micro-channel heat sinks in this study. This model is available in the software of CFD solver of ANSYS Fluent™, and therefore this numerical investigation employs ANSYS Fluent™ to obtain the numerical solutions.

3.2.1 Computational Domain

The computational domain created in this study consists of the micro-channel heat sink with the sub-domains of micro-channel and substrate; inlet extension; and outlet extension in 3D as shown in Figure 3.1. The inlet extension allows the specification of uniform conditions of the inlet of the inlet extension and enables the flow to form hydro-dynamically at the inlet of micro-channel as the real condition. Ensuring the stream to develop hydro-dynamically at the inlet of micro-channel allows proper comparison between the numerical results and experimental data. For this purpose, the inlet extension needs to possess a sufficient length L_{ie} of inlet extension for each Re, and L_{ie} employed in this numerical study is 4 mm. Meanwhile, the outlet extension added to the other end of micro-channel serves the purpose to avoid the influence of the reversed fluid flow on the numerical accuracy. For this

intention, the outlet extension requires a sufficient length L_{oe}, and L_{oe} implemented in this study is 4 mm. In this study, there are two different geometries of micro-channel. The first micro-channel is 264 μm wide, 200 μm high, and 1 cm long with W_{fin} of 200 μm and H_b of 137 μm according to the dimensions employed by Koşar et al. [116]. On the other hand, the second micro-channel is 150 μm wide, 273 μm high, and 15 mm long with W_{fin} of 100 μm and H_b of 112 μm following the dimensions implemented by Bogojevic et al. [65]. In the computational domain, the location of the origin is at the cross-sectional plane of the inlet with $W_c/2$ and $H_c/2$ from the side and bottom surfaces of micro-channel, respectively.

The computational domain defined comprises of the number of grids in a hexahedron shape for the micro-channel, inlet extension, outlet extension, and substrate as shown in Figure 3.2.

For the computational domain with the dimensions of Koşar et al. [116], the numbers of grids of the fluid domains of inlet extension and outlet extension are 400 × 27 × 20 ($x \times y \times z$ along the length, height, and width) and micro-channel is 1000 × 27 × 20, respectively. For the computational domain with the dimensions of Bogojevic et al. [65], the numbers of grids of the fluid region of inlet extension and outlet extension are 400 × 28 × 15 ($x \times y \times z$ along the length, height, and width) and micro-channel is 1500 × 28 × 15, respectively. In both of the computational domains, the fluid domains are having an average value of 10 μm, the length, height, and width along the x-, y-, and z-axis of grids. Consequently, along with y- and z-axis from the edges of the fluid domains, narrower grids are necessary as the locations possess more complex msechanisms of flow and heat transfer. The smaller grids from the sides possess the minimum height and length along with y- and z-axis. The heights and lengths gradually increase from the edges towards the mainstream and reaching the maximum grid height and length, producing a ratio of maximum to minimum grid height and length. This configuration of grids allows better estimation of local values at the edges and convergence of solutions. For this purpose, the ratio of maximum to minimum grid heights and lengths employed in this numerical study is 3.0 which is sufficient for the convergence of solutions.

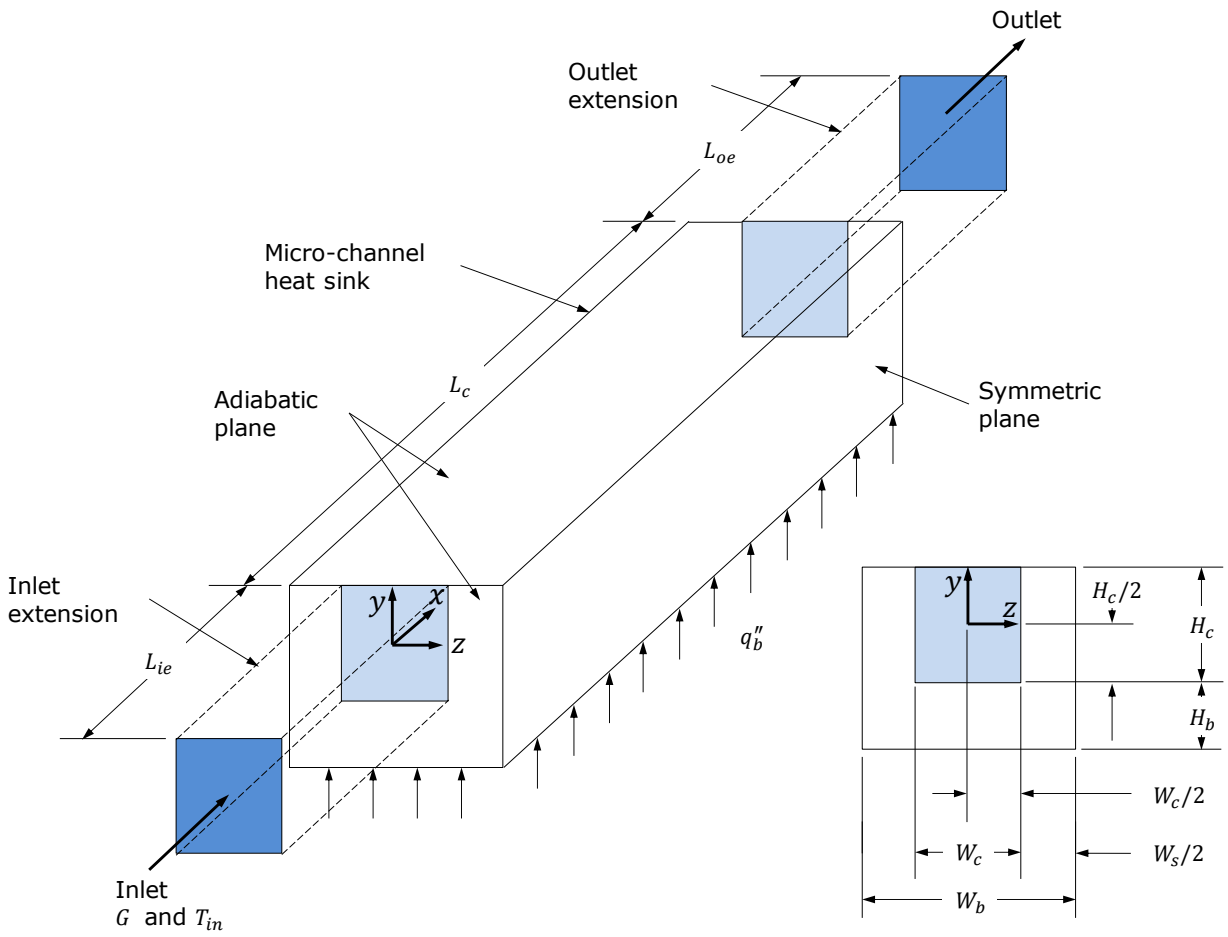


Figure 3.1: Schematic diagram of the computational domain of micro-channel heat sink with the inlet extension and outlet extension

For both computational domains with the dimensions of Koşar et al. [116] and Bogojevic et al. [65], the substrate generated consists of two sections of A and B and one section of C. Each section of A, B, and C possesses different number, length along with x-axis, height along with y-axis, and width along with z-axis of grids. The two parts of A extend from both left and right of side surfaces (y-z plane) of micro-channel. The two sections of B extend from the base of two sections of A. The section of C extends from the bottom surface (x-z plane) of micro-channel. The length along with x-axis of the grids of the substrate for all segments set in this study is uniform at 10.0 μm. For the two sections of A, the number of grids employed in this investigation is 4 with the uniform width along with z-axis of each grid. Meanwhile, the number and height of grids along with y-axis of the two sections of A implemented in this study are identical to the number and height of grids along with y-axis of the micro-channel. For the two parts of B, the number of grids applied in this investigation is 4 with the uniform width along with z-axis. On the other hand, the number of grids along with y-axis of the two sections of B adopted in this study is 6 with the uniform height of each grid. For the segment of

C, the number and breath of grids along z-axis set in this investigation are similar to the number and width of grids along with z-axis of the micro-channel. Meanwhile, the number of grids along with y-axis of the section of C employed in this study is 6 with the uniform height of each grid.

These settings of grids provide the computational domain with 1,356,000 grids for the computational domain with the geometries of Koşar et al. [116] whereas 1,509,000 grids for the computational domain with the geometries of Bogojevic et al. [65].

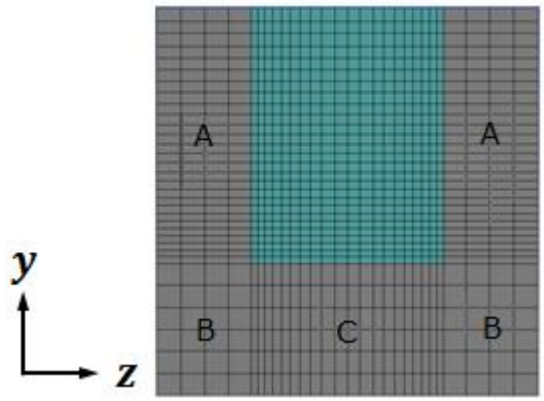


Figure 3.2: Mesh of the computational domain in cross-sectional view (y-z plane)

3.2.2 Governing Equations

This numerical study employs the continuum model (Navier-Stokes equations) associated with the VOF model to address mechanisms of fluid flow and heat transfer during the flow boiling of subcooled liquids in micro-channel heat sinks.

Flow boiling involves the fluids in the phases of liquid and vapour. For this reason, a model with the variable of volume fraction α of different phases is essential in the governing equations of Navier-Stokes to perform the calculations of heat transfer. α of each medium at different locations may vary from 0 to 1. The sum of the volume fraction of liquid α_l and vapour α_v equals to unity as:

$$\alpha_l + \alpha_v = 1 \tag{3.1}$$

With the model of VOF, the mass of fluid between the liquid and vapour phases in each computational cell are traceable from the mass conservation equations of these two phases as:

$$\frac{\partial}{\partial t}(\alpha_l \rho_l) + \nabla \cdot \left(\alpha_l \rho_l \vec{U}_l\right) = \dot{m}'''_{lv} - \dot{m}'''_{vl} \tag{3.2}$$

$$\frac{\partial}{\partial t}(\alpha_v \rho_v) + \nabla \cdot \left(\alpha_v \rho_v \vec{U}_v\right) = \dot{m}'''_{vl} - \dot{m}'''_{lv} \tag{3.3}$$

where ρ is density; t is time; U is mean velocity; $\dot{m}_{lv}'''$ is the mass flow rate from the liquid to vapour per unit volume in the cells due to the evaporation; and $\dot{m}_{vl}'''$ is the mass flow rate from the vapour to liquid per unit volume in the cells due to the condensation. The subscript l and v represent liquid phase and vapour phase, respectively. The equation (3.2) and (3.3) stand for:

Rate of change of mass per unit volume of the cell in liquid or vapour phase	+	Net rate flow of mass by convection per unit volume of the cell in liquid or vapour phase	=	Net mass flow rate per unit volume from liquid to vapour phase or from vapour to liquid phase

Also, each medium possesses different fluid properties. The fluid properties of each computational cell with different phases are obtainable by summing the fraction of fluid properties of the phases at each of the cell. For flow boiling in micro-channels that involve a two-phase system, the expression of ρ in each cell is:

$$\rho = \alpha_l \rho_l + \alpha_v \rho_v \tag{3.4}$$

By assuming ρ_l and ρ_v as constants, the fluid is incompressible, and this study also considers all other properties as constants. In between the liquid and vapour phases, or at the liquid-vapour interface, the net mass flow rate $\dot{m}_{interface}'''$ exists, and the relationship of $\dot{m}_{interface}'''$ is:

$$\dot{m}_{interface}''' = \dot{m}_{interface}'' \frac{A'''}{V_{bub}} \tag{3.5}$$

where A''' is the density of the interfacial area, and V_{bub} is the volume of the bubble. One of the equations of $\dot{m}_{interface}''$ between the liquid and vapour is the equation of Hertz-Knudsen [117] is:

$$\dot{m}_{interface}'' = C_{ac} \sqrt{\frac{\tilde{m}}{2\pi R T_{sat}}} (p - p_{sat}) \tag{3.6}$$

where C_{ac} is the coefficient of accommodation corresponding to the portion of the molecules of the vapour absorbed by the surface of the liquid, $\tilde{m}$ is the molecular weight, and R is the universal constant of gas. C_{ac} approaches 1.0 near the condition of equilibrium at the interface of bubble [115]. p relates to T under the saturation condition, according to the equation of Clausius-Clapeyron as:

$$\begin{aligned} \frac{dp}{dT} &= \frac{\boldsymbol{h}_{lv}}{T_{sat}(1/\rho_v - 1/\rho_l)} \\ p - p_{sat} &= -\frac{\boldsymbol{h}_{lv}}{T_{sat}(1/\rho_v - 1/\rho_l)} (T - T_{sat}) \end{aligned} \tag{3.7}$$

Substituting equation (3.7) into equation (3.6) gives:

$$\dot{m}''_{interface} = C_{ac}\sqrt{\frac{\widetilde{m}}{2\pi R T_{sat}}}\frac{\boldsymbol{h}_{lv}}{T_{sat}(1/\rho_v - 1/\rho_l)}(T_{sat} - T) \tag{3.8}$$

By assuming the diameter of all vapour bubbles are identical, A'''/V_{bub} from equation (3.5) becomes:

$$\frac{A'''}{V_{bub}} = \frac{6\alpha}{d_{sm}} \tag{3.9}$$

where d_{sm} is the Sauter mean diameter which is the average size of bubbles. Substituting equation (3.8) and (3.9) into equation (3.5) gives:

$$\dot{m}'''_{interface} = C_{ac}\sqrt{\frac{\widetilde{m}}{2\pi R T_{sat}}}\frac{\boldsymbol{h}_{lv}}{T_{sat}(1/\rho_v - 1/\rho_l)}(T_{sat} - T)\frac{6\alpha}{d_{sm}} \tag{3.10}$$

From equation (3.10), the derivation of $\dot{m}'''_{lv}$ and $\dot{m}'''_{vl}$ are:

$$\begin{aligned}
\dot{m}'''_{lv} &= \begin{cases} \dfrac{6}{d_{sm}} C_{ac}\sqrt{\dfrac{\widetilde{m}}{2\pi R T_{sat}}}\dfrac{\rho_v \boldsymbol{h}_{lv}}{\rho_l - \rho_v}\alpha_l\rho_l\dfrac{T_{sat} - T_l}{T_{sat}} & T_l \geq T_{sat} \\ 0 & T_l < T_{sat} \end{cases} \\
\dot{m}'''_{vl} &= \begin{cases} \dfrac{6}{d_{sm}} C_{ac}\sqrt{\dfrac{\widetilde{m}}{2\pi R T_{sat}}}\dfrac{\rho_v \boldsymbol{h}_{lv}}{\rho_l - \rho_v}\alpha_l\rho_l\dfrac{T_{sat} - T_v}{T_{sat}} & T_v \leq T_{sat} \\ 0 & T_v > T_{sat} \end{cases}
\end{aligned} \tag{3.11}$$

From equation (3.11), the definition of the frequency of the mass transfer from the liquid to vapour f_{lv} and from the vapour to liquid phase f_{vl} are:

$$\begin{aligned}
f_{lv} &= \frac{6}{d_{sm}} C_{ac}\sqrt{\frac{\widetilde{m}}{2\pi R T_{sat}}}\frac{\rho_v \boldsymbol{h}_{lv}}{\rho_l - \rho_v} \\
f_{vl} &= \frac{6}{d_{sm}} C_{ac}\sqrt{\frac{\widetilde{m}}{2\pi R T_{sat}}}\frac{\rho_l \boldsymbol{h}_{lv}}{\rho_l - \rho_v}
\end{aligned} \tag{3.12}$$

respectively. Substituting equation (3.12) into equation (3.11) provides:

$$\begin{aligned}
\dot{m}'''_{lv} &= \begin{cases} f_{lv}\alpha_l\rho_l\dfrac{T_{sat} - T_l}{T_{sat}} & T_l \geq T_{sat} \\ 0 & T_l < T_{sat} \end{cases} \\
\dot{m}'''_{vl} &= \begin{cases} f_{vl}\alpha_l\rho_l\dfrac{T_{sat} - T_v}{T_{sat}} & T_v \leq T_{sat} \\ 0 & T_v > T_{sat} \end{cases}
\end{aligned} \tag{3.13}$$

C_{ac} and d_{sm} from equation (3.10) to (3.12) are usually unknown, and therefore arbitrarily setting f_{lv} and f_{vl} in equation (3.12) becomes an option to match the numerical results with the experimental data [115]. f_{lv} and f_{vl} vary for different numerical studies in the past. Adopting the extremely high f_{lv} and f_{vl} causes the problem of numerical convergence, while employing too small f_{lv} and f_{vl} yields to a significant deviation between the interfacial and saturation temperatures. The numerical studies of flow boiling in the literature [118, 119] set the f_{lv} and f_{vl} at 100/s numerically to maintain the temperature at the interface of bubble at $T_{sat} \pm 1$ K. However, this is unrealistic as compared to the experimental data during the flow boiling of subcooled liquids in micro-channel heat sinks with the relatively high superheat. On the other hand, the numerical studies in the literature [120, 121] employed 0.1/s for both f_{lv} and f_{vl} for the condition of flow boiling, and this value gives close numerical results with the experimental data. Therefore, both f_{lv} and f_{vl} set are 0.1/s in this numerical study of flow boiling of subcooled liquids in micro-channel heat sinks.

Unlike the mass conversation equations separately tracking the mass of both liquid and vapour phases, the momentum and energy conservation equations consider sharing both mediums in each computational cell in the VOF model.

The momentum conservation equation is:

$$\frac{\partial}{\partial t}\left(\rho\vec{U}\right) + \nabla\cdot\left(\rho\vec{U}\vec{U}\right) = -\nabla p' + \nabla\cdot\left(\mu\left(\nabla\vec{U} + \nabla\vec{U}^{T}\right)\right) + \left(\rho - \rho_{ref}\right)\vec{g} + \vec{F}''' \tag{3.14}$$

where p' is the modified pressure, μ is the dynamic viscosity, ρ_{ref} is the reference density, $\vec{g}$ is the gravitational acceleration vector, and $\vec{F}'''$ is the interfacial force per unit volume vector. Equation (3.14) physically means:

Rate of change of velocity of the cell	+	Net rate of flow velocity out of the cell by convection	=	Modified pressure term in the cell	+	Strain rate term in the cell	+	Gravitational body force per unit volume in the cell	+	Inter-facial force per unit volume in the cell

$\nabla p'$ in equation (3.14) possesses the expression of:

$$\nabla p' = \nabla p - \rho_{ref}\vec{g} \tag{3.15}$$

where p is the pressure that includes the hydrostatic head and ρ_{ref} is the density at the value of a reference. ρ_{ref} set in this numerical study is the density of the lightest phase of the computational domain as suggested in the literature [122], which is the vapour phase. This setting allows the exclusion of the hydrostatic pressure within the lightest medium in the cells and improves the round-off

accuracy of the momentum balance. μ in equation (3.14) involves the relationship of:

$$\mu = \alpha_l \mu_l + \alpha_v \mu_v \tag{3.16}$$

On the other hand, this numerical study adopts the continuum model of the forces acting on surfaces from Brackbill et al. [94] to model $\vec{F}'''$ in equation (3.14). In the model, when a spherical interface appears between the phases in the fluid elements, an interfacial force due to the surface tension σ between the phases raises. The surface tension is the force acting perpendicularly inward of the spherical surface to make the interface contract, thereby increasing the pressure on the concave side of the interface. Hence, $\vec{F}'''$ in equation (3.14) becomes:

$$\vec{F}''' = \sigma \frac{\alpha_l \rho_l \kappa_v \nabla \alpha_v + \alpha_v \rho_v \kappa_l \nabla \alpha_l}{0.5(\rho_l + \rho_v)} \tag{3.17}$$

where κ_l and κ_v are the curvature of the interface of liquid and vapour, respectively, in which $\kappa_l = -\kappa_v$ and $\nabla \alpha_l = -\nabla \alpha_v$, since only two phases present in a cell, which yield:

$$\vec{F}''' = \sigma \frac{(\alpha_l \rho_l + \alpha_v \rho_v) \kappa_v \nabla \alpha_v}{0.5(\rho_l + \rho_v)} \tag{3.18}$$

The energy conservation equation for fluid domains is:

$$\frac{\partial}{\partial t}(\rho E) + \nabla \cdot \left(\vec{U}(\rho E + p')\right) = \nabla \cdot (k \nabla T) + \nabla \cdot \left(\tau \cdot \vec{U}\right) \tag{3.19}$$

where E is specific internal (thermal) energy of the fluid, k is thermal conductivity, T is temperature, τ is shear stress, and q''' is the rate of interfacial heat transfer. Equation (3.19) literally stands for:

Rate of change of energy per unit volume of fluid element	+	Net rate energy per unit volume of fluid element by convection and modified pressure	=	Net rate of heat into fluid element	+	Viscous dissipation of fluid element

E in equation (3.19) has an expression of:

$$E = \frac{\alpha_l \rho_l E_l + \alpha_v \rho_v E_v}{\alpha_l \rho_l + \alpha_v \rho_v} \tag{3.20}$$

where E_l and E_v are specific internal energies of liquid and vapour phases, respectively. E_l and E_v in equation (3.20) possess definitions of:

$$E_l = c_{V,l}\left(T_l - T_{ref}\right) \tag{3.21}$$

and

$$E_v = c_{V,v}\left(T_v - T_{ref}\right) \tag{3.22}$$

respectively. k involves a relationship of:

$$k = \alpha_l k_l + \alpha_v k_v \tag{3.23}$$

The energy conservation equation for the solid domains is:

$$\frac{\partial}{\partial t}(\rho_s E_s) = \nabla \cdot (k_s \nabla T) \tag{3.24}$$

where ρ_s is the density of the solid, E_s is the specific internal energy of solid, and k_s is the thermal conductivity of solid. Equation (3.24) indicates:

Rate of change of energy per unit volume of substrate element	=	Net rate of heat into fluid element

3.2.3 Boundary Conditions

The boundary conditions of computational domain as shown in Figure 3.1 in this numerical study are as following:

- At the inlet of inlet extension (y-z plane at $x = -4$ mm),

$$\alpha_l = \alpha_{l,in} = 1;\ \alpha_g = v = w = 0;\ u = u_{in};\ T = T_{in} \tag{3.25}$$

- At the outlet of outlet extension (y-z plane at $x = 14$ mm),

$$p = p_{out} = 1 \text{ atm};\ \alpha_g = \alpha_{g,backflow,out} = 0;\ T = T_{backflow,out} = 90°\text{C} \tag{3.26}$$

- At the base surface of the micro-channel heat sink (x-z plane at $y = -H_b$), the heat flux is q_b''.
- The computational domain involves a conjugate heat transfer at the interface between the fluid and solid domains (x-y plane at $z = -W_c/2$ and $z = W_c/2$, and $x - z$ plane at $y = -H_c/2$) or the heating surfaces in the micro-channel heat sink. Therefore, at the heating surfaces in the micro-channel heat sink, the average heat flux is $q''_{total,fin}$.
- The surface of the micro-channel heat sink at the top adjacent to the domain of solid and fluid at the x-z plane at $y = H_c$ is at the condition of adiabatic.
- The surfaces of the micro-channel heat sink at front and back adjacent to the solid domain at y-z plane $x = 0$ and $x = L_c$ are at the condition of adiabatic.

- The surfaces of inlet extension, and outlet extensions at the x-y plane at $z = -W_c/2$ and $z = W_c/2$, and $x - z$ plane at $y = 0$ and $y = H_c$ are at the condition of adiabatic.
- At the surfaces adjacent to the fluid domains of micro-channel, inlet extension, and outlet extension, an arbitrary contact angle θ of the liquid to vapour phase set is at 70°. This setting is according to the average value of the experiment of nucleate boiling from Cole [123] with the limited information regarding the dynamic contact angle θ at the surfaces in the micro-channel.
- The side surfaces of the solid domains (x-y planes at $z = -W_c/2 - W_s/2$ and $z = W_c/2 + W_s/2$) are symmetrical.
- All other surfaces of computational domain are smooth.

3.2.4 Initial Conditions

The initial conditions of the computational domain are as follows:

$$p_{init} = 1 \text{ atm};\ \alpha_{v,init} = v_{init} = w_{init} = 0;\ u_{init} = u_{in};\ T_{init} = T_{in} \tag{3.27}$$

3.2.5 Discretisation Methods

This numerical study employs the discretisation methods to solve the governing equations associated with the VOF model involving the variables at the faces of each cell using a solver of CFD, named ANSYS Fluent™. The discretisation method implemented to solve the governing equations is the scheme of the pressure-velocity coupling of Pressure-Implicit with Splitting of Operators (PISO) from Issa [124]. PISO is the recommended scheme for transient flow prediction and able to maintain a stable calculation with more substantial time steps and under-relaxation factors. When considering VOF Model, solving the mass equation of the secondary phase, which is the vapour phase in this study, is needed through a time discretisation. On the other hand, the mass equation of the primary phase, or the liquid phase, is solvable from Equation (3.1). The time discretisation for the mass equation of vapour phase is obtainable through the explicit scheme. Meanwhile, the discretisation methods to solve each term containing the variables at the faces of each cell in the governing equations are available as listed in Table 3.4. The discretisation methods are suitable for the numerical study of flow boiling in micro-channels with excellent levels of convergence, accuracy and robustness [115, 122]. Unlike the other faces of each cell, at the outlet of outlet extension, the velocity, temperature, and volume fraction of fluid are implicitly obtainable from the solution information on the boundary nodes.

Table 3.4: Discretisation methods of each term in governing equations

Term	Discretisation Method
Transient term	First Order Implicit [115]
Convective term	Third Order Upwind [125]
Diffusive term	Central-Differencing [115]
Gradient term	Least Squares Cell-Based [126]
Pressure term	PRESTO! [127]
Volume fraction of the vapour phase	Compressive [115]

3.2.6 Under-relaxation Factors

The under-relaxation factors selected in this numerical investigation is 1 for all variables (pressure, density, body forces, momentum, the mass of vaporisation, and energy) to improve the robustness of numerical calculations and stabilise the behaviour of the convergence of nonlinear iterations in the estimates.

3.2.7 Convergence Criteria

The convergence criteria ensuring the convergence of solutions with high levels of accuracy in the simulation in this numerical study is essential. This investigation justifies the convergence of numerical solutions by making sure that the globally scaled residuals of continuity, and x-, y- and z-velocities decrease below 10^{-4} whereas below 10^{-6} for the energy [122]. By satisfying these criteria, the sufficiently small time step adopted in this study is necessary, and this investigation employs variable time step within small values of 10^{-5}-10^{-10} s. The time step varies while avoiding the maximum global Courant number Co to exceed an amount value manually proposed to ensure the stable and accurate calculations. In this numerical study, the maximum global Co employed is 0.5, and for each of the time step, the maximum number of iterations set was at 40.

On the other hand, the numerical simulation is capable of producing a steady state for the condition of single-phase flow (with $q''_{total,fin} = q''_b A_b / A_{total,fin}$). Dissimilar to the single-phase flow, flow boiling requires a significantly longer time or almost impossible to reach steady state. Thus, this numerical study conducts the numerical simulation up to the time Δt_{fb} of flow boiling of 10 ms for each tested condition. When Δt_{fb} reaches 10 ms, $q''_{total,fin}$ is at least more than 70% of $q''_b A_b / A_{total,fin}$ (with $q''_{total,fin} < q''_b A_b / A_{total,fin}$).

3.2.8 Validation of Numerical Model

Having setup the numerical model for the investigation, the next numerical procedure of this study is to validate the numerical model with existing experimental data and prediction methods. This study implements the experimental data from Koşar et al. [116] and Bogojevic et al. [65] to validate of the numerical

model with the computational domains with the dimensions according to both studies. The computational domains according to the geometries of the micro-channel heat sink of Koşar et al. [116] and Bogojevic et al. [65] are the first and second computational domains, respectively, as described in Section 3.2.1.

The experimental data of Koşar et al. [116] employed to validate the numerical model is $q''_{total,fin}$ against $T_{avg,surf}$. The experimental data are from the operating parameters of working fluid of water, the substrate of silicon, p_{out} of 1 atm, T_{in} of 23°C, and $\dot{m}''$ of 115-389 kg/m^2 s. $q''_{total,fin}$ against $T_{avg,surf}$ from the present numerical model and experimental data of Koşar et al. [65] is evident in Figure 3.3. In Figure 3.3, $q''_{total,fin}$ against $T_{avg,surf}$ from the present numerical model agrees well with the experimental data of Koşar et al. [116] at the beginning stage of flow boiling for each $\dot{m}''$ tested in this study.

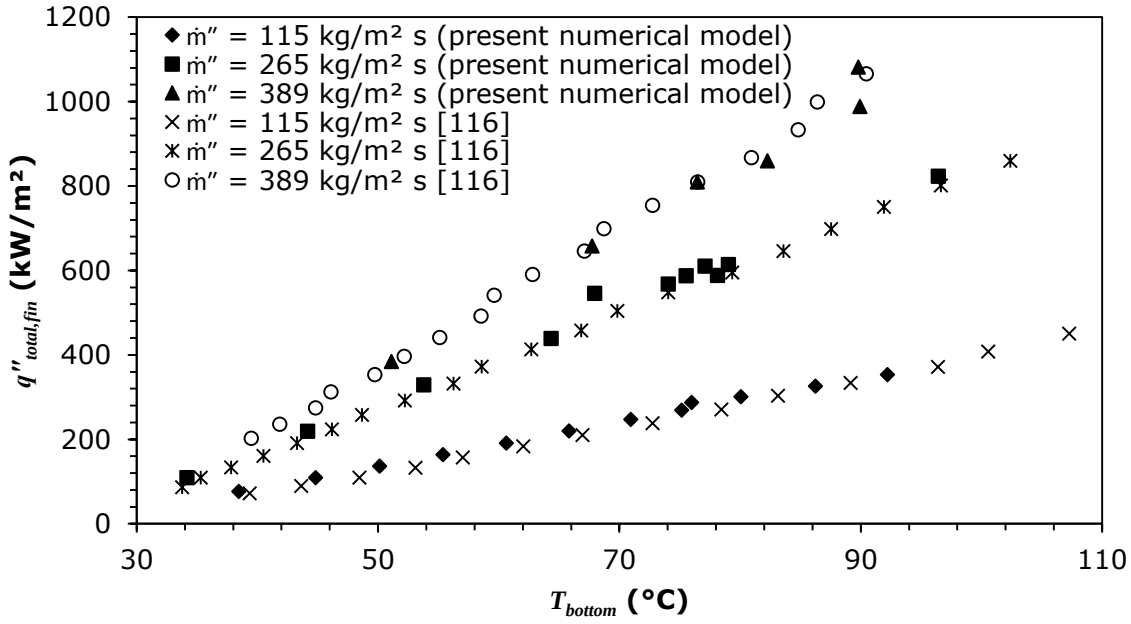


Figure 3.3: $q''_{total,fin}$ against T_{bottom} from the present numerical model and experimental data of Koşar et al. [116]

On the other hand, the experimental data of Bogojevic et al. [65] implemented are height H_{bub} of the bubble at the centre along the length of channel against lifetime t_{bub} of the bubble. The experimental data are from the operating parameters of working fluid of water, substrate of silicon, 1 atm of p_{out}, 445 kW/m^2 of q''_b, 71°C of T_{in}, 153 kg/m^2 s of $\dot{m}''$ as shown in Figure 3.4. In Figure 3.4, there are discrepancies in H_{bub} from the numerical model and the experimental data of Bogojevic et al. [65] for the growth of bubble due to the dissipated heat of the experiment. Nevertheless, H_{bub} against t_{bub} from the numerical model compares well with the experimental data of Bogojevic et al. [65] in overall.

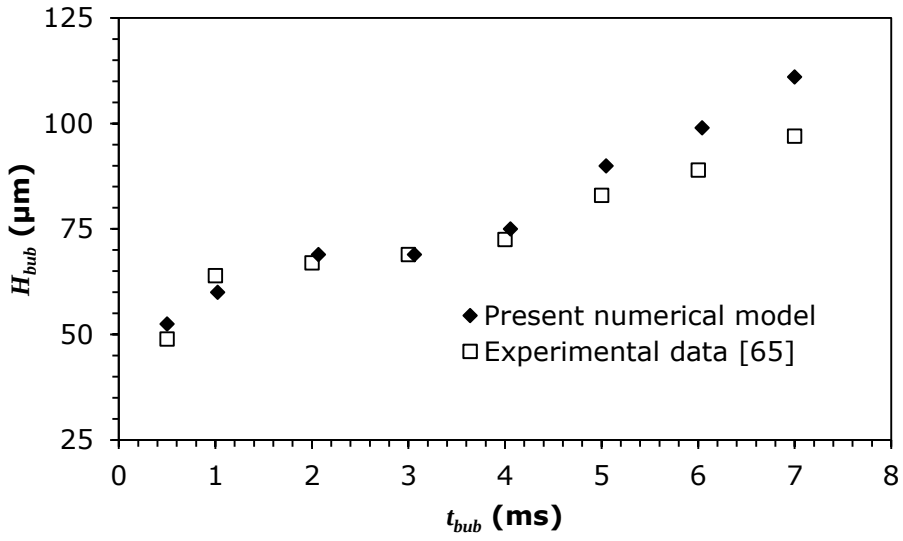


Figure 3.4: H_{bub} at the centre along the length of channel against t_{bub} for the present numerical model and experimental data of Bogojevic et al. [65]

Other than the experimental data, this study also employs the prediction models of ONB from the literature [47, 100, 101, 103, 104] as reviewed in Section 2.6 for the validation of the numerical model. The prediction models predict the trend of q''_{ONB} against ΔT_{sup} at the location of ONB, and this study identifies the slope by finding q''_{ONB} for different ΔT_{sup}. From the numerical model, the trend is obtainable through reading q''_{ONB} and ΔT_{sup} at the location of ONB. With the slope of the prediction models and numerical model, the validation of the numerical model with the prediction model is attainable as illustrated in Figure 3.5. Figure 3.5 shows that the present numerical model agrees well with the existing prediction models of ONB from the literature [47, 100, 101, 103, 104].

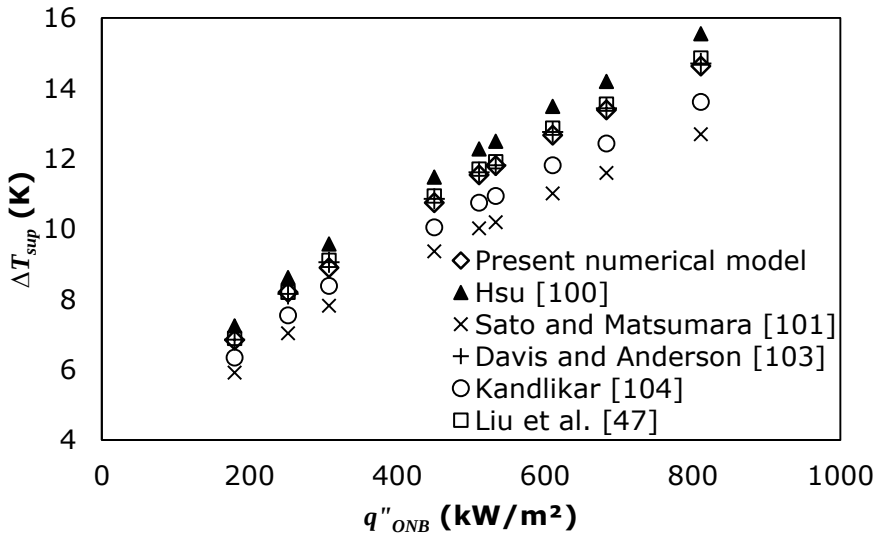


Figure 3.5: ΔT_{sup} against q''_{ONB} for the present numerical results and existing models of ONB from researchers [47, 100, 101, 103, 104]

Chapter 4 Effects of Mass Fluxes, Heat Fluxes, and Inlet Temperatures

This chapter discusses results regarding the mechanisms of fluid flow and heat transfer before and during flow boiling of subcooled water in silicon rectangular micro-channel heat sinks. The micro-channel heat sink had one 200 μm wide, 264 μm high, 1 cm long micro-channel with W_{fin} of 200 μm, and H_b of 137 μm. Also, the micro-channel heat sink was at $\dot{m}''$ of 115-389 kg/m^2 s, q_b'' of 1561-3197 kW/m^2, T_{in} of 23-53°C, and p_{out} of 1 atm.

4.1 Transient Heat Transfer for Different Mass Fluxes, Heat Fluxes and Inlet Temperatures before Flow Boiling

This study started by monitoring the transient heat transfer when water was flowing into the silicon micro-channels before nucleation of first bubble $\Delta t_{fb} < 0$ for different $\dot{m}''$, q_b'', and T_{in}. For different $\dot{m}''$, q_b'', and T_{in}, the transient heat transfer of $q''_{total,fin}$ against $T_{avg,surf}$ before flow boiling is evident in Figure 4.1, Figure 4.2, and Figure 4.3, respectively.

In Figure 4.1, at $\dot{m}''$ of 165 kg/m^2 s, T_{in} = 23°C, and q_b'' = 1561 kW/m^2, $q''_{total,fin}$ increased steadily with $T_{avg,surf}$ up to about 103°C. When $T_{avg,surf}$ further increased, the increment of $q''_{total,fin}$ became relatively larger with the relatively steeper curve in a non-uniform behaviour. This change of trend of the curve indicates that the condition is at the nucleate boiling regime with bubble nucleation. However, the bubble nucleation was absent in the simulation case. The similar outcome was also visible in the study of Lin et al. [128, 129] and Peng and co-workers [38, 42, 80, 81, 130] in which the bubbles were absent although the boiling curve reached the nucleate boiling regime in micro-channels. Peng [31] described this behaviour as the fictitious boiling in which the heat transfer performance possesses nucleate boiling characteristics even though bubbles are absent in channels. He [31] stated an aspect of the fictitious boiling that the liquid has reached nucleate boiling conditions. However, within the liquid, the internal evaporation and bubble growth is absent, or many unseen microbubbles that are unstable exist within the liquid. The liquid reaching the nucleate boiling conditions also indicates the existence of phase change process associated with the unstable flow and the production of the liquid-vapour mixture.

At low $\dot{m}''$ of 165 kg/m^2 s, $T_{avg,surf}$ reached the first mark at about 111°C and Δt_{fb} of −5.8 ms after the steep increase of $q''_{total,fin}$ with the rapid development of nucleate boiling characteristic. Then, $T_{avg,surf}$ reached the second mark at about 113°C where Δt_{fb} at about −2.9 ms and $q''_{total,fin}$ slightly dropped with the unstable flow. Consequently, $q''_{total,fin}$ fluctuated with $T_{avg,surf}$ within the values about 680 and 725 kW/m^2 up to $\Delta t_{fb} = 0$ at the end of the curve at $T_{avg,surf}$ of 121°C associated with the nucleation of the first bubble.

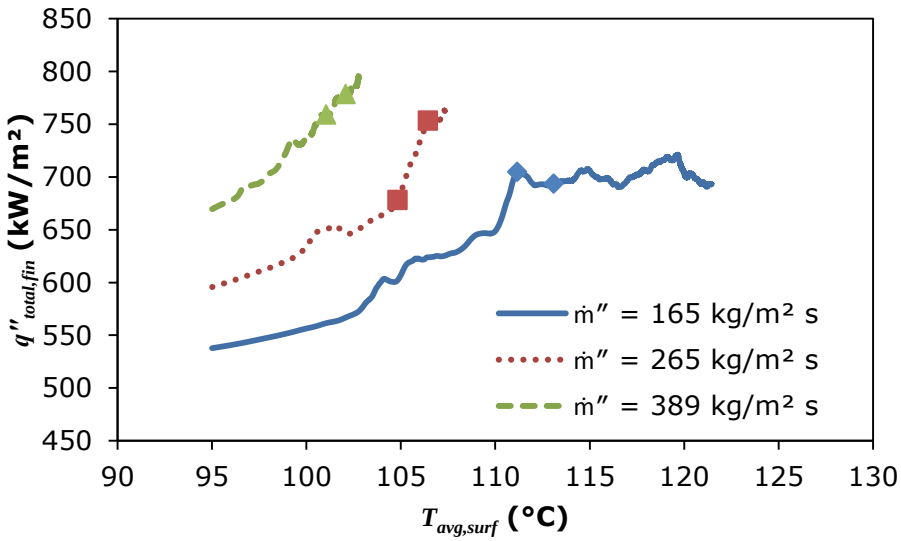


Figure 4.1: Transient heat transfer data of $q''_{total,fin}$ against $T_{avg,surf}$ of water flowing in silicon micro-channels for different $\dot{m}''$ at T_{in} = 23°C and q''_b = 1561 kW/m^2 before flow boiling $\Delta t_{fb} < 0$ (first and second marks at Δt_{fb} about −5.8 and −2.9 ms, respectively, of each curve)

When applied moderate $\dot{m}''$ of 265 kg/m^2 s as illustrated in Figure 4.1, $q''_{total,fin}$ increased at higher ranges with $T_{avg,surf}$ as compared to low $\dot{m}''$ of 165 kg/m^2 s associated with the thinner thermal boundary layer. Also, the change of the trend of the curve from steady to steep and non-uniform occurred at lower $T_{avg,surf}$ about 100°C for the moderate $\dot{m}''$. When $T_{avg,surf}$ reached the first mark with Δt_{fb} about −5.8 ms about 105°C, a steep increase of $q''_{total,fin}$ just began. This trend of the moderate $\dot{m}''$ was unlike the low $\dot{m}''$ in which the steep increase occurred before Δt_{fb} at about −5.8 ms. Then, for the moderate $\dot{m}''$, $T_{avg,surf}$ reached the second mark approximately 107.5°C at about Δt_{fb} of −2.9 ms associated with the steep increase of $q''_{total,fin}$ within Δt_{fb} about −5.8 and −2.9 ms. These occurrences imply that the rapid development of nucleate boiling characteristic occurring at different Δt_{fb} for the low and moderate $\dot{m}''$.

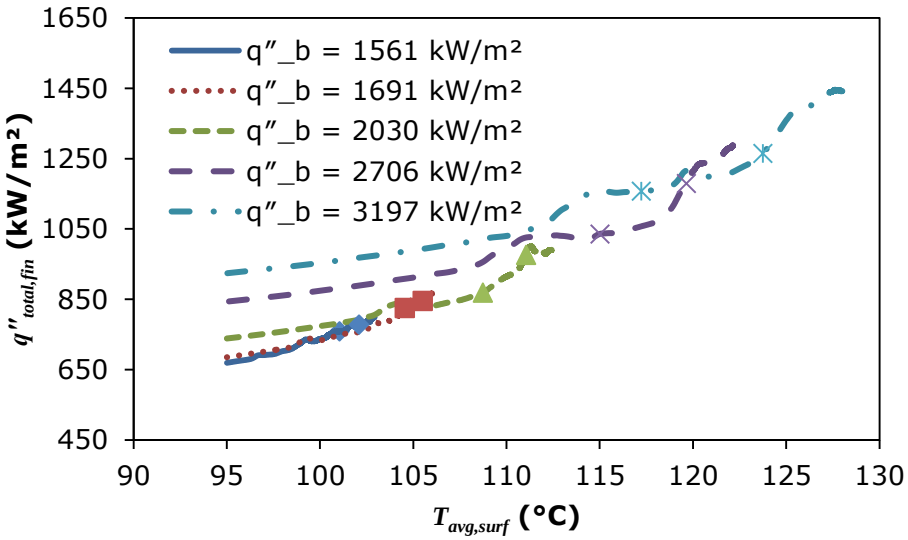


Figure 4.2: Transient heat transfer data of $q''_{total,fin}$ against $T_{avg,surf}$ of water flowing in silicon micro-channels for different q''_b at $\dot{m}'' = 389$ kg/m² s and $T_{in} = 23$°C before flow boiling $\Delta t_{fb} < 0$ (first and second marks at Δt_{fb} about −5.8 and −2.9 ms, respectively, of each curve)

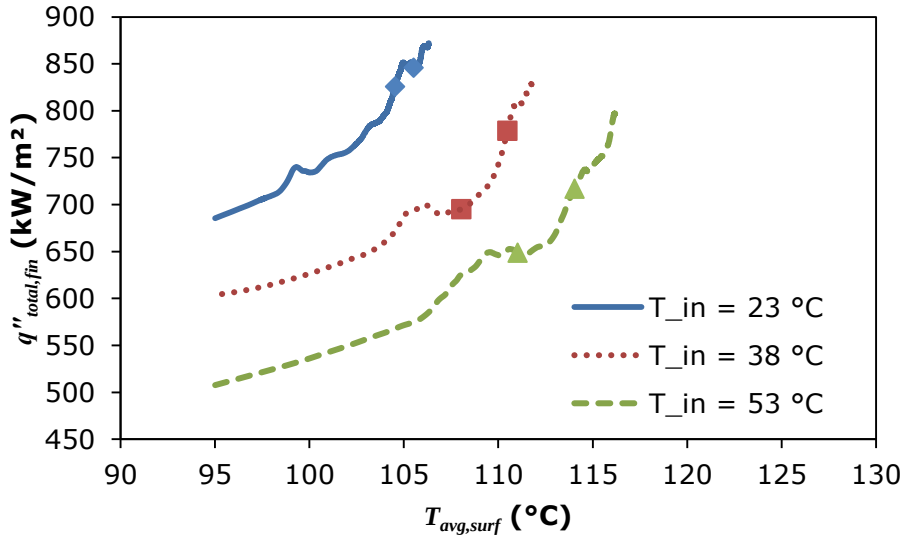


Figure 4.3: Transient heat transfer data of $q''_{total,fin}$ against $T_{avg,surf}$ of water flowing in silicon the micro-channels for different T_{in} at $\dot{m}'' = 389$ kg/m² s and $q''_b = 1691$ kW/m² before flow boiling $\Delta t_{fb} < 0$ (first and second marks at Δt_{fb} about −5.8 and −2.9 ms, respectively, of each curve)

For the low $\dot{m}''$, the trend changed before Δt_{fb} of about −5.8 ms whereas Δt_{fb} at approximately −5.8 ms for the moderate $\dot{m}''$ of 265 kg/m² s as shown in Figure 4.1. This presence is due to the thicker thermal boundary layer, leading to more extensive regions with the unsteady flow as compared to the moderate $\dot{m}''$. The

more unstable flow from the low $\dot{m}''$ requires the larger $T_{avg,surf}$ for the bubble nucleation which is only reachable with longer Δt_{fb} before the bubble nucleation as compared to the moderate $\dot{m}''$. With the longer Δt_{fb} before the bubble nucleation to reach the sufficiently large $T_{avg,surf}$ for the low $\dot{m}''$, Δt_{fb} for the change of trend occurs earlier as compared to the moderate $\dot{m}''$.

When applied high $\dot{m}''$ of 389 kg/m^2 s as depicted in Figure 4.1, $q''_{total,fin}$ increased at higher ranges with $T_{avg,surf}$ associated with the thinner thermal boundary layer as compared to moderate $\dot{m}''$ of 265 kg/m^2 s. Also, the change of the trend of the curves from steady to steep and non-uniform occurred at lower $T_{avg,surf}$ about 96°C with the development of the nucleate boiling characteristic. Then, $T_{avg,surf}$ reached the first mark at about 101°C at Δt_{fb} about -5.8 ms, second mark at about 102°C at Δt_{fb} about -2.9 ms, and about 103°C at $\Delta t_{fb} = 0$ when increased $q''_{total,fin}$.

Nevertheless, for high $\dot{m}''$ of 389 kg/m^2 s, the steep increase of $q''_{total,fin}$ was unavailable due to the thinner thermal boundary layer as compared to lower $\dot{m}''$ of 165 and 265 kg/m^2 s as illustrated in Figure 4.1. With the smaller thermal boundary layer of high $\dot{m}''$, the heating process is slower with lesser superheat producing the lower steepness of boiling curve as compared to lower $\dot{m}''$. The more moderate steepness of boiling curve for high $\dot{m}''$ indicates the less rapid development of nucleate boiling characteristic as compared to lower $\dot{m}''$. With the slower heating process, high $\dot{m}''$ requires longer Δt_{fb} for the bubble nucleation and the increment of $q''_{total,fin}$ was less rapid for high $\dot{m}''$ as compared to lower $\dot{m}''$. The longer Δt_{fb} for the bubble nucleation of high $\dot{m}''$ also implies the earlier change of trend of $q''_{total,fin}$ due to phase change as compared to lower $\dot{m}''$ before Δt_{fb} about -5.8 ms.

When employed low to moderate q''_b of 1561 kW/m^2 to 3197 kW/m^2 as shown in Figure 4.2, $q''_{total,fin}$ increased at higher ranges with $T_{avg,surf}$ before bubble nucleation. These occurrences are due to thinner thermal boundary layer when $q''_{total,fin}$ is at the same value when increasing q''_b requiring more substantial $T_{avg,surf}$ for the bubble nucleation. Nevertheless, at low q''_b of 1561 and 1691 kW/m^2 applied were close to each other as compared to other q''_b employed and produced the boiling curves almost overlapped with each other. From low to moderate q''_b, the change of the trend of boiling curves from steady to steep and non-uniform occurred at higher $T_{avg,surf}$ and $q''_{total,fin}$ also due to the thinner thermal boundary layer. The thinner thermal boundary layer from low to moderate q''_b requires more substantial $T_{avg,surf}$ and $q''_{total,fin}$ to produce the change of the trend of the boiling curves. Also, from low to moderate q''_b, $q''_{total,fin}$ increased rapidly from Δt_{fb} about -5.8 to -2.8 ms with more rapid heat transfer process, indicating the fast

development of nucleate boiling characteristic. However, when employed high q_b'' of 3197 kW/m^2, $q_{total,fin}''$ increased less rapid from Δt_{fb} about −5.8 to −2.8 ms due to the production of more massive amount of liquid-vapour mixture on the heating surfaces inhibiting heat transfer.

When increased T_{in} from 23°C to 53°C at fixed $\dot{m}''$ of 389 kg/m^2 s and q_b'' of 1691 kW/m^2 as illustrated in Figure 4.3, $q_{total,fin}''$ decreased, and $T_{avg,surf}$ increased before the bubble nucleation. In other words, before the bubble nucleation, the change of trend of the boiling curves from steady to steep and non-uniform occurred at lower $q_{total,fin}''$ and higher $T_{avg,surf}$. $q_{total,fin}''$ reduced with the increase of T_{in} is mere as a result of the lesser temperature difference between heating surface and bulk fluid before the bubble nucleation. Meanwhile, $T_{avg,surf}$ increased when increasing T_{in} is due to the relatively thicker thermal boundary layer, causing the more substantial unstable flow restricting the bubble nucleation. With the more unstable flow from the more extensive T_{in} requires more extensive $T_{avg,surf}$ for the bubble nucleation.

On the other hand, when increased T_{in} from 23°C to 38°C, from Δt_{fb} about −5.8 to −2.9 ms, the increment of $q_{total,fin}''$ and $T_{avg,surf}$ became more substantial as depicted in Figure 4.3. This existence is due to the thicker thermal boundary layer for T_{in} of 38°C as compared to T_{in} of 23°C, leading to more significant unstable flow facilitating the larger increment of $q_{total,fin}''$ and $T_{avg,surf}$. When further increased T_{in} from 38° to 53°C, the change of the increment $q_{total,fin}''$ and $T_{avg,surf}$ was less significant. This occurrence is as a result of the generation of more liquid-vapour mixture at larger T_{in} of 53°C suppressing the further increment of $q_{total,fin}''$ and $T_{avg,surf}$ as compared to T_{in} of 38°C.

4.2 Heat Transfer Mechanisms before Flow Boiling

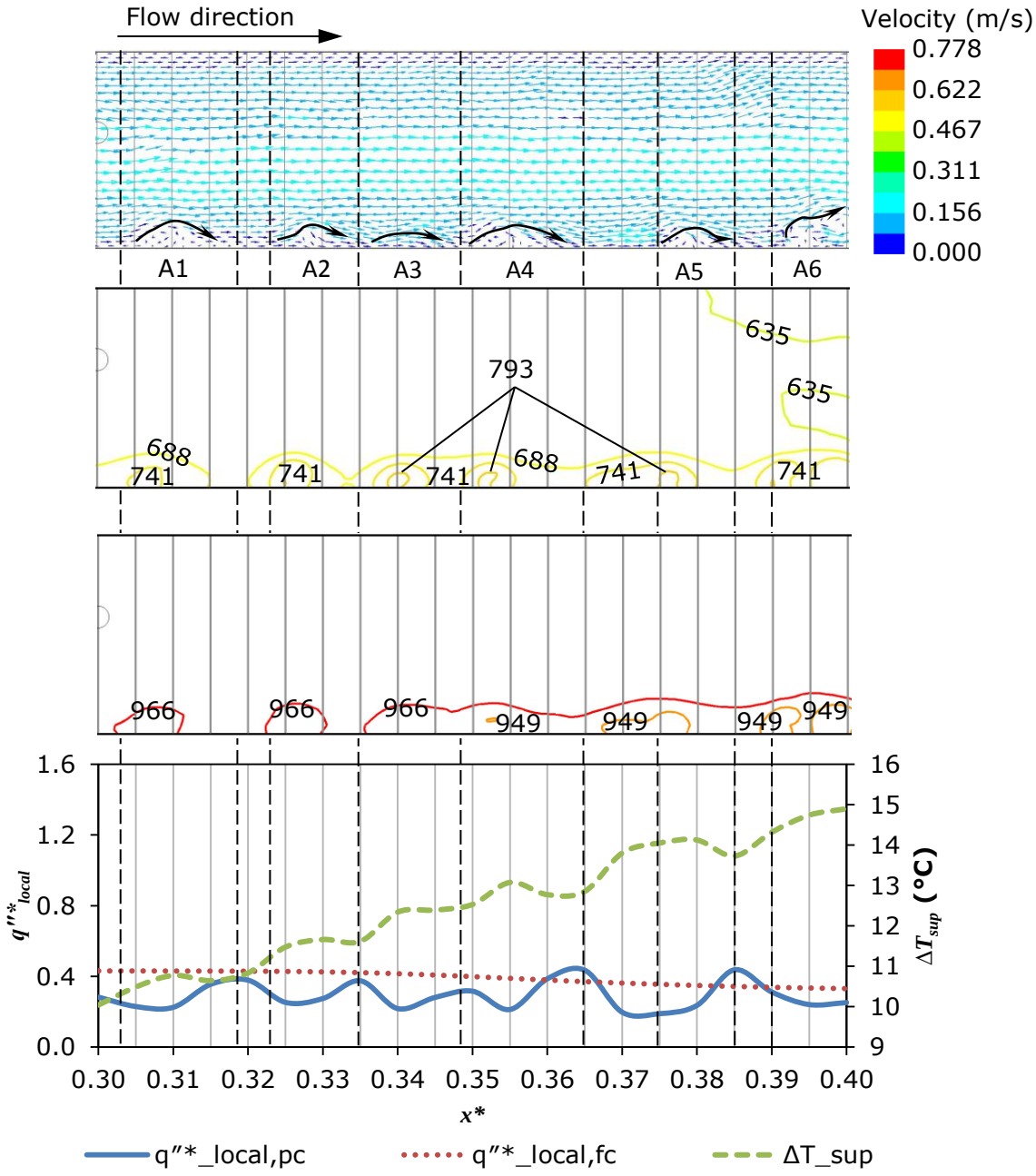
For the understanding of the phenomenon producing the trend of transient heat transfer before flow boiling when applying different conditions, the exploration of the corresponding mechanisms is essential. For this purpose, this study investigates of local hydrodynamic and thermal conditions through velocity vector, pressure, fluid density, and heat transfer distributions before flow boiling ($\Delta t_{fb} \leq 0$ or $t - t_{ONB} \leq 0$).

This study employs $q_{local}''^*$ and ΔT_{sup} for the investigation of the heat transfer distribution. $q_{local}''^*$ is a non-dimensional parameter which is equivalent to $q_{local}''/q_{total,fin}''$ and involves the heat transfer components of $q_{local,pc}''^*$ and $q_{local,fc}''^*$. $q_{local,pc}''^*$ and $q_{local,fc}''^*$ stand for the non-dimensional local heat transfer with and without phase change, respectively. $q_{local,pc}''^*$ and $q_{local,fc}''^*$ are equivalent to $q_{local,pc}''/q_{total,fin}''$ and $q_{local,fc}''/q_{total,fin}''$, respectively. $q_{local,fc}''$ is the local heat flux of single-phase flow forced convection of liquid without undergoing the phase change. $q_{local,fc}''$ is

obtainable by repeating the simulation of the similar condition without phase change process. On the other hand, $q''^{*}_{local,pc}$ stands for $q''_{local,pc}/q''_{total,fin}$. $q''_{local,pc}$ is the local heat flux involving phase change. By reading $q''^{*}_{local,fc}$ and $q''^{*}_{local,pc}$ at similar Δt_{fb} and location, the heat transfer enhancement of $q''^{*}_{local,pc}$ from $q''^{*}_{local,fc}$ was identifiable.

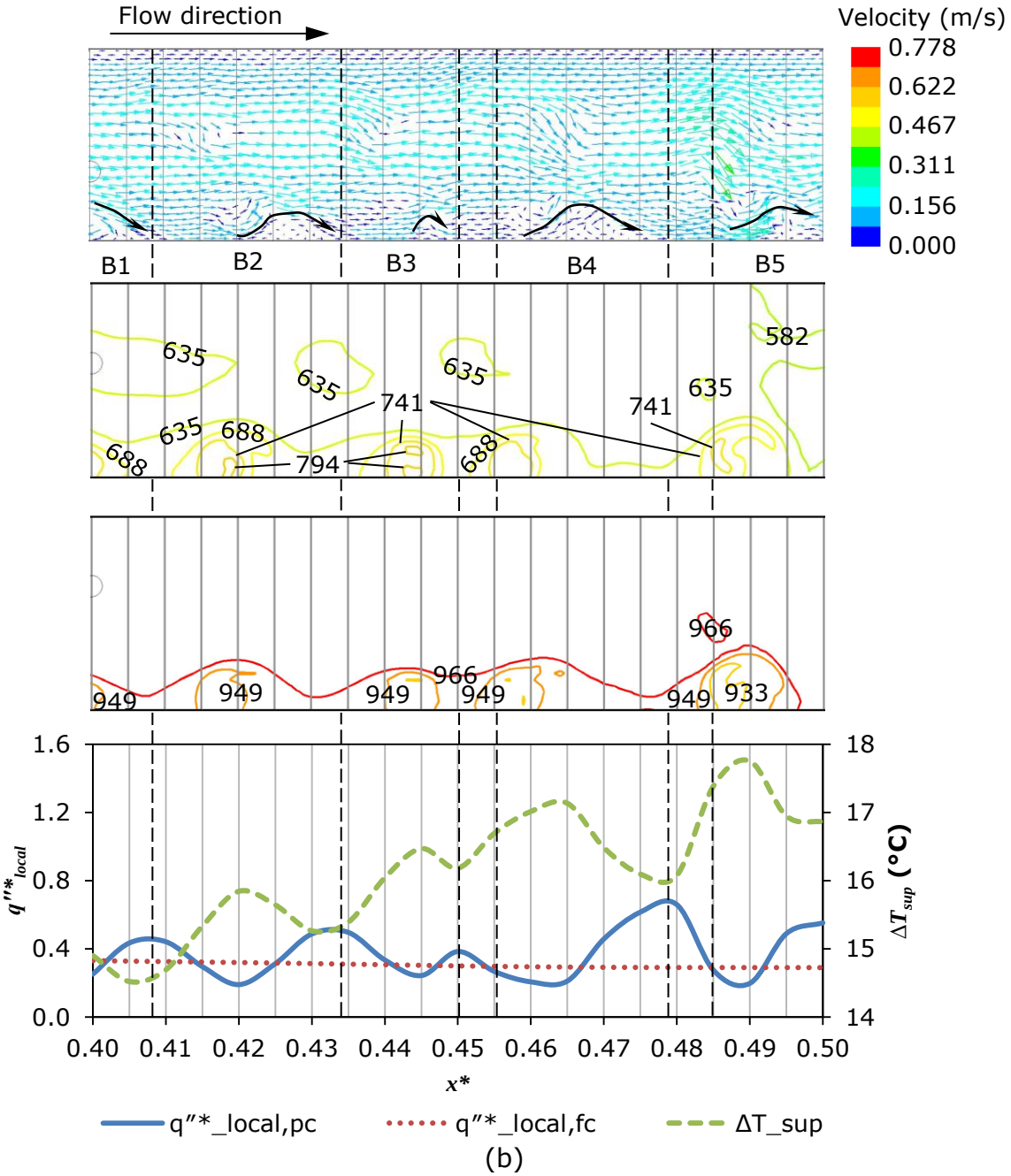
The local hydrodynamic and thermal conditions first investigated were at $\dot{m}''$, T_{in}, and q''_b of 165 kg/m^2 s, 23°C, and 1561 kW/m^2, respectively in x-y planes at $z =$ 0.08 mm at Δt_{fb} of about -5.8 ms with the plots in Figure 4.4. The x-y planes chosen was at $z =$ 0.08 mm since the plane was near to the location for the nucleation of the first bubble to show the flow characteristics related to the discussion. At of x-y planes at $z =$ 0.08 mm, the variation of flow from liquid-phase flow forced convection occurred at x^* of about 0.3-1.0, and therefore the plots presented are at x^* of 0.3-1.0. The velocity vector distributions and plots of q''^{*}_{local} and ΔT_{sup} against x^* included dash lines to distinguish different fluid flow patterns with parallel flow of fluid on the bottom heating surface.

For x^* of 0.3-0.4, as shown in Figure 4.4a, even before bubble nucleation, five short ranges of ascending and descending flows in A1-A5 became apparent. Meanwhile, in other regions, the current retained parallel to the heating surface. Indeed, the variation of flow before bubble nucleation during pool boiling also appeared in the experimental studies of Semaria [131], Brown [132] and Wang et al. [133, 134]. Wang et al. [133, 134] encountered ascending jet flow before nucleate boiling occurred, indicating the presence of the density difference within the fluid causing the buoyancy effects induced by the phase change process. According to Semaria [131] and Wang et al. [133, 134], the jet flow is hardly visible from bared eyes. They were only able to observe the jet flow ascended in all directions above heating surfaces before pool boiling by employing the zoom light routine and CCD camera. This observation also implies that the similar phenomenon of ascending jet flow is also possible to occur before flow boiling although none of the existing experimental studies observed with current experimental techniques.



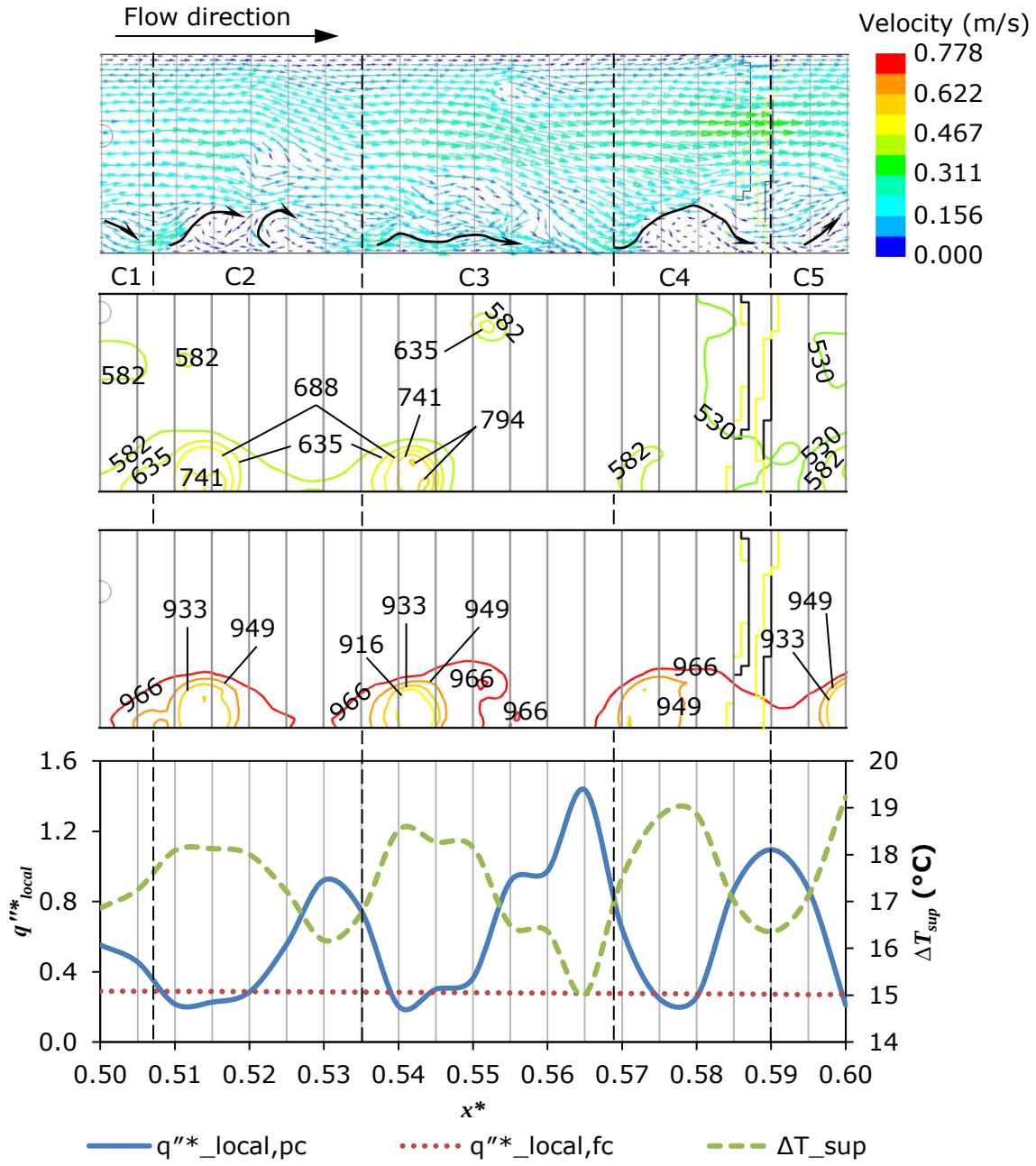
(a)

(Continued next page)



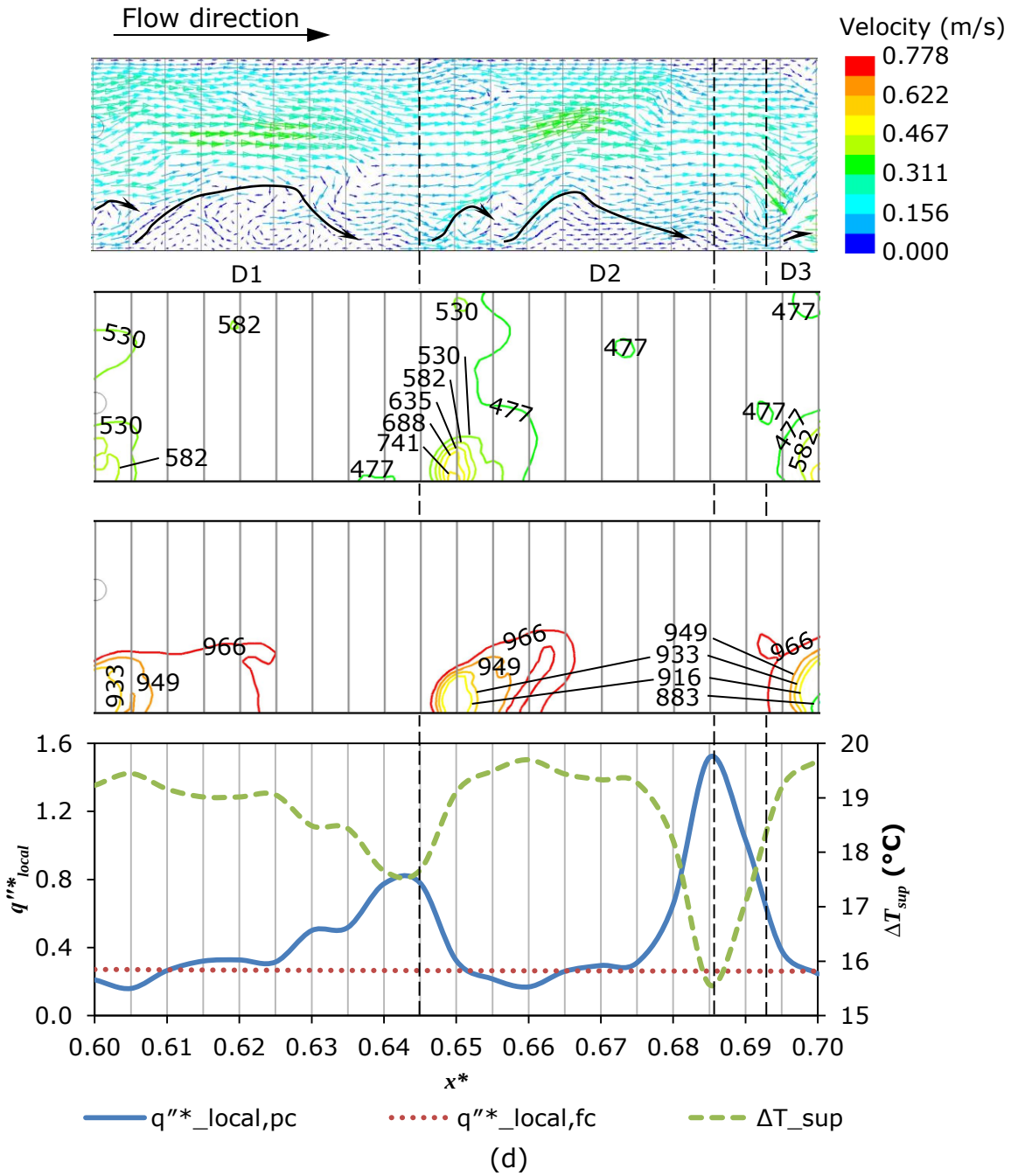
(b)

(Continued next page)



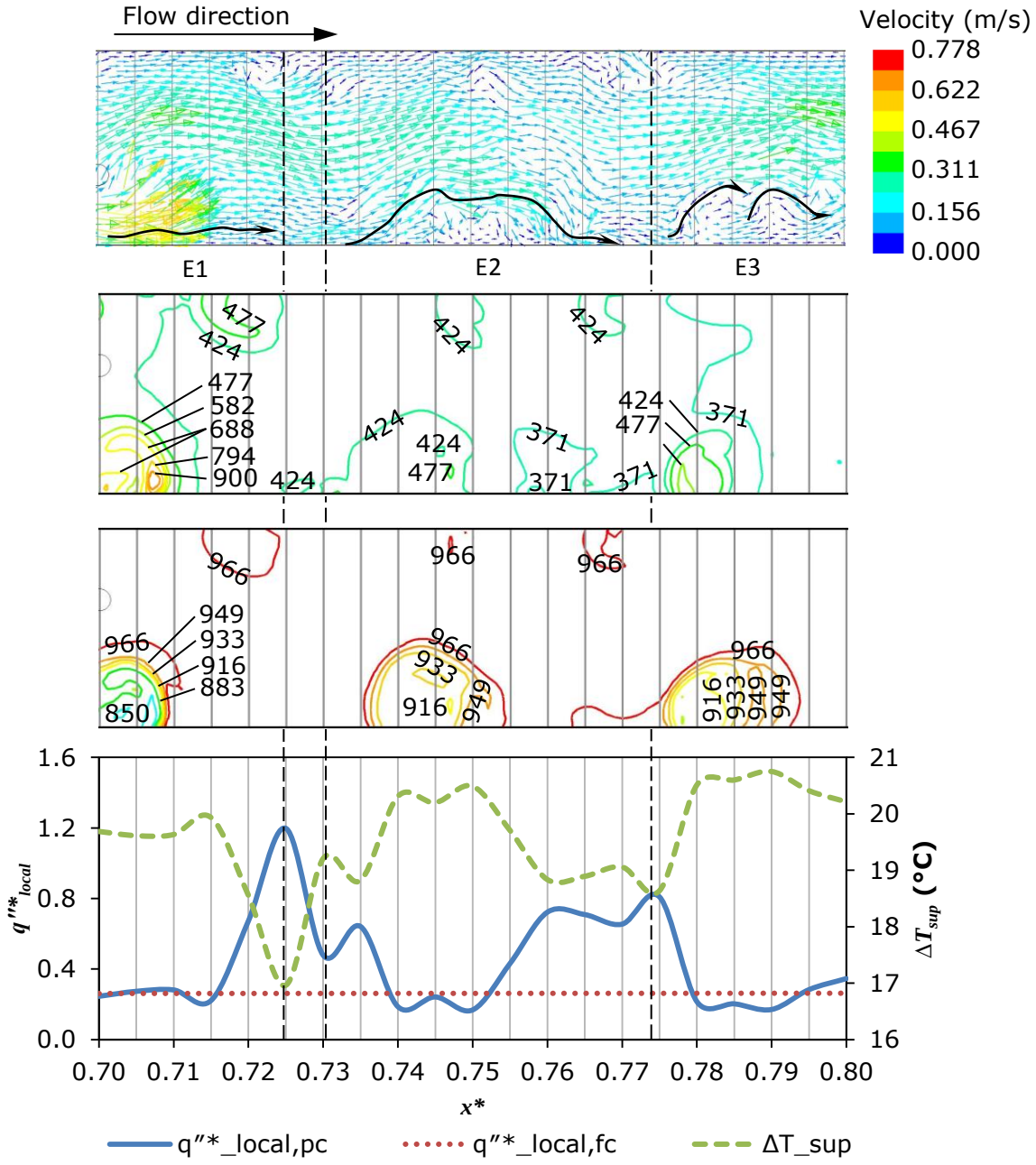
(c)

(Continued next page)



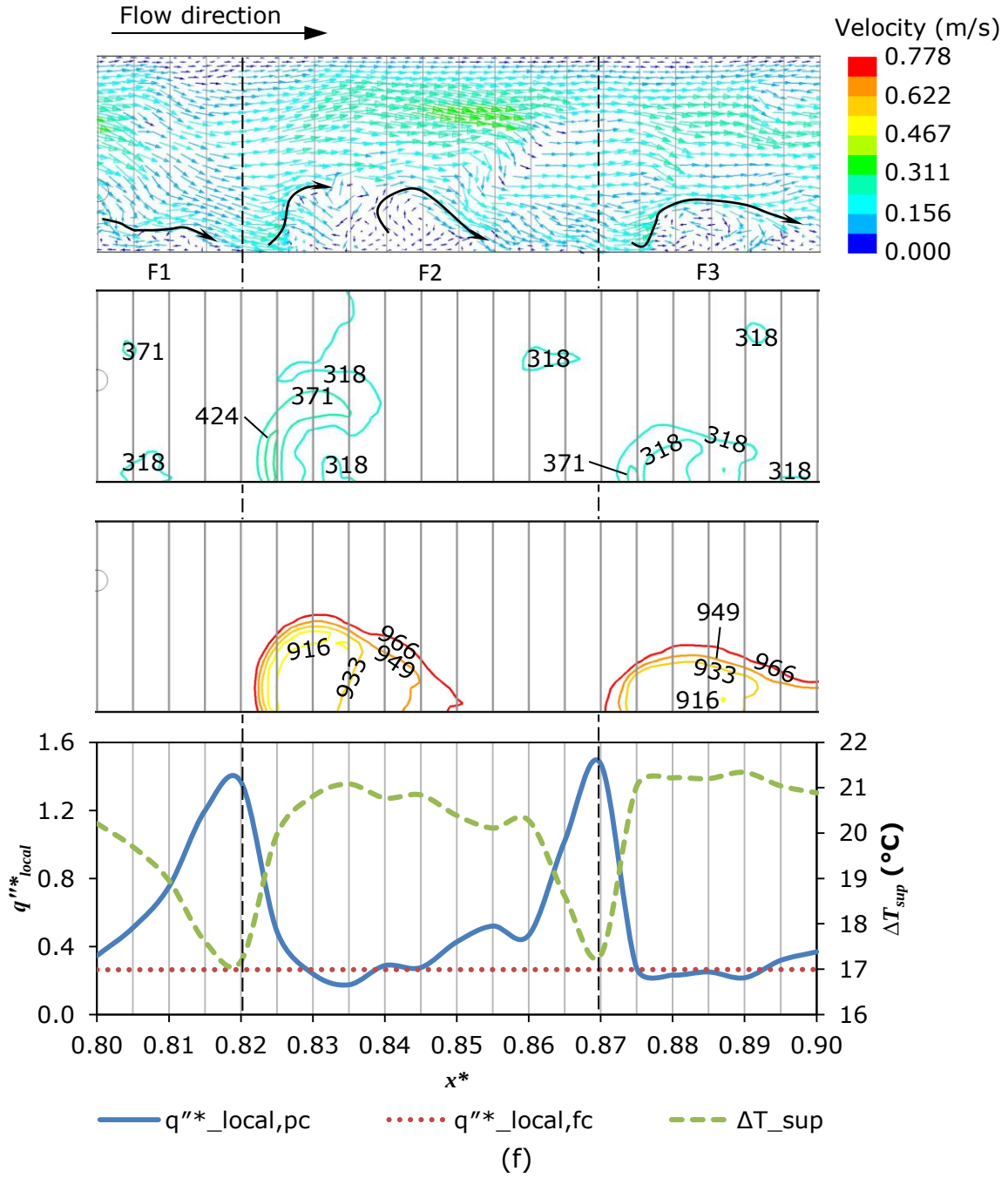
(d)

(Continued next page)



(e)

(Continued next page)



(f)

(Continued next page)

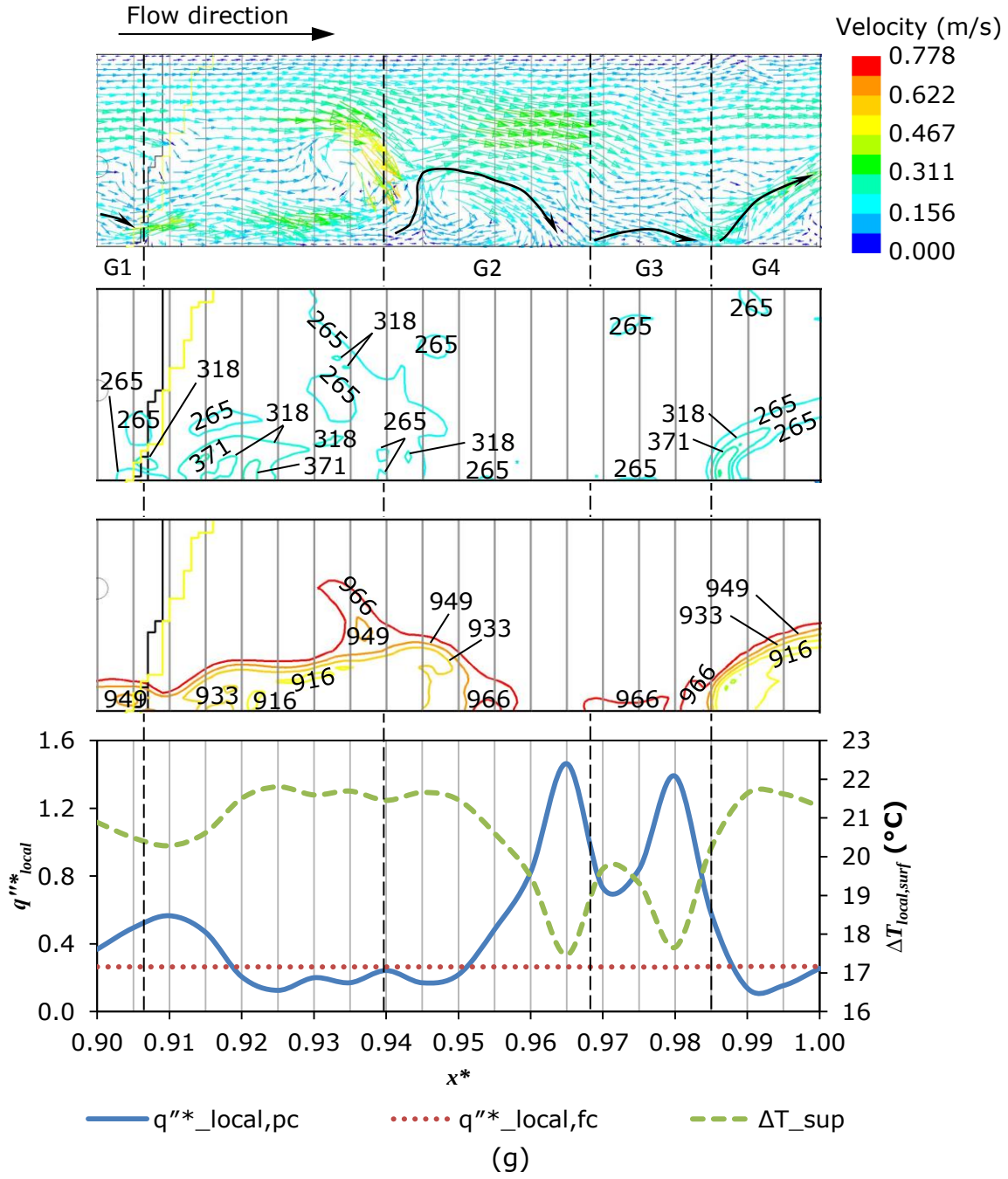


Figure 4.4: Velocity vector, pressure (Pa), and density (kg/m³) distributions at x-y plane and q''^{*}_{local} and ΔT_{sup} against x^{*} at $y = 0$ at $z = 0.08$ mm when $\Delta t_{fb} = -5.8$ ms for $q''_b = 1561$ kW/m², $\dot{m}'' = 165$ kg/m² s, and $T_{in} = 23$°C in silicon micro-channel

The ascending and descending flows triggered when liquid-vapour mixture formed before flow boiling as observed in fluid density distribution in Figure 4.4a. The liquid-vapour mixture created as a result of phase change process assumed in

the phase change model. Although the liquid-vapour mixture formed, the formation of bubbles was absent due to the incomplete phase change process. This observation matches with the explanations from Peng [31] regarding one of the possible reason for the occurrence of fictitious boiling before flow boiling. Peng [31] postulated one of the reasons for the presence of the fictitious boiling is due to the existence of the nucleate boiling conditions of the liquid that is unstable.

Other than Peng [31], Semaria [131] and Wang et al. [133, 134] also explained that the existence of liquid-vapour mixture is possible when they observed jet flow before pool boiling. Wang et al. [133, 134] stated that the liquid-vapour mixture presents with the condensation of vapour in the jets before the bubble nucleation. They [133, 134] also found that the downward jet flows changed direction upward gradually due to buoyancy effect, implying that the jet flow has an apparent density difference from the ambient liquid due to phase change. Collier and Thome [135] also stated that the nucleation of the bubble is absent, but the hot liquid jets travelled from a superheated layer unto the cold liquid during the incipient pool boiling in the sub-cooled liquid. The jet flow associated with the ascending flow before pool boiling observed from Wang et al. [133, 134] facilitates the higher heat transfer. Therefore, these phenomena observed during pool boiling is also possible to occur during flow boiling, contributing to the fictitious boiling with the nucleate boiling characteristics before the flow boiling as found by Peng [31]. Nevertheless, the descending flow was absent for jet flow in the studies of Wang et al. [133, 134] before pool boiling. On the other hand, before flow boiling in this study, the fluid flow along the channel imposed the descending flow.

When the liquid-vapour mixture formed in the channel, the local rise of pressure gradient became apparent at A1-A6 as depicted in pressure distribution in Figure 4.4a. Figure 4.4a also illustrates that the local velocities decreased while the ascending and descending flows occurred on the heating surface in these regions as illustrated Figure 4.4a. These occurrences obey Bernoulli's principle (with Bernoulli equation of $dp/dx = -\rho U\, dU/dx$) in which the pressure gradient of flow is proportional to the convective acceleration in opposite sign as stated by Nechayev [136] and in Schlichting et al. [137]. Nechayev [136] also mentioned that the reversed flow is possible when the local pressure exceeds the flow pressure drop. This stream also characterises the early transition to the turbulent flow from the low flow rates or mass fluxes of the bulk liquid.

From the plots of the velocity vector, pressure, and density distribution and q''^{*}_{local} and ΔT_{sup} against x^{*} of 0.3-0.4 in Figure 4.4a, the first mode of heat transfer mechanisms became apparent at A1-A5. In the first mode, the flow from the heating surface ascended and the local velocities decreased with the regional rise of pressure gradients when the liquid-vapour mixture appeared from the phase change process. The local increase in pressure gradients with the local decrease of

velocities or weak momentum of flow within on the heating surface obeys the Bernoulli's principle. Since the pressure gradients were relatively higher than the bulk liquid, flow reversal appeared within the low velocities of the liquid.

During the first mode of heat transfer mechanism at A1-A5 within x^* as illustrated in Figure 4.4a, $q''^*_{local,pc}$ began at low values. $q''^*_{local,pc}$ decreased with the small local flow velocities associated with the liquid-vapour mixture on the heating surface impeding the heat transfer. Also, $q''^*_{local,pc}$ fluctuated near these areas due to the turbulent flow causing the high tendency of the fluctuation of local thickness of thermal layer as stated by Hsu and Graham [106]. The flow began to descend while $q''^*_{local,pc}$ increased and ΔT_{sup} slightly decreased with the existence of ascending and descending flows from the phase change. The descending flow brings the colder bulk fluid on the heating surface with the lesser amount of vapour to allow the local increase of transient heat conduction. Although the liquid-vapour mixture was apparent, the bubble nucleation was absent in these regions. At the downstream of A5, A6 consisted of ascending flow, and the descending flow occurred at B1 as shown in Figure 4.4b that possessed the first mode of heat transfer mechanism.

In most of the regions of x^* of 0.3-0.4, $q''^*_{local,pc}$ was relatively lower than $q''^*_{local,fc}$ with the insignificant length scales of ascending and descending flows as illustrated in Figure 4.4a. This incidence causes lesser interaction with colder bulk fluid, and therefore these regions are too small to affect the heat transfer. Also, in most of the regions of x^* of 0.3-0.4, the liquid-vapour mixture existed on the heating surface, leading to the impedance of the heat transfer. Nevertheless, the descending flow occurred with the increment of $q''^*_{local,pc}$. This presence is as a result of the relatively colder fluid descending on the heating surface with the lesser amount of vapour inducing the transient conduction. In x^* of 0.3-0.4, the vicinity with $q''^*_{local,pc}$ exceeding $q''^*_{local,fc}$ only occurred at x^* of 0.365 and 0.385.

In x^* of 0.4-0.5 as displayed in Figure 4.4b, the ascending and descending flows occurred at B2, B3, B4, and B5 involved the second mode of heat transfer mechanism. When the current near the heating surface entered these regions, both pressure gradient and the amount of vapour rose, indicating that the liquid-vapour mixture present due to the phase change process. However, the amount of the vapour increased more significant than the increase of pressure gradient with the rise of ΔT_{sup}. When the amount of the vapour increased, the flow travelled parallel to the heating surface in relatively higher velocities to satisfy the conservation of momentum. At the flow near to the downstream part of the liquid-vapour mixture, the flow ascended due to the micro-convection. This occurrence resembles the mechanism in which micro-convection produced circulation within the liquid slug while evaporation at the receding liquid-vapour interface (in which the contact angle decreased) at the left-hand side of the circulation flow as encountered by Kandlikar [36]. The micro-convection imposes flow resistance in the bulk fluid in

which the fluid convection pushed towards the bulk fluid and therefore the flow velocities within the micro-convection on the heating surface is relatively low.

The ascending and descending flows at x^* of 0.4-0.5 as shown in Figure 4.4b occurred at relatively larger length scales than x^* of 0.3-0.4 as depicted in Figure 4.4a. At x^* of 0.4-0.5, the amount of liquid-vapour mixture was also more than x^* of 0.3-0.4 with the more substantial ΔT_{sup}, allowing more activities of phase change. The considerable length scales of ascending and descending flows also appeared due to more significant buoyancy and gravity effects with the more substantial amount of liquid-vapour mixture. The more extensive buoyancy effects cause the flow to ascend to the bulk fluid in larger length scales, and then to descend with gravity effects. This occurrence imposes broader regions with flow resistance associated with low flow velocities for x^* of 0.4-0.5 as compared to 0.3-0.4.

In the regions of B2, B3, B4, and B5 as displayed in Figure 4.4b, $q''^*_{local,pc}$ began at values slightly lower than $q''^*_{local,fc}$ once the ascending flow occurred. This phenomenon was also part of the second mode of heat transfer mechanism with the existence of more massive liquid-vapour mixture. Then, $q''^*_{local,pc}$ increased with the transient conduction and local ΔT_{sup} decreased gradually within these regions along x^* when the flow descended, implying the increase of local heat transfer. $q''^*_{local,pc}$ also increased with the transient conduction when the liquid-vapour mixture was sliding along with the heating surface at the upstream of the mixture. Although the mixture present, the bubble nucleation was absent in these regions. At B5, an ascending flow emerged, and another part of descending flow occurred at C1 as shown in Figure 4.4c that possessed the second mode of heat transfer mechanism. On the other hand, at x^* of 0.4-0.5, the first mode of heat transfer mechanism was absent.

In overall, at x^* of 0.4-0.5 as illustrated in Figure 4.4b, more regions possessed $q''^*_{local,pc}$ above $q''^*_{local,fc}$ with as compared to x^* of 0.3-0.4 as shown in Figure 4.4a. The more regions with $q''^*_{local,pc}$ above $q''^*_{local,fc}$ occurred with the broader length scales of ascending and descending flows for x^* of 0.4-0.5 as compared to x^* of 0.3-0.4. This occurrence is due to the relatively more significant heat transfer rates at x^* of 0.4-0.5 as compared to x^* of 0.3-0.4. With the larger heat transfer rates, x^* of 0.4-0.5 possesses the larger length scales of ascending and descending flows as compared to x^* of 0.3-0.4. The broader length scales of ascending and descending flows bring the more substantial amount of the colder bulk fluid with the lesser amount of vapour on the heating surface enhancing the heat transfer.

At x^* of 0.5-0.6 as depicted in Figure 4.4c, the third mode of heat transfer mechanism became apparent in C2 and C5. Meanwhile, C3 and C5 possessed the fourth mode of heat transfer mechanism. The first mode of heat transfer mechanism emerged in C4.

In C2 as shown in Figure 4.4c, the third mode of heat transfer mechanism resembled some feature as the first mode in which the flow decelerated and ascended once local pressure gradient rose. The pressure gradient rose together with the formation of the liquid-vapour mixture in the broader scales with the more substantial heat transfer rates at C2 as compared to the upstream. In C2, from the downstream of the liquid-vapour mixture, the second ascending and descending flows occurred. The second ascending stream emerged due to the micro-convection associated with the buoyancy and gravity effects. This occurrence is also evident in the second mode of heat transfer mechanism. C5 also involved the ascending flow, and decelerating flow appeared in the region of the local rise of pressure gradient with the liquid-vapour mixture. The ascending flow at C5 also continued with the descending flow at the downstream portion of the liquid-vapour mixture as evident in D1 as illustrated in Figure 4.4d. Also, from the downstream of the liquid-vapour mixture in D1, another ascending flow occurred from the heating surface as a result of the micro-convection associated with buoyancy and gravity effects. Therefore, C5 and D1 comprised the third mode of heat transfer mechanism. However, the current in D1 rose further towards the bulk fluid as compared to the ascended flow C2 induced by the micro-convection. This presence is due to the more substantial buoyancy effects and the more massive amount of liquid-vapour mixture generated from more significant heat transfer rates at D1 as compared to C2 at the upstream.

During the third mode of heat transfer mechanism as evident in C2 and C5 as depicted in Figure 4.4c and D1 in Figure 4.4d, from the liquid-vapour mixture, $q''^{*}_{local,pc}$ was lower than $q''^{*}_{local,fc}$. Meanwhile, in C2 and D1, at the downstream of the liquid-vapour mixture, the increment of $q''^{*}_{local,pc}$ above $q''^{*}_{local,fc}$ became more significant while ΔT_{sup} decreased further with the ascending and descending flows. The increment of $q''^{*}_{local,pc}$ above $q''^{*}_{local,fc}$ became more significant while ΔT_{sup} decreased further at the downstream of the liquid-vapour mixture in C2 and D1 due to the micro-convection as compared to the upstream. Also, the micro-convection occurs with the more significant buoyancy and gravity effects with the more massive liquid-vapour mixture in C2 and D1 as compared to the upstream. With the more substantial buoyancy and gravity effects during the micro-convection occurred at the downstream of the liquid-vapour mixture, the increment of $q''^{*}_{local,pc}$ above $q''^{*}_{local,fc}$ became more significant while ΔT_{sup} decreased further. Meanwhile, the local rise of $q''^{*}_{local,pc}$ in C2 and D1 also occurred at the upstream of the liquid-vapour mixture due to the transient conduction when the liquid-vapour mixture is moving along the heating surface. However, bubble nucleation was absent in these regions.

The fourth mode of heat transfer mechanism as depicted in Figure 4.4c occurred in C3. In C3, the flow travelled almost parallel and along the heating surface at relatively higher velocities. The more elevated velocities of flow appeared as the

amount of vapour from the phase change process rises more significant in C3 as compared to the local increase in pressure gradient. Since the amount of vapour significantly rose, the local velocities increased and travelled parallel along the heating surface to satisfy the conservation of momentum. This presence is similar to the second mode of heat transfer mechanism. Nevertheless, unlike the second mode, the ascending and descending flows were insignificant in this fourth mode of heat transfer mechanism. The flow near to the liquid-vapour mixture possessed low $q''^{*}_{local,pc}$ which is close to $q''^{*}_{local,fc}$ in C3. When the flow moved away from the region with the liquid-vapour mixture, $q''^{*}_{local,pc}$ significantly increased while ΔT_{sup} reduced, indicating the increase of the heat transfer. Meanwhile, the local rise of $q''^{*}_{local,pc}$ became apparent at the upstream of the liquid-vapour mixture due to the transient conduction when the liquid-vapour mixture moved along the heating surface. However, bubble nucleation was absent in these regions.

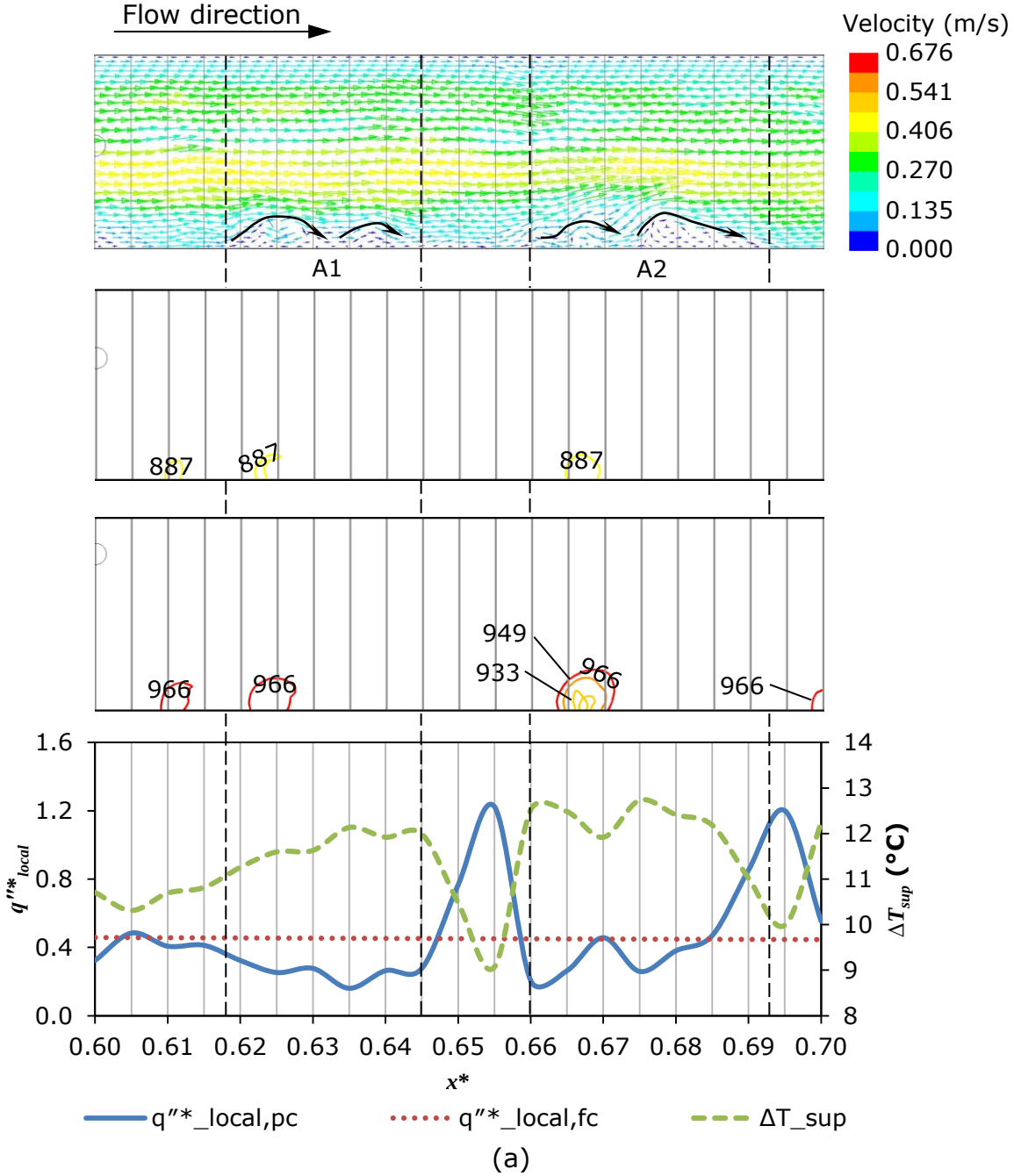
For the remaining regions in x^{*} of 0.6-0.9 as displayed from Figure 4.4d to Figure 4.4g, the heat transfer mechanisms from first to fourth modes also became apparent. The first mode of heat transfer mechanism emerged in E2, F3-G1, G3, and G4. Meanwhile, G2 involved the second mode of heat transfer mechanism. The third mode of heat transfer mechanism became evident in D2, E3-F1, and F2. On the other hand, D3 and E1 experienced the fourth mode of heat transfer mechanism. The flow in D3-E1 travelled at relatively higher velocities with lower local densities as compared to the current in C4 with the fourth mode of heat transfer mechanism. The more elevated velocities occurred with the relatively higher amount of vapour phase change with lower local densities on the heating surface to conserve the momentum at the downstream as compared the upstream.

Each mode of heat transfer mechanism appeared to occur in statistical behaviour with different tendencies along the micro-channel before flow boiling as observed in Figure 4.4. The probability of the occurrence of the first mode of heat transfer mechanism was higher at the onset of ascending and descending flows of the channel nearest to the inlet. The second and third mode of heat transfer mechanism became apparent slightly downstream of the micro-channel with the higher rise of the amount of vapour near the heating surface as compared to the increase of pressure gradient. On the other hand, along with the length of the micro-channel, only a few regions involved the fourth mode of heat transfer mechanism. Towards the downstream, in overall, the region with $q''^{*}_{local,pc}$ above $q''^{*}_{local,fc}$ became broader as compared to the upstream with the more active ascending and descending flows due to phase change enhancing heat transfer. The ascended flow imposed more extensive regions with flow resistance associated with low flow velocities. When the current began to descend with colder bulk fluid to the heating surface towards the downstream, $q''^{*}_{local,pc}$ substantially increased through the transient conduction while ΔT_{sup} decreased in the vicinity.

The evaluation of the local hydrodynamic and thermal conditions continued with larger $\dot{m}''$ of 389 kg/m^2 s at fixed T_{in} = 23°C and q_b'' = 1561 kW/m^2 at Δt_{fb} about -5.8 ms (Δt_{fb} of -5.787 ms). This condition is accessible from velocity vector, pressure, and fluid density distributions and $q_{local}''^*$ and ΔT_{sup} against x^* as illustrated in Figure 4.5. In this case, the first bubble nucleated at Δt_{fb} of 0 near $z = -0.08$ mm and therefore x-y planes selected was at $z = -0.08$ mm for the evaluation. At x-y planes at $z = -0.08$ mm, the variation of flow from liquid-phase flow forced convection at this condition began at x^* of 0.6-0.7. Therefore, the plots presented are only for x^* of 0.6-1.0 from Figure 4.5a to Figure 4.5d at this condition. At Δt_{fb} about -5.8 ms, the variation of flow for $\dot{m}''$ of 389 kg/m^2 s began closer to the outlet as compared to $\dot{m}''$ of 165 kg/m^2 s as shown in Figure 4.4.

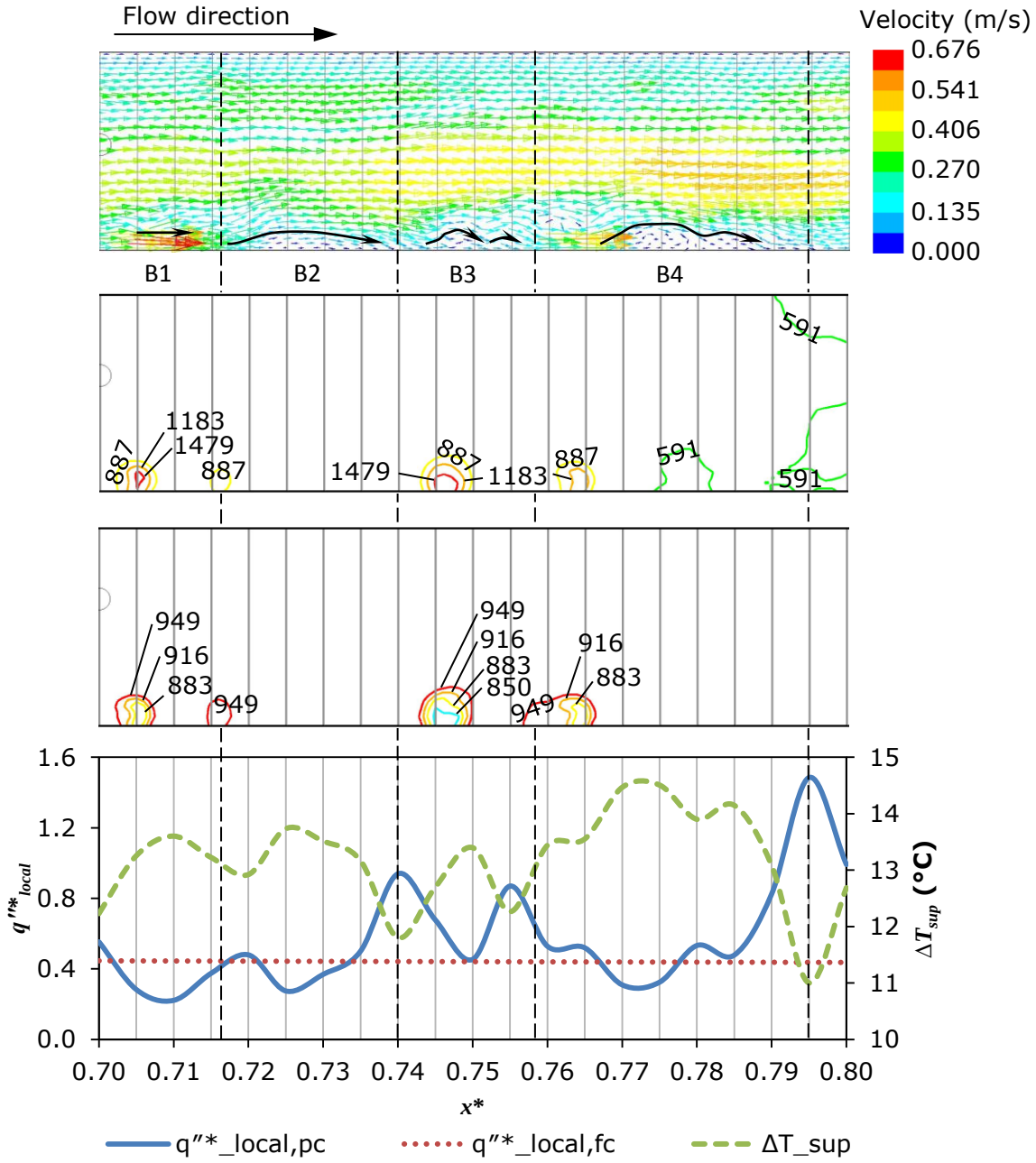
At $\dot{m}''$ of 389 kg/m^2 s as depicted in Figure 4.5, ascending and descending flows also occurred associated with the four modes of heat transfer mechanisms. The first mode occurred at C3 and D3. Meanwhile, B2, B4, C1, and D1 experienced the second mode. The third mode was evident at A1, A2, B3, C4, and D2. On the other hand, B1 and C2 involved the fourth mode. The first mode occurred lesser with higher $\dot{m}''$ of 389 kg/m^2 s than $\dot{m}''$ of 165 kg/m^2 s. Similar to $\dot{m}''$ of 165 kg/m^2 s, the fourth mode at $\dot{m}''$ of 389 kg/m^2 s occurred less frequent before flow boiling as compared to other modes of heat transfer mechanisms.

Within x^* of 0.6-1.0 at $\dot{m}''$ of 389 kg/m^2 s at Δt_{fb} about -5.8 ms as shown in Figure 4.5, the region with $q_{local,pc}''^*$ lower than $q_{local,fc}''^*$ was relatively broad. This area at $\dot{m}''$ of 389 kg/m^2 s was more extensive than the region at smaller $\dot{m}''$ of 165 kg/m^2 s as illustrated in Figure 4.4 for each mode of heat transfer mechanism. Also, $q_{local,pc}''^*$ below $q_{local,fc}''^*$ was relatively larger for $\dot{m}''$ of 389 kg/m^2 s as compared to $\dot{m}''$ of 165 kg/m^2 s. Furthermore, this region generated relatively lower length scales of ascending and descending flows from the regional rise of pressure gradients while the liquid-vapour mixture retained on the heating surface. These incidences are due to the suppression of micro-convection associated with buoyancy and gravity effects with the thinner thermal boundary layer from higher $\dot{m}''$. The lower length scales of ascending and descending flows indicates the cold bulk fluid falling on the heating surface is lesser associated with the liquid-vapour mixture suppressing the heat transfer for higher $\dot{m}''$.



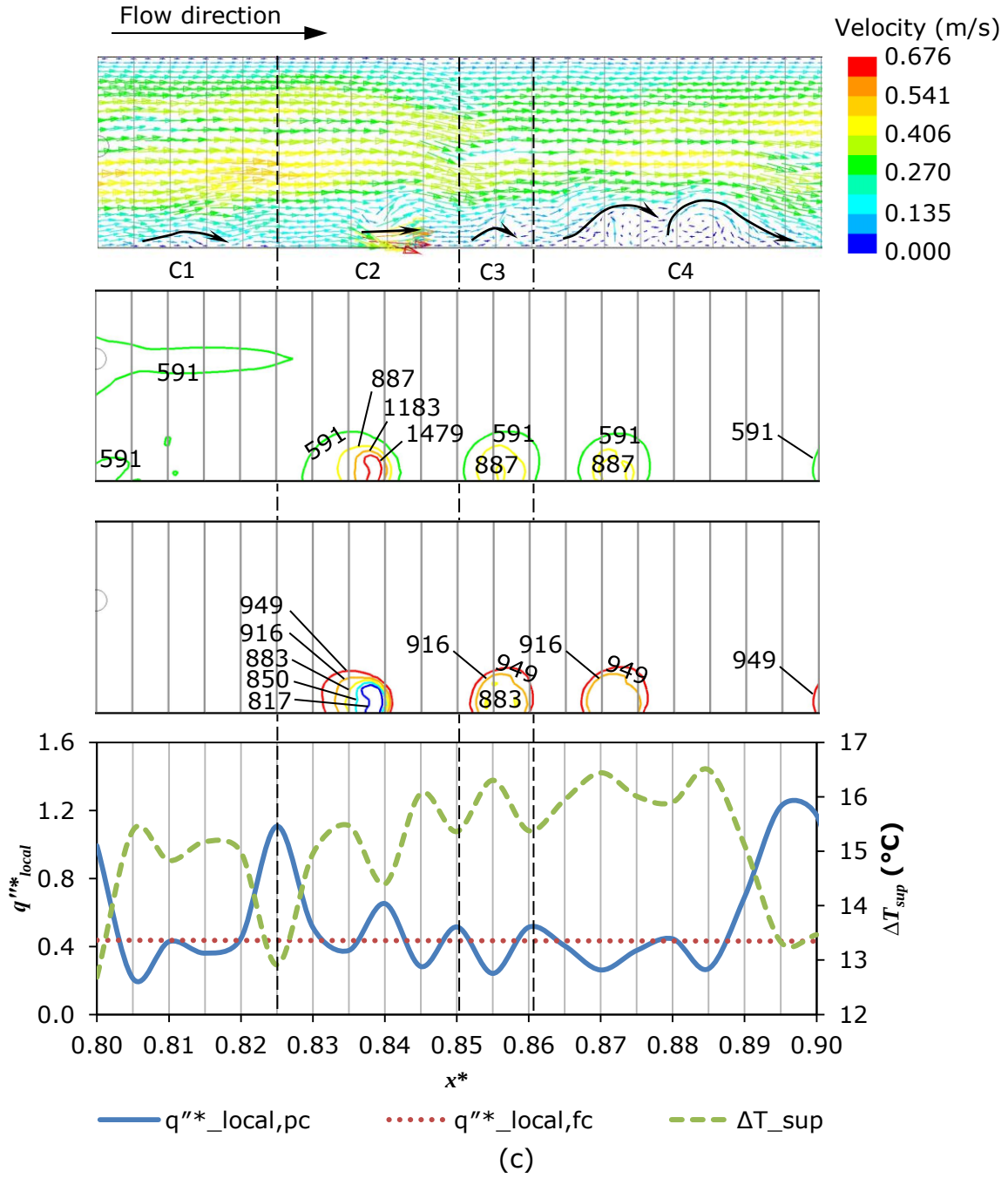
(a)

(Continued next page)



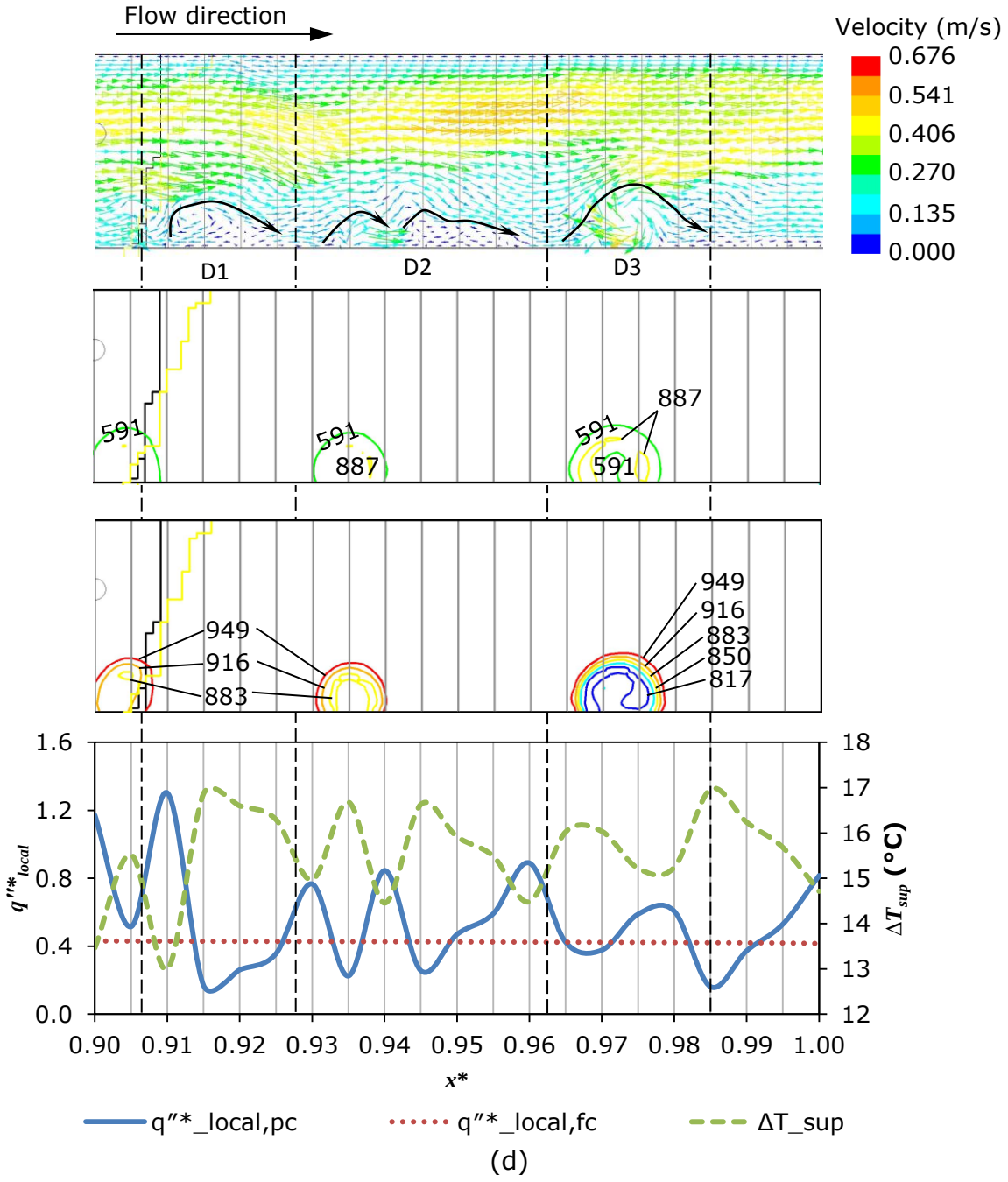
(b)

(Continued next page)



(c)

(Continued next page)



(d)

Figure 4.5: Velocity vector, pressure (Pa), and density (kg/m³) distributions at x-y plane and q''^{*}_{local} and ΔT_{sup} against x^{*} at $y = 0$ at $z = -0.08$ mm when $\Delta t_{fb} = -5.8$ ms for $q''_b = 1561$ kW/m², $\dot{m}'' = 389$ kg/m² s, and $T_{in} = 23$°C in silicon micro-channel

Once completed exploring the local hydrodynamic and thermal conditions for different $\dot{m}''$, this study advanced by evaluating the impacts of employing higher q''_b

on the conditions. The higher q_b'' implemented in this study is 2030 kW/m^2 at fixed $\dot{m}''$ = 389 kg/m^2 s and T_{in} = 23°C at Δt_{fb} about −5.8 ms (Δt_{fb} of −5.742 ms). At Δt_{fb} about −5.8 ms, the variation of flow for q_b'' of 2030 kW/m^2 began further from the outlet as compared to q_b'' of 1561 kW/m^2 as shown in Figure 4.5.

When applied higher q_b'' of 2030 kW/m^2, the ascending and descending flows occurred, and the first mode of heat transfer mechanism was dominant. Meanwhile, none of the regions experienced the second mode of heat transfer mechanism, and few areas involved the third and fourth mode of heat transfer at q_b'' of 2030 kW/m^2. At q_b'' of 2030 kW/m^2, the amount of liquid-vapour mixture accumulating on the heating surface was more massive due to phase change as compared to q_b'' of 1561 as shown in Figure 4.5. Meanwhile, at about Δ_{fb} of −5.8 ms, the ascending and descending flows due to phase change was less active with the thinner thermal boundary layer at q_b'' of 2030 kW/m^2 as compared to 1561 kW/m^2. Moreover, the higher q_b'' of 2030 kW/m^2 also caused more regions experienced $q_{local,pc}''^*$ lower than $q_{local,fc}''^*$ with higher ΔT_{sup}. The less active ascending and descending flows at q_b'' of 2030 kW/m^2 at Δ_{fb} of −5.8 ms cause the weaker transient conduction, leading to more regions with $q_{local,pc}''^*$ below $q_{local,fc}''^*$.

Other than varying $\dot{m}''$ and q_b'', this study also continued to explore the change of T_{in} on the local hydrodynamic and thermal conditions. These conditions are accessible from velocity vector, pressure, and fluid density distributions and $q_{local}''^*$ and ΔT_{sup} against x^* for higher T_{in}. The higher T_{in} employed in this study was 53°C at fixed $\dot{m}''$ = 389 kg/m^2 s and q_b'' = 1561 kW/m^2 at about Δt_{fb} of −5.8 ms. At Δt_{fb} about −5.8 ms, the heat transfer mechanism at most of the regions near the location of first bubble nucleation still maintained as single-phase flow forced convection with the parallel flow on the heating surface. This occurrence implies that the significance of nucleate boiling characteristic becomes lesser when increasing T_{in} before the bubble nucleation.

4.3 Effects of Mass Fluxes before Flow Boiling

From the different modes of heat transfer mechanisms, this study continued to evaluate the effects of mass fluxes on these heat transfer mechanisms before flow boiling. The investigation accessed the heat transfer mechanisms through the local and average heat transfer components, and the heat transfer enhancement of phase change.

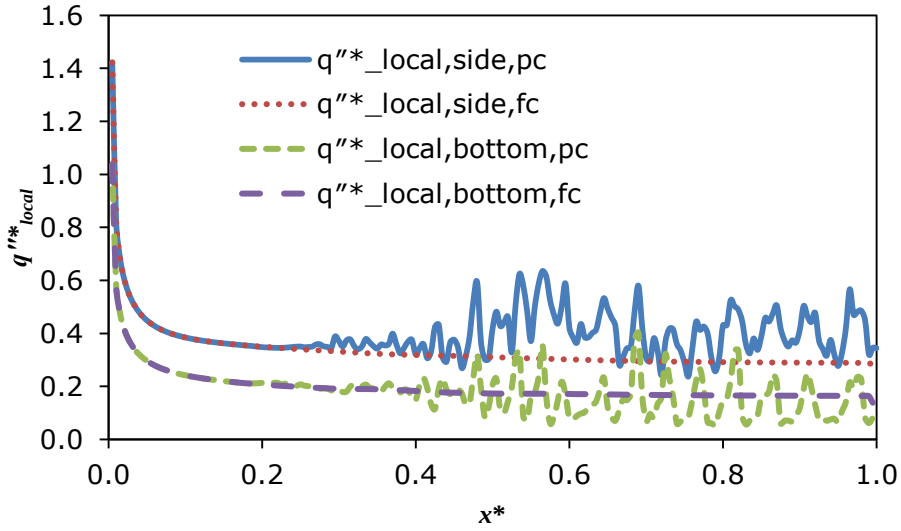
This study examined the local peripheral average heat transfer components with the non-dimensional term of $q_{local}''^*$ which stands for $q_{local}''/q_{total,fin}''$. $q_{local}''/q_{total,fin}''$ consists of $q_{local,side,pc}''/q_{total,fin}''$, $q_{local,side,fc}''/q_{total,fin}''$, $q_{local,bottom,pc}''/q_{total,fin}''$, and $q_{local,bottom,fc}''/q_{total,fin}''$ which denote as $q_{local,side,pc}''^*$, $q_{local,side,fc}''^*$, $q_{local,bottom,pc}''^*$, and $q_{local,bottom,fc}''^*$, respectively. $q_{local,side,pc}''$ and $q_{local,side,fc}''$ are local peripheral average

heat flux at the side surface with phase change and forced convection without phase change, respectively. $q''_{local,bottom,pc}$ and $q''_{local,bottom,fc}$ are local peripheral average heat flux at the bottom surface with phase change and forced convection without phase change, respectively. $q''_{local,side,fc}$ and $q''_{local,bottom,fc}$ are obtainable by repeating the simulation of the similar condition without phase change process. By reading these heat transfer components, the changes of heat transfer of $q''^{*}_{local,side,pc}$ from $q''^{*}_{local,side,fc}$ and $q''^{*}_{local,bottom,pc}$ from $q''^{*}_{local,bottom,fc}$ along x/L_c are identifiable. The local peripheral average heat flux of each component along the channel obtained also reflects the change of transient heat transfer data in Figure 4.1.

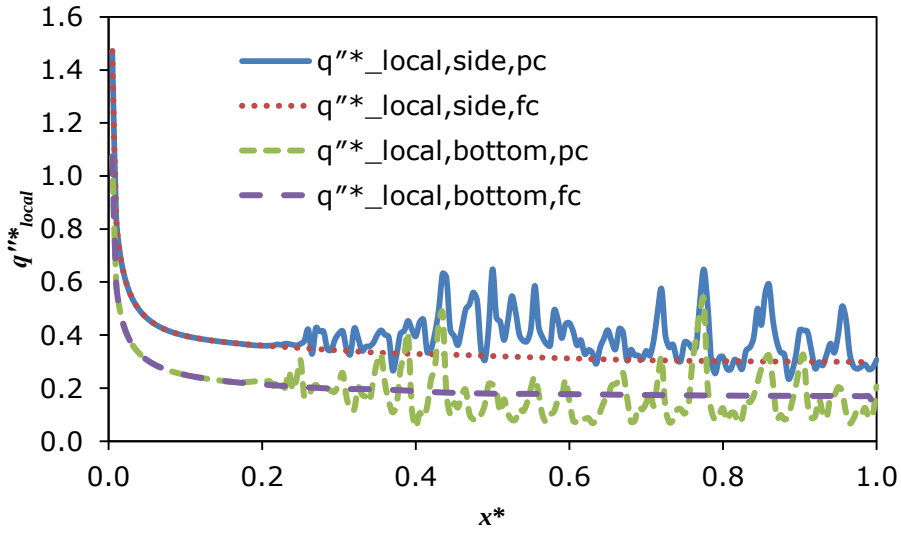
In this study, the selected Δt_{fb} along x^* were at about -5.8 and -2.9 ms for each tested $\dot{m}''$ of 165, 265, and 389 kg/m^2 s as depicted in Figure 4.6, Figure 4.7, and Figure 4.8, respectively. For each tested $\dot{m}''$ at about Δt_{fb} of -5.8 and -2.9 ms, the peaks of $q''^{*}_{local,side,pc}$ raised above $q''^{*}_{local,side,fc}$ at the side surfaces when phase change occurred. Also, at about Δt_{fb} of -5.8 and -2.9 ms for each $\dot{m}''$ tested in this study, the peaks of $q''^{*}_{local,bottom,pc}$ also raised above $q''^{*}_{local,bottom,fc}$ when phase change occurred. Nevertheless, the peaks of $q''^{*}_{local,side,pc}$ were relatively more than $q''^{*}_{local,bottom,pc}$ for each $\dot{m}''$ employed in this investigation. This presence is due to the stronger ascending and descending flows at side surface as compared to the bottom surface. Also, along x^*, the regions with $q''^{*}_{local,bottom,pc}$ below $q''^{*}_{local,bottom,fc}$ were more than the regions with $q''^{*}_{local,side,pc}$ lower than $q''^{*}_{local,side,fc}$. This occurrence is mainly due to the relatively larger $T_{avg,total}$ at the bottom surface, generating more liquid-vapour mixture covering the bottom surface as observed in Figure 4.4 as compared to the side surfaces.

For low $\dot{m}''$ of 165 kg/m^2 s at about Δt_{fb} of -5.8 ms illustrated in Figure 4.6a, the peaks of $q''^{*}_{local,side,pc}$ and $q''^{*}_{local,bottom,pc}$ triggered. Also, at about Δt_{fb} of -5.8 ms for the low $\dot{m}''$, $q''_{total,fin}$ increased steeply with $T_{avg,surf}$ before Δt_{fb} of -5.8 ms as observed in Figure 4.1. This presence indicates that the nucleate boiling characteristic develops through the rise of these peaks. These peaks raised are mainly due to ascending and descending flows from relatively thick thermal boundary layer according to the observation from Figure 4.4, regardless of which modes of heat transfer mechanism. At Δt_{fb} about -2.9 ms as shown in Figure 4.6b, the number of peaks of $q''^{*}_{local,side,pc}$ and $q''^{*}_{local,bottom,pc}$ reduced at the side surface. Meanwhile, $q''^{*}_{local,bottom,pc}$ below $q''^{*}_{local,bottom,fc}$ occupied the larger regions at Δt_{fb} about -2.9 ms while $q''_{total,fin}$ dropped slightly at Δt_{fb} about -2.9 ms from -5.8 ms. This incidence is due to the larger amount of liquid-vapour mixture covering the heating surfaces when Δt_{fb} increases with more heat entering into the micro-channel, especially at the bottom surface. From Δt_{fb} about -5.8 to -2.8 ms, bubble nucleation was absent. This incidence is due to the disturbance of ascending and

descending flows that suppressed the bubble nucleation, causing the bubble nucleation occurs only at higher ΔT_{sup} at $\Delta t_{fb} = 0$ while $q''_{total,fin}$ fluctuating.

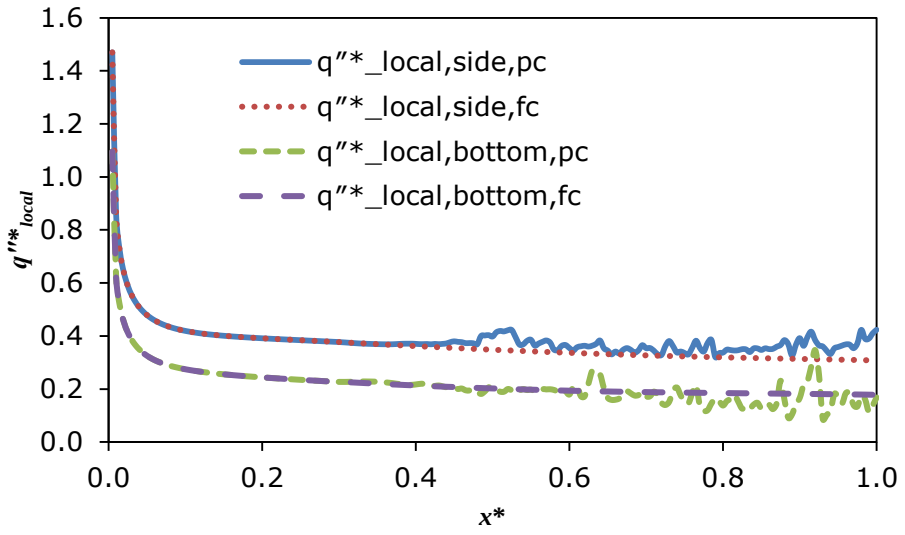


(a)

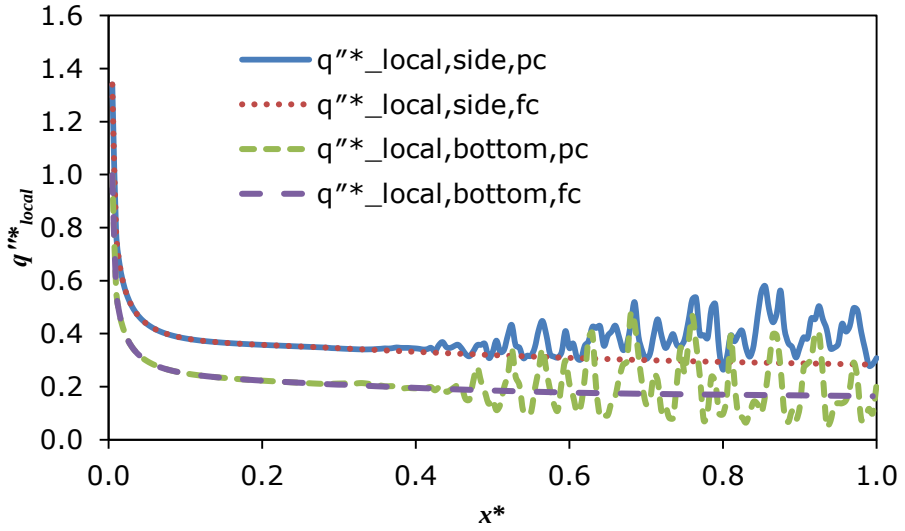


(b)

Figure 4.6: q''^{*}_{local} along x^{*} for $\dot{m}''$ of 165 kg/m² s at q''_b of 1561 kW/m² and T_{in} of 23°C at Δt_{fb} about (a) −5.8 and (b) −2.9 ms

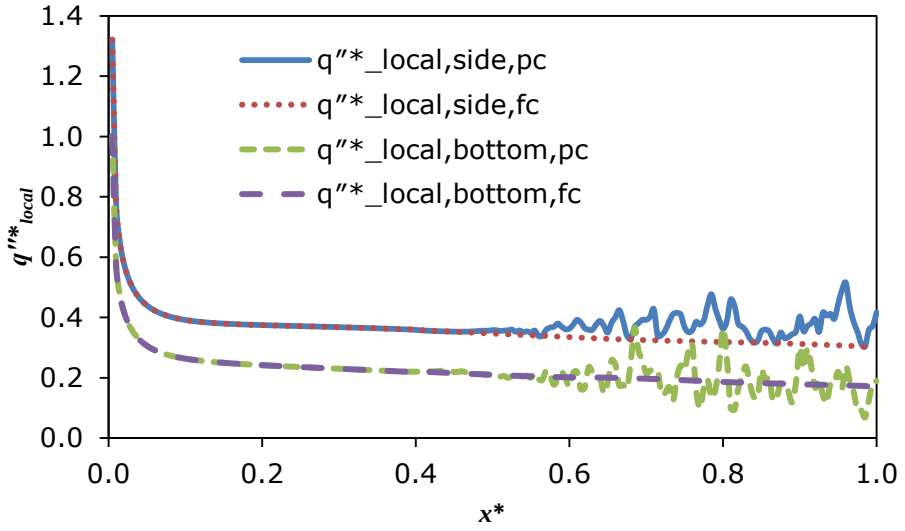


(a)

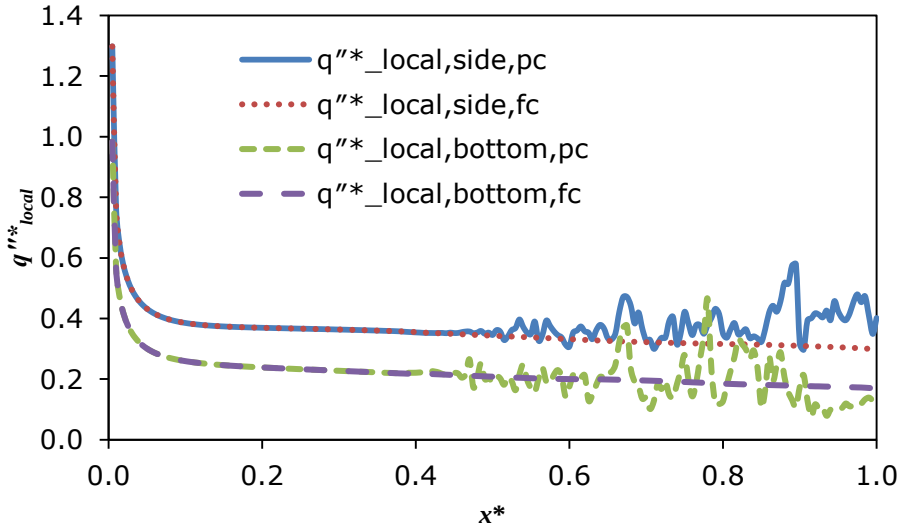


(b)

Figure 4.7: q''^{*}_{local} along x^{*} for $\dot{m}''$ of 265 kg/m² s at q''_b of 1561 kW/m² and T_{in} of 23°C at Δt_{fb} about (a) −5.8 and (b) −2.9 ms



(a)



(b)

Figure 4.8: q''^{*}_{local} along x^{*} for $\dot{m}''$ of 389 kg/m² s at q''_b of 1561 kW/m² and T_{in} of 23°C at Δt_{fb} about (a) −5.8 and (b) −2.9 ms

For moderate $\dot{m}''$ of 265 kg/m² s, from Δt_{fb} at about −5.8 ms as shown in Figure 4.7, the peaks of $q''^{*}_{local,side,pc}$ and $q''^{*}_{local,bottom,pc}$ also appeared. However, the peaks for the moderate $\dot{m}''$ began closer to the downstream of the channel as compared to low $\dot{m}''$ of 165 kg/m² s as shown in Figure 4.6. On the other hand, the number and magnitudes from moderate were still relatively lesser than the low $\dot{m}''$. The peaks caused the steep increase of $q''_{total,fin}$ at different Δt_{fb} for the low and moderate $\dot{m}''$ as evident in Figure 4.1. However, for low $\dot{m}''$, the steep rise of $q''_{total,fin}$ began

before Δt_{fb} about −5.8 ms whereas for the moderate $\dot{m}''$, the steep increase began at Δt_{fb} about −5.8 ms depicted in Figure 4.1. Therefore, at about Δt_{fb} of −5.8 ms for the moderate $\dot{m}''$ shows that the lower number and magnitude of peaks with the lesser intensity of nucleate boiling characteristic as compared to the small $\dot{m}''$. These occurrences are due to the thinner thermal boundary layer for the moderate $\dot{m}''$, causing the less substantial ascending and descending flows as compared to the low $\dot{m}''$. The less significant ascending and descending flows for the low $\dot{m}''$ facilitates the bubble nucleation with the more stable flow. The more stable flow from the moderate $\dot{m}''$ requires the lesser superheat for the bubble nucleation which is reachable with shorter Δt_{fb} before the bubble nucleation as compared to the low $\dot{m}''$. With the shorter Δt_{fb} before the bubble nucleation to reach the sufficiently high $T_{avg,surf}$ for the small $\dot{m}''$, at Δt_{fb} about −5.8 ms, the number and magnitudes were more than the moderate $\dot{m}''$.

From Δt_{fb} at about −5.8 ms to −2.9 ms for moderate $\dot{m}''$ of 265 kg/m^2 s, the peaks of $q''^{*}_{local,side,pc}$ and $q''^{*}_{local,bottom,pc}$ became more significant as depicted in Figure 4.7. These peaks are the factor for the steep increase of $q''_{total,fin}$ with $T_{avg,surf}$ inducing more substantial nucleate boiling characteristic from Δt_{fb} about −5.8 to −2.9 ms as shown in Figure 4.1. On the other hand, $T_{avg,surf}$ between Δt_{fb} of 0 at the bubble nucleation and −2.9 ms was closer for moderate $\dot{m}''$ as compared to low $\dot{m}''$. This situation indicates that moderate $\dot{m}''$ requires the more additional rise of $T_{avg,surf}$ for the bubble nucleation from Δt_{fb} about −2.9 to 0 ms as compared to low $\dot{m}''$. This difference is due to the relatively more rapid growth of the ascending and descending flows with Δt_{fb} for $\dot{m}''$ of 165 kg/m^2 s as compared to $\dot{m}''$ of 265 kg/m^2 s. The more massive flow disturbance of $\dot{m}''$ of 165 kg/m^2 s acquires more additional rise of $T_{avg,surf}$ for the bubble nucleation as compared to $\dot{m}''$ of 265 kg/m^2 s. Meanwhile, when Δt_{fb} reached about −2.9 ms, the regions with $q''^{*}_{local,bottom,pc}$ below $q''^{*}_{local,bottom,fc}$ extended more for $\dot{m}''$ of 265 kg/m^2 s. This incidence is due to the generation of the more liquid-vapour mixture at the bottom surface with more heat travelled on the bottom heating surface.

When applied high $\dot{m}''$ of 389 kg/m^2 s at Δt_{fb} about −5.8 ms, the peaks of $q''^{*}_{local,side,pc}$ and $q''^{*}_{local,bottom,pc}$ appeared as depicted in Figure 4.8a. However, the peaks for the high $\dot{m}''$ was more significant as compared to moderate $\dot{m}''$ of 265 kg/m^2 s as shown in Figure 4.7a. The peaks also began closer to the downstream of the channel at Δt_{fb} about -5.8 ms for high $\dot{m}''$ as compared to moderate $\dot{m}''$. Nevertheless, at Δt_{fb} about −5.8 ms, the peaks were relatively higher in magnitude for high $\dot{m}''$ as compared to moderate $\dot{m}''$. Meanwhile, for high $\dot{m}''$, $T_{avg,surf}$ was smaller at any $q''_{total,fin}$ as compared to moderate $\dot{m}''$ associated with smaller increment of $q''_{total,fin}$ as depicted in Figure 4.1. Also, for the high $\dot{m}''$, the change of

trend of $q''_{total,fin}$ began much earlier than Δt_{fb} of -5.8 ms while close to about Δt_{fb} of -5.8 ms for the moderate $\dot{m}''$.

The observation from the heat distribution and transient heat transfer for high $\dot{m}''$ of 389 kg/m^2 s at Δt_{fb} about -5.8 ms as observed in Figure 4.8a and Figure 4.1 is due to the slow heating process. For high $\dot{m}''$ of 389 kg/m^2 s, the heating process is slower than the moderate $\dot{m}''$ of 265 kg/m^2 s, and therefore the thermal boundary layer is thinner. With the more gradual heating process, the high $\dot{m}''$ requires longer Δt_{fb} for the bubble nucleation and the increment of $q''_{total,fin}$ was less rapid for high $\dot{m}''$ as compared to the moderate $\dot{m}''$. Also, the susbtantial $\dot{m}''$ possesses the earlier change of trend of $q''_{total,fin}$ before Δt_{fb} about -5.8 ms associated with the more previous development of nucleate boiling characteristic as compared to the moderate $\dot{m}''$. Therefore, at Δt_{fb} about -5.8 ms, for the high $\dot{m}''$, the nucleate boiling characteristic halfway developed whereas the development was just near to initial stage for the moderate $\dot{m}''$. Consequently, at Δt_{fb} about -5.8 ms, the peaks were relatively higher in magnitude for the high $\dot{m}''$ as compared to the moderate $\dot{m}''$. Meanwhile, from the low to moderate $\dot{m}''$, the region with $q''^{*}_{local,bottom,pc}$ below $q''^{*}_{local,bottom,fc}$ was smaller due to the slower heating process to generate the liquid-vapour mixture inhibiting the heat transfer.

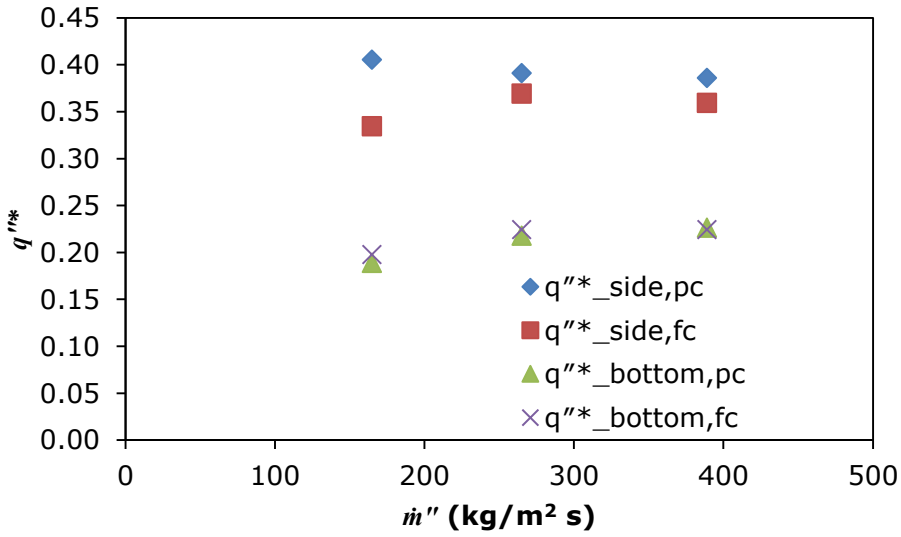
For high $\dot{m}''$ of 389 kg/m^2 s, when Δt_{fb} reached about -2.9 ms as shown in Figure 4.8b from Δt_{fb} about -5.8 ms as illustrated in Figure 4.8a, the peaks developed towards upstream with slightly larger magnitude. However, the change was less significant from Δt_{fb} of -5.8 to -2.9 ms for $\dot{m}''$ of 389 kg/m^2 s as compared to $\dot{m}''$ of 265 kg/m^2 s. Also, high $\dot{m}''$ possessed smaller $T_{avg,surf}$ with the less rapid increment of $q''_{total,fin}$ as compared to moderate $\dot{m}''$ as illustrated in Figure 4.1. These occurrences induce the lesser amount of ascending and descending flows for high $\dot{m}''$, producing less rapid development of nucleate boiling characteristic as compared to moderate $\dot{m}''$. Moreover, for high $\dot{m}''$, the heating process is slower with the thinner thermal boundary layer as compared to moderate $\dot{m}''$. Meanwhile, for high $\dot{m}''$, the increment of regions with $q''^{*}_{local,bottom,pc}$ below $q''^{*}_{local,bottom,fc}$ was lesser from Δt_{fb} about -5.8 to -2.9 ms as compared to moderate $\dot{m}''$. However, these regions at high $\dot{m}''$ were smaller than $\dot{m}''$ of 265 kg/m^2 s associated with the slower heating process, creating the lesser liquid-vapour mixture.

With the local peripheral average heat transfer components along x^* from Figure 4.6 to Figure 4.8, the average heat transfer components are attainable for different $\dot{m}''$ at different Δt_{fb} as illustrated in Figure 4.9. The average heat transfer components are presentable in the non-dimensional term of q''^* which stands for $q''/q''_{total,fin}$. q''^* comprises of $q''^{*}_{side,pc}$, $q''^{*}_{side,fc}$, $q''^{*}_{bottom,pc}$, $q''^{*}_{bottom,fc}$ which are $q''_{side,pc}/$

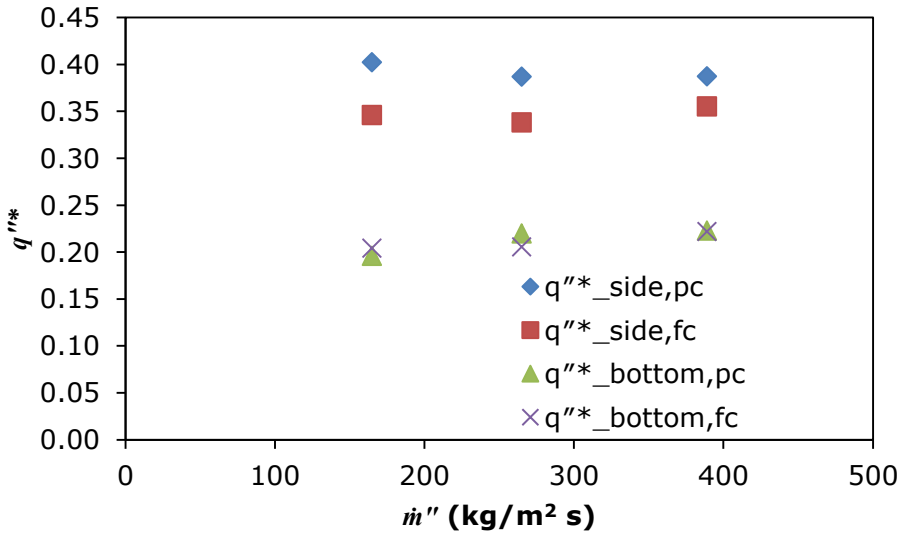
$q''_{total,fin}$, $q''_{side,fc}/q''_{total,fin}$, $q''_{bottom,pc}/q''_{total,fin}$, and $q''_{bottom,fc}/q''_{total,fin}$, respectively. $q''_{side,pc}$ and $q''_{side,fc}$ represent the heat transfer with and without phase change, respectively, at the side surface in the micro-channel. On the other hand, $q''_{bottom,pc}$ and $q''_{bottom,fc}$ represent the heat transfer with and without phase change, respectively, at the bottom surface in the micro-channel. By obtaining these local peripheral average heat transfer components, the overall heat transfer contribution due to phase change is identifiable.

For low $\dot{m}''$ of 165 kg/m^2 s at about Δt_{fb} of -5.8 ms, the increment of $q''^{*}_{side,pc}$ from $q''^{*}_{side,fc}$ was apparent as depicted in Figure 4.9a. Also, the increment of $q''^{*}_{side,pc}$ from $q''^{*}_{side,fc}$ for the low $\dot{m}''$ was more significant than moderate $\dot{m}''$ of 265 kg/m^2 s. Meanwhile, $q''^{*}_{bottom,pc}$ was close to but slightly lower than $q''^{*}_{bottom,fc}$ for both the low and moderate $\dot{m}''$ of 165 and 265 kg/m^2 s, respectively. At the high $\dot{m}''$, the increment of $q''^{*}_{side,pc}$ from $q''^{*}_{side,fc}$ became slightly more substantial than the lower $\dot{m}''$. Meanwhile, $q''^{*}_{bottom,pc}$ was almost identical to $q''^{*}_{bottom,fc}$ at high $\dot{m}''$ of 389 kg/m^2 s.

When Δt_{fb} reached about -2.9 ms as shown in Figure 4.9b, the increment of $q''^{*}_{side,pc}$ from $q''^{*}_{side,fc}$ for low $\dot{m}''$ of 165 kg/m^2 s dropped from Δt_{fb} about -5.8 ms illustrated in Figure 4.9a. Meanwhile, for the low $\dot{m}''$, $q''^{*}_{bottom,pc}$ retained close to but slightly lower than $q''^{*}_{bottom,fc}$. At moderate $\dot{m}''$ of 265 kg/m^2 s at Δt_{fb} about -2.9 ms, increment of $q''^{*}_{side,pc}$ from $q''^{*}_{side,fc}$ was significantly larger as compared to Δt_{fb} about -5.8 ms. Meanwhile, the slight increment of $q''^{*}_{bottom,pc}$ from $q''^{*}_{bottom,fc}$ was also evident. At high $\dot{m}''$ at Δt_{fb} about -2.9 ms, the increment of $q''^{*}_{side,pc}$ from $q''^{*}_{side,fc}$ was slightly higher than Δt_{fb} about -5.8 ms. Meanwhile, $q''^{*}_{bottom,pc}$ retained almost close to $q''^{*}_{bottom,fc}$ at high $\dot{m}''$ at about Δt_{fb} of -2.9 ms. For each $\dot{m}''$, the increment of $q''^{*}_{side,pc}$ from $q''^{*}_{side,fc}$ was more substantial than the increment of $q''^{*}_{bottom,pc}$ from $q''^{*}_{bottom,fc}$. This occurrence is mainly due to the more significant ascending and descending flows facilitating the transient conduction as the side surface as compared to the bottom surface at each $\dot{m}''$. Also, at each $\dot{m}''$, the more massive amount of liquid-vapour mixture is accumulating on the bottom surface and impeding the heat transfer.



(a)



(b)

Figure 4.9: q''^* against $\dot{m}''$ at q_b'' 1561 kW/m² and T_{in} of 23°C at Δt_{fb} about (a) −5.8 and (b) −2.9 ms

The following part of the study is to evaluate the overall heat transfer enhancement from phase change through h^* ($(h_{pc} - h_{fc})/h_{fc}$) for different $\dot{m}''$ at Δt_{fb} about −5.8 and −2.9 ms as plotted in Figure 4.10. When applied low $\dot{m}''$ of 165 kg/m² s, h^* was relatively high at Δt_{fb} about −5.8 ms. The larger h^* is mainly as a result of the ascending and descending flows facilitating the transient heat transfer, indicating more significant nucleate boiling characteristic at the low $\dot{m}''$ at about Δt_{fb} of −5.8 ms. Then, h^* slightly dropped when Δt_{fb} reached about −2.9 ms at the low

$\dot{m}''$. h^* dropped at Δt_{fb} about -2.9 ms mainly due to the relatively more considerable amount of liquid-vapour mixture that caused the slightly lesser amount of peaks as compared to Δt_{fb} about -5.8 ms. When employed moderate $\dot{m}''$ of 265 kg/m^2 s, h^* was low at Δt_{fb} about -5.8 ms and then significantly rose when Δt_{fb} reached about -2.9 ms and higher than h^* at the low $\dot{m}''$. Therefore, for the moderate $\dot{m}''$, h^* increased rapidly with Δt_{fb} by triggering more ascending and descending flows facilitating transient conduction, implying the significant development of nucleate boiling characteristic before bubble nucleation. For high $\dot{m}''$ of 389 kg/m^2 s, h^* was relatively higher than the moderate $\dot{m}''$ at about Δt_{fb} of -5.8 ms and slightly increased when Δt_{fb} reached -2.9 ms. This occurrence is due to the slow heating process with thin thermal boundary layer at the high $\dot{m}''$, leading to the less rapid development of nucleate boiling characteristic.

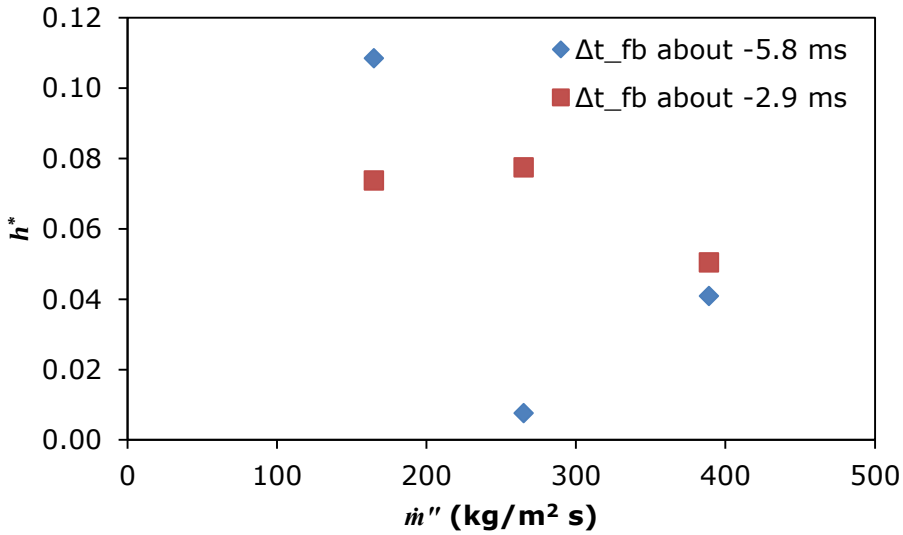


Figure 4.10: h^* against $\dot{m}''$ at q_b'' 1561 kW/m^2 and T_{in} of 23°C at Δt_{fb} about -5.8 and -2.9 ms

4.4 Effects of Mass Fluxes during Flow Boiling

Once completed addressing the effects of $\dot{m}''$ on the local and average heat transfer and heat transfer enhancement before flow boiling, the investigation proceeded with these effects during flow boiling. When flow boiling occurs, the heating surface involves heat transfer towards liquid and vapour associated with the expression of $q''_{total,fin}$ as:

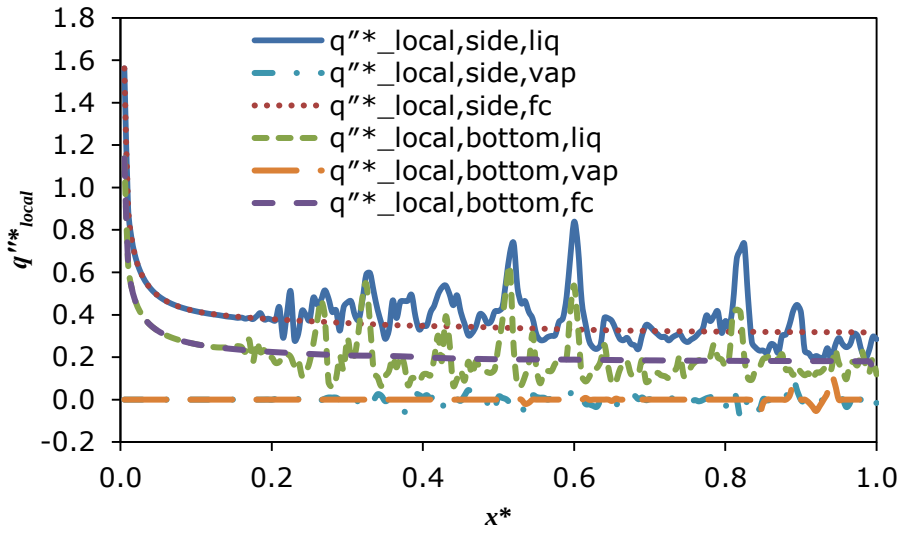
$$q''_{total,fin} = \frac{q_{liq}}{A_{surf}} + \frac{q_{vap}}{A_{surf}} = q''_{liq} + q''_{vap} \tag{4.1}$$

Since $q''_{total,fin}$ involves heat flux components of q''_{liq} and q''_{vap}, the exploration of the local peripheral average distribution of q''_{liq} and q''_{vap} at the side and bottom

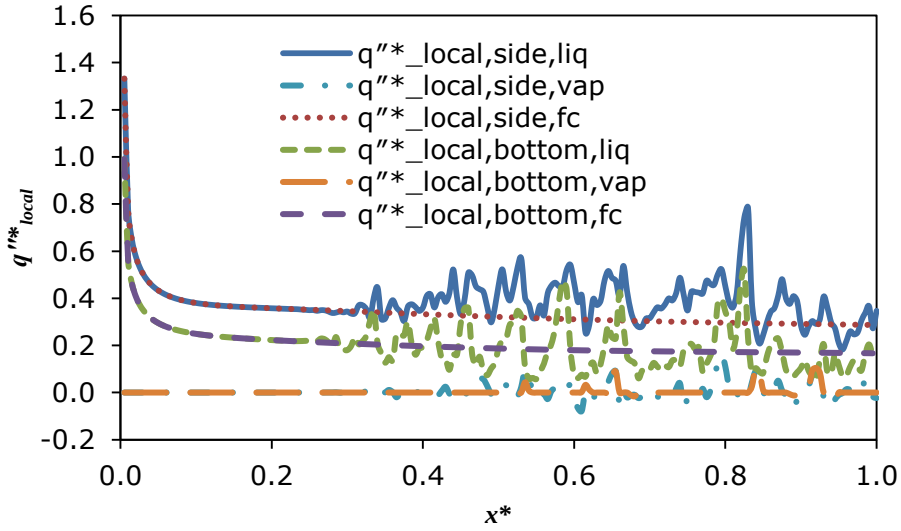
surfaces along the channel are necessary. The local peripheral average q''_{liq} and q''_{vap} at the side surfaces are $q''_{local,side,liq}$ and $q''_{local,side,vap}$, respectively. On the other hand, the local q''_{liq} and q''_{vap} at bottom surface are $q''_{local,bottom,liq}$ and $q''_{local,bottom,vap}$, respectively. Adding $q''_{local,side,liq}$, $q''_{local,side,vap}$, $q''_{local,bottom,liq}$, and $q''_{local,bottom,vap}$ at each location is equivalent to q''_{local}. The local heat transfer are presentable through a non-dimensional term of q''^{*}_{local} which is $q''_{local}/q''_{total,fin}$. Meanwhile, dividing the local heat transfer components of $q''_{local,side,liq}$, $q''_{local,side,vap}$, $q''_{local,bottom,liq}$, and $q''_{local,bottom,vap}$ by $q''_{total,fin}$ give the non-dimensional terms of $q''^{*}_{local,side,liq}$, $q''^{*}_{local,side,vap}$, $q''^{*}_{local,bottom,liq}$, and $q''^{*}_{local,bottom,vap}$, respectively. The heat transfer enhancement of flow boiling at the side surfaces is observable by comparing $q''^{*}_{local,side,liq}$ and $q''^{*}_{local,side,vap}$ with $q''^{*}_{local,side,fc}$. $q''^{*}_{local,side,fc}$ is a non-dimensional component referring to $q''_{local,side,fc}/q''_{total,fin}$, and $q''_{local,side,fc}$ is the local heat flux at side surface without phase change. On the other hand, the heat transfer improvement from flow boiling at the bottom surface is approachable by comparing $q''^{*}_{local,bottom,liq}$ and $q''^{*}_{local,bottom,vap}$ with $q''^{*}_{local,bottom,fc}$. $q''^{*}_{local,bottom,fc}$ is a non-dimensional component representing $q''_{local,bottom,fc}/q''_{total,fin}$, and $q''_{local,bottom,fc}$ is the local heat flux at bottom surface without phase change.

The local heat transfer of flow boiling along x^{*} at Δt_{fb} about 10 ms at the side and bottom surfaces for different $\dot{m}''$ is evident in Figure 4.11. Also, the regions with $q''^{*}_{local,side,liq}$ below $q''^{*}_{local,side,fc}$ were lesser than the regions with $q''^{*}_{local,bottom,liq}$ below $q''^{*}_{local,bottom,fc}$ for each $\dot{m}''$. At each $\dot{m}''$, amount and magnitude of peaks of $q''^{*}_{local,side,liq}$ were relatively higher than $q''^{*}_{local,bottom,liq}$. This occurrence is due to the more substantial amount of liquid-vapour mixture covering the bottom surface with larger ΔT_{sup}, suppressing the heat transfer as compared to the side surfaces for each $\dot{m}''$.

However, from low to high $\dot{m}''$ of 165 to 389 kg/m^2 s, the regions with peaks of $q''^{*}_{local,side,liq}$ and $q''^{*}_{local,bottom,liq}$ began closer towards the downstream as shown in Figure 4.11. Also, from the low to high $\dot{m}''$, the number and magnitude of the peaks became more significant. Meanwhile, from the low to high $\dot{m}''$, the regions with $q''^{*}_{local,bottom,liq}$ below than $q''^{*}_{local,bottom,fc}$ extended lesser from the downstream towards the upstream of the bottom surface. These occurrences are due to the thinner thermal boundary layer and the smaller amount of liquid-vapour mixture for the ascending and descending flows enhancing the heat transfer at side surfaces for higher $\dot{m}''$. Also, from the low to high $\dot{m}''$, the number and magnitude of the peaks became more substantial.

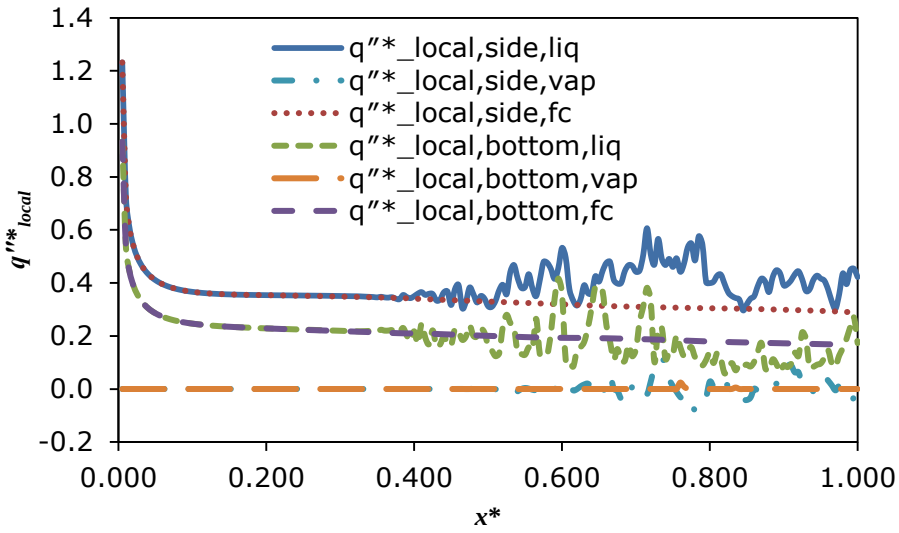


(a)



(b)

(Continued next page)



(c)

Figure 4.11: q''^{*}_{local} along x^{*} for $\dot{m}''$ of (a) 165, (b) 265, and (c) 389 kg/m² s at q''_b of 1561 kW/m² and T_{in} of 23°C at Δt_{fb} about 10 ms

Meanwhile, at each $\dot{m}''$ as shown in Figure 4.11, the regions with $q''^{*}_{local,side,vap}$ below zero was evident and some small peaks of $q''^{*}_{local,side,vap}$ above zero emerged. Also, these regions and peaks were more than the areas with $q''^{*}_{local,bottom,vap}$ below zero and the peaks of $q''^{*}_{local,side,vap}$. This incidence coincides with the observation from Federov and Viskanta [138]. They [138] observed that the heat at first comes from bottom surface with least convective resistance. Then, the heat passes through the fluid and enters into the substrate at side surfaces of corners instead of transferring to the bulk fluid. This process leads to the formation of more vortexes of heat at the side surface near the corners as compared to the bottom surface. Subsequently, at the side surface near the corners, the local negative heat fluxes in which heat transferred from the fluid to the solid is more than the bottom surface. This incidence becomes more apparent in the vapour phase mostly forming near to the corners as compared to the liquid phase for each $\dot{m}''$ in this study. When $\dot{m}''$ increased, the peaks of $q''_{local,side,vap}$ and the regions with negative heat fluxes of $q''^{*}_{local,side,vap}$ reduced and began closer to the downstream. Meanwhile, when increased $\dot{m}''$, changes of $q''^{*}_{local,side,vap}$ and $q''^{*}_{local,bottom,vap}$ became less significant due to the thinner thermal boundary layer. In general, both $q''^{*}_{local,side,vap}$ and $q''^{*}_{local,bottom,vap}$ in most regions with phase change were close to 0 for each $\dot{m}''$ due to the low conductivity of the vapour phase.

Based on local peripheral average heat flux components, the corresponding average values for each $\dot{m}''$ at Δt_{fb} about 10 ms are identifiable as depicted in Figure 4.12. In Figure 4.12, when $\dot{m}''$ increased, the increment of $q''^{*}_{side,liq}$ from $q''^{*}_{side,fc}$

was relatively higher. This occurrence is mainly due to the more intensive ascending and descending flows enhancing the heat transfer. On the other hand, $q''^{*}_{bottom,liq}$ was almost close to $q''^{*}_{bottom,fc}$ for each $\dot{m}''$. This incidence is due to the more massive liquid-vapour mixture on the bottom surface for each $\dot{m}''$ inhibiting the heat transfer. On the other hand, both $q''^{*}_{side,vap}$ and $q''^{*}_{bottom,vap}$ were almost close to zero for each $\dot{m}''$ due to the weak thermal conductivity of the vapour phase.

This study continued to access the overall heat transfer enhancement of h^{*} for different $\dot{m}''$ at Δt_{fb} about 10 ms. When $\dot{m}''$ increased, h^{*} increased as shown Figure 4.13 with the higher increment of $q''^{*}_{side,liq}$ from $q''^{*}_{side,fc}$ during flow boiling as illustrated in Figure 4.12. The larger h^{*} presents with the formation of more massive ascending and descending flows with transient conduction, indicating the more substantial development of nucleate boiling characteristic.

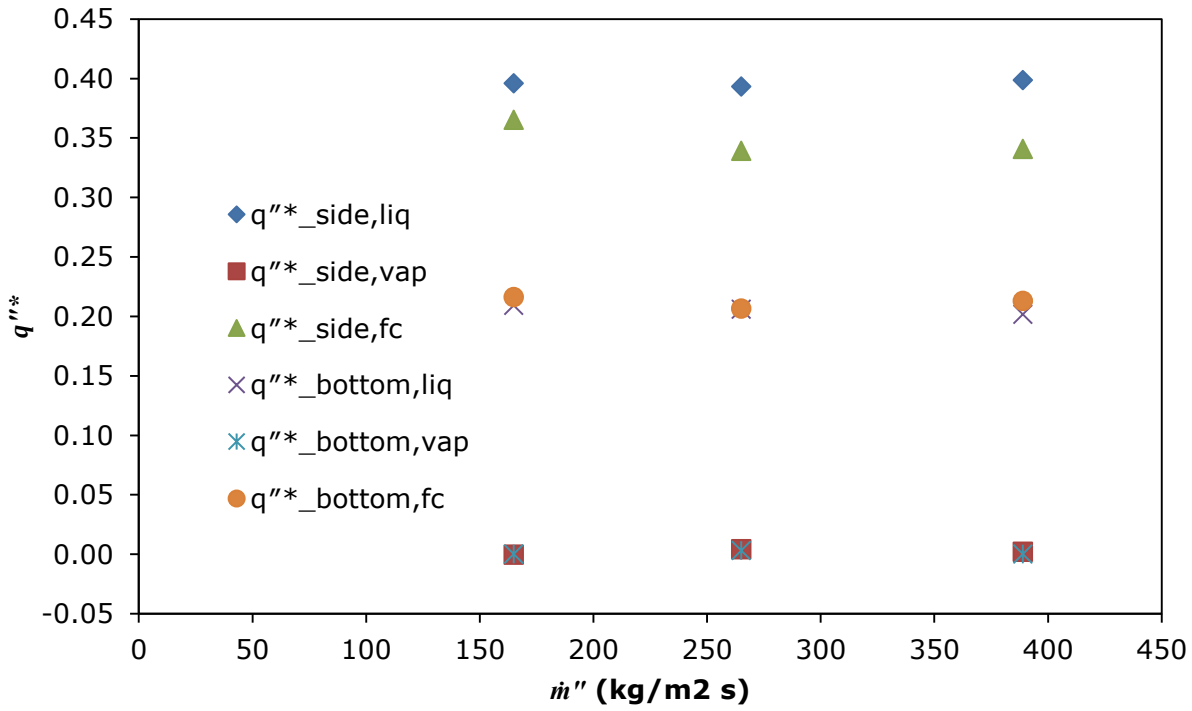


Figure 4.12: q''^{*} against $\dot{m}''$ at q''_b of 1561 kW/m² and T_{in} of 23°C at Δt_{fb} about 10 ms

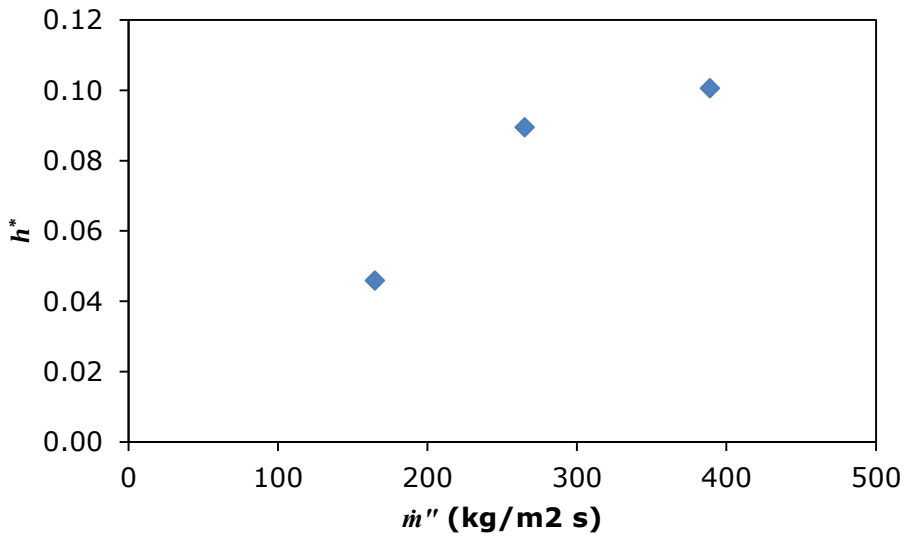


Figure 4.13: h^* against $\dot{m}''$ at q_b'' of 1561 kW/m^2 and T_{in} of 23°C at Δt_{fb} about 10 ms

4.5 Location of Bubble Nucleation for Different Mass Fluxes

Once completed accessing the heat transfer, the next section of the study is to examine the location of bubble nucleation within the cross-section during flow boiling for different $\dot{m}''$. The site of bubble nucleation includes the corner, side and bottom within the cross-section of the micro-channel.

When $\dot{m}''$ increased, the number of bubbles reduced as evident in Figure 4.14 during flow boiling at about Δt_{fb} of 10 ms due to the thinner thermal boundary layer impeding the bubble nucleation. The bubbles mainly nucleated at the corner while few bubbles nucleated at side surfaces and none of the bubble nucleated at the bottom surface for each $\dot{m}''$. For each $\dot{m}''$, the bubbles nucleated the most at the corners since the corners possess the characteristic of nucleation site, facilitating for the bubble nucleation. Meanwhile, for each $\dot{m}''$, more bubble nucleated at the side surfaces due to the larger amount of the heat conduction as compared to the bottom surface.

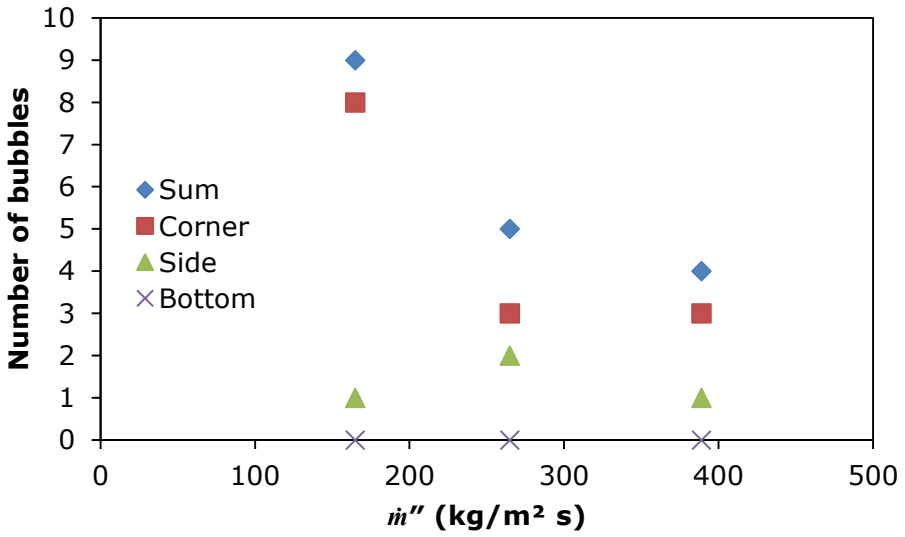
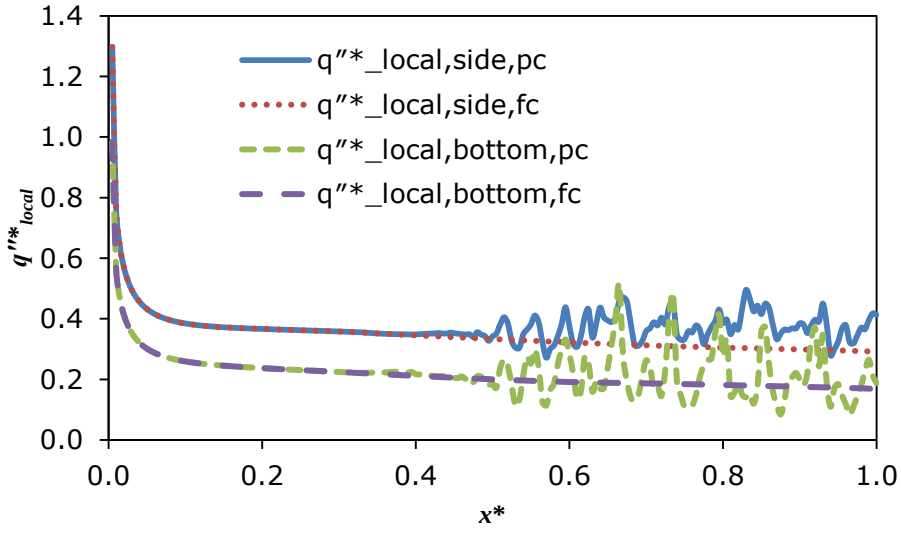


Figure 4.14: Location of bubble nucleation against $\dot{m}''$ at q_b'' of 1561 kW/m² and T_{in} of 23°C at Δt_{fb} within 0 and 10 ms

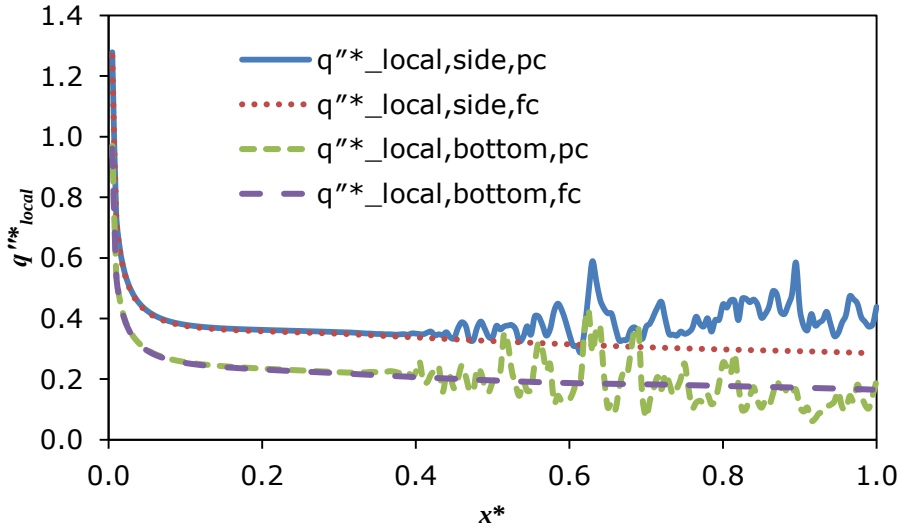
4.6 Effects of Heat Fluxes before Flow Boiling

Attempted the evaluation of effects of $\dot{m}''$, the study proceeded with the examination of the impacts of q_b'' on the local and average heat transfer and heat transfer enhancement before flow boiling. The local and average heat transfer components observed for different q_b'' helps to explain the trends of transient heat transfer data in Figure 4.2.

The local heat transfer components for different q_b'' are observable from $q_{local}''^*$ for each component along x^* as illustrated in Figure 4.8 and from Figure 4.15 to Figure 4.18. From Figure 4.8 and from Figure 4.15 to Figure 4.18, q_b'' is from 1561 to 3197 kW/m² at $\dot{m}''$ of 389 kg/m² s and T_{in} of 23°C at about Δt_{fb} of −5.8 ms and −2.9 ms. For each q_b'' at about Δt_{fb} of -5.8 and -2.9 ms, the peaks of $q_{local,side,pc}''^*$ and $q_{local,bottom,pc}''^*$ rose above $q_{local,side,fc}''^*$ and $q_{local,bottom,fc}''^*$, respectively. However, the peaks of $q_{local,side,pc}''^*$ were relatively more than $q_{local,bottom,pc}''^*$ for each q_b''. Meanwhile, for each q_b'', the regions with $q_{local,bottom,pc}''^*$ below $q_{local,bottom,fc}''^*$ were more than the regions with $q_{local,side,pc}''^*$ below $q_{local,side,fc}''^*$. These peaks and regions $q_{local,bottom,pc}''^*$ below $q_{local,bottom,fc}''^*$ became greater and began further towards the downstream from Δt_{fb} of −5.8 ms and −2.9 ms for each q_b''. These occurrences are observable when varying $\dot{m}''$ as evident in Section 4.3.

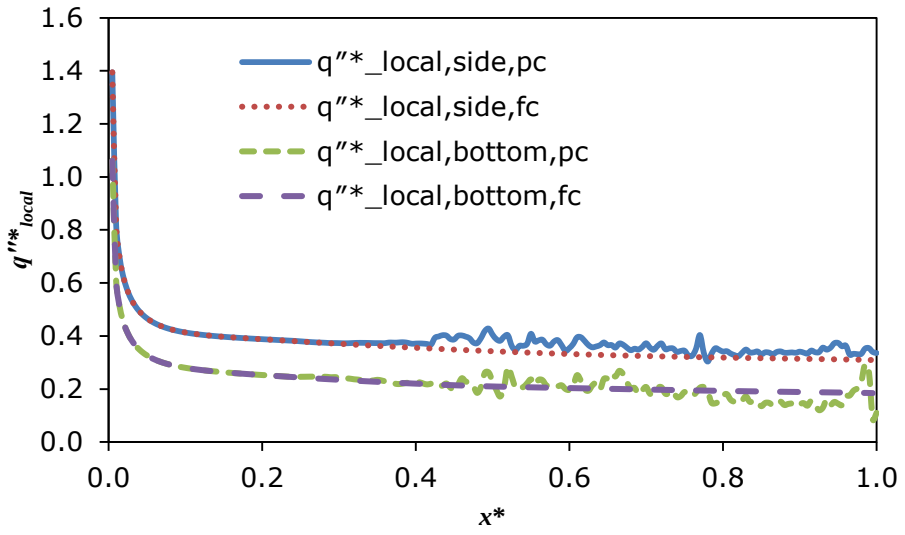


(a)

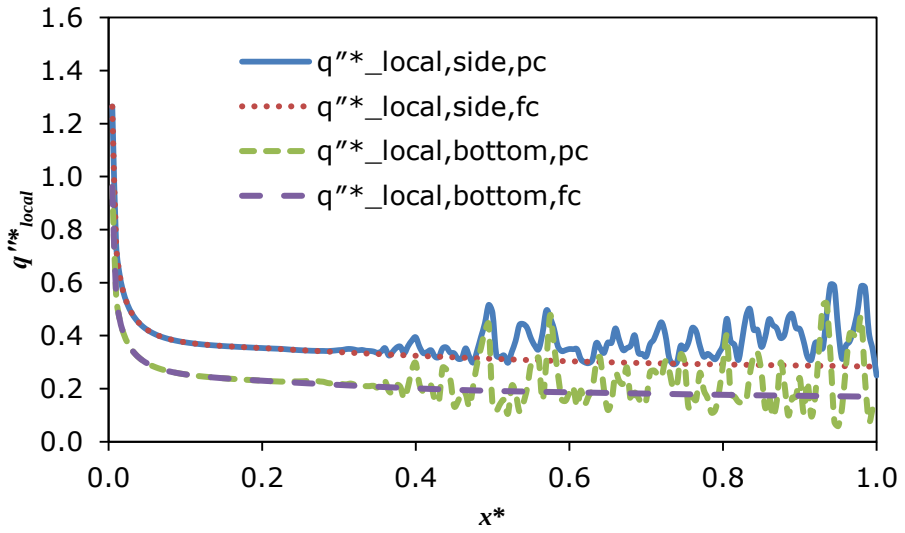


(b)

Figure 4.15: q''^{*}_{local} along x^{*} for q''_b of 1691 kW/m² at $\dot{m}''$ of 389 kg/m² s and T_{in} of 23°C at Δt_{fb} about (a) −5.8 and (b) −2.9 ms

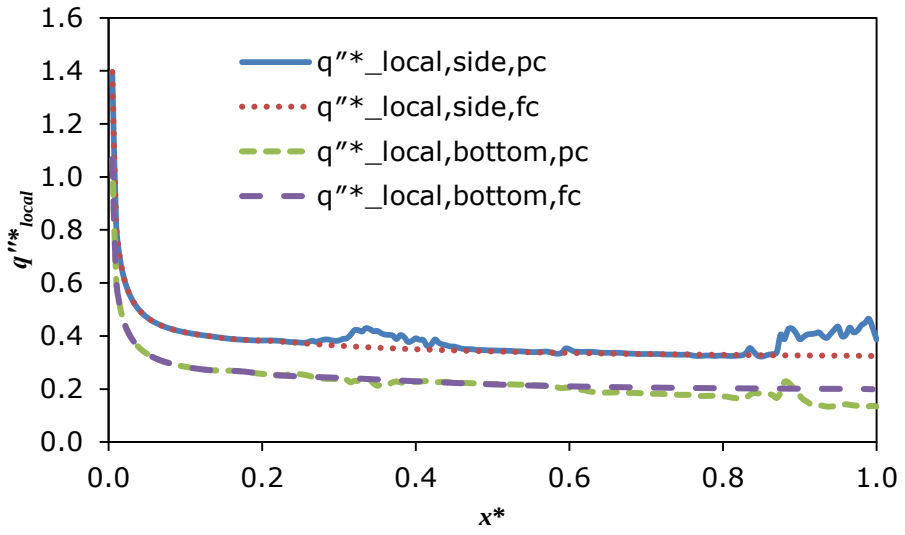


(a)

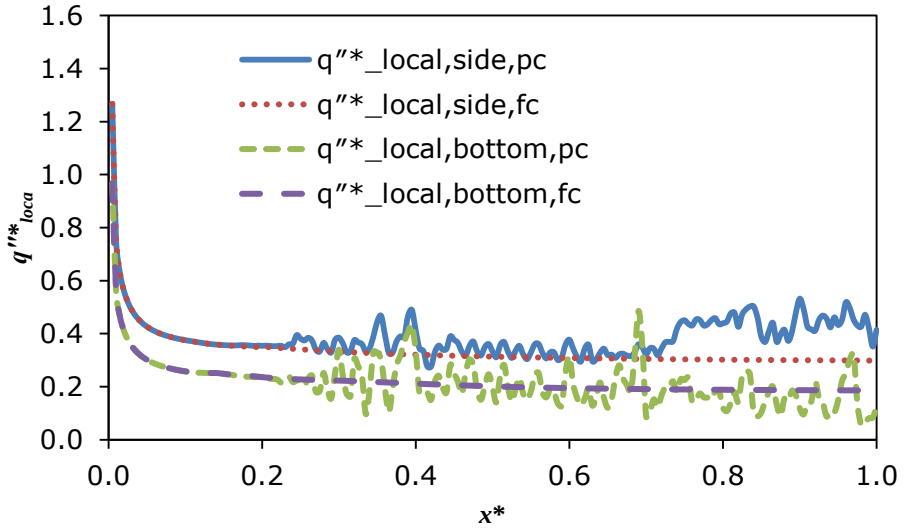


(b)

Figure 4.16: q''^*_{local} along x^* for q''_b of 2030 kW/m² at $\dot{m}''$ of 389 kg/m² s and T_{in} of 23°C at Δt_{fb} about (a) −5.8 and (b) −2.9 ms

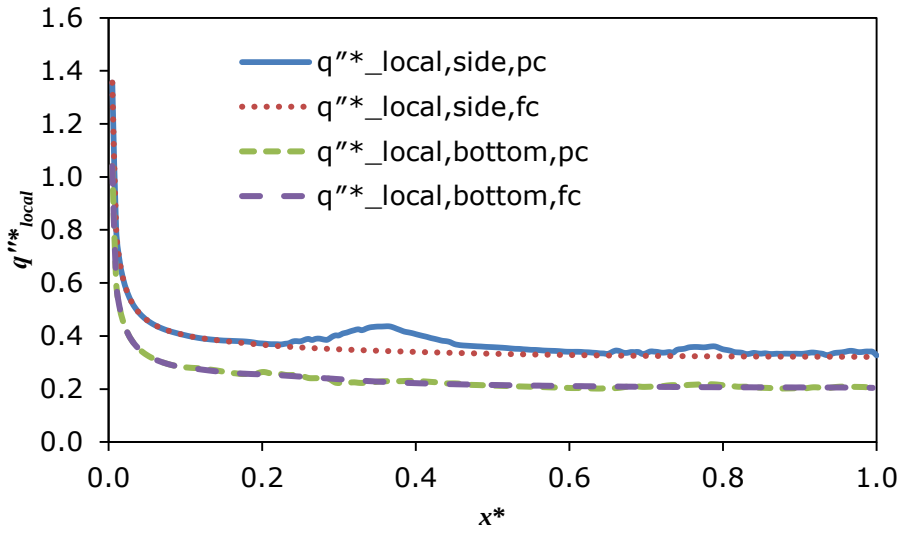


(a)

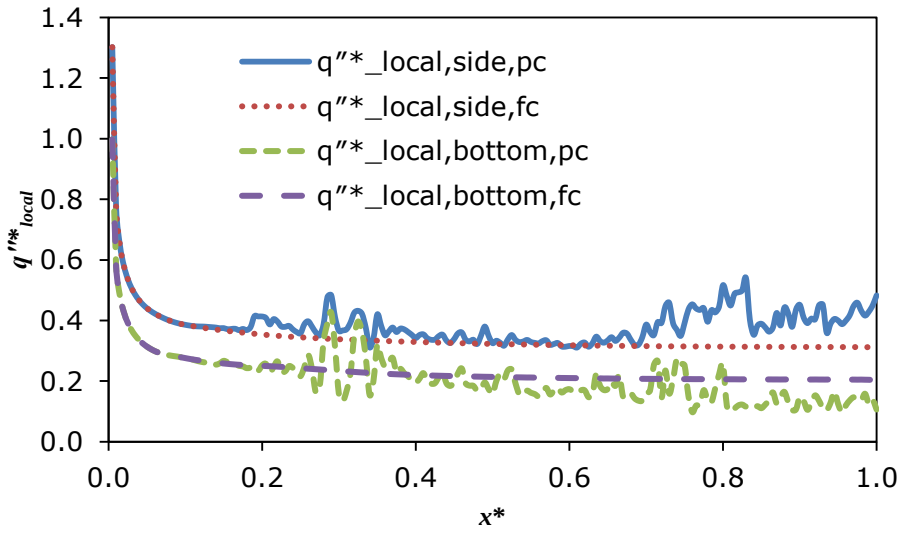


(b)

Figure 4.17: q''^{*}_{local} along x^{*} for q''_b of 2706 kW/m² at $\dot{m}''$ of 389 kg/m² s and T_{in} of 23°C at Δt_{fb} about (a) −5.8 and (b) −2.9 ms



(a)



(b)

Figure 4.18: q''^{*}_{local} along x^{*} for q''_b of 3197 kW/m² at $\dot{m}''$ of 389 kg/m² s and T_{in} of 23°C at Δt_{fb} about (a) −5.8 and (b) −2.9 ms

When increased q''_b from 1561 to 3197 kW/m² as depicted in Figure 4.8 and from Figure 4.15 to Figure 4.18, the onset of peaks of $q''^{*}_{local,side,pc}$ and $q''^{*}_{local,bottom,pc}$ moved towards upstream. From low to moderate q''_b of 1561 to 2706 kW/m², at about Δt_{fb} of −5.8 ms, the peaks became relatively lower in magnitudes. Meanwhile, from the low to moderate q''_b, the increment of $q''_{total,fin}$ also became less significant as illustrated in Figure 4.2. This incidence implies the lesser significance of nucleate boiling characteristic from the low to moderate q''_b. Also, from the small to moderate

q_b'', regions with $q''^*_{local,bottom,pc}$ below $q''^*_{local,bottom,fc}$ became lesser with the lower magnitude. These occurrences are mainly due to the thinner thermal boundary layer extending more towards the inlet from the low to moderate q_b''. As a result, from the small to moderate q_b'' at about Δt_{fb} of -5.8 ms, the ascending and descending flows became less intense. The less substantial ascending and descending flows cause the lesser magnitudes of peaks and lower occupancy of the liquid-vapour mixture reducing the regions with $q''^*_{local,bottom,pc}$ below $q''^*_{local,bottom,fc}$ from the low to moderate q_b''.

At moderate q_b'' of 2706 kW/m^2 at Δt_{fb} about -5.8 ms, the peaks of $q''^*_{local,side,pc}$ formed over broad regions of x^* of 0.3-0.4 as shown in Figure 4.17a. This occurrence is due to the sufficiently high ΔT_{sup} at side surfaces to induce the ascending and descending flows as evident in Figure 4.19.

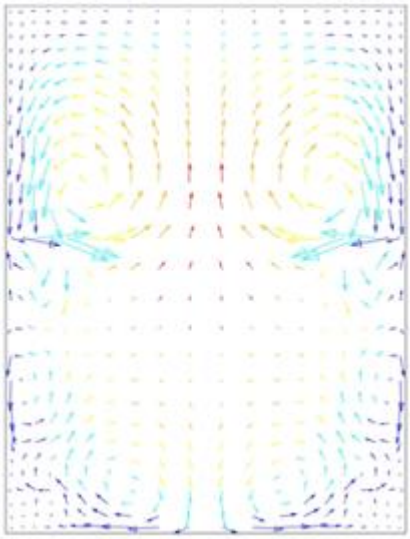


Figure 4.19: Ascending and descending flows formed from side surfaces

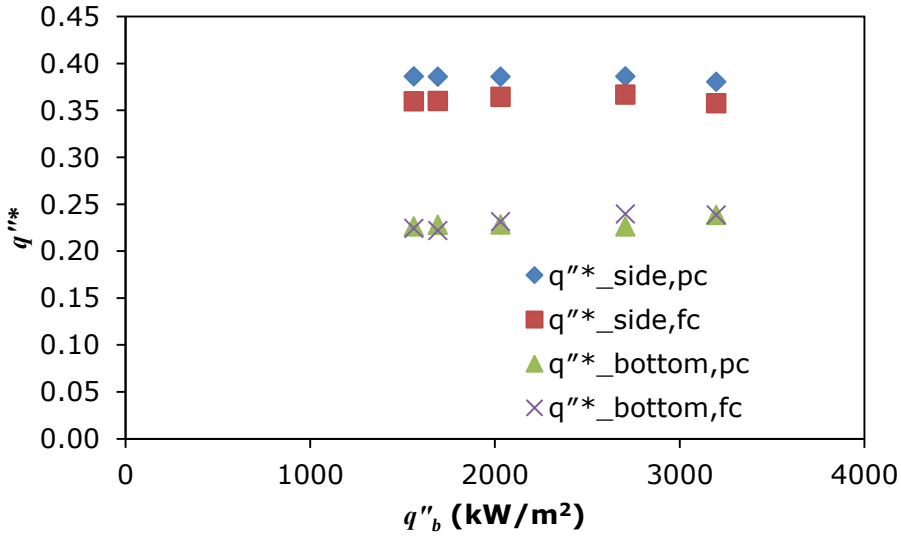
At Δt_{fb} about -2.9 ms, from low to moderate q_b'' of 1561 to 2706 kW/m^2, the amount and magnitude of peaks of increased significantly as evident in Figure 4.8b and from Figure 4.15b to Figure 4.17b. The significant increase of the number of peaks occurring with the more considerable rise of $q''_{total,fin}$ from low to moderate q_b'' of 1561 to 2706 kW/m^2 when Δt_{fb} reached about -2.9 ms from -5.8 ms shown in Figure 4.2. Therefore, the significant increase of peaks from the low to moderate q_b'' when Δt_{fb} reached -2.9 ms from -5.8 ms induces more rapid development of nucleate boiling characteristic. Also, from the small to moderate q_b'', when Δt_{fb} reached about of -2.9 ms from -5.8 ms, the regions with $q''^*_{local,bottom,pc}$ below $q''^*_{local,bottom,fc}$ became more extensive. This incidence is due to the more rapid rise and the substantial amount of heat entering into the micro-channel generating more liquid-vapour mixture impeding the heat transfer.

When applied high q_b'' of 3197 kW/m^2 at Δt_{fb} about −5.8 ms as depicted in Figure 4.18a, two peaks of $q''^*_{local,side,pc}$ as encountered at moderate q_b'' of 2706 kW/m^2 emerged as illustrated in Figure 4.17a. These peaks formed at x^* of 0.2-0.5 and 0.7-0.8 for the high q_b'' at about Δt_{fb} of −5.8 ms. However, the peaks at x^* of 0.2-0.5 for the high q_b'' was broader than the peaks at x^* of 0.3-0.4 for q_b'' of 2706 kW/m^2 as shown in Figure 4.17a. This presence is due to the relatively larger ΔT_{sup} at side surfaces at the big q_b'' facilitating larger ascending and descending flows as compared to the moderate q_b''. At x^* of 0.2-0.5 for the high q_b'', the ascending and descending flows formed from the side surfaces were at the similar pattern as shown in Figure 4.19. Meanwhile, at the high q_b'', $q''^*_{local,bottom,pc}$ was almost close to $q''^*_{local,bottom,fc}$ due to the small thermal boundary layer causing insignificant activation of the ascending and descending flows. Also, with the thin thermal boundary layer, the amount of the liquid-vapour mixture is less significant for the high q_b'' as compared to lower q_b''. With these occurrences, the nucleate boiling characteristic becomes less significant at such high q_b'' at about Δt_{fb} of −5.8 ms.

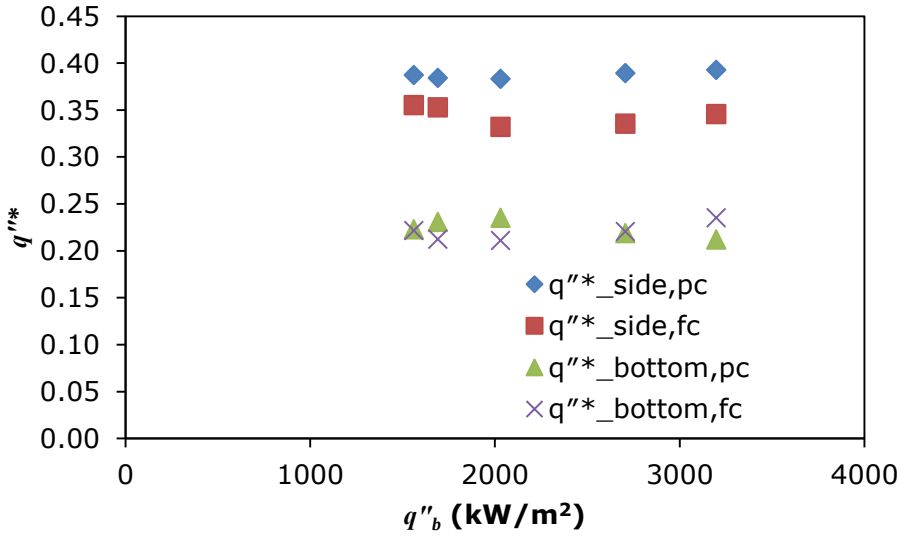
When Δt_{fb} reached about −2.9 ms for high q_b'' of 3197 kW/m^2, the peaks of $q''^*_{local,side,pc}$ became more significant as compared to Δt_{fb} at about −5.8 ms as shown in Figure 4.18b. At about and $q''^*_{local,bottom,pc}$ Meanwhile, at the high q_b'', the increment of $q''_{total,fin}$ was lesser with the more elevated $T_{avg,surf}$ as compared to the moderate q_b'' from Δt_{fb} about −5.8 ms to −2.9 ms as depicted in Figure 4.2. These occurrences are as a result of the more rapid heating process at the high q_b'' generating the larger amount of liquid-vapour mixture suppressing the heat transfer with the less significant nucleate boiling characteristic. However, more regions with $q''^*_{local,bottom,pc}$ lower than $q''^*_{local,bottom,pc}$ formed for the high q_b'' as compared to the moderate q_b''. Meanwhile, the massive q_b'' possessed lower increment of $q''_{total,fin}$ from Δt_{fb} of −5.8 ms to −2.9 ms as compared to the moderate q_b''. This occurrence is due to the relatively higher amount of liquid-vapour mixture impeding the heat transfer at the large q_b''.

From the local average peripheral heat transfer components, the corresponding average values are approachable for different q_b'' at different Δt_{fb} by plotting q''^* of each heat transfer element as illustrated in Figure 4.20. In general, the increment of $q''^*_{side,pc}$ from $q''^*_{side,fc}$ was larger than the increment of $q''^*_{bottom,pc}$ from $q''^*_{bottom,fc}$ for each q_b''. Meanwhile, for each q_b'', $q''^*_{bottom,pc}$ was almost close to $q''^*_{bottom,fc}$. In Figure 4.20a, at Δt_{fb} about −5.8 ms, the increment of $q''^*_{side,pc}$ from $q''^*_{side,fc}$ was relatively less for each q_b''. Nevertheless, from low to moderate q_b'' of 1561 to 2706 kW/m^2 at Δt_{fb} about −5.8 ms, the increment of $q''^*_{side,pc}$ from $q''^*_{side,fc}$ slightly decreased. On the other hand, the increment of $q''^*_{side,pc}$ from $q''^*_{side,fc}$ slightly increased from moderate q_b'' of 2706 kW/m^2 to high q_b'' of 3197 kW/m^2. When Δt_{fb} reached about −2.9 ms from

−5.8 ms for each q_b'' as shown in Figure 4.20b, the increment of $q_{side,pc}''^*$ from $q_{side,fc}''^*$ became more significant. From low to moderate q_b'' at Δt_{fb} about −2.9 ms, the increment of $q_{side,pc}''^*$ from $q_{side,fc}''^*$ became larger. Meanwhile, increment of $q_{bottom,pc}''^*$ from $q_{bottom,fc}''^*$ increased and then decreased from low to moderate q_b''. When employed high q_b'' of 3197 kW/m^2, the increment of both $q_{side,pc}''^*$ from $q_{side,fc}''^*$ and $q_{bottom,pc}''^*$ from $q_{side,fc}''^*$ reduced. Also, $q_{bottom,pc}''^*$ dropped further from $q_{bottom,fc}''^*$ from moderate to high q_b''.



(a)



(b)

Figure 4.20: q''^* against q_b'' at $\dot{m}''$ of 389 kg/m^2 s and T_{in} of 23°C at Δt_{fb} about (a) −5.8 and (b) −2.9 ms

In overall, according to Figure 4.20, $q''^{*}_{side,pc}$ increased from $q''^{*}_{side,fc}$ was more than the $q''^{*}_{bottom,pc}$ raised from $q''^{*}_{bottom,fc}$ for each q''_b. This presence is mainly due to the more extensive ascending and descending flows, enhancing the heat transfer of the side surfaces as compared to the bottom surface for each q''_b. On the other hand, for each q'', the amount of liquid-vapour mixture accumulating on the bottom surface is more significant as compared to side surfaces and impeding the heat transfer.

This investigation then proceeded with the evaluation of the overall heat transfer enhancement of h^* for different q''_b at different Δt_{fb} as illustrated in Figure 4.21. In Figure 4.21, from low to moderate q''_b of 1561 to 2706 kW/m^2 at about Δt_{fb} of -5.8 ms, h^* reduced. This occurrence is mainly as a result of the thinner thermal boundary layer leading to lesser amount and magnitudes of ascending and descending flows of higher q''_b. From Δt_{fb} about -5.8 ms to -2.9 ms, h^* increased from low to moderate q''_b. From low to moderate q''_b at Δt_{fb} about -2.9 ms, h^* increased with the significantly more intense ascending and descending flows with the significant nucleate boiling characteristic. In overall, from low to moderate q''_b, the trend of h^* decreased with q''_b changed to h^* increased with q''_b when Δt_{fb} increased before flow boiling.

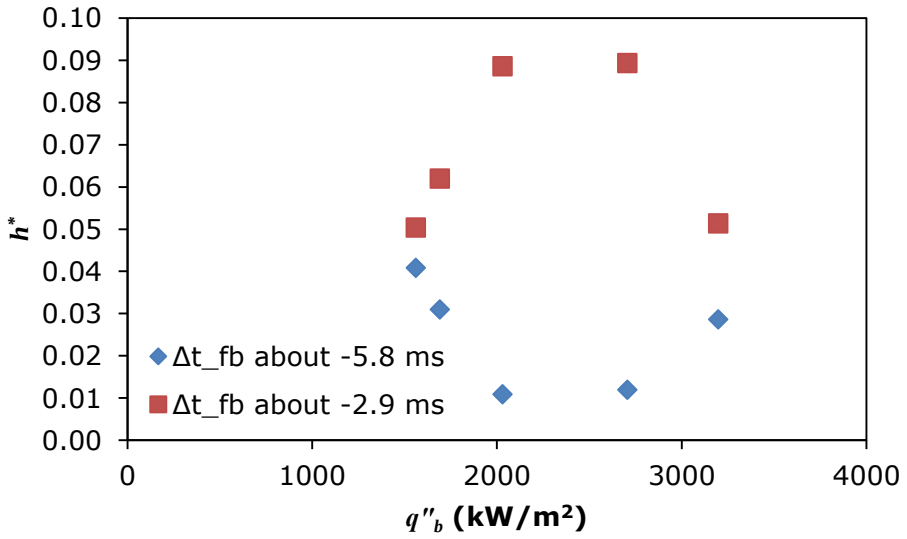


Figure 4.21: h^* against q''_b at $\dot{m}''$ of 389 kg/m^2 s and T_{in} of 23°C at Δt_{fb} about -5.8 and -2.9 ms

When applied high q''_b of 3197 kW/m^2 at about Δt_{fb} of -5.8 ms, h^* increased as illustrated in Figure 4.21. This presence is primarily due to the sufficiently high ΔT_{sup}, causing more intense ascending and descending flows. When Δt_{fb} reached -2.9 ms, h^* for high q''_b increased. From moderate to high q''_b at about Δt_{fb} of -2.9 ms, h^* dropped. This incidence implies the more liquid-vapour mixture that suppressing the heat transfer for high q''_b at about Δt_{fb} of -2.9 ms. From moderate to high q''_b

before flow boiling, the trend of h^* increased with q_b'' changed to h^* decreased with q_b'' when Δt_{fb} before flow boiling increased.

In general, from Figure 4.21, the more substantial h^* leads to that the more significant nucleate boiling characteristic. From low to moderate q_b'', the increment of h^* with Δt_{fb} became more significant, indicating the rapid development of nucleate boiling characteristic. On the other hand, the increase of h^* with Δt_{fb} became smaller from moderate to high q_b'', implying the less rapid development of nucleate boiling characteristic.

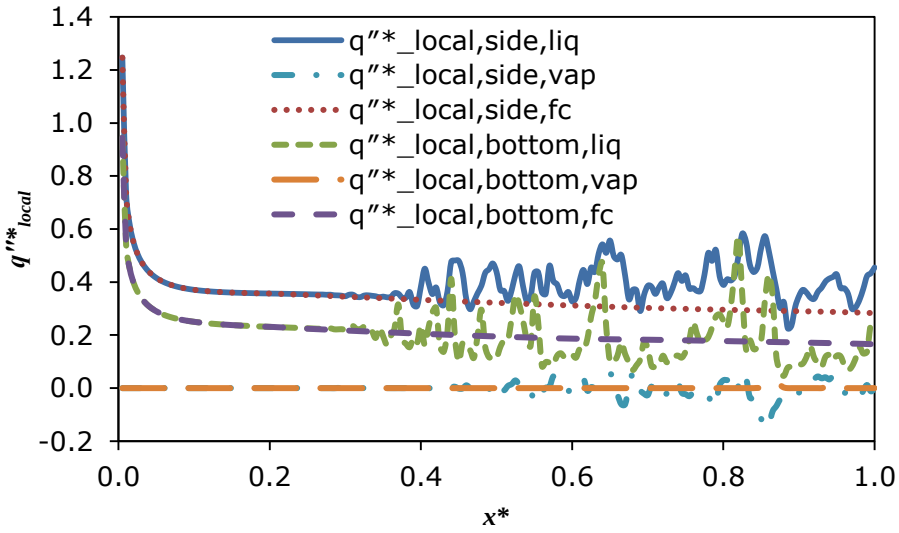
4.7 Effects of Heat Fluxes during Flow Boiling

When finished addressing the effects of q_b'' on the local and average heat transfer enhancement and heat transfer enhancement before flow boiling, the investigation proceeded by examining these changes during flow boiling.

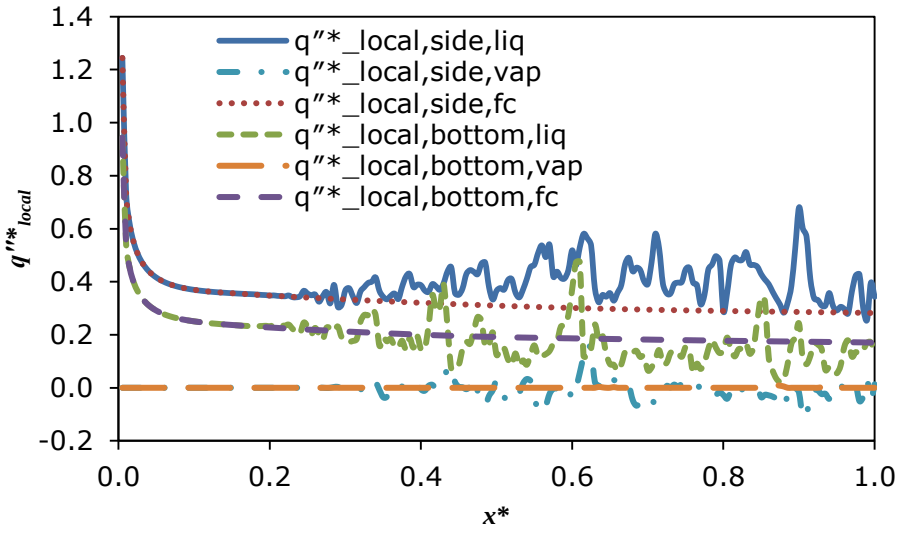
The study of local heat transfer for different q_b'' during flow boiling is accessible through the plots of $q_{local}''^*$ of each heat transfer component along x^*. For the study, the conditions selected were from Figure 4.11c while increasing q_b'' from the default value of 1561 kW/m^2 at Δt_{fb} about 10 ms as depicted in Figure 4.22. At each q_b'', the amount and magnitudes of peaks of $q_{local,side,liq}''^*$ above $q_{local,side,fc}''^*$ were relatively higher than $q_{total,bottom,liq}''^*$ above $q_{total,bottom,fc}''^*$. Also, the regions with $q_{local,bottom,liq}''^*$ below $q_{local,bottom,fc}''^*$ were more than the regions with $q_{local,side,liq}''^*$ below $q_{local,side,fc}''^*$ for each q_b''. On the other hand, for each q_b'', peaks of $q_{local,side,vap}''^*$ and regions with negative heat fluxes especially from $q_{local,side,vap}''^*$ appeared. Moreover, the regions of negative heat fluxes of $q_{local,side,vap}''^*$ were more than the regions of negative heat fluxes of $q_{local,bottom,vap}''^*$ for each q_b''. In overall, both $q_{local,side,vap}''^*$ and $q_{local,bottom,vap}''^*$ at most regions were close to zero for each q_b''. These occurrences are also observable when changing $\dot{m}''$ as evident in Section 4.4.

From low to high q_b'' of 1561 to 3197 kW/m^2 as illustrated in Figure 4.11c and from Figure 4.22a to Figure 4.22d, the peaks of $q_{local,side,liq}''^*$ began nearer to the inlet towards downstream. Also, during flow boiling, the number of the peaks also became more substantial from the low to high q_b''. This existence is mainly due to the higher superheat of the heating surfaces, causing more ascending and descending flows enhancing the heat transfer. Nevertheless, from low to moderate q_b'', especially at the bottom surface, the regions with $q_{local,bottom,liq}''^*$ below $q_{local,bottom,fc}''^*$ was relatively larger. This occurrence is primarily due to the more substantial amount of liquid-vapour mixture accumulating on the heating surface and restricting the heat transfer from low to moderate q_b''. On the other hand, from the moderate to high q_b'' of 3197 kW/m^2, as compared to side surfaces, the number of peaks at the bottom surface became relatively lower. Also, the bottom surface

produced more extensive regions with $q''^{*}_{local,bottom,liq}$ below $q''^{*}_{local,bottom,fc}$ as compared to the side surfaces at the high q''_b. These presences are as a result of the higher $T_{avg,surf}$ at the bottom surface, generating the more significant amount of liquid-vapour mixture on the heating surface impeding the heat transfer from moderate to high q''_b. On the other hand, when increased q''_b, the regions with the peaks of $q''^{*}_{local,side,vap}$ extended more towards the inlet from the outlet. This occurrence is due to larger $T_{avg,surf}$ of side surface generating more vortexes in the vapour phase when increasing q''_b.

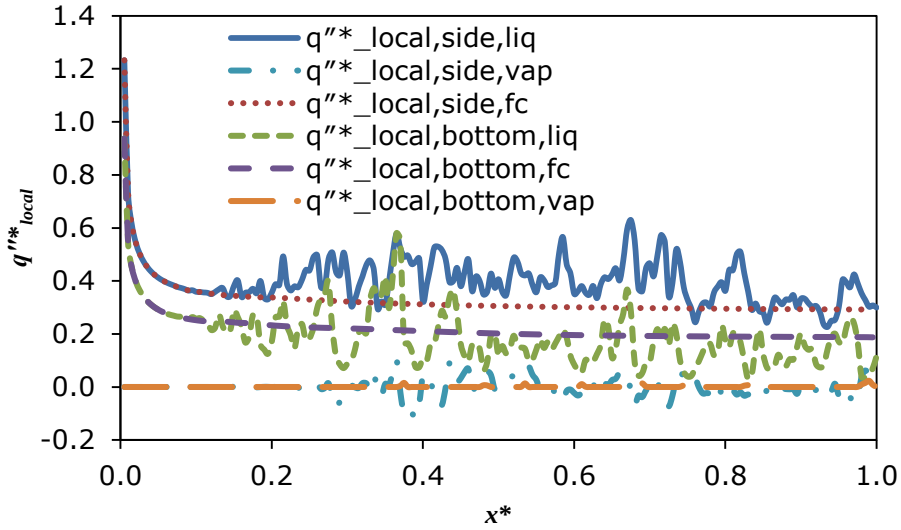


(a)

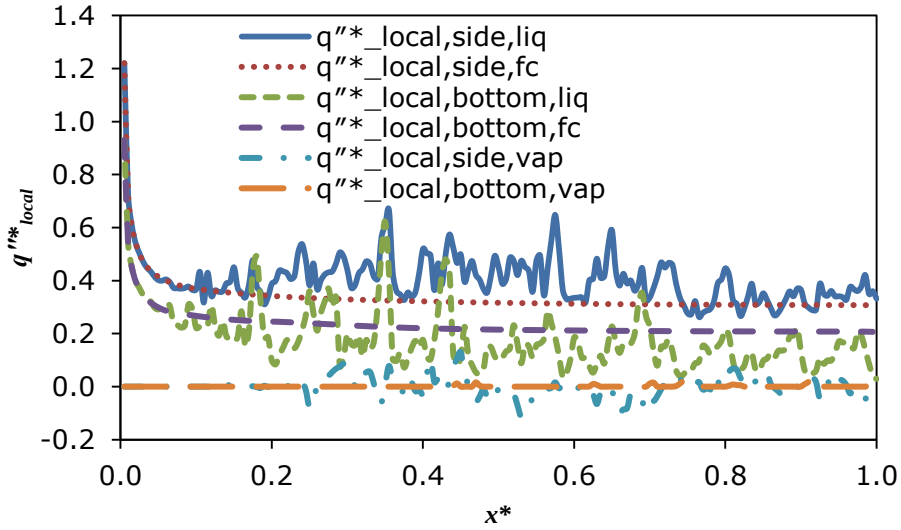


(b)

(Continued next page)



(c)



(d)

Figure 4.22: q''^{*}_{local} along x^{*} for q''_b of (a) 1691, (b) 2030, (c) 2706, and (d) 3197 kW/m² at $\dot{m}''$ of 389 kg/m² s and T_{in} of 23°C at Δt_{fb} about 10 ms

With the local average peripheral distribution of each heat flux component, the corresponding average values for different q''_b at Δt_{fb} about 10 ms are observable as shown in Figure 4.23. In Figure 4.23, from low to moderate q''_b of 1561 to 2706 kW/m², the increment of $q''^{*}_{side,liq}$ from $q''^{*}_{side,fc}$ became slightly larger. This occurrence is mainly as a result of the more massive amount of ascending and descending flows enhancing the heat transfer from low to moderate q''_b of 1561 to 2706 kW/m².

Nevertheless, from low to moderate q_b'', $q_{bottom,liq}''^*$ reduced further from $q_{bottom,fc}''^*$ due to the larger amount of liquid-vapour mixture inhibiting the heat transfer. When further increased q_b'' to 3197 kW/m^2, increment of $q_{side,liq}''^*$ from $q_{side,fc}''^*$ reduced and $q_{bottom,liq}''^*$ reduced even further from $q_{bottom,fc}''^*$. These presences are primarily due to the even larger amount of liquid-vapour mixture suppressing the heat transfer from moderate to high q_b''. For each q_b'', $q_{side,vap}''^*$ and $q_{bottom,vap}''^*$ were almost close to zero with the low thermal conductivity of the vapour phase.

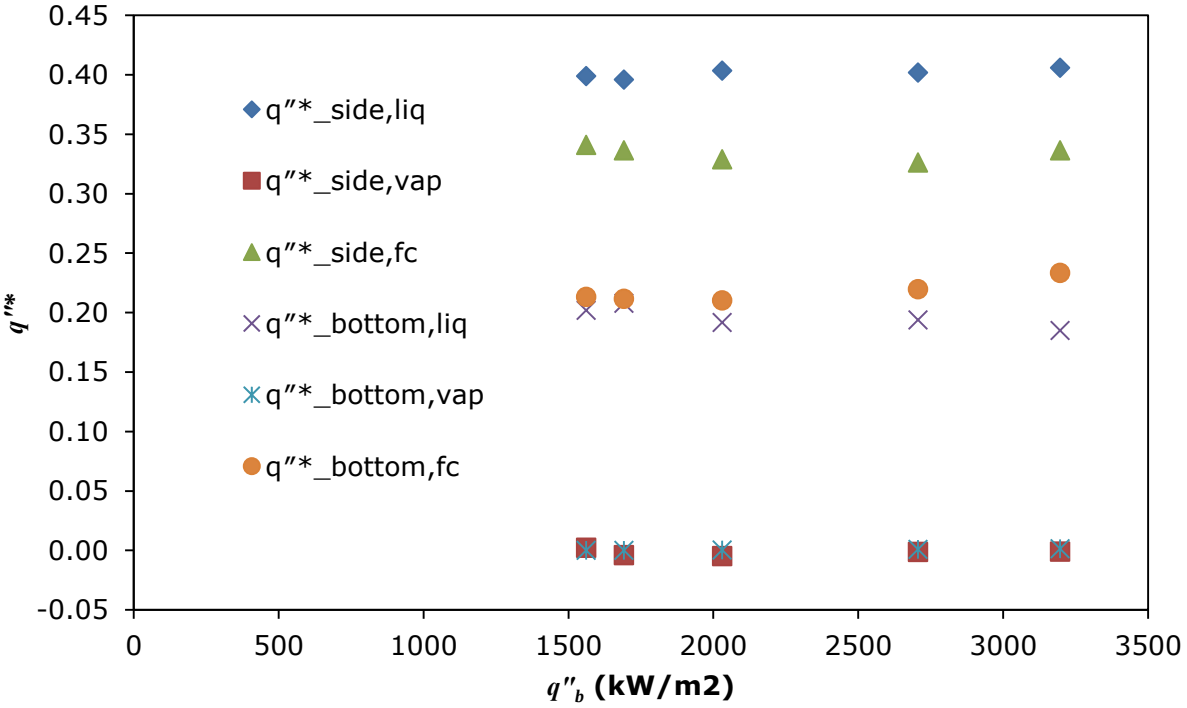


Figure 4.23: q''^* against q_b'' at $\dot{m}''$ of 389 kg/m^2 s and T_{in} of 23°C at Δt_{fb} about 10 ms

The study then continued with the examination of the overall heat transfer enhancement of h^* for different q_b'' at Δt_{fb} about 10 ms as illustrated in Figure 4.24. In Figure 4.24, at low q_b'' of 1561 kW/m^2, h^* was higher as compared to q_b'' of 1691 and 2030 kW/m^2. This difference is explainable by referring to the heating state for different q_b''. For low q_b'' of 1561 kW/m^2, $q_{total,fin}''$ reached about 98% of $(q_b'' \times A_b)/A_c$ (A_b is the base area, and A_c is channel surface area) within Δt_{fb} of 10 ms which was close to quasi-steady state. This occurrence also indicates that the development of nucleate boiling characteristic is also almost reaching the steady state and becoming significant for low q_b'' of 1561 kW/m^2 at this condition at Δt_{fb} of 10 ms. With the massive nucleate boiling characteristic, the ascending and descending flows are substantial with the transient conduction for low q_b'' of 1561 kW/m^2 at Δt_{fb} of 10 ms. However, for larger q_b'' of 1691 and 2030 kW/m^2, $q_{total,fin}''$ reached about

96 and 93 %, respectively, at Δt_{fb} about 10 ms which were further from the quasi-steady state. This incidence also implies that the nucleate boiling characteristic is still developing for larger q_b'' of 1691 and 2030 kW/m^2 at Δt_{fb} of 10 ms. In other words, the larger q_b'' requires longer Δt_{fb} to reach the quasi-steady state and ultimately develop the nucleate boiling characteristic.

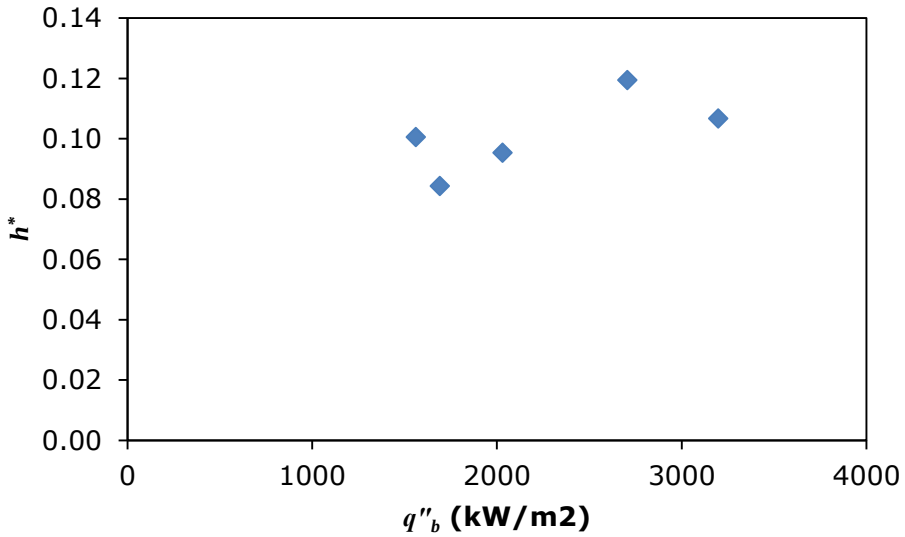


Figure 4.24: h^* against q_b'' at $\dot{m}''$ of 389 kg/m² s and T_{in} of 23°C at Δt_{fb} about 10 ms

When further increased q_b'' from 1691 to 2706 kW/m^2, h^* raised as illustrated in Figure 4.24. This presence is as a result of the more massive ascending and descending flows that enhanced heat transfer, indicating more significant nucleate boiling characteristic when increasing q_b'' from 1691 to 2706 kW/m^2. When further increased q_b'' to 3197 kW/m^2, h^* dropped. This occurrence is primarily due to significantly increase the amount of liquid-vapour mixture, especially on the bottom surface that restricted heat transfer, and therefore the nucleate boiling characteristic is lesser when further rising q_b''.

4.8 Location of Bubble Nucleation for Different Heat Fluxes

Once finished analysing the heat transfer, the investigation continued to identify the effects of q_b'' on the location of bubble nucleation within the cross-section.

When q_b'' increased, the number of bubbles rose during flow boiling at about Δt_{fb} of 10 ms as illustrated in Figure 4.25 with more substantial heat conduction to activate more nucleation sites. The bubbles mainly nucleated at the corners while the number of bubbles nucleated at the side and bottom surfaces increased slightly with larger q_b''. The bubbles at the side surfaces were relatively more than the bubbles at the bottom surface for each q_b''. These occurrences also observable when

varying $\dot{m}''$ as evident in Section 4.5. The bubbles nucleated at the bottom surface increased slightly with higher q_b''.

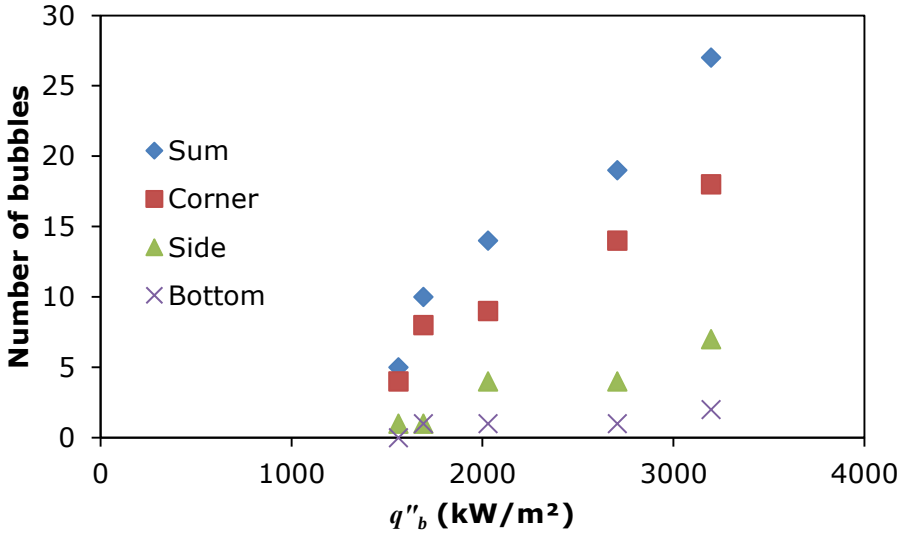
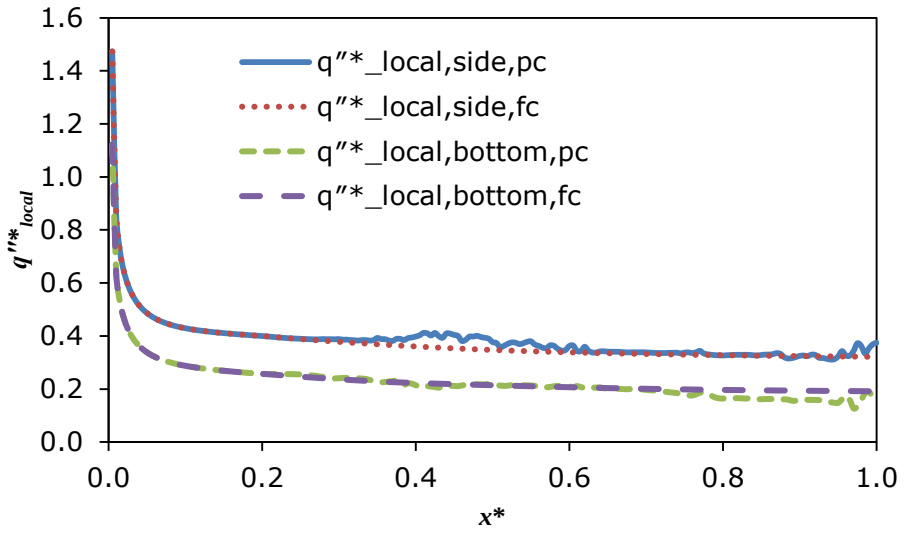


Figure 4.25: Location of bubble nucleation against q_b'' at $\dot{m}''$ of 389 kg/m² s and T_{in} of 23°C at Δt_{fb} within 0 and 10 ms

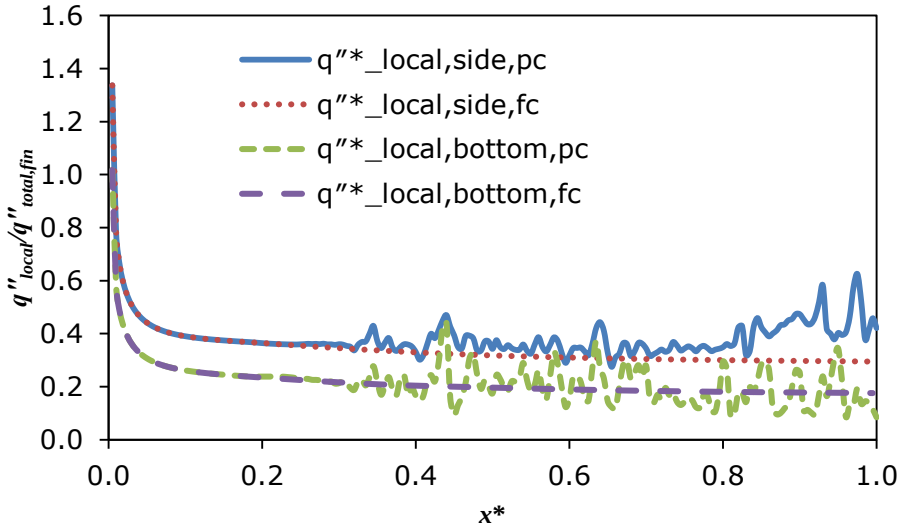
4.9 Effects of Inlet Temperatures before Flow Boiling

Addressed the effects of $\dot{m}''$ and q_b'', the investigation proceeded with the identification of the impacts of T_{in} on the local and average heat transfer components and heat transfer enhancement before flow boiling. The local and overall heat transfer elements observed for different T_{in} assist to explain the trends of transient heat transfer data in Figure 4.3.

The local heat transfer components for different T_{in} are attainable from q''_{local} for each component along x^* as depicted in Figure 4.15, Figure 4.26, and Figure 4.27. From Figure 4.15, Figure 4.26, and Figure 4.27, T_{in} are 23, 38, and 53°C, respectively, at $\dot{m}''$ of 389 kg/m² s and q_b'' of 1691 kW/m² at about Δt_{fb} of −5.8 and −2.9 ms. For each T_{in} at about Δt_{fb} of −5.8 and −2.9 ms, the peaks of $q''^*_{local,side,pc}$ and $q''^*_{local,bottom,pc}$ rose above $q''^*_{local,side,fc}$ and $q''^*_{local,bottom,fc}$, respectively. However, the peaks of $q''^*_{local,side,pc}$ were relatively more than $q''^*_{local,bottom,pc}$ for each T_{in}. Meanwhile, for each T_{in}, the regions with $q''^*_{local,bottom,pc}$ below $q''^*_{local,bottom,fc}$ were more than the regions with $q''^*_{local,side,pc}$ below $q''^*_{local,side,fc}$. These peaks and regions $q''^*_{local,bottom,pc}$ below $q''^*_{local,bottom,fc}$ became greater and further towards the downstream from Δt_{fb} of −5.8 ms and −2.9 ms for each T_{in}. These existence are observable when varying $\dot{m}''$ and q_b'' as found in Section 4.3 and Section 4.6, respectively.



(a)

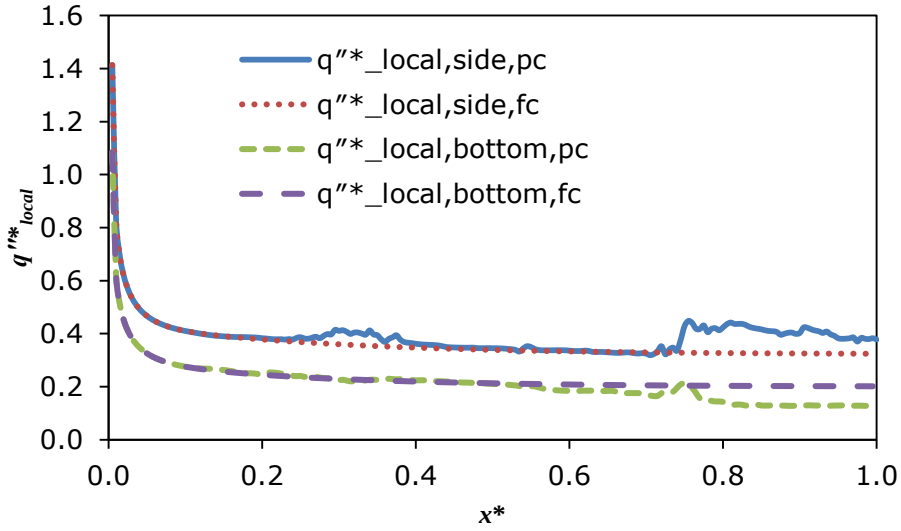


(b)

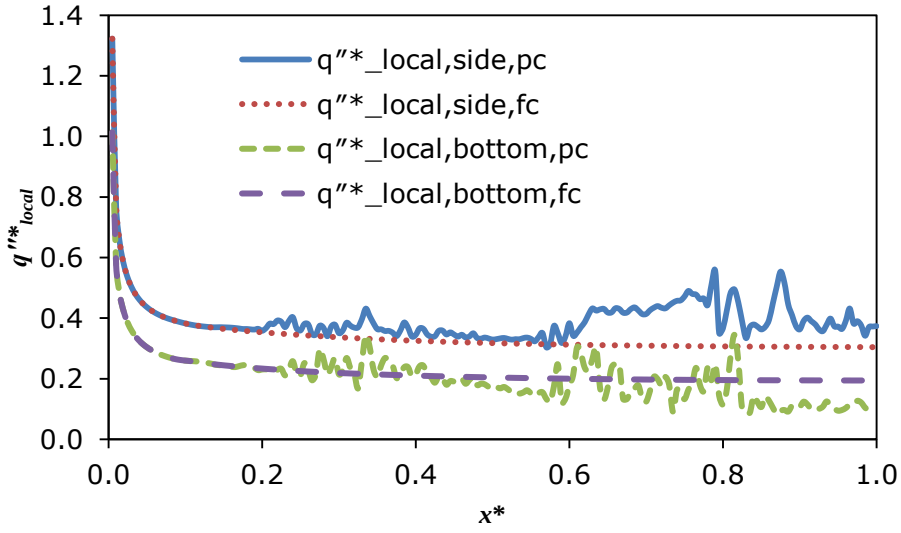
Figure 4.26: q''^{*}_{local} along x^{*} for T_{in} of 38°C at $\dot{m}''$ of 389 kg/m² s and q''_b of 1691 kW/m² at Δt_{fb} about (a) −5.8 and (b) −2.9 ms

When increased T_{in} to 38°C from the condition employed in Figure 4.15, at Δt_{fb} about −5.8 ms, peaks of $q''^{*}_{local,side,pc}$ and $q''^{*}_{local,bottom,pc}$ generated nearer to upstream as depicted in Figure 4.26a. However, the peaks were significantly lesser in amount and magnitude as compared to T_{in} of 23°C shown in Figure 4.15a. Meanwhile, when increased T_{in} from 23 to 38°C at about Δt_{fb} of −5.8 ms, $T_{avg,surf}$ increased as illustrated in Figure 4.3. Also, regions with $q''^{*}_{local,bottom,pc}$ below $q''^{*}_{local,bottom,fc}$ also lesser when increased T_{in} to 38°C. These occurrences are due to the lesser

temperature difference between heating surfaces and bulk fluid when increasing T_{in} from 23°C to 38°C, causing less intense ascending and descending flows and liquid-vapour mixture. Therefore, from T_{in} of 23°C to 38°C at about Δt_{fb} of −5.8 ms, the nucleate boiling characteristic becomes weaker, causing lesser amount and magnitude of peaks and regions with $q''^{*}_{local,bottom,pc}$ below $q''^{*}_{local,bottom,fc}$.



(a)



(b)

Figure 4.27: q''^{*}_{local} along x^{*} for T_{in} of 53°C at $\dot{m}''$ of 389 kg/m² s and q''_{b} of 1691 kW/m² at Δt_{fb} about (a) −5.8 and (b) −2.9 ms

When Δt_{fb} reached about −2.9 ms for T_{in} of 38°C as illustrated in Figure 4.26b, significant amount and magnitude of peaks of $q''^{*}_{local,side,pc}$ and $q''^{*}_{local,bottom,pc}$ formed.

Also, the number of peaks was more than T_{in} of 23°C as depicted in Figure 4.15b. Meanwhile, when applying larger T_{in}, $T_{surf,avg}$ increased more with Δt_{fb} as evident in Figure 4.3. In Figure 4.3, at T_{in} of 38°C, $T_{avg,surf}$ between Δt_{fb} of -5.8 ms and 0 ms and between Δt_{fb} of -2.9 ms and 0 ms were more significant as compared to T_{in} of 23°C. $T_{avg,surf}$ between Δt_{fb} of -5.8 ms and 0 ms for T_{in} of 38°C is 5.0°C whereas 2.0°C for T_{in} of 23°C. On the other hand, $T_{avg,surf}$ between Δt_{fb} of -2.9 ms and 0 ms for T_{in} of 38°C was 2.0°C whereas 1.0°C for T_{in} of 23°C. The more substantial differences of $T_{avg,surf}$ between the duration of Δt_{fb} of -5.8 and -2.9 ms for T_{in} of 38° as compared to 23°C imply the more substantial increase of $T_{surf,avg}$ with Δt_{fb}. With the more significant rate of rising of $T_{surf,avg}$ when higher rates of heat entering into the micro-channel for higher T_{in} within the given Δt_{fb}, the thermal boundary layer is thicker before the bubble nucleation. Also, for larger T_{in}, the thermal boundary layer developed is relatively thicker causing larger length scales of ascending and descending flows to allow more substantial heat transfer at about Δt_{fb} of -2.9 ms. This occurrence also indicates the more rapid development of nucleate boiling characteristic for higher T_{in}. Meanwhile, regions with $q''^{*}_{local,bottom,pc}$ below $q''^{*}_{local,bottom,fc}$ increased when Δt_{fb} reached about -2.9 ms as a result of the more substantial amount of liquid-vapour mixture on the bottom surface suppressing the heat transfer.

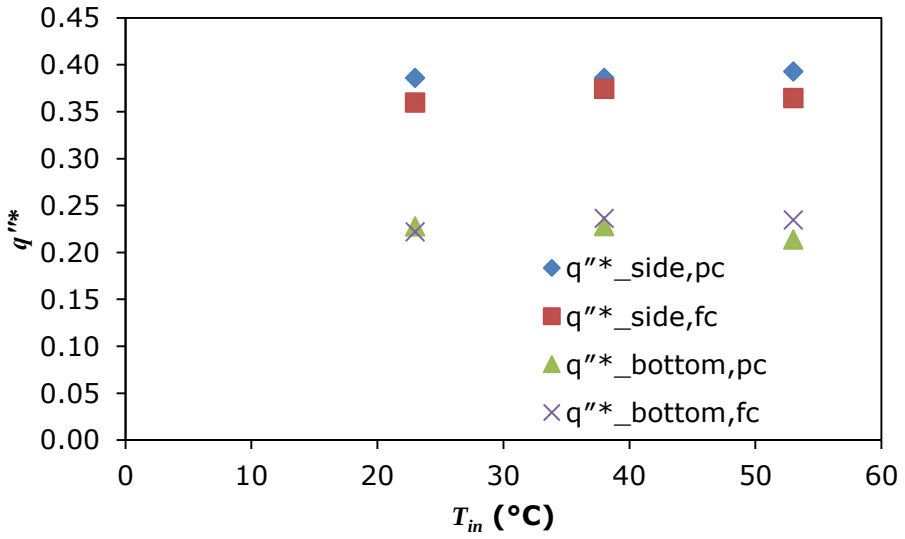
When further increased T_{in} to 53°C, at Δt_{fb} about -5.8 ms as illustrated in Figure 4.27a, peaks of $q''^{*}_{local,side,pc}$ formed nearer to upstream as compared to T_{in} of 38°C as shown in Figure 4.26a. The peaks of $q''^{*}_{local,side,pc}$ for T_{in} to 53°C was also higher especially near the outlet at x/L_c 0.7-1.0 as compared to T_{in} of 38°C. This occurrence is due to sufficiently high ΔT_{sup} at side surfaces to initiate larger length scales of ascending and descending flows enhancing the heat transfer when further increasing T_{in} at about Δt_{fb} of -5.8 ms. Meanwhile, at x/L_c of 0.7-1.0, the region with $q''^{*}_{local,bottom,pc}$ below $q''^{*}_{local,bottom,pc}$ appeared and was more substantial for T_{in} of 53°C as compared to T_{in} of 38°C.

When Δt_{fb} reached about -2.9 ms for T_{in} of 53°C as illustrated in Figure 4.27b, significant amount and magnitude of peaks of $q''^{*}_{local,side,pc}$ and $q''^{*}_{local,bottom,pc}$ formed. The amount and magnitude of peaks of $q''^{*}_{local,side,pc}$ at T_{in} of 53°C at about Δt_{fb} of -2.9 ms was relatively more than T_{in} of 38°C as shown in Figure 4.26b. This presence occurred with the similar mechanisms when increasing T_{in} to 38°C from 23°C as denoted in Figure 4.15 and from about Δt_{fb} of -5.8 ms to -2.9 ms. However, the peaks of $q''^{*}_{local,bottom,pc}$ for T_{in} of 53°C at about Δt_{fb} of -2.9 ms were relatively lesser as compared to T_{in} of 38°C. Also, for T_{in} of 53°C at about Δt_{fb} of -2.9 ms, the regions with $q''^{*}_{local,bottom,pc}$ below $q''^{*}_{local,bottom,fc}$ for T_{in} of 53°C were more than T_{in} of 38°C. This incidence is due to the more significant amount of

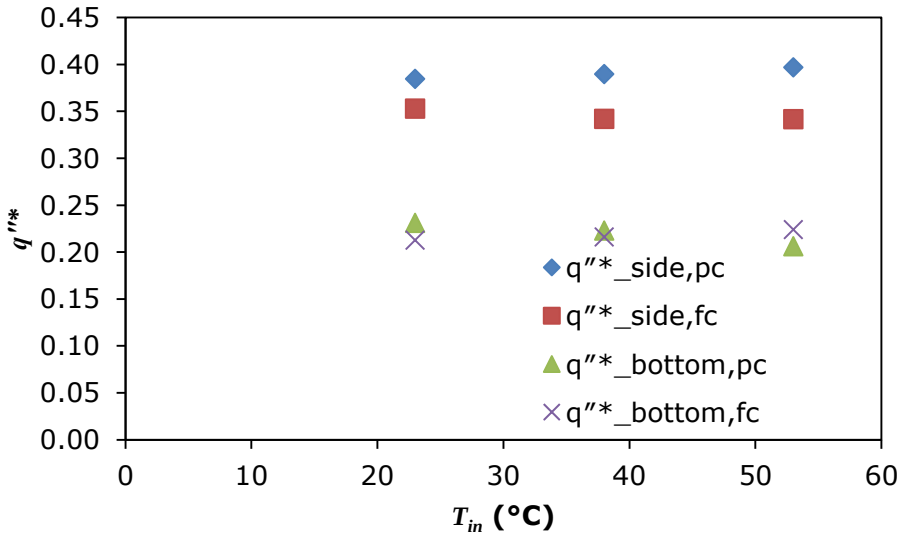
liquid-vapour mixture on the bottom surface suppressing the heat transfer for larger T_{in} of 53°C as compared to 38°C. For T_{in} of 53°C, although the number of peaks of $q''^{*}_{local,side,pc}$ was higher as compared to lower T_{in}, the number of peaks of $q''^{*}_{local,bottom,pc}$ was lesser as compared to lower T_{in}. These combined outcomes of T_{in} of 53°C occurred with the increment of $q''_{total,fin}$ with $T_{avg,surf}$ almost similar to T_{in} of 38°C as illustrated in Figure 4.3.

Through the local average peripheral heat fluxes along channels, the corresponding average values are attainable for different T_{in} at different Δt_{fb} as shown in Figure 4.28. From T_{in} of 23°C to 38°C at about Δt_{fb} of -5.8 as illustrated in Figure 4.28a, the increment of $q''^{*}_{side,pc}$ from $q''^{*}_{side,pc}$ reduced. Also, when increased T_{in} from 23°C to 38°C, $q''^{*}_{bottom,pc}$ was slightly lower than $q''^{*}_{bottom,fc}$. When T_{in} further increased to 53°C, increment of $q''^{*}_{side,pc}$ from $q''^{*}_{side,pc}$ became higher. Meanwhile, at T_{in} of 53°C, $q''^{*}_{bottom,pc}$ dropped and became even lower than $q''^{*}_{bottom,fc}$. When Δt_{fb} reached about -2.9 ms as illustrated in Figure 4.28b, the increment of $q''^{*}_{side,pc}$ from $q''^{*}_{side,fc}$ slightly increased when T_{in} increased. At T_{in} of 23°C, 38°C, and 53°C, respectively, $q''^{*}_{bottom,pc}$ was above, near to, and below $q''^{*}_{bottom,fc}$, respectively, at about Δt_{fb} of -2.9 ms. In other words, $q''^{*}_{bottom,pc}$ dropped when T_{in} increased at about Δt_{fb} of -2.9 ms. In general, the increment of $q''^{*}_{side,pc}$ from $q''^{*}_{side,fc}$ for each T_{in} is mainly due to the more ascending and descending flows facilitating the transient conduction. On the other hand, for each T_{in}, the decrement of $q''^{*}_{bottom,pc}$ from $q''^{*}_{bottom,fc}$ became more apparent at higher T_{in}. This incidence implies that the more substantial amount of liquid-vapour mixture accumulates on the bottom surface with higher T_{in} impeding the heat transfer.

The next part of the study is to identify the overall heat transfer enhancement due to phase change for different T_{in} and Δt_{fb}. The investigation of the overall heat transfer enhancement is observable by plotting h^{*} against T_{in} at Δt_{fb} about -5.8 and -2.9 ms as illustrated in Figure 4.29. In Figure 4.29, from T_{in} of 23 to 38°C, h^{*} dropped at Δt_{fb} about -5.8 ms. This occurrence is as a result of the lower temperature difference between heating surface and bulk fluid suppressing more the ascending and descending flows and inhibiting the heat transfer as compared to T_{in} of 23°C at about Δt_{fb} of -5.8 ms. When applied high T_{in} of 53°C, h^{*} became slightly higher. This occurrence is due to sufficiently large ΔT_{sup} at side surfaces facilitating ascending and descending flows for heat transfer enhancement for T_{in} of 53°C as compared to T_{in} of 38°C at about Δt_{fb} fo -5.8 ms. When Δt_{fb} reached about -2.9 ms as depicted in Figure 4.29, h^{*} increased with T_{in}. This presence is due to the more rapid development of nucleate boiling characteristic with Δt_{fb} for higher T_{in}.



(a)



(b)

Figure 4.28: q''^* against T_{in} at $\dot{m}''$ of 389 kg/m² s and q''_b of 1691 kW/m² at Δt_{fb} about (a) −5.8 and (b) −2.9 ms

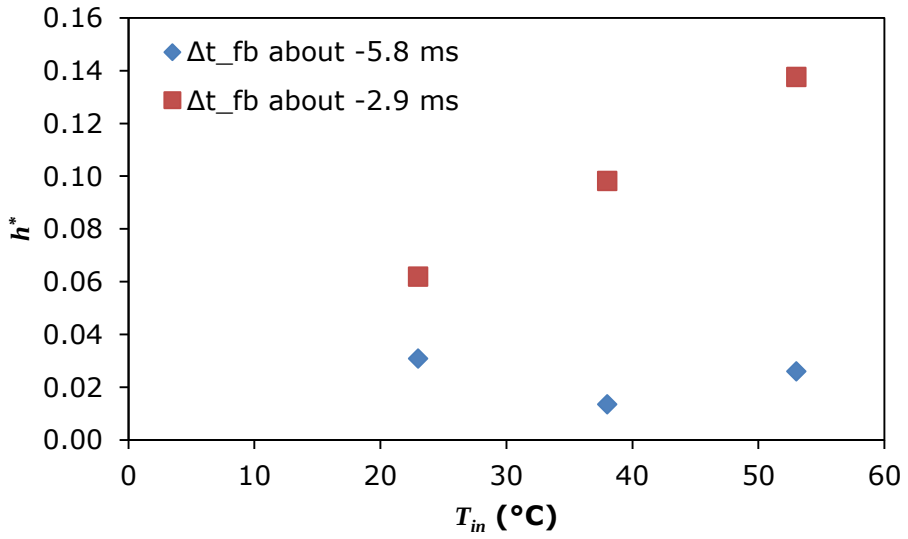


Figure 4.29: h^* against T_{in} at $\dot{m}''$ of 389 kg/m² s and q_b'' of 1691 kW/m² at Δt_{fb} about −5.8 and −2.9 ms

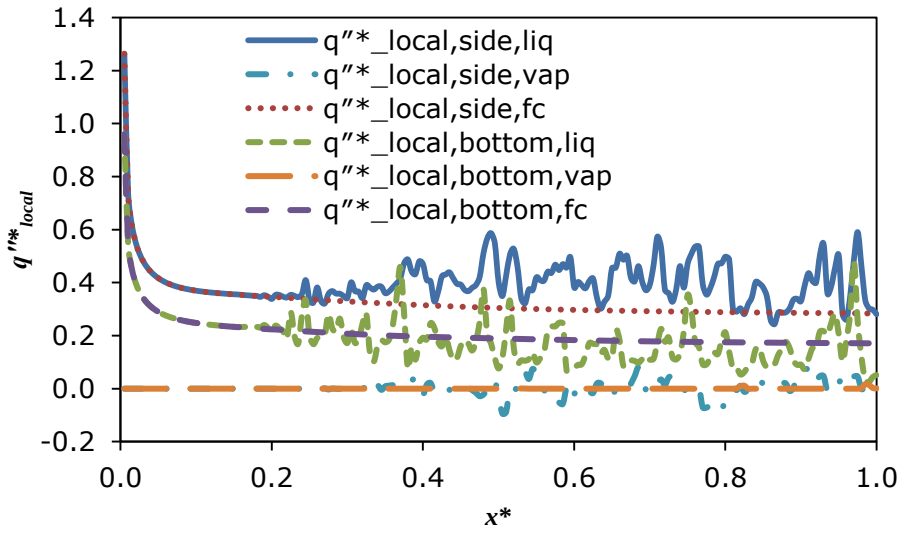
4.10 Effects of Inlet Temperatures during Flow Boiling

Once examined changes of T_{in} before flow boiling, the next part of the investigation is local and average heat transfer components and heat transfer enhancement for different T_{in} during flow boiling in micro-channels.

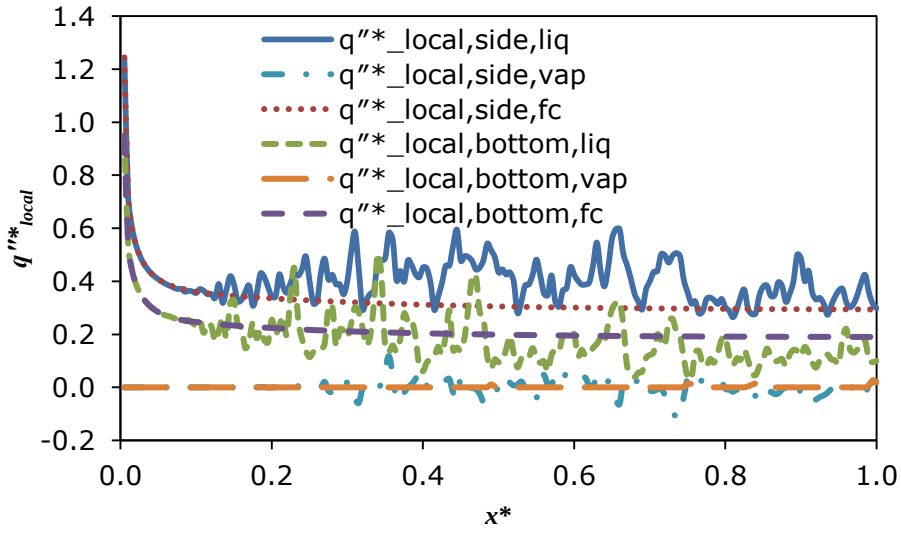
The estimation of the local heat transfer for different T_{in} during flow boiling is attainable from the plots of q''^*_{local} of each heat transfer component along x^*. The chosen conditions are from Figure 4.22a while increasing T_{in} from the default value of 23°C at Δt_{fb} about 10 ms as depicted in Figure 4.30. At each T_{in}, the amount and magnitudes of peaks of $q''^*_{local,side,liq}$ were relatively higher than the peaks of $q''^*_{local,bottom,liq}$. Also, the regions with $q''^*_{local,bottom,liq}$ below $q''^*_{local,bottom,fc}$ were more than the regions with $q''^*_{local,side,liq}$ below $q''^*_{local,side,fc}$ for each T_{in}. On the other hand, for each T_{in}, the number of peaks of $q''^*_{local,side,vap}$ and negative heat fluxes from $q''^*_{local,side,vap}$ became apparent. In general, both $q''^*_{local,side,vap}$ and $q''^*_{local,bottom,vap}$ at most regions were close to zero for each T_{in} due to the low thermal conductivity of the vapour phase. These occurrences are also evident for different $\dot{m}''$ and q_b'' as discussed in Section 4.4 and Section 4.7, respectively.

When increased T_{in} as depicted in Figure 4.22a and Figure 4.30a, and Figure 4.30b, peaks of $q''^*_{local,side,liq}$ and $q''^*_{local,bottom,liq}$ began closer to the inlet and the number of peaks also increased. These occurrences are due to the more substantial amount of ascending and descending flows enhancing the heat transfer with higher T_{in}. Meanwhile, with larger T_{in}, larger regions with $q''^*_{local,bottom,liq}$ below $q''^*_{local,bottom,fc}$ formed at the bottom surface. This incidence is as a result of the thicker thermal

boundary layer with larger ΔT_{sup}, forming the more massive amount of liquid-vapour mixture impeding the heat transfer. When increased T_{in}, the number of peaks of $q''_{local,side,vap}$ and regions with negative $q''^{*}_{local,side,vap}$ appeared due to the formation of the larger amount of vortexes at corners and nearer to the upstream towards downstream. Meanwhile, $q''^{*}_{local,bottom,vap}$ was almost close to zero along the micro-channel for each T_{in}.



(a)



(b)

Figure 4.30: q''^{*}_{local} along x^{*} for T_{in} of (a) 38 and (b) 53°C at $\dot{m}''$ of 389 kg/m² s and q''_b of 1691 kW/m² at Δt_{fb} about 10 ms

From each local heat flux component, the corresponding average heat transfer components are obtainable by plotting q''^* against T_{in} at Δt_{fb} about 10 ms as depicted in Figure 4.31. In Figure 4.31, when T_{in} increased, increment of $q''^*_{side,liq}$ from $q''^*_{side,fc}$ became slightly larger. This change is due to the larger length scales of ascending and descending flows for larger T_{in}. Meanwhile, when increased T_{in}, $q''^*_{bottom,liq}$ reduced further from $q''^*_{bottom,fc}$. This incidence is due to the larger amount of liquid-vapour mixture formed particularly on the bottom surface when increasing T_{in}. On the other hand, $q''^*_{side,vap}$ and $q''^*_{bottom,vap}$ for each T_{in} were almost close to 0 is due to the low thermal conductivity of the vapour phase.

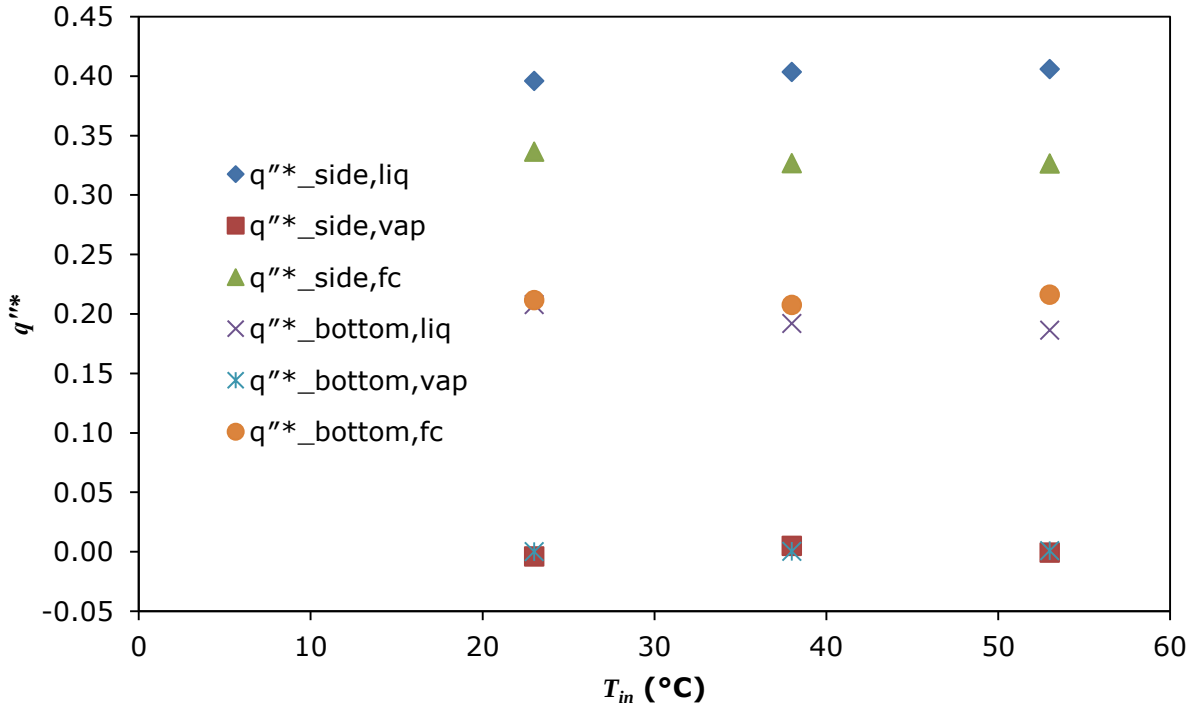


Figure 4.31: q''^* against T_{in} at $\dot{m}''$ of 389 kg/m² s and q''_b of 1691 kW/m² at Δt_{fb} about 10 ms

This investigation then continued with the evaluation of the heat transfer enhancement of h^* for different T_{in} during flow boiling as illustrated in Figure 4.32. In Figure 4.32 in which Δt_{fb} was at about 10 ms, from T_{in} of 23°C to 38°C, h^* increased with the relatively more peaks of $q''^*_{local,bottom,liq}$ as illustrated in Figure 4.30a. This presence is as a result of the more ascending and descending flows enhancing the heat transfer from T_{in} of 23°C to 38°C associated with the more substantial nucleate boiling characteristic. Consequently, h^* reduced from T_{in} of 38°C to 53°C. This existence is due to the higher amount of liquid-vapour mixture accumulating on the bottom surface impeding the heat transfer with the less intense nucleate boiling characteristic from T_{in} of 38°C to 53°C.

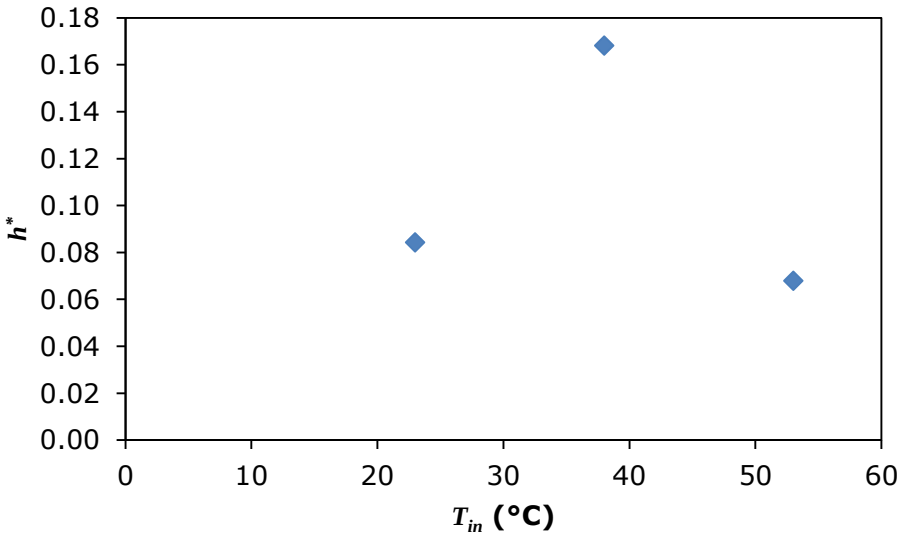


Figure 4.32: h^* against T_{in} at $\dot{m}''$ of 389 kg/m² s and q_b'' of 1691 kW/m² at Δt_{fb} about 10 ms

4.11 Location of Bubble Nucleation for Different Inlet Temperatures

When completed evaluating the heat transfer components and enhancements, this study proceeded to identify the location of bubble nucleation within the cross-section during flow boiling for different T_{in}.

When increased T_{in}, the number of bubbles increased due to the relatively larger ΔT_{sup} to activate more nucleation sites during flow boiling at about Δt_{fb} of 10 ms as depicted in Figure 4.33. For each T_{in}, the bubbles mainly nucleated at the corner. In general, for each T_{in}, the bubbles nucleated at side surfaces was more than the bottom surface. The number of bubbles at side surfaces was relatively higher as compared to the bottom surface for each T_{in}. This presence also achievable when changing $\dot{m}''$ and q_b'' as evident in Section 4.5 and Section 4.8, respectively. However, when increased T_{in} bubbles nucleated on bottom surface was absent.

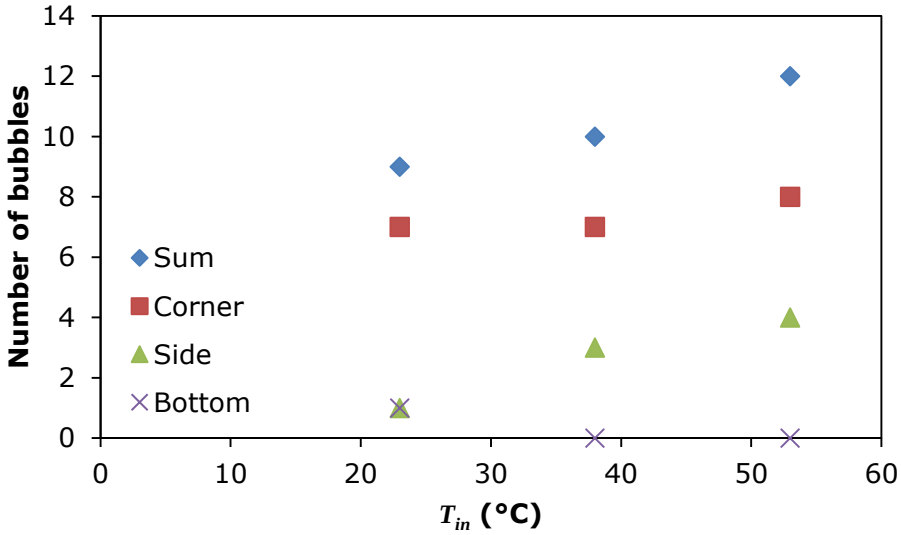


Figure 4.33: Location of bubble nucleation against T_{in} at $\dot{m}''$ of 389 kg/m² s and q_b'' of 1691 kW/m² at Δt_{fb} within 0 and 10 ms

Chapter 5 Effects of Substrate Materials

This chapter presents the result and discussion regarding the effects of substrate materials on the mechanisms of fluid flow and heat transfer before and during flow boiling of water in a rectangular micro-channel heat sink. The micro-channel heat sink has one 200 μm wide, 264 μm high, and 1 cm long micro-channel with W_{fin} of 200 μm and H_b of 137 μm. Also, the micro-channel is at $\dot{m}''$ of 389 kg/m^2 s, q_b'' of 2030 kW/m^2, T_{in} of 23°C, and p_{out} of 1 atm. The selected substrate materials in this study are silicon, aluminium, stainless steel, and copper.

5.1 Transient Heat Transfer for Different Substrate Materials before Flow Boiling

This study began by observing the transient heat transfer of water in the substrates of micro-channel heat sinks made of different materials of silicon, aluminium, stainless steel, and copper before flow boiling. The transient heat transfer is attainable by plotting $q''_{total,fin}$ against $\Delta T_{avg,surf}$ for these substrate materials before flow boiling as illustrated in Figure 5.1.

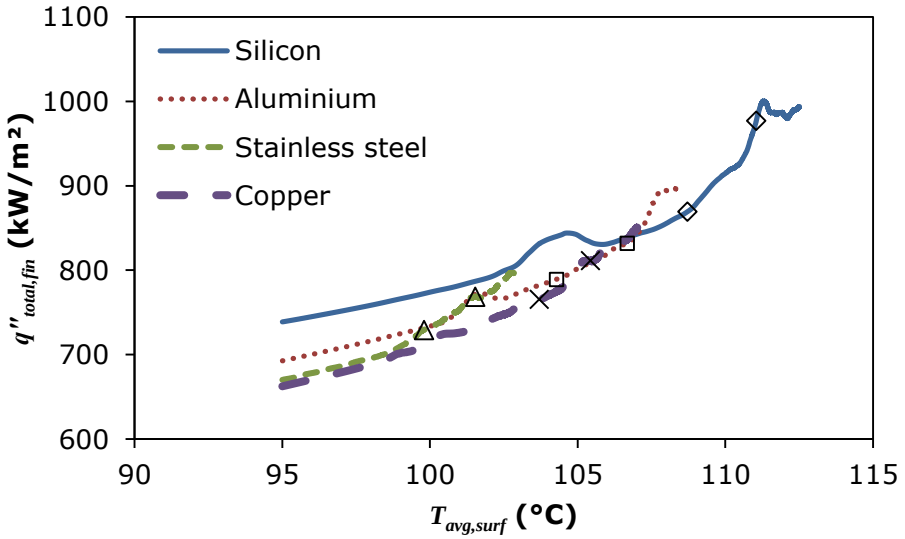


Figure 5.1: Transient heat transfer data of $q''_{total,fin}$ against $T_{avg,surf}$ for the substrates of micro-channel heat sinks made of different materials before flow boiling $\Delta t_{fb} < 0$ (the first and second marks at each curve are at Δt_{fb} about −5.8 and −2.9 ms, respectively, and the marks at each curve from the substrate materials of silicon, aluminium, stainless steel, and copper are oval, square, triangle, and cross, respectively)

In Figure 5.1, at about $T_{avg,surf}$ of 95°C, $q''_{total,fin}$ was higher in the order of copper, stainless steel, aluminium, and silicon. This difference is as a result of lower density ρ_s in this order of substrate materials as stated in Table 3.1. The lower ρ_s in this order of substrate materials allows more substantial heat transfer rate to enter into the micro-channel with $T_{avg,surf}$ when the flow is still at the single-phase at the unsteady state.

At Δt_{fb} about −5.8, −2.9, and 0 (the end of each curve) ms before the bubble nucleation, and 0 ms as depicted in Figure 5.1, $q''_{total,fin}$ and $T_{avg,surf}$ decreased in the order of silicon, aluminium, and copper. This occurrence is due to the combined effects of higher thermal conductivities k_s and thermal diffusivities a_s in this order of substrate materials as depicted in Table 3.1. The more considerable thermal conductivities k_s and thermal diffusivities a_s in this order of substrate materials possess the lower thermal resistance of the heat transferring from the bottom surface at the exit of the micro-channel towards the upstream. Therefore, the substrate materials with higher k_s cause the more extensive heat conduction towards upstream and the side surfaces at the similar $q''_{total,fin}$ as also observed during the single-phase flow in the literature [23-25]. The higher a_s of substrate materials facilitates more substantial heat transfer rates from the hotter to colder regions within the substrate. Therefore, in this order of the substrate materials, the amount of heat conducting towards the downstream and side surfaces becomes more significant at the higher rate before the bubble nucleation before the bubble nucleation. Consequently, before the bubble nucleation, with the larger k_s and a_s in this order of the substrate materials, the vicinities with the unstable flow significantly become lesser. Also, in this order of the substrate materials, the regions of unsteady flow, leading to the smaller $q''_{total,fin}$ and $T_{avg,surf}$ before the bubble nucleation.

However, $q''_{total,fin}$ and $T_{avg,surf}$ reduced less significant in the order of the substrate materials of silicon, aluminium, and copper became less significant before the bubble nucleation as illustrated in Figure 5.1. For the substrate materials of silicon, aluminium, and copper, $q''_{total,fin}$ reached about 88.8%, 76.4%, and 73.8% of $(q''_b \times A_b)/A_c$, respectively, during the bubble nucleation at about Δt_{fb} of 0. Before the bubble nucleation, the larger a_s producing larger heat conduction rate when changing the substrate material from silicon to aluminium also produce less significant increment of $q''_{total,fin}$ and $T_{avg,surf}$ with Δt_{fb}. However, even higher k_s and a_s when changing the substrate material from aluminium to copper is superfluous with the slight increment of the heat conduction and the rates from hotter to colder locations. Consequently, the minor increase in the amount and rates of heat conduction when changing the substrate material from aluminium to copper produces less significant decrement of the unstable flow regions. Therefore, with the less substantial decrement of the unstable flow regions, the decrement of

$q''_{total,fin}$ and $T_{avg,surf}$ becomes lesser when changing the substrate material from aluminium to copper before the bubble nucleation. Before the bubble nucleation, the excessive a_s when changing the substrate material from aluminium to copper causes an insignificant variation of the increment of $q''_{total,fin}$ and $T_{avg,surf}$ with Δt_{fb}.

Also, in the order of the substrate materials of silicon, copper, and aluminium, the increment of $q''_{total,fin}$ and $T_{avg,fin}$ with Δt_{fb} from about -5.8 ms to 0 ms became less substantial as depicted in Figure 5.1. These incidences imply that the combined effects of higher k_s, a_s, and volumetric heat capacities $\rho_s c_{p,s}$ in this order of the substrate materials. The higher k_s and a_s in this order of the substrate materials cause the more significant amount and rates of heat conduction from the hotter to colder regions, producing the lesser unstable flows. Meanwhile, the higher $\rho_s c_{p,s}$ provides the lower heat transfer rates from the surrounding into a body according to the lumped system analysis from the transient heat transfer as evident in Çengel and Ghajar [139]. Hence, the higher $\rho_s c_{p,s}$ in this order of the substrate materials produce the lesser heat transfer rates from the base to the substrate and smaller unstable flow regions. The lesser unstable flow regions in this order of the substrate materials with the higher k_s, a_s, and $\rho_s c_{p,s}$ facilitate substantially lower increment of $q''_{total,fin}$ and $T_{avg,surf}$ with Δt_{fb} before the bubble nucleation.

On the other hand, when changed the substrate material to stainless steel, the ranges of $q''_{total,fin}$ and $T_{avg,surf}$ became lower before the bubble nucleation as depicted in Figure 5.1. This incidence is due to the combined effects of significantly lower k_s and a_s of stainless steel as compared to other substrate materials tested in this study as stated in Table 3.1. The substantially small k_s of the substrate with high thermal resistance causing more heat concentrates on the bottom surface from the downstream is also apparent during the single-phase flow in the literature [23-25]. The considerable low a_s of the substrate material causes low heat transfer rates from the hotter to colder vicinities within the substrate. At the bottom surface, with the more heat conduction, the unstable flow regions become more extensive before the bubble nucleation from stainless steel among the substrate materials tested in this study. Also, before the bubble nucleation, the heat conduction to the bottom surface is more than the side surfaces from stainless steel as compared to other substrate materials tested in this investigation. Therefore, with the more heat on the bottom surface than the side surfaces for stainless steel as compared to other substrate materials examined in this study, $q''_{total,fin}$ and $T_{avg,surf}$ are significantly lower.

Also, the substrate material of stainless steel before the bubble nucleation produced the less substantial increment of $q''_{total,fin}$ and $T_{avg,surf}$ with Δt_{fb} from -5.8 ms to 0 ms. This presence is due to the combined effects of significantly lower k_s, a_s, and higher $\rho_s c_{p,s}$ of stainless steel as compared to other substrate materials

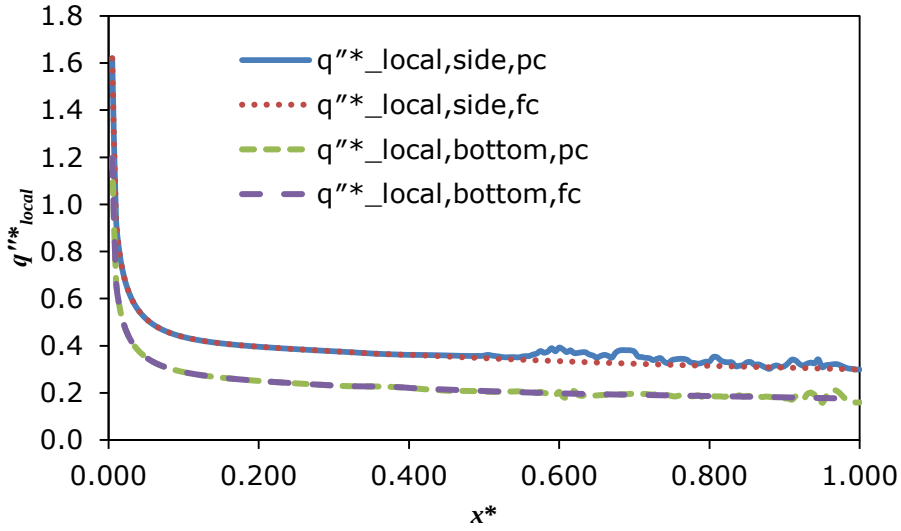
tested in this evaluation. With the lower k_s and a_s of stainless steel as compared to others in this study, more heat concentrates on the bottom surface than side surfaces. Also, the higher $\rho_s c_{p,s}$ allows lesser heat transfer rates from the base to the substrate as compared to other substrate materials. As a result, these combined effects cause the less insignificant increment of $q''_{total,fin}$ and $T_{avg,surf}$ with Δt_{fb}.

5.2 Effects of Substrate Materials before Flow Boiling

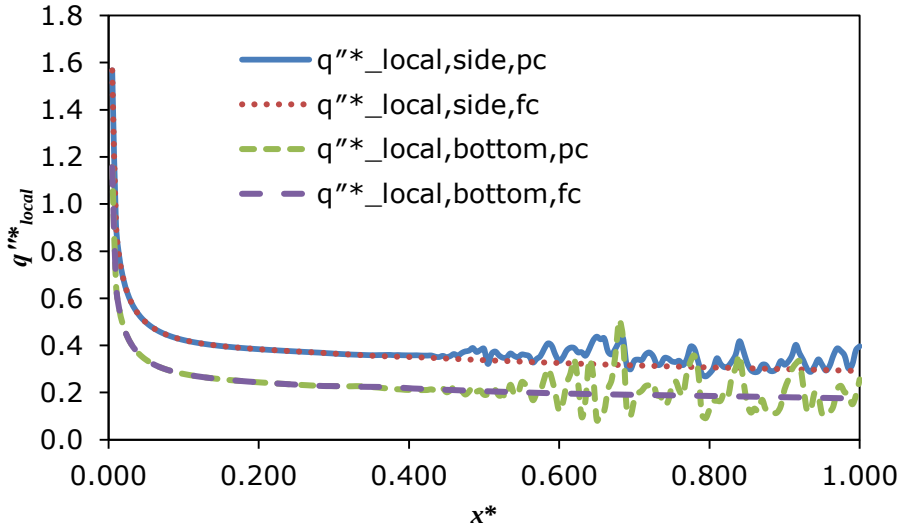
Evaluated the transient heat transfer, the investigation continued with the analysis the local and average heat transfer elements and heat transfer enhancement for different substrate materials at different Δt_{fb} . The local and average heat components for different substrate materials assist in explaining the trend of transient heat transfer data as shown in Figure 5.1.

The local heat transfer components for different substrate materials at different Δt_{fb} are accessible by plotting q''^{*}_{local} of each heat transfer element along the micro-channel as illustrated in Figure 4.16, Figure 5.2, Figure 5.3, and Figure 5.4. From Figure 4.16, Figure 5.2, Figure 5.3, and Figure 5.4, the substrate materials are silicon, aluminium, copper, and stainless steel, respectively, at q''_b of 2030 kW/m^2, $\dot{m}''$ of 389 kg/m^2 s, and T_{in} of 23°C. In overall, the increment of $q''^{*}_{local,side,pc}$ from $q''^{*}_{local,side,fc}$ were more than the increment of $q''^{*}_{local,bottom,pc}$ from $q''^{*}_{local,bottom,fc}$ for all the substrate materials for both Δt_{fb} about -5.8 and -2.9 ms. From about Δt_{fb} of -5.8 ms to -2.9 ms, more peaks and regions with $q''^{*}_{local,bottom,pc}$ below $q''^{*}_{local,bottom,fc}$ grew and began further from the downstream for each substrate material. This occurrence is also observable when varying $\dot{m}''$, q''_b, and T_{in} as discussed in Section 4.3, 4.6, and 4.9, respectively.

The substrate material of silicon produced different heat distribution as shown in Figure 4.16 as compared to the substrate materials of aluminium and copper as depicted in Figure 5.2 and Figure 5.3. Compared to the substrate materials of silicon before the bubble nucleation, aluminium and copper produced lesser amount and magnitude of peaks of $q''^{*}_{local,side,pc}$ and $q''^{*}_{local,bottom,pc}$. Meanwhile, the peaks began nearer to downstream when changed the substrate material from silicon to aluminium and copper. Moreover, when replaced the substrate material from silicon to aluminium and copper, the regions with $q''^{*}_{local,bottom,pc}$ below $q''^{*}_{local,bottom,fc}$ became less extensive. Furthermore, the substrate materials of aluminium and copper possessed lower ranges of $q''_{total,fin}$ and $T_{avg,surf}$ as compared to silicon before the bubble nucleation as illustrated in Figure 5.1.

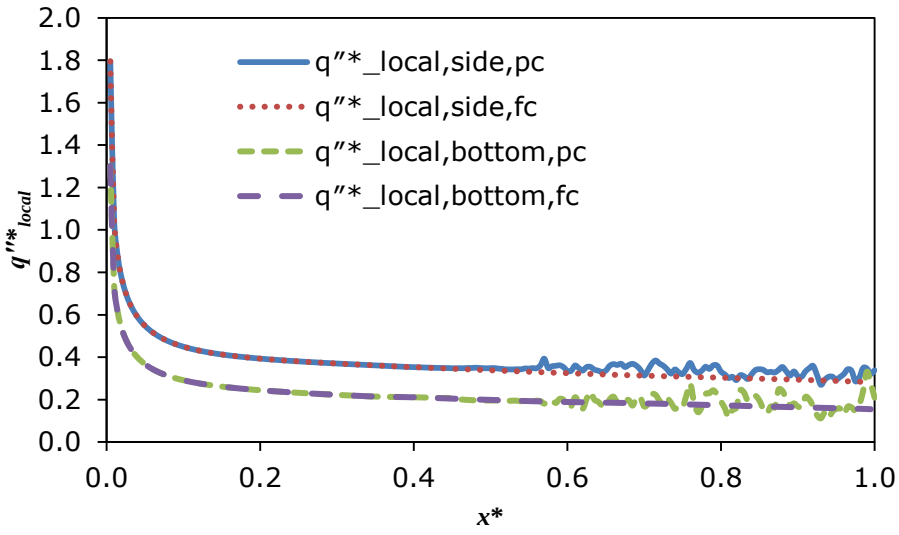


(a)

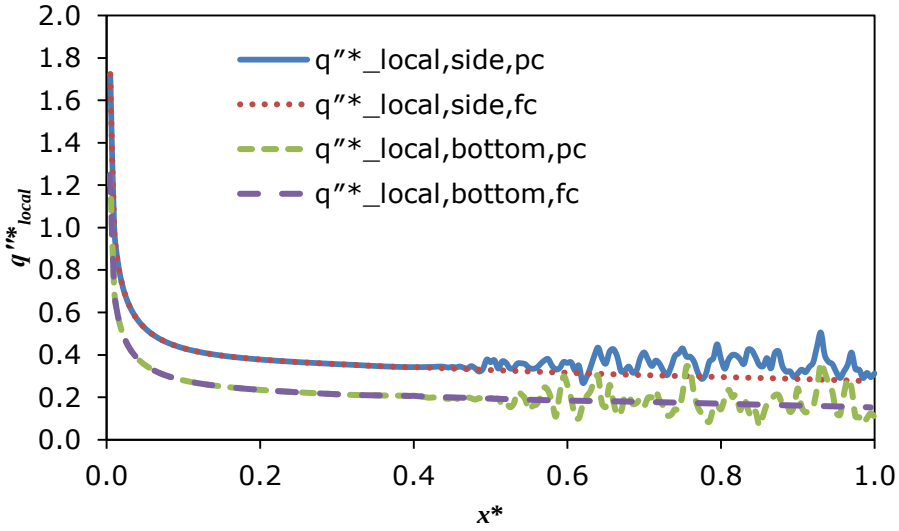


(b)

Figure 5.2: q''^{*}_{local} along x^{*} for aluminium micro-channel at Δt_{fb} about (a) −5.8 and (b) −2.9 ms

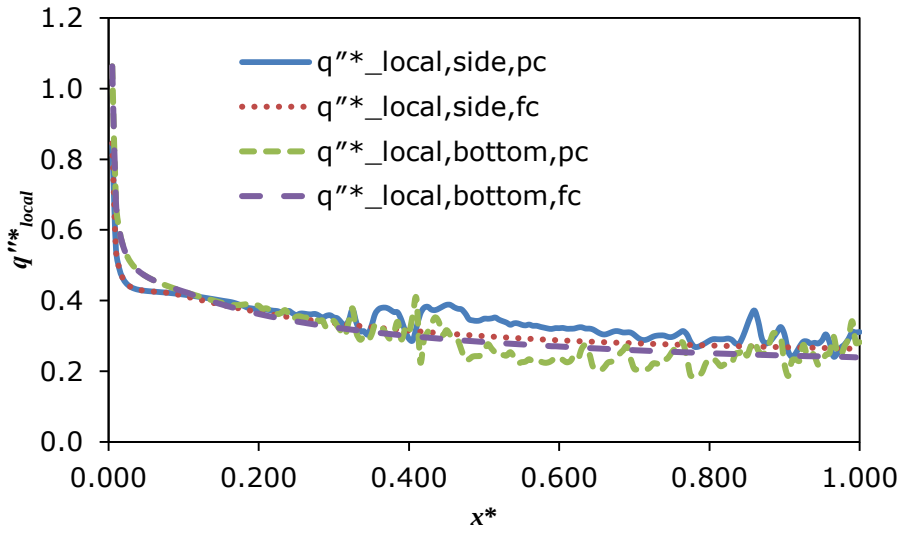


(a)

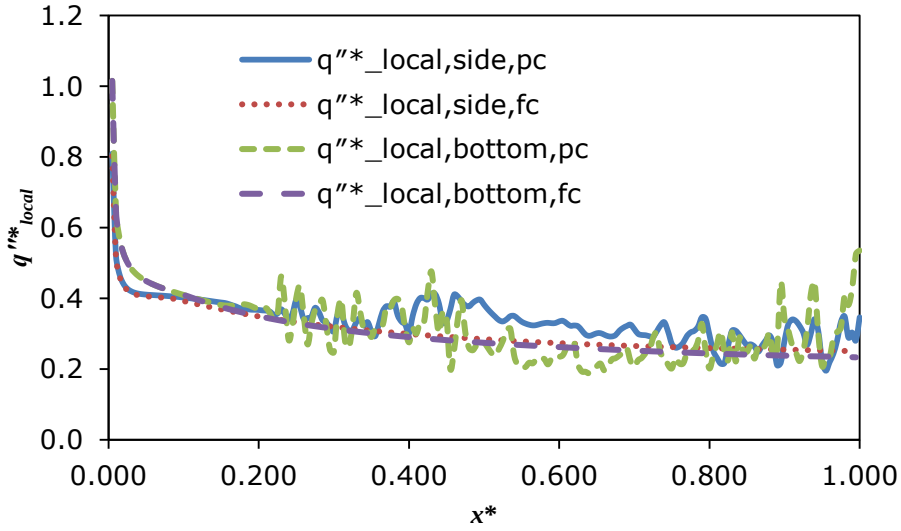


(b)

Figure 5.3: q''^{*}_{local} along x^{*} for copper micro-channel at Δt_{fb} about (a) −5.8 and (b) −2.9 ms



(a)



(b)

Figure 5.4: q''^{*}_{local} along x^{*} for stainless steel micro-channel at Δt_{fb} about (a) −5.8 and (b) −2.9 ms

The differences of the substrate material of silicon as shown in Figure 4.16 with of aluminium and copper as illustrated in Figure 5.2 and Figure 5.3, respectively, are due to the different k_s. The substrate material of silicon possesses the larger k_s than aluminium and copper, producing lower thermal resistance, leading to higher heat conduction towards upstream and side surfaces. The higher heat conduction causes lesser heat to concentrate from the downstream and lesser unstable flows with the insignificant nucleate boiling characteristic of the substrate materials of aluminium and copper as compared to silicon. The fewer unsteady flow leads to the

smaller amount and amplitudes of the peaks for the substrate materials with higher k_s of aluminium and copper as compared to silicon before the bubble nucleation. The lesser amount and magnitudes of the peaks from the substrate materials of aluminium and copper imply that the length scales of ascending and descending flows are smaller than silicon before the bubble nucleation.

From Δt_{fb} about -5.8 ms to -2.9 ms, the change of heat distribution of the substrate materials of silicon, aluminium, and copper is also evident in Figure 4.16, Figure 5.2, and Figure 5.3, respectively. The substrate material of silicon, aluminium, and copper produced more significant amount and magnitudes of peaks of $q''^{*}_{local,side,pc}$ and $q''^{*}_{local,bottom,pc}$ from Δt_{fb} about -5.8 ms to -2.9 ms. However, the peaks begin further from the downstream for the substrate material of silicon as compared to aluminium and copper from Δt_{fb} about -5.8 ms to -2.9 ms. Also, the substrate materials of aluminium and copper produced the smaller increment of the amount and magnitudes of the peaks from Δt_{fb} about -5.8 ms to -2.9 ms as compared to silicon. Meanwhile, from Δt_{fb} about -5.8 ms to -2.9 ms, the increment of $q''_{total,fin}$ with $T_{avg,surf}$ for the substrate material was more significant as compared to aluminium and copper as evident in Figure 5.1. Furthermore, from Δt_{fb} about -5.8 ms to -2.9 ms, the regions with $q''^{*}_{local,bottom,pc}$ below $q''^{*}_{local,bottom,fc}$ became lesser for the substrate materials of aluminium and copper as compared to silicon.

The change of heat distribution with Δt_{fb} of the substrate materials of silicon, aluminium, and copper as shown in in Figure 4.16, Figure 5.2, and Figure 5.3, respectively, is due to the different a_s and $\rho_s c_{p,s}$. The higher a_s of the substrate materials of aluminium and copper causes higher heat conduction rates on the bottom surface from the downstream to the upstream and side surfaces as compared to silicon. The more substantial heat conduction rates on the bottom surface from the downstream to the upstream and side surfaces cause the smaller amount of heat concentrating on the bottom surface from the downstream. Meanwhile, the higher $\rho_s c_{p,s}$ of the substrate materials cause lesser heat transfer rates from the base to the substrate. This presence leads to the lower increment of the amount and magnitudes of the peaks from about Δt_{fb} of -5.8 ms to -2.9 ms for the substrate material of aluminium and copper as compared to silicon. Therefore the substrate materials of aluminium and copper possess the less significant development of the nucleate boiling characteristic as compared to the substrate material of silicon from Δt_{fb} about -5.8 ms to -2.9 ms. Also, from Δt_{fb} about -5.8 ms to -2.9 ms, the liquid-vapour mixture produced from the substrate material of aluminium and copper is lesser than silicon with the lower heat from the downstream. With the less massive liquid-vapour mixture of the substrate material of aluminium and copper from Δt_{fb} about -5.8 ms to -2.9 ms, the regions with $q''^{*}_{local,bottom,pc}$ below $q''^{*}_{local,bottom,fc}$ are lesser as compared to silicon.

From the substrate materials of aluminium and copper, the peaks of $q''^{*}_{local,side,pc}$ began at the almost identical location as shown in Figure 5.2 and Figure 5.3, respectively, at about Δt_{fb} of -5.8 and -2.9 ms. Meanwhile, at about Δt_{fb} of -5.8, -2.9, and 0 ms, $q''_{total,fin}$ and $T_{avg,surf}$ for the substrate material of aluminium and copper were almost similar as depicted in Figure 5.1. This occurrence implies that the increase of k_s and a_s when changing the substrate material from aluminium to copper is excessive for the heat conduction and its rates at the side surfaces. With the smaller increment of the magnitudes and rates of heat conduction when switching the substrate material from aluminium to copper before the bubble nucleation, the peaks commence at almost the similar location. When Δt_{fb} reached about -2.9 ms from -5.8 ms, for both the substrate materials of aluminium and copper, the peaks begin at the site further from the downstream with more heat entering into the micro-channel.

Nevertheless, the substrate material of copper as illustrated in Figure 5.3 produced slightly larger magnitudes of peaks of $q''^{*}_{local,side,pc}$ than aluminium as depicted in Figure 5.2 at both Δt_{fb} about -5.8 and -2.9 ms. Meanwhile, at both Δt_{fb} about -5.8, -2.9, and 0 ms, the substrate material of copper produced slightly lesser $q''_{total,fin}$ and $T_{avg,surf}$ as compared to aluminium for each Δt_{fb} as illustrated in Figure 5.1. This presence is as a result of the relatively higher k_s and a_s of the substrate material of copper as compared to aluminium. The higher k_s of the substrate material of copper as compared to aluminium allows more heat conduction towards the upstream and side surfaces from the bottom surface at the downstream. With higher a_s when changing the substrate material from aluminium to copper, the heat conduction rates into the micro-channel are more substantial when the unsteady flow with the colder fluid descending on hotter heating surfaces. These combined effects cause more unstable streams at the side surfaces with the larger magnitudes of peaks for the substrate material of copper as compared to the aluminium before the bubble nucleation. Hence, the heat distribution on the bottom surface becomes slightly lesser for the substrate material of copper as compared to aluminium at both Δt_{fb} about -5.8 and -2.9 ms. Therefore, for the substrate material of copper, the unsteady flows on the bottom surface become lesser as compared to aluminium for the bubble nucleation. With the smaller unstable streams on the bottom surface of the substrate material of copper, at about Δt_{fb} of -5.8, -2.9, and 0 ms with lesser $q''_{total,fin}$ and $T_{avg,surf}$ as compared to aluminium.

On the other hand, at about Δt_{fb} of -5.8 ms, the peaks of $q''^{*}_{local,bottom,pc}$ was absent for the substrate material of aluminium as depicted in Figure 5.2a. However, few peaks of $q''^{*}_{local,bottom,pc}$ appeared for the substrate material of copper as illustrated in Figure 5.3a. Meanwhile, for the substrate material of copper, the regions of $q''^{*}_{local,bottom,pc}$ below $q''^{*}_{local,bottom,fc}$ appeared whereas absent for the

substrate material of aluminium. This presence is due to the increase of a_s when changing the substrate material from aluminium to copper. The larger a_s when changing the substrate material from aluminium to copper produces higher heat transfer rates from the hotter to colder regions when unstable flows appear from the downstream.

When Δt_{fb} reached -2.9 ms, the substrate material of aluminium as shown in Figure 5.2b produced relatively more massive peaks of $q''^{*}_{local,bottom,pc}$ as compared to copper as illustrated in Figure 5.3b. Also, the regions of $q''^{*}_{local,bottom,pc}$ below $q''^{*}_{local,bottom,fc}$ for the substrate material of aluminium appeared with larger amplitude as compared to copper. This existence is due to the relatively lower $\rho_s c_{p,s}$ of the substrate material of aluminium as compared to copper. The smaller $\rho_s c_{p,s}$ of the substrate material of aluminium as compared to copper allows higher heat transfer rates from the base to the substrate. With the higher heat transfer rates from the base to the substrate of aluminium as compared to copper, relatively more massive peaks of $q''^{*}_{local,bottom,pc}$ become apparent at about Δt_{fb} -2.9 ms. Also, before the bubble nucleation, the more substantial heat conduction from the base to the substrate causes slightly greater liquid-vapour mixture from the substrate material of aluminium as compared to copper. The mass massive liquid-vapour mixture from the substrate material of aluminium as compared to copper leads to more extensive regions with $q''^{*}_{local,bottom,pc}$ below $q''^{*}_{local,bottom,fc}$.

Comparing to the substrate materials of silicon, aluminium, and stainless steel as illustrated in Figure 4.16, Figure 5.2, and Figure 5.3, respectively, the outcomes from stainless steel was dissimilar as shown in Figure 5.4. When employed the substrate material of stainless steel, the curves of $q''^{*}_{local,side,pc}$ and $q''^{*}_{local,bottom,pc}$ with peaks almost overlapped to each other before the bubble nucleation at both Δt_{fb}. Also, the peaks of $q''^{*}_{local,side,pc}$ from $q''^{*}_{local,side,fc}$ for the substrate materials of stainless steel is more than the peaks of $q''^{*}_{local,bottom,pc}$ from $q''^{*}_{local,bottom,fc}$. Meanwhile, the substrate material of stainless steel produced the lower range of $q''_{total,fin}$ and $T_{avg,surf}$ at both Δt_{fb} as compared to others employed in this study as depicted in Figure 5.1.

From Figure 4.16, Figure 5.2, Figure 5.3, and Figure 5.4, the differences of the outcomes for the substrate material of stainless steel as compared to others in this study are due to extremely low k_s and a_s. With the substantially low k_s and a_s of stainless steel as compared to others in this investigation, the heat conduction concentrating on the bottom surface is even higher at the lower rates. The massive heat accumulating on the bottom surface of the substrate material of stainless steel is also almost comparable to the side surfaces as compared to other substrate materials. Consequently, for the substrate material of stainless steel with the massive heat accumulating on the bottom surface, the curves of $q''^{*}_{local,side,pc}$ and

$q''^{*}_{local,bottom,pc}$ with peaks almost overlapped to each other. With more substantial heat on the bottom surface for the substrate material of stainless steel as compared to others, the thick thermal boundary layer formed from the bottom surface as evident in Figure 5.5. Meanwhile, the peaks of $q''^{*}_{local,side,pc}$ from the substrate material of stainless steel formed mainly from high-temperature gradients of the thermal boundary layer. The high-temperature gradients of the thermal boundary layer of the substrate material of stainless steel commonly appeared at the top part of the side surfaces, causing the peaks of $q''^{*}_{local,side,pc}$ more than $q''^{*}_{local,bottom,pc}$.

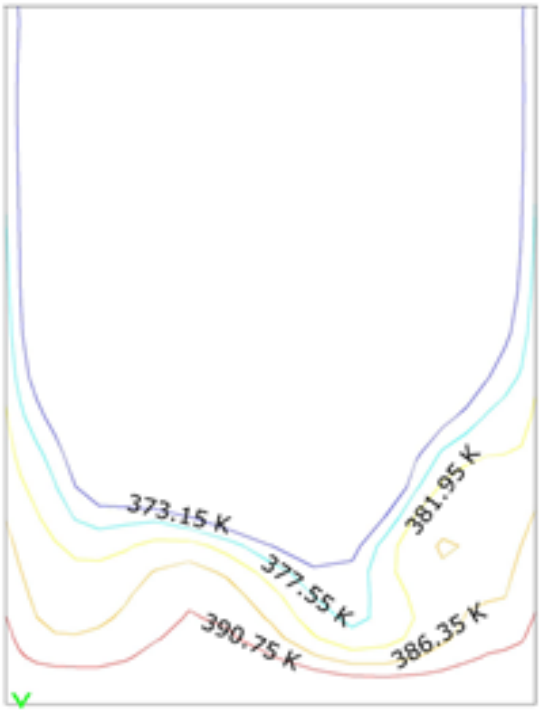


Figure 5.5: A thermal boundary layer in the micro-channel heat sink made of stainless steel at a cross-section with the liquid-vapour mixture before flow boiling

From Δt_{fb} about −5.8 ms to −2.9 ms, for the substrate material of stainless steel, the increment of the amount and magnitude of the peaks of $q''^{*}_{local,side,pc}$ was insignificant as evident in Figure 5.4. The substrate material of stainless steel also produced the less substantial increment of the regions with $q''_{local,bottom,pc}$ below $q''_{local,bottom,fc}$. Also, for the substrate material of stainless steel, the increment of $q''_{total,fin}$ and $T_{avg,surf}$ before the bubble nucleation was evident as observed in Figure 5.1, indicating the insignificant development of nucleate boiling characteristic. This incidence is due to the substantially low k_s and a_s for the substrate material of stainless steel as compared to others in this study. The considerably low k_s of the substrate material of stainless steel causes more heat concentrating on the bottom

surface as compared to other substrate materials in this study. The significantly low a_s for the substrate material of stainless steel produces low heat transfer rate from hotter to colder regions of the substrate, leading to the lesser increment of the peaks. The lower rate of heat transferring mostly to the bottom surface for the substrate material of stainless steel as compared to others causes the smaller increment of the peaks of $q''^{*}_{local,side,pc}$ with Δt_{fb}. Also, the substrate material of stainless steel with the lower rate of heat transferring mostly to the bottom surface produces the insignificant increase of the liquid vapour mixture with Δt_{fb} as compared to others. This incidence causes the less significant increment of the regions with $q''_{local,bottom,pc}$ below $q''_{local,bottom,fc}$ with Δt_{fb} for the substrate material of stainless steel as compared to others.

However, for the substrate material of stainless steel, the increment of the number of peaks of $q''_{local,bottom,pc}$ was considerably high when Δt_{fb} reached -2.9 ms from -5.4 ms as evident in Figure 5.4. Also, the increment of the peaks of $q''_{local,bottom,pc}$ with Δt_{fb} for the substrate material of stainless steel was larger as compared to others in this study as illustrated in Figure 4.16, Figure 5.2, and Figure 5.3. Moreover, the peaks produced from the substrate material of stainless steel began further from the downstream when Δt_{fb} reached -2.9 ms as compared to others in this study. This occurrence is due to significantly low k_s providing more heat accumulating on the bottom surface for the substrate material of stainless steel as compared to others tested in this investigation. The substrate material of stainless steel producing more massive heat on the bottom surface causes the considerably larger increment of the peaks when Δt_{fb} reaches about -2.9 ms. At about Δt_{fb} of -2.9 ms, the more substantial heat on the bottom surface of the substrate material of stainless steel also causes more massive amount liquid-vapour mixtures as compared to others in this investigation. This incidence causes the broader regions with $q''^{*}_{local,bottom,pc}$ below $q''^{*}_{local,bottom,fc}$ for the substrate material of stainless steel as compared to other in this study.

Based on the local average peripheral heat fluxes due to phase change along the micro-channel for different substrate materials at Δt_{fb} about -5.8 and -2.9 ms, the corresponding average values are observable as illustrated in Figure 5.6.

At about Δt_{fb} of -5.8 ms as depicted in Figure 5.6a, the increment of $q''^{*}_{side,pc}$ from $q''^{*}_{side,fc}$ for the substrate material of silicon was slightly higher as compared to aluminium and copper. On the other hand, the increment of $q''^{*}_{side,pc}$ from $q''^{*}_{side,fc}$ for the substrate material of aluminium was slightly lower than copper. For the substrate material of silicon, aluminium, and copper, $q''^{*}_{bottom,pc}$ was nearly close to $q''^{*}_{bottom,fc}$. $q''^{*}_{side,pc}$ and $q''^{*}_{side,fc}$ for the substrate material of stainless steel was significantly lower as compared to other substrate materials tested in this study at about Δt_{fb} of -5.8 ms. At about Δt_{fb} of -5.8 ms, $q''^{*}_{bottom,pc}$ and $q''^{*}_{bottom,pc}$ for the

substrate material of stainless steel was substantially larger as compared to other tested substrate materials employed in this investigation. Therefore, for the substrate material of stainless steel, at about Δt_{fb} of -5.8 ms, all the heat transfer components were closer to each other as compared to other substrate materials implemented in this study. Moreover, for the substrate material of stainless steel, $q''^{*}_{bottom,pc}$ was slightly lower than $q''^{*}_{bottom,fc}$ at about Δt_{fb} of -5.8 ms. Meanwhile, $q''^{*}_{side,pc}$ was larger than $q''^{*}_{side,fc}$ for the substrate material of stainless steel at about Δt_{fb} of -5.8 ms.

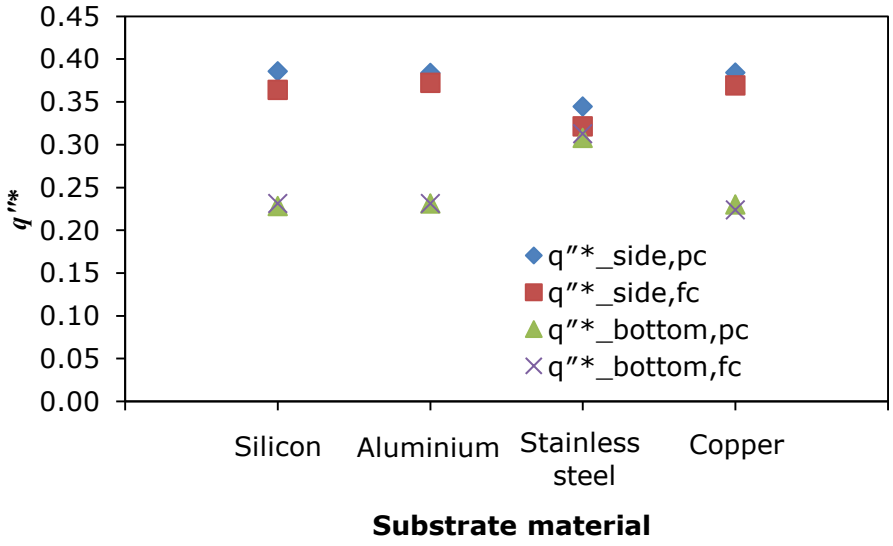
When Δt_{fb} reached about -2.9 ms, in general, the increment of $q''^{*}_{side,pc}$ from $q''^{*}_{side,fc}$ became more significant for all the substrate materials from Δt_{fb} about -5.8 ms depicted in Figure 5.6. Nevertheless, the substrate material of silicon produced significantly larger increment of $q''^{*}_{side,pc}$ from $q''^{*}_{side,fc}$ as compared to aluminium and copper at about Δt_{fb} of -2.9 ms. Also, at about Δt_{fb} of -2.9 ms, the increment of $q''^{*}_{bottom,pc}$ from $q''^{*}_{bottom,fc}$ was also present for the substrate material of silicon. On the other hand, the increment of $q''^{*}_{side,pc}$ from $q''^{*}_{side,fc}$ for the substrate material of copper was higher than aluminium at about Δt_{fb} of -2.9 ms. Meanwhile, at about Δt_{fb} of -2.9 ms, $q''^{*}_{bottom,pc}$ was almost close to $q''^{*}_{bottom,fc}$ for both of the substrate materials of aluminium and copper.

In Figure 5.6, in general, the increment of $q''^{*}_{side,pc}$ was more than $q''^{*}_{bottom,pc}$ for each substrate material. The increment of $q''^{*}_{side,pc}$ from each substrate material is mainly due to the ascending and descending flows created in the micro-channel enhancing the heat transfer. Meanwhile, the insignificant increment of $q''^{*}_{side,pc}$ is as a result of the considerable amount of the liquid-vapour mixture on the bottom surface from each substrate material.

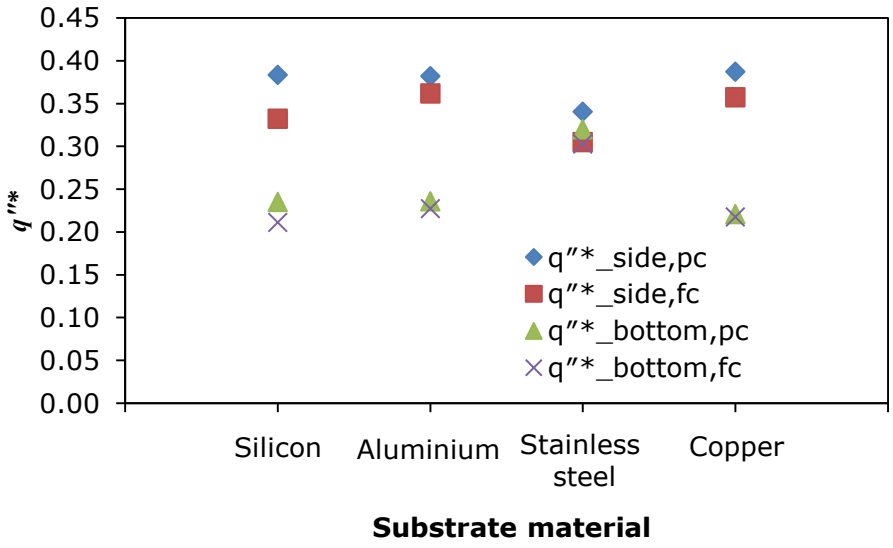
Consequently, this study continued with the corresponding heat transfer enhancement h^{*} of the substrate material was studied as shown in Figure 5.7.

In Figure 5.7, at about Δt_{fb} of -5.8 ms, h^{*} was higher for the substrate material of silicon as compared to aluminium and copper. This incidence is due to the relatively lower k_s for the substrate material of silicon as compared to aluminium and copper. The lower k_s of the substrate material of silicon allows more heat to concentrate on the bottom surface near the outlet, causing the relatively more massive amount of the liquid-vapour mixture on the bottom surface as compared to aluminium and copper. When Δt_{fb} reached about -2.9 ms, h^{*} for the substrate material of silicon substantially increased more than others in this study. This presence is due to the lower k_s, a_s, and $\rho_s c_{p,s}$ for the substrate material of silicon as compared to aluminium and copper. The lower k_s and a_s of the substrate material of silicon facilitate more heat conduction on the bottom surface from the outlet at the higher rates as compared to aluminium and copper. On the other hand, the lower

$\rho_s c_{p,s}$ for the substrate material of silicon allows higher heat transfer rates from the bottom surface to the body of the substrate. The more substantial heat transfer rates for the substrate material of silicon as compared to aluminium and copper produce the more rapid increment of ascending and descending flows enhancing the heat transfer. Therefore, with the more extensive increment of ascending and descending streams from the substrate material of silicon, h^* increased significantly with Δt_{fb} as compared to aluminium and copper.



(a)



(b)

Figure 5.6: q''^* for micro-channels made of different substrate materials at Δt_{fb} about (a) −5.8 and (b) −2.9 ms

Meanwhile, the substrate material of copper produced higher h^* as compared to aluminium at about Δt_{fb} of -5.8 ms as shown in Figure 5.7. When Δt_{fb} reached about -2.9 ms, h^* for the substrate material of copper was also more than aluminium. This occurrence is as a result of the more extensive k_s and $c_{p,s}$ for the substrate material of copper as compared to aluminium. The higher k_s and a_s of the substrate material of copper produce more heat conduction towards the side surfaces and upstream from the outlet at the lesser rates as compared to copper. The more substantial a_s for the substrate material of copper also causes more rapid heat transfer rates from the heating surfaces towards the colder fluid descending on the surfaces as compared to aluminium. Subsequently, the more substantial heat transfer rates towards the side surfaces and upstream of the substrate material of copper lead to higher h^* as compared to aluminium.

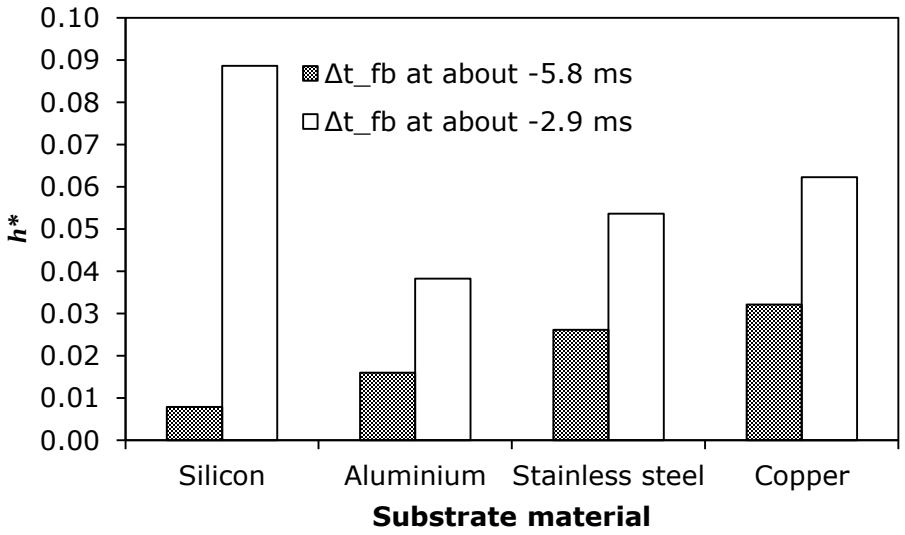


Figure 5.7: h^* for micro-channels made of different substrate materials at Δt_{fb} about -5.8 and -2.9 ms

However, the substrate material of stainless steel produced the larger h^* with the even lower k_s as compared to silicon at about Δt_{fb} of -5.8 ms as depicted in Figure 5.7. This occurrence is as a result of the even more extensive heat accumulating on the bottom surface with significantly low k_s for the substrate material of stainless steel as compared to silicon. With more substantial heat on the bottom surface for the substrate material of stainless steel as compared to silicon, the thick thermal boundary layer formed from the bottom surface as evident in Figure 5.5. Meanwhile, the peaks of $q''^*_{local,side,pc}$ from the substrate material of stainless steel formed mainly from high-temperature gradients of the thermal boundary layer. The high-temperature gradients of the thermal boundary layer of the substrate material of stainless steel commonly appeared at the top part of the side surfaces, leading to the higher h^* as compared to silicon.

Nevertheless, when Δt_{fb} reached about -2.9 ms, the increment of h^* for the substrate material of stainless steel was lesser as compared to silicon as illustrated in Figure 5.7. This incidence is as a result of the substantially lower k_s and a_s and higher $c_{p,s}\rho_s$ for the substrate material of stainless steel as compared to silicon. The lower k_s and a_s for the substrate material of stainless steel causes more heat accumulating on the bottom surface with the more moderate rates as compared to silicon. Meanwhile, the higher $\rho_s c_{p,s}$ for the substrate material of stainless steel produces lower heat transfer rates from the bottom surface towards the body of the substrate as compared to silicon. Therefore, with the combined effects of significantly lower k_s and a_s and higher $c_{p,s}\rho_s$ for the substrate material of stainless steel, the increment of h^* with Δt_{fb} becomes less significant as compared to silicon.

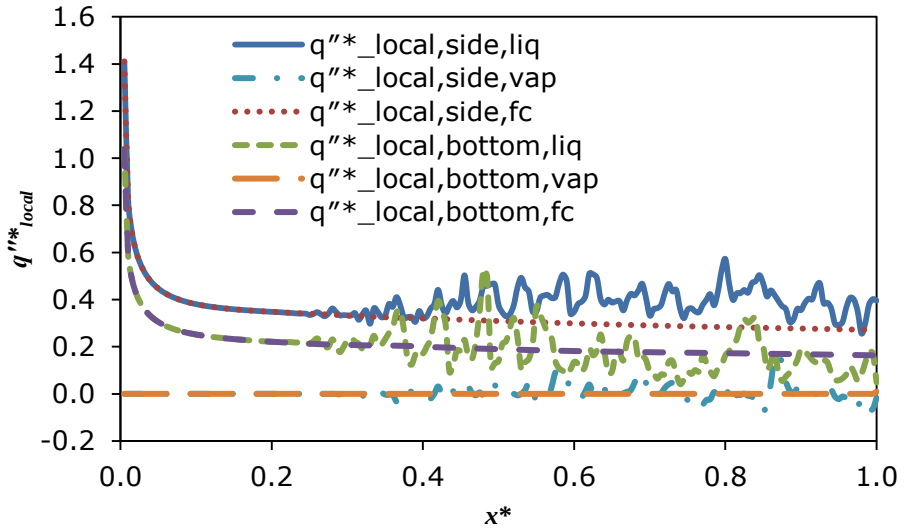
5.3 Effects of Substrate Materials during Flow Boiling

Once completed addressing the heat transfer before flow boiling, the next evaluation is regarding the effects of each substrate material on local and average heat transfer and heat transfer enhancement during flow boiling.

The investigation of the local heat transfer during flow boiling is obtainable through plotting q''^*_{local} for each heat transfer element along x^* of each substrate material. For the plots, the conditions chosen are from Figure 4.22b while changing the substrate materials at Δt_{fb} about 10 ms as illustrated in Figure 5.8. For the substrate materials of silicon, aluminium, and copper, the amount and magnitudes of peaks of $q''^*_{local,side,liq}$ were more than the peaks of $q''^*_{local,bottom,liq}$ during flow boiling. On the other hand, the regions with $q''^*_{local,bottom,liq}$ below $q''^*_{local,bottom,fc}$ were more than the regions with $q''^*_{local,side,liq}$ below $q''^*_{local,side,fc}$ for each substrate material. Meanwhile, for each substrate material, the number of peaks of $q''^*_{local,side,vap}$ and negative heat fluxes from $q''^*_{local,side,vap}$ emerged during flow boiling. Furthermore, the regions with the negative heat fluxes of $q''^*_{local,side,vap}$ during flow boiling were more than $q''^*_{local,bottom,vap}$ for each substrate material. In general, during flow boiling, both $q''^*_{local,side,vap}$ and $q''^*_{local,bottom,vap}$ at most regions during flow boiling were close to zero. These occurrences are also evident for different $\dot{m}''$, q''_b, and T_{in} as discussed in Section 4.4, Section 4.7, and Section 4.10, respectively. However, the amount and magnitudes of peaks of $q''^*_{local,bottom,liq}$ for the substrate material of stainless steel was more than $q''^*_{local,side,liq}$ in which the discussion regarding this outcome is available in this section.

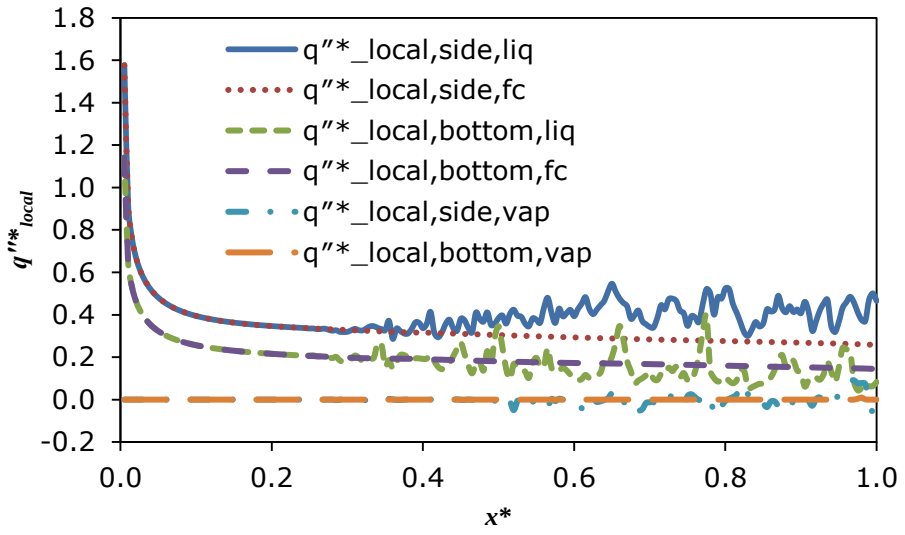
In Figure 4.22b and Figure 5.8, during flow boiling at Δt_{fb} about 10 ms, in the order of the substrate materials of silicon, aluminium, and copper, the peaks of $q''^*_{local,side,liq}$ began nearer from the downstream. Also, the amount and magnitude of peaks of $q''^*_{local,side,liq}$ slightly decreased in this order of the substrate materials during

flow boiling. Meanwhile, the regions with peaks of $q''^{*}_{local,side,vap}$ and regions with $q''^{*}_{local,side,vap}$ below $q''^{*}_{local,side,fc}$ became less extensive in this order of the substrate materials. These occurrences are due to the relatively higher k_s producing more heat conduction towards upstream and side surfaces in this order of the substrate materials during flow boiling. Hence, the heat concentrating on the bottom surface in this order of the substrate materials became lesser. The fewer heat accumulating on the bottom surface produces less significant ascending flows of hotter fluid and descending of colder fluid towards the side surfaces in this order of the substrate materials. Meanwhile, in this order of the substrate materials, vortexes at the corners became lesser. With the fewer eddies at the corners in this order of the substrate materials, the amount and magnitude of peaks of $q''^{*}_{local,side,liq}$ and $q''^{*}_{local,side,vap}$ slightly decreased during flow boiling. During flow boiling, the less substantial vortexes at the corners also result in lesser regions and began nearer to downstream with $q''^{*}_{local,side,vap}$ below $q''^{*}_{local,side,fc}$ in this order of the substrate materials.

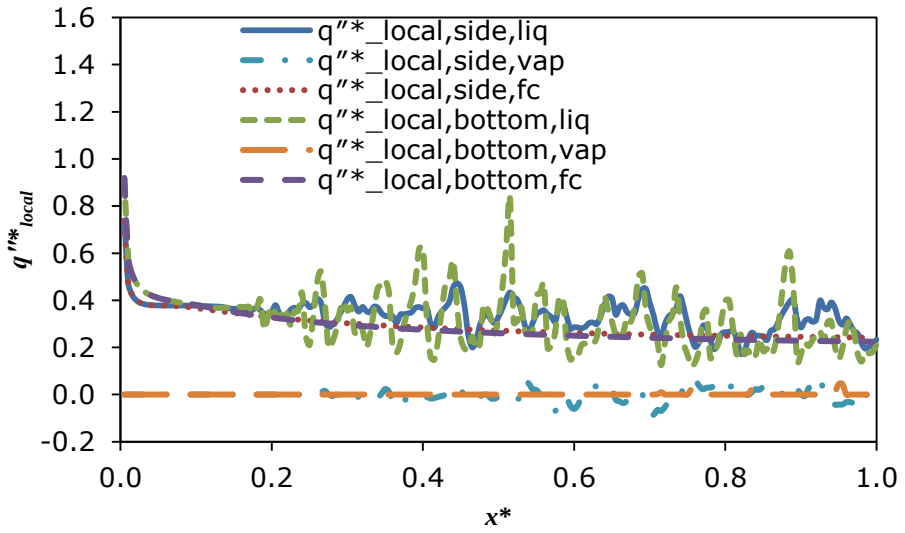


(a)

(Continued next page)



(b)



(c)

Figure 5.8: q''^*_{local} along x^* for (a) aluminium, (b) copper, and (c) stainless steel micro-channels at Δt_{fb} about 10 ms

In the order of the substrate materials of silicon, aluminium, and copper, the regions with $q''^*_{local,bottom,liq}$ below $q''^*_{local,bottom,fc}$ also began further from the downstream as illustrated in Figure 4.22b and Figure 5.8. As this order of the substrate materials possesses the larger k_s with lesser heat concentrating on the bottom surface, the amount of the liquid-vapour mixture becomes relatively less massive during flow boiling. The less extensive amount of liquid-vapour mixture in this order of the substrate materials causes the smaller vicinities with $q''^*_{local,bottom,liq}$ below $q''^*_{local,bottom,fc}$ at the bottom surface during flow boiling.

When changed the substrate material to stainless steel, unlike others, the heat fluxes at the side surfaces and bottom surface almost overlapped each other during flow boiling as illustrated in Figure 4.22b and Figure 5.8. Also, during flow boiling, the peaks of $q''^{*}_{local,side,liq}$ and $q''^{*}_{local,bottom,liq}$ began further from the downstream for the substrate material of stainless steel as compared to others in this study. Moreover, the magnitudes of peaks of $q''^{*}_{local,bottom,liq}$ was relatively higher than $q''^{*}_{local,side,liq}$ for the substrate material of stainless steel as compared to others in this investigation during flow boiling. Meanwhile, during flow boiling, for the substrate material of stainless steel, the regions with $q''^{*}_{local,bottom,vap}$ below $q''^{*}_{local,bottom,fc}$ extended further from the outlet as compared to others in this investigation.

These outcomes from Figure 4.22b and Figure 5.8 are due to the extremely small k_s of the substrate material of stainless steel allowing significantly more massive heat accumulating on the bottom surface as compared to others in this study. With more heat transferring to the bottom surface of the substrate material of stainless steel, the relatively high magnitude of peaks of $q''^{*}_{local,bottom,liq}$ emerged as compared to $q''^{*}_{local,side,liq}$. Meanwhile, during flow boiling, for the substrate material of stainless steel, with more heat transferring to the bottom surface, the amount of liquid-vapour mixture on the bottom surface becomes more massive. The more extensive amount of liquid-vapour mixture for the substrate material of stainless steel as compared to others in this study produces more considerable regions with $q''^{*}_{local,bottom,vap}$ below $q''^{*}_{local,bottom,fc}$. Also, for the substrate material of stainless steel, the more heat accumulating on the bottom surface also causes the significantly thicker thermal boundary as compared to others in this study during flow boiling. With the substantially thicker thermal boundary layer of the substrate material of stainless steel, the temperature gradients of the top part of the side surfaces are steeper, forming the peaks of $q''^{*}_{local,side,liq}$.

From the local heat flux values, the corresponding average heat fluxes at each surface are accessible for different substrate materials at Δt_{fb} about 10 ms. For the substrate material of silicon, the increment of $q''^{*}_{side,liq}$ from $q''^{*}_{side,fc}$ was evident during flow boiling as depicted in Figure 5.9. Meanwhile, during flow boiling, for the substrate material of silicon, $q''^{*}_{bottom,liq}$ below $q''^{*}_{bottom,fc}$ also became apparent. When changed the substrate material from silicon to aluminium and copper, the increment of $q''^{*}_{side,liq}$ from $q''^{*}_{side,fc}$ was almost similar during flow boiling. On the other hand, for both the substrate materials of aluminium and copper, during flow boiling, $q''^{*}_{bottom,liq}$ was nearer to $q''^{*}_{bottom,fc}$. When changed the substrate material from silicon, aluminium, or copper to stainless steel, $q''^{*}_{side,liq}$ and $q''^{*}_{side,fc}$ decreased during flow boiling. Meanwhile, for the substrate material of stainless steel, $q''^{*}_{bottom,liq}$ and $q''^{*}_{bottom,fc}$ increased during flow boiling. Therefore, during flow boiling, for the substrate material of stainless steel, all heat transfer components were closer to

each other. Also, the increment of $q''^{*}_{side,liq}$ from $q''^{*}_{side,fc}$ was less significant for the substrate material of stainless steel as compared to others in this study during flow boiling. Similar to other substrate materials employed in this study, stainless steel produced $q''^{*}_{bottom,liq}$ almost close to $q''^{*}_{bottom,fc}$ during flow boiling.

In overall, the increment of $q''^{*}_{side,liq}$ from $q''^{*}_{side,fc}$ was more than $q''^{*}_{bottom,liq}$ from $q''^{*}_{bottom,fc}$ for each substrate material during flow boiling. This occurrence is due to as a result of more massive ascending and descending flows during flow boiling from the side surfaces as compared to the bottom surface. Also, from all the substrate materials, the insignificant variation of $q''^{*}_{bottom,liq}$ from $q''^{*}_{bottom,fc}$ during flow boiling. This incidence is due to the higher amount of the liquid-vapour mixture on the bottom surfaces as compared to the side surfaces during flow boiling. On the other hand, from all the substrate materials, the changes of $q''^{*}_{side,vap}$ and $q''^{*}_{bottom,vap}$ were also less significant during flow boiling due to the low thermal conductivity of the vapour phase.

Once examined local and average heat transfer, the following section of the investigation is the corresponding heat transfer enhancement of h^{*} for different substrate materials during flow boiling. The analysis is achievable by plotting h^{*} for different substrate materials at Δt_{fb} about 10 ms during flow boiling as shown in Figure 5.10. In Figure 5.10, in the order of the substrate materials of silicon, aluminium, and copper, h^{*} increased. This occurrence is due to the higher k_s in this order of the substrate materials, allowing more heat conduction towards the upstream and side surfaces with lesser heat concentrating on the bottom surface. With the fewer heat accumulating on the bottom surface in this order of the substrate materials, the formation of the amount of liquid-vapour mixture impeding the heat transfer became lesser. The lesser generation of the amount of liquid-vapour mixture on the heating surface in this order of the substrate materials during flow boiling causes h^{*} to increase.

For the substrate material of stainless steel, h^{*} was slightly larger although k_s is significantly lower as compared to silicon as evident in Figure 5.10. This presence is due to more heat accumulating on the bottom surface of the substrate material of stainless steel, causing more intensive ascending and descending flows as compared to others in this study. The more active ascending and descending currents facilitate more heat transfer enhancement with larger h^{*} for the substrate material of stainless steel as compared to silicon. The more extensive heat concentrating on the bottom surface also produces the more massive liquid-vapour mixture for the substrate material of stainless steel as compared to others in this study. Nevertheless, the ascending and descending flows are intensively suppressing the impact of liquid-vapour mixture inhibiting the heat transfer for the substrate material of stainless steel as compared to others in this study.

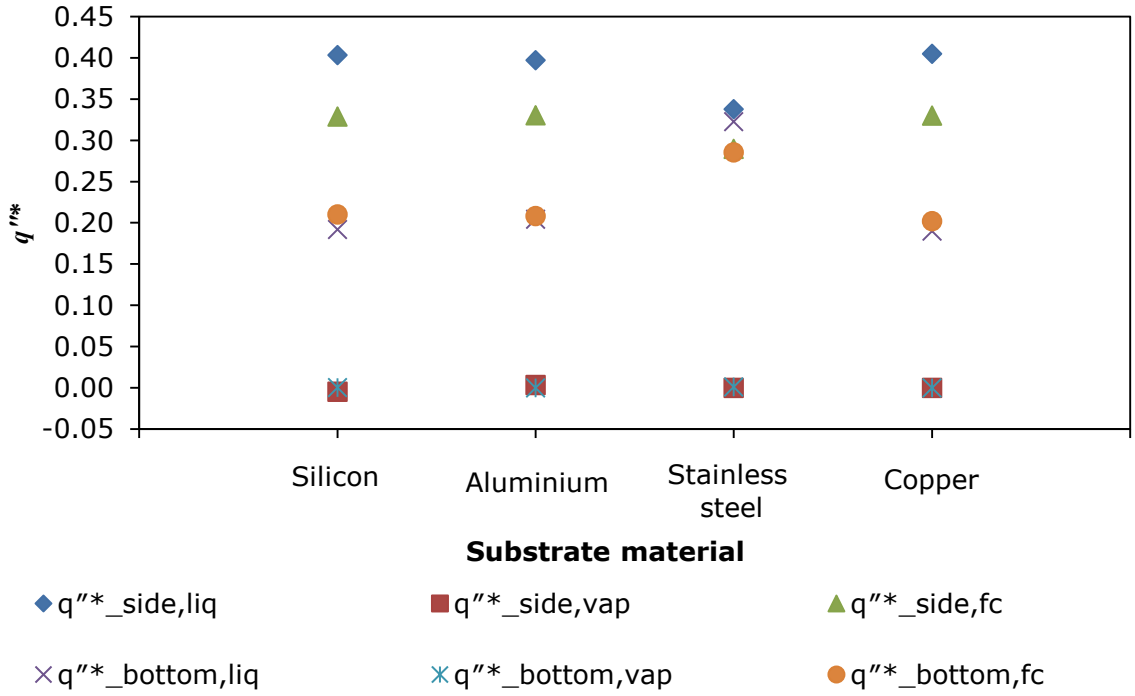


Figure 5.9: q''^{*} for micro-channels made of different substrate materials at Δt_{fb} about 10 ms

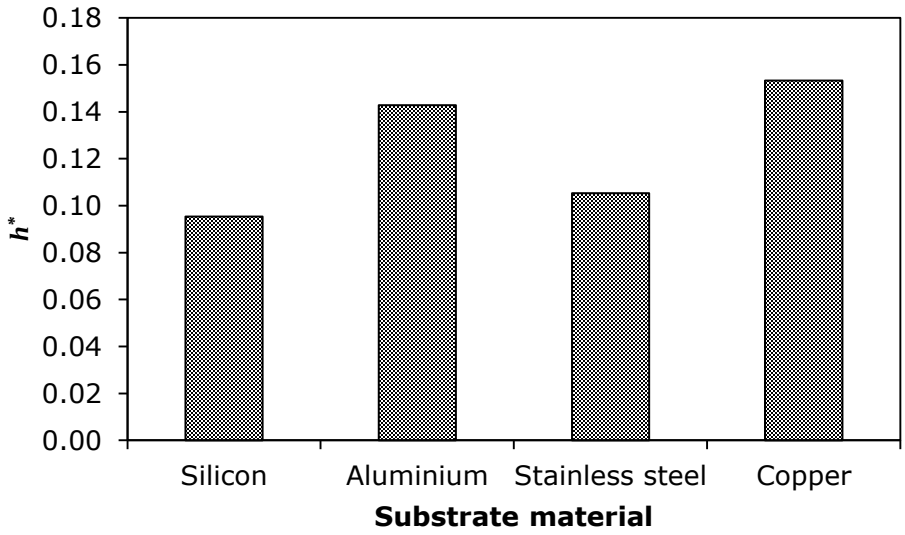


Figure 5.10: h^{*} for micro-channels made of different substrate materials at Δt_{fb} about 10 ms

5.4 Location of Bubble Nucleation and Bubble Growth for Different Substrate Materials

Once finished studying the heat transfer, the study proceeded to investigate the location of bubble nucleation within the cross-section of the micro-channel during flow boiling for different substrate materials.

In the order of the substrate materials of silicon, aluminium, and copper, the number of bubbles during flow boiling became less substantial at about Δt_{fb} of 10 ms as illustrated in Figure 5.11. This incidence is due to relatively larger k_s of in this order of the substrate materials, causing lesser heat concentrating on the bottom surface inducing the lesser bubble nucleation. When changed the substrate material to stainless steel, the number of bubbles were also smaller than silicon, although the stainless steel possesses significantly lesser k_s than silicon. This presence is due to the even more heat accumulating with substantially lower k_s for the substrate material of stainless steel as compared to silicon. With the even more heat concentrating on the bottom surface, the ascending and descending streams becomes more intensive for the substrate material of stainless steel as compared to silicon. The more massive ascending and descending flows indicate the more unstable flow suppresses the bubble nucleation for the substrate material of stainless steel as compared to silicon.

During flow boiling at about Δt_{fb} of 10 ms, the bubbles mainly nucleated at the corners and the lesser number of bubbles nucleated at the side and bottom surfaces for the substrate materials of silicon, aluminium, and copper as depicted in Figure 5.11. In this order of the substrate materials with the larger k_s, the number of bubbles at the corners and side surfaces became lesser during flow boiling. This incidence is due to the relatively more heat conduction towards the side surfaces in this order of the substrate materials with the larger k_s. With the more heat conduction to the side surfaces, the flow at the side surfaces becomes more unstable, inhibiting the bubble nucleation in this order of the substrate materials during flow boiling. Meanwhile, during flow boiling, the substrate material of copper produced more bubbles at the bottom surface as compared to silicon and aluminium. This occurrence is also as a result of larger k_s for the substrate material of copper as compared to silicon and aluminium, resulting in more heat conduction towards the upstream and side surfaces. With the more heat conduction towards the upstream and side surfaces for the substrate material of copper, the heat accumulating on the bottom surface becomes lesser as compared to silicon and aluminium. The fewer heat concentrating on the bottom surface leads to more stable flow facilitating the bubble nucleation on the bottom surface for the substrate material of copper as compared to silicon and aluminium.

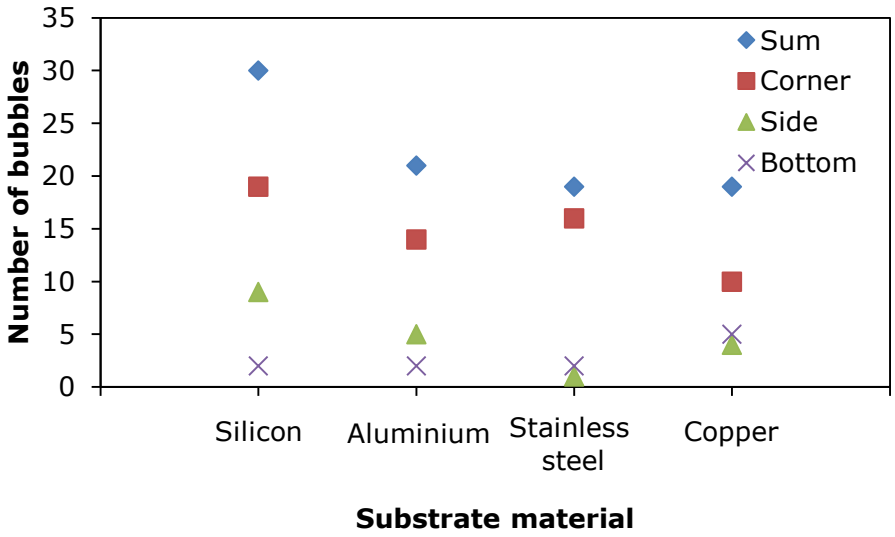


Figure 5.11: Location of bubble nucleation against substrate material at Δt_{fb} within 0 and 10 ms

For the substrate material of stainless steel, the majority of the bubbles also nucleated at the corners during flow boiling at about Δt_{fb} of 10 ms as shown in Figure 5.11. However, the number of bubbles at the corners of the substrate material of stainless steel was lesser as compared to silicon, although the more heat concentrating on the bottom surface. This incidence is also due to the extremely low k_s of stainless steel, allowing more heat accumulating at the corners associated with the more unstable flow suppressing slightly more the bubble nucleation as compared to silicon.

Meanwhile, the number of bubbles at the side surfaces for the substrate material of stainless steel was few and comparable to silicon and aluminium as illustrated in Figure 5.11. This occurrence is due to the insufficiently high k_s of the substrate material of stainless steel, silicon, and aluminium, causing the heat accumulating on the bottom surface to generate unstable flow. Also, the unsteady flow induced from the substrate material of stainless steel, silicon, and aluminium is sufficient to suppress the bubble nucleation, causing the comparable bubble nucleation on the bottom surface. On the other hand, the bubble nucleation at the side surfaces of the substrate material of stainless steel was the least among the substrate materials due to the significantly low k_s. With the significantly low k_s of the substrate material of stainless steel, the amount heat conduction towards the side surfaces is considerably lesser to generate the phase change regions for the bubble nucleation.

Chapter 6 Effects of Working Fluids

This chapter presents results and discussion regarding effects of working fluids on mechanisms of heat transfer and fluid flow before and during flow boiling in silicon rectangular micro-channels. The micro-channel heat sink has one 200 μm wide, 264 μm high, and 1 cm long micro-channel with W_{fin} of 200 μm and H_b of 137 μm. Also, the micro-channel is at $\dot{m}''$ of 389 kg/m^2 s, T_{in} of 23°C, and p_{out} of 1 atm. For each working fluid, instead of fixing q_b'' for each working fluid, this study selected $\Delta T_{avg,sup}$ $(= T_{avg,surf} - T_{sat})$ at the final Δt_{fb} as the controlling input parameter. For each working fluid, setting appropriate q_b'' is necessary to control $\Delta T_{avg,sup}$ and produce almost similar $\Delta T_{avg,sup}$ at the final Δt_{fb}. In this study, $\Delta T_{avg,sup}$ chosen was 16°C at the selected final Δt_{fb} at about 10 ms for each working fluid. The selected working fluids in this study were water and ethanol. $\Delta T_{avg,surf}$ of 16°C at Δt_{fb} about 10 ms of water was obtainable with q_b'' of 2030 kW/m^2 as the conditions as shown in Figure 4.16. For ethanol, $\Delta T_{avg,sup}$ reached 16°C at Δt_{fb} about 10 ms at q_b'' of 566 kW/m^2.

6.1 Transient Heat Transfer for Different Working Fluids before Flow Boiling

This investigation starts with the evaluation of the transient heat transfer behaviour of water and ethanol flowing in silicon rectangular micro-channels before the nucleation of first bubble $\Delta t_{fb} < 0$. This analysis is attainable by plotting $q''_{total,fin}$ against $\Delta T_{avg,surf}$ for water and ethanol before flow boiling as illustrated in Figure 6.1.

In Figure 6.1, water was at the higher range of $q''_{total,fin}$ associated with higher q_b'' to obtain $\Delta T_{avg,surf}$ of 16°C at Δt_{fb} about 10 ms as compared to ethanol. Also, for the working fluid of water, the increment of $q''_{total,fin}$ and $\Delta T_{avg,sup}$ was more significant as compared to ethanol from Δt_{fb} about −5.8 ms to 0. Also, the curve from Δt_{fb} about -5.8 ms to 0 was steeper for the working fluid of water as compared to ethanol, indicating the more rapid development of nucleate boiling characteristic. Kim et al. [140] also observed that the working fluid of water produced higher heat transfer rates as compared to saturated FC-72. This outcome is as a result of larger latent heats $\boldsymbol{h}_{lv}$ (24 times) and thermal diffusivity a_l (5.5 times) of the working fluid of water as compared to saturated FC-72. In this study, $\boldsymbol{h}_{lv}$ of the working fluid of water is 2.3 times, and a_l is about 2.2 times larger than ethanol, allowing higher heat transfer rates of phase change. During flow boiling in micro-channels, the surface tension σ produces insignificant effects on the heat transfer as found in the numerical study of Mukherjee and Kanlikar [74]. Therefore,

the change of σ produces the negligible effect on the increment of $q''_{total,fin}$ and $\Delta T_{avg,sup}$.

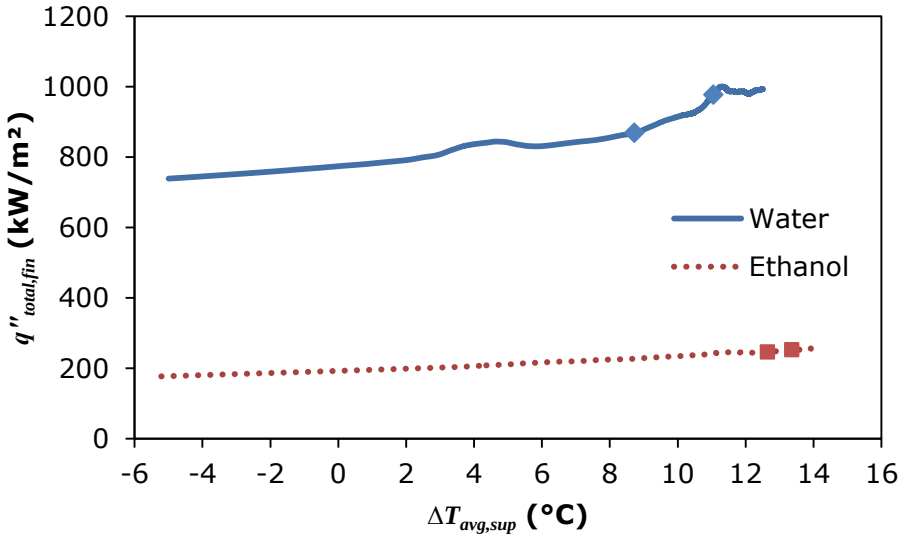
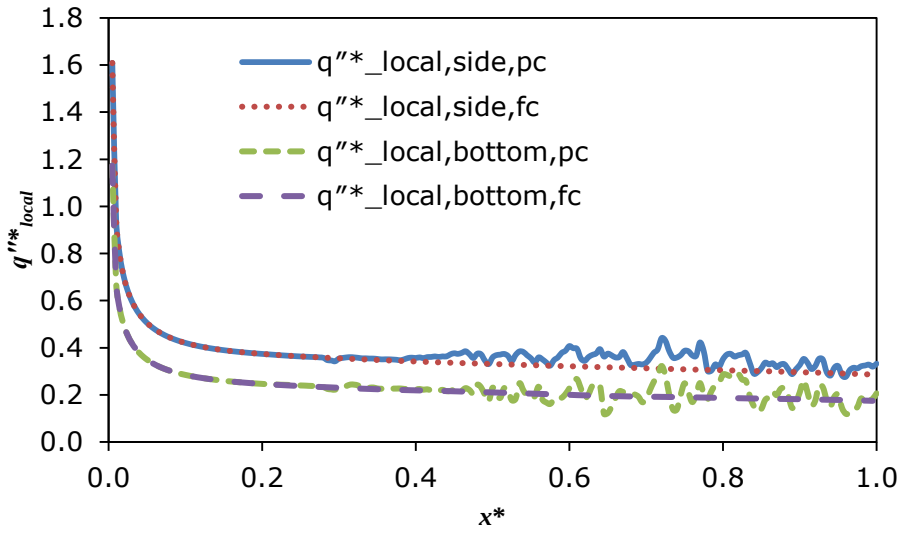


Figure 6.1: Transient heat transfer data of $q''_{total,fin}$ against $T_{avg,surf}$ of different working fluids flowing in micro-channels made at $\dot{m}'' = 389$ kg/m² s, $\Delta T_{avg,surf}$ about 16°C at Δt_{fb} of 10 ms, and $T_{in} = 23$°C before flow boiling $\Delta t_{fb} < 0$ (first and second marks at Δt_{fb} about -5.8 and -2.9 ms, respectively)

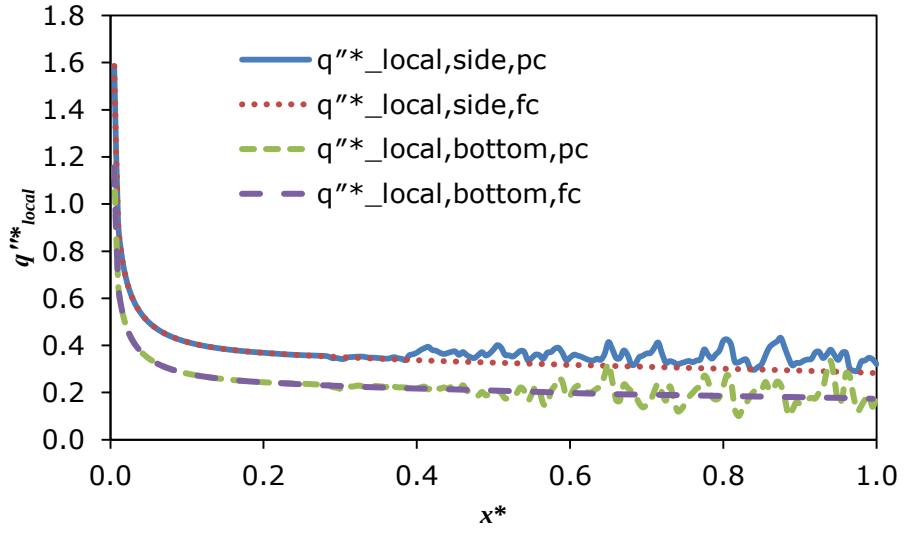
6.2 Effects of Working Fluids before Flow Boiling

Examined the transient heat transfer, this study proceeded with the exploration of the local heat transfer behaviour for different working fluids before flow boiling. For the investigation of the local heat transfer behaviour, the plots of q''^{*}_{local} for each heat transfer component at each surface along the micro-channel for different working fluids before flow boiling are essential. The plots for the working fluid of water at Δt_{fb} about -5.8 and -2.9 ms are available in Figure 4.16 whereas for ethanol are evident in Figure 6.2.

For each working fluid, the increment of $q''^{*}_{local,side,pc}$ from $q''^{*}_{local,side,fc}$ was more than the increment of $q''^{*}_{local,bottom,pc}$ from $q''^{*}_{local,bottom,fc}$ at both Δt_{fb} about -5.8 and -2.9 ms as shown in Figure 4.16 and Figure 6.2. Also, at both Δt_{fb} about -5.8 and -2.9 ms, the regions with $q''^{*}_{local,bottom,pc}$ below $q''^{*}_{local,bottom,fc}$ were more than the regions with $q''^{*}_{local,side,pc}$ below $q''^{*}_{local,side,fc}$. From about Δt_{fb} of -5.8 ms to -2.9 ms, more peaks and regions with $q''^{*}_{local,bottom,pc}$ below $q''^{*}_{local,bottom,fc}$ grew and began further from the downstream for each working fluid. This occurrence is also observable when varying $\dot{m}''$, q''_b, T_{in}, and substrate materials as discussed in Section 4.3, 4.6, 4.9, and 5.2, respectively.



(a)



(b)

Figure 6.2: q''^{*}_{local} along x^{*} for ethanol flowing in silicon micro-channel at $\dot{m}''$ of 389 kg/m^2 s, $\Delta T_{avg,sup}$ of 16°C at Δt_{fb} about 10 ms, and T_{in} of 23°C at Δt_{fb} about (a) −5.8 and (b) −2.9 ms

From Figure 4.16a and Figure 6.2a, at Δt_{fb} about −5.8 ms, the amount and magnitude of peaks of $q''^{*}_{local,side,pc}$ for the working fluid of water was still less significant as compared to ethanol. Also, for the working fluid of water, the amount and magnitude of peaks of $q''^{*}_{local,bottom,pc}$ was less substantial as compared to ethanol. Moreover, for the working fluid of water, the regions with $q''^{*}_{local,bottom,pc}$ below $q''^{*}_{local,bottom,fc}$ was also larger than ethanol. These occurrences are due to the

relatively larger $\boldsymbol{h}_{lv}$ and a_l of the working fluid of water as compared to ethanol, producing higher heat transfer rates of phase change as also observed by Kim et al. [140]. The more significant heat transfer rates for the working fluid of water facilitates the formation of the ascending and descending flows associated with the liquid-vapour mixture. However, at Δt_{fb} about -5.8 ms, the working fluid of water is still at the initial stage of phase change in which the ascending and descending flows are still less intense. Instead, the liquid-vapour mixture on the heating surfaces is more significant at Δt_{fb} about -5.8 ms. With the less intensive ascending and descending flows for the working fluid of water at Δt_{fb} about -5.8 ms, the amount and magnitude of peaks of $q''^{*}_{local,side,pc}$ and $q''^{*}_{local,bottom,pc}$ are lesser as compared to ethanol. Meanwhile, with the more massive liquid-vapour mixture at Δt_{fb} about -5.8 ms, the regions with $q''^{*}_{local,bottom,pc}$ below $q''^{*}_{local,bottom,fc}$ for the working fluid of water are more substantial than ethanol.

At about Δt_{fb} of -2.9 ms, the amount and magnitude of peaks of $q''^{*}_{local,side,pc}$ from the working fluid of water was more significant as compared to ethanol as displayed in Figure 4.16b and Figure 6.2b. Moreover, the working fluid of water possessed the more substantial amount and magnitude of peaks of $q''^{*}_{local,bottom,pc}$ as compared to ethanol at about Δt_{fb} of -2.9 ms. Furthermore, the working fluid of water produced the steeper increment of $q''_{total,fin}$ with $T_{avg,surf}$ as compared to ethanol as shown in Figure 6.1. Meanwhile, at about Δt_{fb} of -2.9 ms, for the working fluid of water, the regions with $q''^{*}_{local,bottom,pc}$ below $q''^{*}_{local,bottom,fc}$ were more massive than ethanol. These occurrences are also due to the more substantial $\boldsymbol{h}_{lv}$ and a_l facilitating the higher heat transfer rates of phase change for the working fluid of water as compared to ethanol. With the more intense heat transfer rates during phase change when Δt_{fb} reached -2.9 ms for the working fluid of water, the peaks of $q''^{*}_{local,side,pc}$ and $q''^{*}_{local,bottom,pc}$ are more massive as compared to ethanol. Also, for the working fluid of water at about Δt_{fb} of -2.9 ms, the higher heat transfer rates during phase change also induce more massive liquid-vapour mixture on the bottom surface. With the more massive liquid-vapour mixture, the regions with $q''^{*}_{local,bottom,pc}$ below $q''^{*}_{local,bottom,fc}$ becomes more for the working fluid of water as compared to ethanol at about Δt_{fb} of -2.9 ms.

Based on the local distribution of heat fluxes due to phase change, the average heat fluxes for different working fluids at Δt_{fb} about -5.8 and -2.9 ms is accessible. At Δt_{fb} about -5.8 as depicted in Figure 6.3a, the increment of $q''^{*}_{side,pc}$ from $q''^{*}_{side,fc}$ for the working fluid of water was relatively lower than ethanol. Meanwhile, $q''^{*}_{bottom,pc}$ for the working fluid of water was also almost close to but slightly lower than $q''^{*}_{bottom,fc}$. On the other hand, for the working fluid of ethanol, $q''^{*}_{bottom,pc}$ was also almost near to but slightly higher than $q''^{*}_{bottom,fc}$. From Δt_{fb} about -5.8 ms to

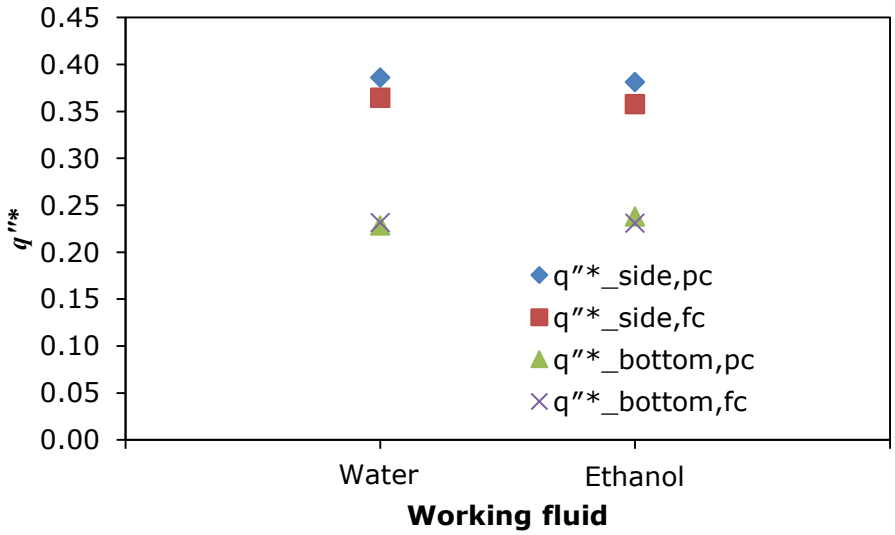
-2.9 ms as shown in Figure 6.3b, the increment of peaks of $q''^{*}_{side,pc}$ from $q''^{*}_{side,fc}$ became more apparent for the working fluid of water. Also, for the working fluid of water, the increment of $q''^{*}_{bottom,pc}$ from $q''^{*}_{bottom,fc}$ also existed at about Δt_{fb} of -2.9 ms. However, for the working fluid of ethanol, the increment of $q''^{*}_{side,pc}$ from $q''^{*}_{side,fc}$ was lesser as compared to water. On the other hand, $q''^{*}_{bottom,pc}$ was still almost closer to $q''^{*}_{bottom,fc}$ at about Δt_{fb} of -2.9 ms for the working fluid of ethanol as compared to water.

In overall, the increment of $q''^{*}_{side,pc}$ from $q''^{*}_{side,fc}$ was more than $q''^{*}_{bottom,pc}$ from $q''^{*}_{bottom,fc}$ for each working fluid as depicted in Figure 6.3. This presence is as a result of more intensive ascending and ascending flows on the side surfaces as compared to the bottom surface enhancing the heat transfer for each working fluid. On the other hand, the insignificant variation of $q''^{*}_{bottom,pc}$ from $q''^{*}_{bottom,fc}$ is due to the existence of the liquid-vapour mixture on the bottom surface inhibiting the heat transfer.

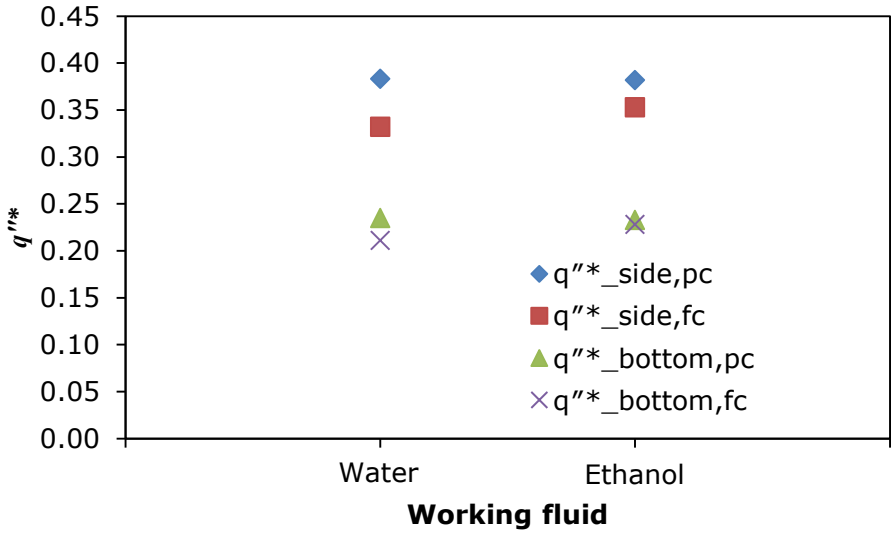
Once finished studying the local and average heat fluxes, the following section of the investigation is to evaluate the heat transfer enhancement of h^{*} for different working fluids before flow boiling. The heat transfer enhancement is observable by plotting h^{*} for water and ethanol at Δt_{fb} about -5.8 and -2.9 ms as evident in Figure 6.4. In Figure 6.4, h^{*} for water was still lower than ethanol at Δt_{fb} about -5.8 ms. This presence is due to the larger $\boldsymbol{h}_{lv}$ and a_l producing the higher heat transfer rates of phase change for the working fluid of water as compared to ethanol. With the higher heat transfer rates during phase change, at Δt_{fb} about -5.8 ms, the working fluid of water is even at the beginning stage of the phase change process. During the beginning stage of the phase change process, the ascending and descending flows are still less active for the working fluid of water. Instead, at the beginning stage of the phase change process, the liquid-vapour mixture formed is more significant for the working fluid of water, causing the lower h^{*} at Δt_{fb} about -5.8 ms. On the other hand, for the working fluid of ethanol, at Δt_{fb} about -5.8 ms, the phase change process develops more than water associated with more active as compared to water. With the more significant development of the phase change process, h^{*} for the substrate material of ethanol is higher than water at about Δt_{fb} of -5.8 ms.

When Δt_{fb} reached about -2.9 ms, h^{*} for the working fluid of water was higher with the more significant increment as compared to ethanol. These occurrences are due to the larger $\boldsymbol{h}_{lv}$ and a_l for the working fluid of water as compared to ethanol. The larger $\boldsymbol{h}_{lv}$ and a_l contributes to the more substantial heat transfer rates of phase change for the working fluid of water as compared to ethanol. With the larger heat transfer rates during phase change for the working fluid of water, the formation of the ascending and descending flows becomes more rapid as compared

to ethanol. Therefore, the more rapid creation of the ascending and descending streams for the working fluid of water produces the more significant change of h^* with Δt_{fb} as compared to ethanol.



(a)



(b)

Figure 6.3: q''^* for different working fluids flowing in silicon micro-channel at $\dot{m}''$ of 389 kg/m² s, $\Delta T_{avg,sup}$ of 16°C at Δt_{fb} about 10 ms, and T_{in} of 23°C at Δt_{fb} about (a) −5.8 and (b) −2.9 ms

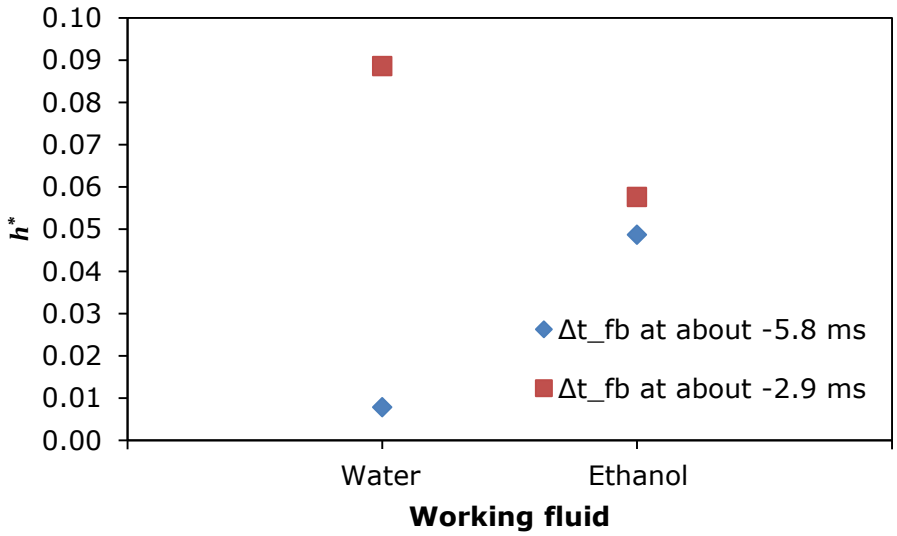


Figure 6.4: h^* for different working fluids at $\dot{m}''$ of 389 kg/m² s, $\Delta T_{avg,sup}$ of 16°C at Δt_{fb} about 10 ms, and T_{in} of 23°C at Δt_{fb} about −5.8 and −2.9 ms

6.3 Effects of Working Fluids during Flow Boiling

Once finished studying the mechanisms before flow boiling, the investigation continued with the examination of the mechanisms during flow boiling for different working fluids.

The study of the local heat transfer is accessible during flow boiling by plotting each q''^*_{local} of each heat transfer component along x^* for each working at about Δt_{fb} of 10 ms. For the investigation, the conditions selected were from Figure 4.22b for the working fluid of water while changing the working fluid to ethanol as illustrated in Figure 6.5. For each working fluid, the amount and magnitudes of peaks of $q''^*_{local,side,liq}$ above $q''^*_{local,side,fc}$ were relatively higher than $q''^*_{local,bottom,liq}$ above $q''^*_{local,bottom,fc}$. Also, the regions with $q''^*_{local,bottom,liq}$ below $q''^*_{local,bottom,fc}$ were more than the regions with $q''^*_{local,side,liq}$ below $q''^*_{local,side,fc}$ for each for each working fluid. On the other hand, for each working fluid, the number of peaks of $q''^*_{local,side,vap}$ and negative heat fluxes from $q''^*_{local,side,vap}$ became apparent. In general, both $q''^*_{local,side,vap}$ and $q''^*_{local,bottom,vap}$ at most regions were close to zero for each working fluid due to the low thermal conductivity of the vapour phase. These presences are also evident for different $\dot{m}''$, q''_b,and T_{in} as discussed in Section 4.4, Section 4.7, Section 4.10, and Section 5.3, respectively.

During flow boiling, from Figure 4.22b and Figure 6.5, when changed the working fluid of water to ethanol, the amount and magnitude of peaks of $q''^*_{local,side,liq}$ and $q''^*_{local,bottom,liq}$ became relatively smaller. Meanwhile, the regions with $q''^*_{local,bottom,liq}$ below $q''^*_{local,bottom,fc}$ for the working fluid of ethanol were also lesser as

compared to water. On the other hand, the peaks of $q''^{*}_{local,side,vap}$ and regions with $q''^{*}_{local,side,vap}$ below zero for ethanol also became less significant as compared to water. These occurrences are as a result of more substantial $\boldsymbol{h}_{lv}$ and a_l producing larger heat transfer rates of phase change for the working fluid of water as compared to ethanol. The more significant heat transfer rates of phase change facilitate larger length scales of ascending and descending flows while the larger amount of liquid-vapour mixture for the working fluid of water compared to ethanol.

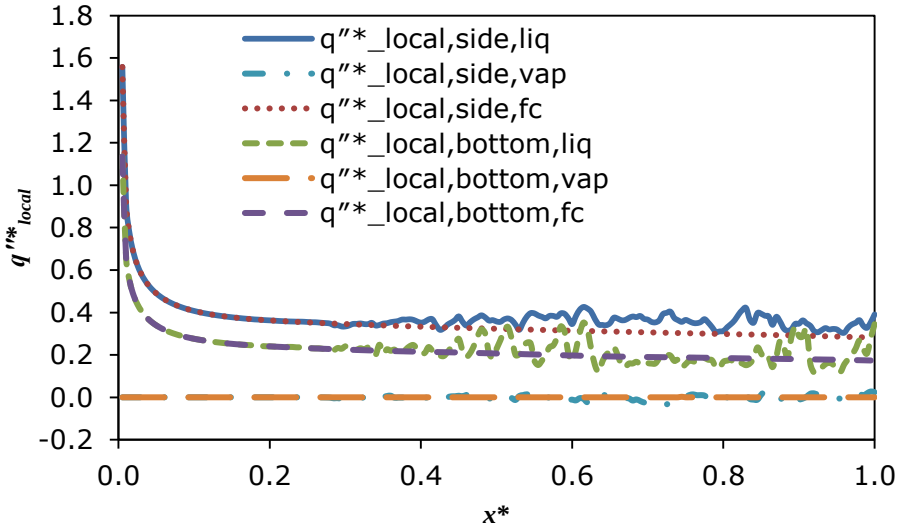


Figure 6.5: q''^{*}_{local} along x^{*} for ethanol at Δt_{fb} about 10 ms

Based on local heat fluxes, the corresponding average heat fluxes for different working fluids during flow boiling at Δt_{fb} about 10 ms are attainable as depicted in Figure 6.6. In Figure 6.6, the increment of $q''^{*}_{side,liq}$ from $q''^{*}_{side,fc}$ was more substantial for the working fluid of water as compared to ethanol during flow boiling. On the other hand, during flow boiling, $q''^{*}_{bottom,liq}$ dropped from $q''^{*}_{bottom,fc}$ for the working fluid of water. Meanwhile, $q''^{*}_{bottom,liq}$ slightly increased from $q''^{*}_{bottom,fc}$ for the working fluid of ethanol during flow boiling. For both water and ethanol, $q''^{*}_{side,vap}$ and $q''^{*}_{bottom,vap}$ were almost close to zero. In general, the increment of $q''^{*}_{side,liq}$ from $q''^{*}_{side,fc}$ was more substantial than $q''^{*}_{bottom,liq}$ from $q''^{*}_{bottom,fc}$ for each working fluid. This presence is due to the more massive ascending and descending flows during flow boiling for the working fluid of water as compared to ethanol. Also, from all the working fluids, the insignificant variation of $q''^{*}_{bottom,liq}$ from $q''^{*}_{bottom,fc}$ is due to the existence of the liquid-vapour mixture during flow boiling. On the other hand, from all the working fluids, the changes of $q''^{*}_{side,vap}$ and $q''^{*}_{bottom,vap}$ were also less significant during flow boiling due to the low thermal conductivity of the vapour phase.

Once assessed local and average heat fluxes, the investigation continued with the corresponding heat transfer enhancement h^* for different working fluids during flow boiling at Δt_{fb} about 10 ms. h^* for the working fluid of water was higher as compared to ethanol during flow boiling as depicted in Figure 6.7. These different outcomes are due to more substantial $\boldsymbol{h}_{lv}$ and a_l producing the more significant heat transfer rates of phase change for the working fluid of water as compared to ethanol. The higher heat transfer rates of phase change for the working fluid of water produce larger length scales of ascending and descending flows enhancing the heat transfer, leading to more extensive h^* as compared to ethanol.

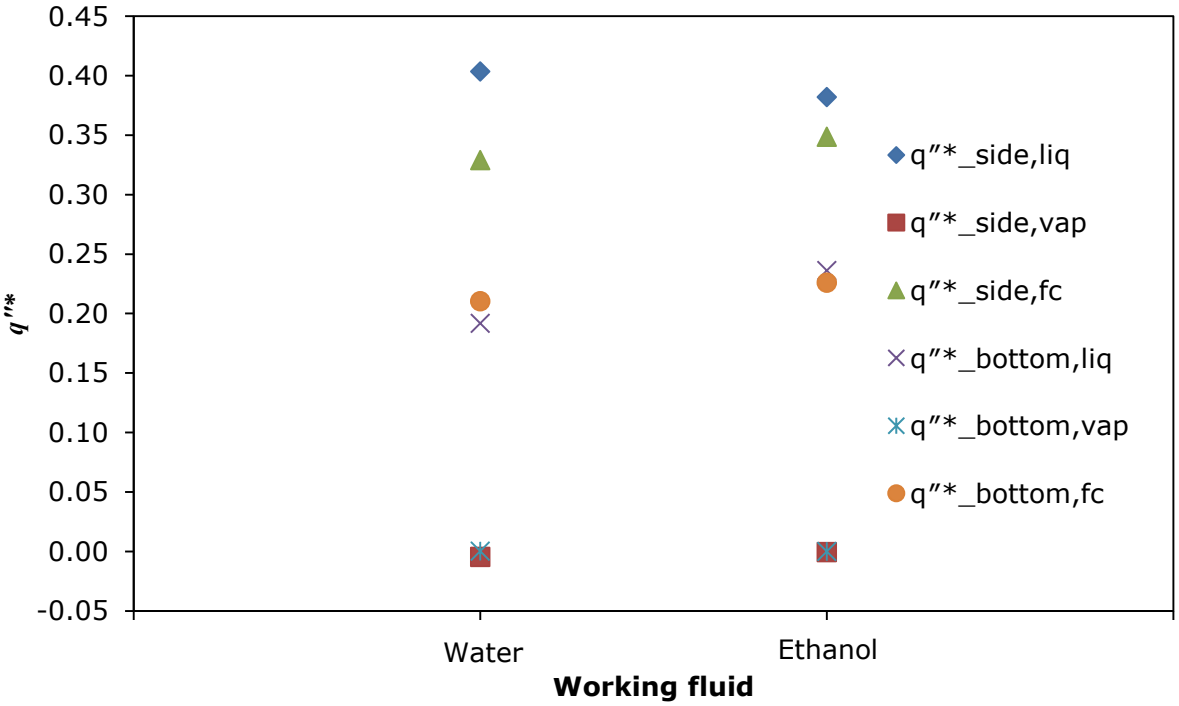


Figure 6.6: q''^* for micro-channels made of different working fluids at Δt_{fb} about 10 ms

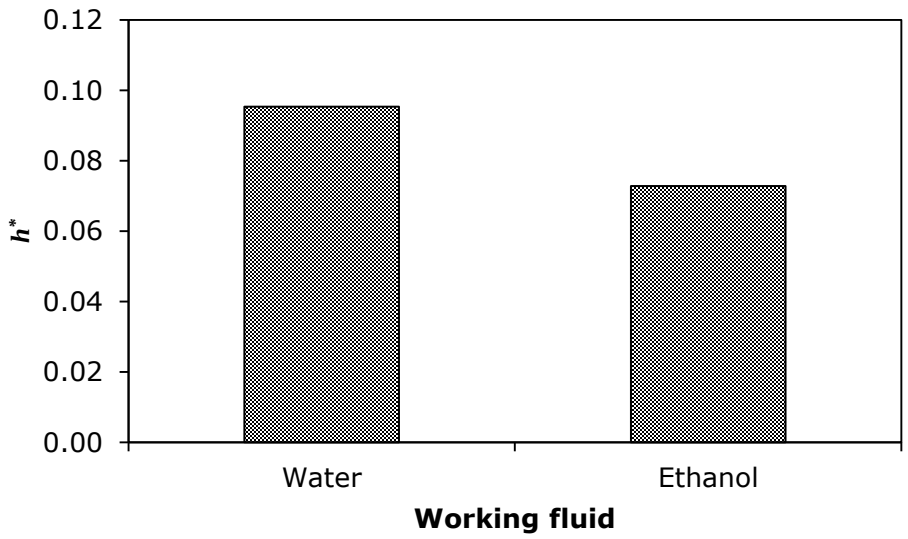


Figure 6.7: h^* for micro-channels made of different working fluids at Δt_{fb} about 10 ms

6.4 Location of Bubble Nucleation and Bubble Growth for Different Working Fluids

Once completed studying the heat transfer, the investigation proceeded to evaluate the location of bubble nucleation within the cross-section of the micro-channel during flow boiling for different working fluids.

The working fluid of water produced the more substantial number of bubbles as compared to ethanol as illustrated in Figure 5.11. The bubbles mainly nucleated at the corners of both working fluids while the bubbles nucleating at the side and bottom surfaces were only observable for the working fluid of water during flow boiling. These occurrences are due the larger h_{lv} and a_s for the working fluid of water, aiding to the higher tendency for the bubble nucleation as compared to ethanol.

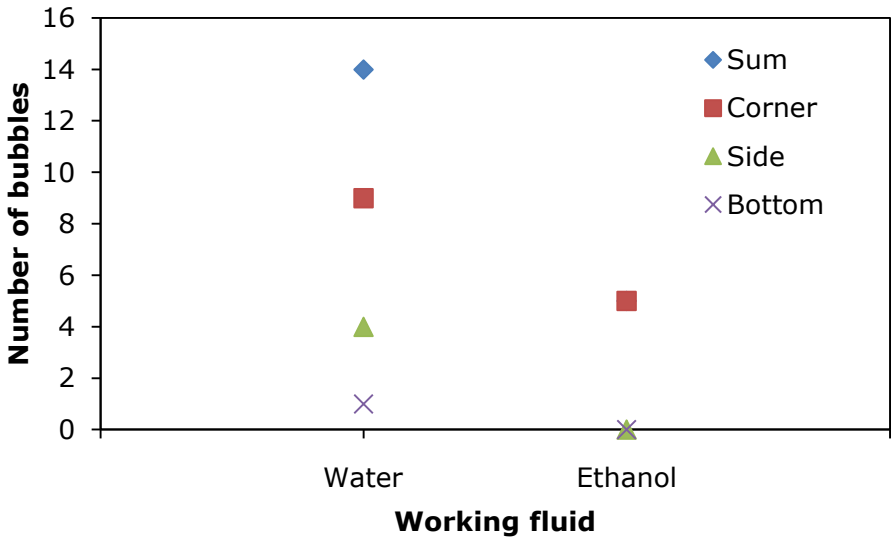


Figure 6.8: Location of bubble nucleation against working fluid at Δt_{fb} within 0 and 10 ms

Chapter 7 Conclusions

This study investigated the mechanisms of heat transfer before and during subcooled flow boiling with the bubbly flow in the rectangular micro-channel heat sink. For the investigation of this condition, operating parameters of p, q_b'', $\dot{m}''$, T_{in} set were 1 atm, 500-3197 kW/m^2, 115-389 kg/m^2 s, 23-53°C, 200 μm, 264 μm, 200 μm, and 264 μm, respectively. The micro-channels employed in this study consist of different substrate materials which were silicon, aluminium, copper, and steel whereas the selected working fluids chosen were water and ethanol. For the study of the mechanisms, this study conducted the numerical simulations by employing numerical model with Navier-Stokes equations and phase change model of VOF that considers 3D conjugate heat transfer. The numerical model agrees well with the existing experimental data, indicating that the numerical model is sufficiently accurate.

Although the bubble nucleation was absent, heat transfer in micro-channels behaved as the characteristic of nucleate boiling according to transient boiling curves plotted. This occurrence is due to the presence of liquid-vapour mixture from incomplete evaporation. With the presence of liquid-vapour mixture, the transient conduction occurs when the mixture moving on heating surfaces and therefore enhancing the heat transfer. The liquid-vapour mixture appears while pressure gradients rise on the heating surface causing the jet flow. When the jet flow becomes apparent, the hot fluid from the heating surface raises to the bulk fluid while the colder fluid descends on the heating surface enhancing the heat transfer.

Four different modes of heat transfer mechanisms appear before flow boiling associated with ascending and descending flows to enhance heat transfer. The first mode occurs when the local pressure gradient rises with the generation of the liquid-vapour mixture causing the ascending and descending streams. The second mode becomes apparent when the local increase of the amount of liquid-vapour mixture is more significant than pressure rise, leading to the ascending and descending flows to occur when the current travelling near the downstream of the region with the local increase of pressure gradient. The third mode mainly occurs further from the location of onset of ascending and descending flows with the thicker thermal boundary layer. During third mode, similar to the first mode, ascending and descending flows occur at the location with the local rise of pressure gradient and amount of liquid-vapour mixture. At the downstream of the liquid-vapour mixture with the local increase in the pressure gradient, the micro-convection occurs and causes another ascending and descending flows. The micro-convection combined with the effect of gravity and buoyancy effects with the existence of the liquid vapour mixture. The liquid-vapour mixture becomes more

massive with thicker thermal boundary layer towards the downstream with the more substantial effects of the gravity and buoyancy, leading to the more intense ascending and descending flows. At the fourth mode, the flow almost parallel to heating surface although local pressure rise occurred due to the extremely high amount of liquid-vapour mixture formed on the heating surface.

Before flow boiling, the heat transfer in micro-channels due to the transient conduction and ascending and descending flows become more significant towards downstream at lower mass fluxes. At the low mass flux, the first mode occurs near to the location of onset of ascending and descending flows followed by second modes and consequently third mode along the micro-channel. The fourth mode occurs lesser in overall. When increasing $\dot{m}''$, the first mode occurred relatively less frequent at the similar time before the bubble nucleation. At the same time before the bubble nucleation, when increased q_b'' the first mode occurred more frequent.

The increase and decrease of local heat transfer as a result of phase change on the side and bottom surfaces before and during flow boiling for each tested conditions are possible. The increase of local heat transfer is as a result of the more active ascending and descending flows generated from the phase change process enhancing the heat transfer. On the other hand, the decrease of the local heat transfer is due to the existence of liquid-vapour mixture created from the phase change process impeding the heat transfer. During flow boiling, the local increase and decrease of heat transfer of the vapour phase are also observable for all conditions employed in this study, especially at the side surfaces. However, the heat fluxes to the vapour phase with the low thermal conductivity on the side and bottom surfaces are almost close to zero for all conditions set in this study. The bubbles mainly nucleate at the corners with the smaller number of bubbles nucleates at the side and bottom surfaces during flow boiling for all conditions tested in this study.

At the low mass flux, the heat transfer enhancement due to phase change is relatively high and decreases with time before the bubble nucleation. At the moderate mass flux, before flow boiling, the heat transfer enhancement due to phase change raises significantly with time. At the high mass flux, the increment of heat transfer enhancement due to phase change becomes less substantial with time. When increasing the mass fluxes during flow boiling, the heat transfer due to phase change at the side surfaces increases with mass fluxes and is insignificant at the bottom surface. During flow boiling, the heat transfer enhancement due to phase change increases when increasing the mass fluxes. When raising the mass fluxes, the number of bubbles decreases during flow boiling.

Before flow boiling, from low to moderate base heat fluxes, the increment of heat transfer enhancement with time becomes more substantial. On the other hand, from moderate to high base heat fluxes, the decrement of heat transfer

enhancement with time becomes apparent. When increasing the base heat fluxes, during flow boiling, the heat transfer due to phase change at the side surfaces increases and then decreases during flow boiling. Meanwhile, the heat transfer due to phase change at the bottom surface decreases with the base heat fluxes. At 10 ms from the time of onset of flow boiling, the low base heat flux produces almost complete development of nucleate boiling characteristic as compared to the moderate base heat flux. Therefore, from small to moderate base heat fluxes, at 10 ms from the time of onset of flow boiling, the heat transfer enhancement due to phase change becomes less substantial. Then, the heat transfer enhancement due to phase change increases when further increasing the base heat fluxes. When employing the even higher base heat flux, the heat transfer enhancement due to phase change decreases again with the generation of more massive liquid-vapour mixture inhibiting the heat transfer. On the other hand, the number of bubbles increases with base heat fluxes during flow boiling.

Before flow boiling, in overall, the heat transfer due to phase change at the side surfaces increases with the inlet temperature while decreases with the inlet temperature at the bottom surface. When increasing the inlet temperature, the increment of heat transfer enhancement with time becomes more substantial. When increasing inlet temperature, the regions with the phase change become broader during flow boiling. Also, the heat transfer due to phase change at the side surfaces increases while decreases at the bottom surface when increasing the inlet temperature during flow boiling. As a result, when increasing the inlet temperature, the heat transfer enhancement increases and then decreases during flow boiling. Also, during flow boiling, the number of bubbles increase when increasing the inlet temperature.

Before flow boiling, the regions with the phase change become lesser at both side and bottom surfaces in the order of the substrate materials of silicon, aluminium, and copper. The substrate material of silicon produces the most rapid increment of the heat transfer enhancement due to phase change before flow boiling. The heat transfer enhancement for the substrate material of aluminium is lesser than copper before flow boiling. Meanwhile, the increment of heat transfer enhancement with time due to phase change before flow boiling for the substrate material of aluminium is comparable with copper. On the other hand, the increment of heat transfer enhancement with time due to phase change for the substrate material of stainless steel is less significant as compared to silicon before flow boiling.

In the order of the substrate materials of silicon, aluminium, and copper with higher thermal conductivities, the regions with the phase change become higher on both side and bottom surfaces during flow boiling. Nevertheless, during flow boiling, for the substrate material of stainless steel, the heat transfer enhancement of stainless steel with the significantly lower thermal conductivity is slightly more

significant as compared to silicon. During flow boiling, in the order of the substrate materials of silicon, aluminium, and copper, the number of bubbles at the corners surfaces during flow boiling became less substantial. The quantity of bubbles for the substrate material of stainless steel on the side surface is lesser as compared to silicon. The number of bubbles at the bottom surface of the substrate material of stainless steel is few and comparable to silicon and aluminium while slightly more significant for copper. On the other hand, the bubble nucleation at the side surface of the substrate material of stainless steel was the least among the substrate materials.

Before flow boiling, the increment of regions with phase change and heat transfer due to phase change with Δt_{fb} for the working fluid of water is more rapid as compared to ethanol. The vicinities with phase change and heat transfer enhancement due to phase change for the working fluid of water is more extensive as compared to ethanol during flow boiling. During flow boiling, the working fluid of water produces the more substantial number of bubbles as compared to ethanol.

This study provides the insights regarding the heat transfer mechanisms due to phase change before and during flow boiling in micro-channels from the exploration for the researchers and designers in industries. The understandings assist the researchers and designers to develop the more reliable prediction methods of the heat transfer performance of micro-channel heat sinks under flow boiling condition with the consideration of these mechanisms. The more reliable prediction methods aid to avoid repeating experiments which are costly and tedious in procedures.

References

[1] R. S. Prasher, J.-Y. Chang, I. Sauciuc, S. Narasimhan, D. Chau, G. Chrysler, A. Myers, S. Prstic, and C. Hu, "Nano and micro technology-based next-generation package-level cooling solutions," *Intel Technol. J.,* vol. 9, pp. 285-296, 2005.

[2] G. Hetsroni, M. Gurevich, and R. Rozenblit, "Sintered porous medium heat sink for cooling of high-power mini-devices," *Int. J. Heat Fluid Flow,* vol. 27, pp. 259-266, 2006.

[3] L. P. Yarin, A. Mosyak, and G. Hetsroni, *Fluid Flow, Heat Transfer and Boiling in Micro-Channels*. Berlin/Heidelberg, Germ.: Springer-Verlag, 2009.

[4] D. B. Tuckerman and R. F. W. Pease, "High-performance heat sinking for VLSI," *IEEE Electron Device Lett.,* vol. 2, pp. 126-129, 1981.

[5] I. Mudawar, "Assessment of high-heat-flux thermal management schemes," *IEEE Trans. Compon. Packag. Technol.,* vol. 24, pp. 122-141, 2001.

[6] W. Qu and I. Mudawar, "Prediction and measurement of incipient boiling heat flux in micro-channel heat sinks," *Int. J. Heat Mass Transfer,* vol. 45, pp. 3933-3945, 2002.

[7] S. S. Mehendale, A. M. Jacobi, and R. K. Shah, "Fluid flow and heat transfer at micro-and meso-scales with application to heat exchanger design," *Appl. Mech. Rev.,* vol. 53, pp. 175-193, 2000.

[8] S. G. Kandlikar and W. J. Grande, "Evolution of microchannel flow passages – Thermohydraulic performance and fabrication technology," *Heat Transfer Eng.,* vol. 24, pp. 3-17, 2003.

[9] S. G. Kandlikar, S. Joshi, and S. Tian, "Effect of channel roughness on heat transfer and fluid flow characteristics at low Reynolds numbers in small diameter tubes," in *Proc. 35th Natl. Heat Transfer Conf.*, Anaheim, California, 2001.

[10] T. H. Yen, M. Shoji, F. Takemura, Y. Suzuki, and N. Kasagi, "Visualization of convective boiling heat transfer in single microchannels with different shaped cross-sections," *Int. J. Heat Mass Transfer,* vol. 49, pp. 3884-3894, 2006.

[11] J. Li and P. Cheng, "Bubble cavitation in a microchannel," *Int. J. Heat Mass Transfer,* vol. 47, pp. 2689-2698, 2004.

[12] I. Tiselj, G. Hetsroni, B. Mavko, A. Mosyak, E. Pogrebnyak, and Z. Segal, "Effect of axial conduction on the heat transfer in micro-channels," *Int. J. Heat Mass Transfer,* vol. 47, pp. 2551-2565, 2004.

[13] S. G. Kandlikar, "History, advances, and challenges in liquid flow and flow boiling heat transfer in microchannels: A critical review," *J. Heat Transfer,* vol. 134, pp. 034001-1-034001-15, 2012.

[14] S. Szczukiewicz, M. Magnini, and J. R. Thome, "Proposed models, ongoing experiments, and latest numerical simulations of microchannel two-phase flow boiling," *Int. J. Multiphase Flow,* vol. 59, pp. 84-101, 2014.

[15] S. K. Saha, *Microchannel Phase Change Transport Phenomena*. Amsterdam, Neth.: Elsevier Inc., 2015.

[16] W. Qu and I. Mudawar, "Flow boiling heat transfer in two-phase micro-channel heat sinks––I. Experimental investigation and assessment of correlation methods," *Int. J. Heat Mass Transfer,* vol. 46, pp. 2755-2771, 2003.

[17] J. Lee and I. Mudawar, "Two-phase flow in high-heat-flux micro-channel heat sink for refrigeration cooling applications: Part II—heat transfer characteristics," *Int. J. Heat Mass Transfer,* vol. 48, pp. 941-955, 2005.

[18] T. Chen and S. V. Garimella, "Measurements and high-speed visualizations of flow boiling of a dielectric fluid in a silicon microchannel heat sink," *Int. J. Multiphase Flow,* vol. 32, pp. 957-971, 2006.

[19] D. Liu and S. V. Garimella, "Flow boiling heat transfer in microchannels," *J. Heat Transfer,* vol. 129, pp. 1321-1332, 2007.

[20] T. Harirchian and S. V. Garimella, "Microchannel size effects on local flow boiling heat transfer to a dielectric fluid," *Int. J. Heat Mass Transfer,* vol. 51, pp. 3724-3735, 2008.

[21] I. Mudawar and T. M. Anderson, "Parametric investigation into the effects of pressure, subcooling, surface augmentation and choice of coolant on pool boiling in the design of cooling systems for high-power-density electronic chips," *J. Electron. Packag.,* vol. 112, pp. 375-382, 1990.

[22] E. Galvis and R. Culham, "Measurements and flow pattern visualizations of two-phase flow boiling in single channel microevaporators," *Int. J. Multiphase Flow,* vol. 42, pp. 52-61, 2012.

[23] W. Qu and I. Mudawar, "Analysis of three-dimensional heat transfer in micro-channel heat sinks," *Int. J. Heat Mass Transfer,* vol. 45, pp. 3973-3985, 2002.

[24] W. H. Wong and N. M. Ghazali, "Numerical simulation of a microchannel for microelectronic cooling," *Jurnal Teknologi,* vol. 46(A), pp. 1-16, 2007.

[25] M. K. Moharana, P. K. Singh, and S. Khandekar, "Optimum Nusselt number for simultaneously developing internal flow under conjugate conditions in a square microchannel," *J. Heat Transfer,* vol. 134, pp. 071703-1-071703-10, 2012.

[26] F. Houshmand and Y. Peles, "Impact of flow dynamics on the heat transfer of bubbly flow in a microchannel," *J. Heat Transfer,* vol. 136, pp. 022902-1-022902-8, 2014.

[27] G. Wang, P. Cheng, and A. E. Bergles, "Effects of inlet/outlet configurations on flow boiling instability in parallel microchannels," *Int. J. Heat Mass Transfer,* vol. 51, pp. 2267-2281, 2008.

[28] G. Gamrat, M. Favre-Marinet, and D. Asendrych, "Conduction and entrance effects on laminar liquid flow and heat transfer in rectangular microchannels," *Int. J. Heat Mass Transfer,* vol. 48, pp. 2943-2954, 2005.

[29] A. Mukherjee and S. G. Kandlikar, "Numerical simulation of growth of a vapor bubble during flow boiling of water in a microchannel," *Microfluid. Nanofluid.,* vol. 1, pp. 137-145, 2005.

[30] L. Cheng and H. Zou, "Evaluation of flow boiling heat transfer correlations with experimental data of R134a, R22, R410a and R245fa in microscale channels," *Int. J. Microscale Nanoscale Therm. Fluid Transp. Phenom.,* pp. 363-380, 2011.

[31] X. Peng, *Micro Transport Phenomena During Boiling*. Beijing, China Berlin/Heidelberg, Germ.: Tsinghua Univ. Press Springer-Verlag, 2011.

[32] T. Harirchian and S. V. Garimella, "Effects of channel dimension, heat flux, and mass flux on flow boiling regimes in microchannels," *Int. J. Multiphase Flow,* vol. 35, pp. 349-362, 2009.

[33] M. E. Steinke and S. G. Kandlikar, "An experimental investigation of flow boiling characteristics of water in parallel microchannels," *J. Heat Transfer,* vol. 126, pp. 518-526, 2004.

[34] T. Chen and S. V. Garimella, "Flow boiling heat transfer to a dielectric coolant in a microchannel heat sink," *IEEE Trans. Compon. Packag. Technol.,* vol. 30, pp. 24-31, 2007.

[35] G. Ribatski, L. Wojtan, and J. R. Thome, "An analysis of experimental data and prediction methods for two-phase frictional pressure drop and flow boiling heat transfer in micro-scale channels," *Exp. Therm. Fluid Sci.,* vol. 31, pp. 1-19, 2006.

[36] S. G. Kandlikar, "Scale effects on flow boiling heat transfer in microchannels: A fundamental perspective," *Int. J. Therm. Sci.,* vol. 49, pp. 1073-1085, 2010.

[37] J. Lee and I. Mudawar, "Fluid flow and heat transfer characteristics of low temperature two-phase micro-channel heat sinks–Part 2. Subcooled boiling pressure drop and heat transfer," *Int. J. Heat Mass Transfer,* vol. 51, pp. 4327-4341, 2008.

[38] X. Peng and B. Wang, "Forced convection and flow boiling heat transfer for liquid flowing through microchannels," *Int. J. Heat Mass Transfer,* vol. 36, pp. 3421-3427, 1993.

[39] X. Peng and B. Wang, "Liquid flow and heat transfer in microchannels with/without phase change," in *Proc. 10th Inst. Chem. Eng. Symp. Ser.*, Brighton, UK, 1994, pp. 159-177.

[40] X. Peng and B. Wang, "Evaporation space and fictitious boiling for internal evaporation of liquid," *Sci. Found. China,* vol. 2, pp. 55-59, 1994.

[41] X. Peng and B. Wang, "Forced-convection and boiling characteristics in microchannels," in *Heat Transfer 1998, Proc. 11th Int. Heat Transfer Conf.*, Kyongju, Korea, 1998, pp. 371-390.

[42] X. F. Peng, H. Y. Hu, and B. X. Wang, "Boiling nucleation during liquid flow in microchannels," *Int. J. Heat Mass Transfer,* vol. 41, pp. 101-106, 1998.

[43] M. Sussman, P. Smereka, and S. Osher, "A level set approach for computing solutions to incompressible two-phase flow," *J. Comput. Phys.,* vol. 114, pp. 146-159, 1994.

[44] N. Basu, G. R. Warrier, and V. K. Dhir, "Onset of nucleate boiling and active nucleation site density during subcooled flow boiling," *J. Heat Transfer,* vol. 124, pp. 717-728, 2002.

[45] S. G. Kandlikar, "Heat transfer characteristics in partial boiling, fully developed boiling, and significant void flow regions of subcooled flow boiling," *J. Heat Transfer,* vol. 120, pp. 395-401, 1998.

[46] A. Mosyak, L. Rodes, and G. Hetsroni, "Boiling incipience in parallel micro-channels with low mass flux subcooled water flow," *Int. J. Multiphase Flow,* vol. 47, pp. 150-159, 2012.

[47] D. Liu, P. S. Lee, and S. V. Garimella, "Prediction of the onset of nucleate boiling in microchannel flow," *Int. J. Heat Mass Transfer,* vol. 48, pp. 5134-5149, 2005.

[48] J. Lee and I. Mudawar, "Fluid flow and heat transfer characteristics of low temperature two-phase micro-channel heat sinks–Part 1: Experimental methods and flow visualization results," *Int. J. Heat Mass Transfer,* vol. 51, pp. 4315-4326, 2008.

[49] T. Harirchian and S. V. Garimella, "The critical role of channel cross-sectional area in microchannel flow boiling heat transfer," *Int. J. Multiphase Flow,* vol. 35, pp. 904-913, 2009.

[50] S. S. Bertsch, E. A. Groll, and S. V. Garimella, "Effects of heat flux, mass flux, vapor quality, and saturation temperature on flow boiling heat transfer in microchannels," *Int. J. Multiphase Flow,* vol. 35, pp. 142-154, 2009.

[51] T. Harirchian and S. V. Garimella, "An investigation of flow boiling regimes in microchannels of different sizes by means of high-speed visualization," in *2008 11th Intersoc. Conf. Therm. Thermomech. Phenomena in Electron. Syst.*, Orlando, FL, 2008, pp. 197-206.

[52] Y. Wang, K. Sefiane, and S. Harmand, "Flow boiling in high-aspect ratio mini- and micro-channels with FC-72 and ethanol: experimental results and heat transfer correlation assessments," *Exp. Therm. Fluid Sci.,* vol. 36, pp. 93-106, 2012.

[53] Y. Wang and K. Sefiane, "Single bubble geometry evolution in micro-scale space," *Int J. Therm. Sci.,* vol. 67, pp. 31-40, 2013.

[54] M. M. Mahmoud and T. G. Karayiannis, "Heat transfer correlation for flow boiling in small to micro tubes," *Int. J. Heat Mass Transfer,* vol. 66, pp. 553-574, 2013.

[55] A. Koşar, C. J. Kuo, and Y. Peles, "Boiling heat transfer in rectangular microchannels with reentrant cavities," *Int. J. Heat Mass Transfer,* vol. 48, pp. 4867-4886, 2005.

[56] H. Y. Zhang, D. Pinjala, and T. N. Wong, "Experimental characterization of flow boiling heat dissipation in a microchannel heat sink with different orientations," in *2005 7th Electron. Packag. Technol. Conf.*, Singapore, 2005, pp. 670-676.

[57] T. Harirchian and S. V. Garimella, "A comprehensive flow regime map for microchannel flow boiling with quantitative transition criteria," *Int. J. Heat Mass Transfer,* vol. 53, pp. 2694-2702, 2010.

[58] C. J. Kuo and Y. Peles, "Flow boiling instabilities in microchannels and means for mitigation by reentrant cavities," *J. Heat Transfer,* vol. 130, pp. 72402-1-72402-10, 2008.

[59] V. P. Carey, *Liquid Vapor Phase Change Phenomena: An Introduction to the Thermophysics of Vaporization and Condensation Processes in Heat Transfer Equipment*, 3rd ed. Boca Raton, U. S. : CRC Press, 2016.

[60] S. G. Kandlikar, "Fundamental issues related to flow boiling in minichannels and microchannels," *Exp. Therm. Fluid Sci.,* vol. 26, pp. 389-407, 2002.

[61] L. Zhang, K. E. Goodson, and T. W. Kenny, *Silicon Microchannel Heat Sinks: Theories and Phenomena*. Berlin/Heidelberg, Germ.: Springer-Verlag, 2004.

[62] P. Balasubramanian and S. G. Kandlikar, "Experimental Study of Flow Patterns, Pressure Drop, and Flow Instabilities in Parallel Rectangular Minichannels," *Heat Transfer Eng.,* vol. 26, pp. 20-27, 2005.

[63] J. Y. Lee, M.-H. Kim, M. Kaviany, and S. Y. Son, "Bubble nucleation in microchannel flow boiling using single artificial cavity," *Int. J. Heat Mass Transfer,* vol. 54, pp. 5139-5148, 2011.

[64] T. P. Lagus and F. A. Kulacki, "Two-Phase Heat Transfer and Bubble Characteristics in a Microchannel Array," *J. Heat Transfer,* vol. 134, pp. 071502-1-071502-11, 2012.

[65] D. Bogojevic, K. Sefiane, G. Duursma, and A. J. Walton, "Bubble dynamics and flow boiling instabilities in microchannels," *Int. J. Heat Mass Transfer,* vol. 58, pp. 663-675, 2013.

[66] S. G. Kandlikar, "Similarities and differences between flow boiling in microchannels and pool boiling," *Heat Transfer Eng.,* vol. 31, pp. 159-167, 2010.

[67] J. Barber, D. Brutin, K. Sefiane, and L. Tadrist, "Bubble confinement in flow boiling of FC-72 in a "rectangular" microchannel of high aspect ratio," *Exp. Therm. Fluid Sci.,* vol. 34, pp. 1375-1388, 2010.

[68] S. G. Kandlikar, M. D. Cartwright, and V. R. Mizo, "A photographic study of nucleation characteristics of cavities in flow boiling," in *Convective Flow Boiling, Proc. Convective Flow Boiling, An Int. Conf. Banff Center Conf.*, 1995, pp. 73-78.

[69] Z. Guo, D. F. Fletcher, and B. S. Haynes, "A review of computational modelling of flow boiling in microchannels," *J. Comput. Multiphase Flows,* vol. 6, pp. 79-110, 2014.

[70] R. Zhuan and W. Wang, "Simulation on nucleate boiling and frictional pressure drop in micro channel," presented at the Int. Refrig. Air Cond. Conf., Purdue Univ., Indiana, 2008.

[71] R. Zhuan and W. Wang, "Simulation on nucleate boiling in micro-channel," *Int. J. Heat Mass Transfer,* vol. 53, pp. 502-512, 2010.

[72] R. Zhuan and W. Wang, "Simulation of subcooled flow boiling in a micro-channel," *Int. J. Refrig.,* vol. 34, pp. 781-795, 2011.

[73] A. Mukherjee and S. G. Kandlikar, "Numerical study of effect of contact angle on bubble growth and wall heat transfer during flow boiling of water in a microchannel," in *Int. Heat Transfer Conf. 13*, Sydney, Australia, 2006.

[74] A. Mukherjee and S. G. Kandlikar, "Numerical study of the effect of surface tension on vapor bubble growth during flow boiling in microchannels," in *Proc. 4th Int. Conf. Nanochannels, Microchannels, Minichannels, Parts A B*, Limerick, Ireland, 2006, pp. 61-66.

[75] W. Lee and G. Son, "Bubble dynamics and heat transfer during nucleate boiling in a microchannel," *Numer. Heat Transfer, Part A,* vol. 53, pp. 1074-1090, 2008.

[76] Y. Suh, W. Lee, and G. Son, "Bubble dynamics, flow, and heat transfer during flow boiling in parallel microchannels," *Numer. Heat Transfer, Part A,* vol. 54, pp. 390-405, 2008.

[77] A. Mukherjee, "Contribution of thin-film evaporation during flow boiling inside microchannels," *Int. J. Therm. Sci.,* vol. 48, pp. 2025-2035, 2009.

[78] A. Mukherjee and S. G. Kandlikar, "The effect of inlet constriction on bubble growth during flow boiling in microchannels," *Int. J. Heat Mass Transfer,* vol. 52, pp. 5204-5212, 2009.

[79] A. Mukherjee, S. G. Kandlikar, and Z. J. Edel, "Numerical study of bubble growth and wall heat transfer during flow boiling in a microchannel," *Int. J. Heat Mass Transfer,* vol. 54, pp. 3702-3718, 2011.

[80] C. W. Hirt and B. D. Nichols, "Volume of fluid (VOF) method for the dynamics of free boundaries," *J. Comput. Phys.,* vol. 39, pp. 201-225, 1981.

[81] W. J. Rider and D. B. Kothe, "Reconstructing volume tracking," *J. Comput. Phys.,* vol. 141, pp. 112-152, 1998.

[82] M. Rudman, "Volume-tracking methods for interfacial flow calculations," *Int. J. Numer. Methods Fluids,* vol. 24, pp. 671-691, 1997.

[83] O. Ubbink and R. I. Issa, "A method for capturing sharp fluid interfaces on arbitrary meshes," *J. Comput. Phys.,* vol. 153, pp. 26-50, 1999.

[84] S. Osher and J. A. Sethian, "Fronts propagating with curvature-dependent speed: algorithms based on Hamilton-Jacobi formulations," *J. Comput. Phys.,* vol. 79, pp. 12-49, 1988.

[85] R. R. Nourgaliev, S. Wiri, N. T. Dinh, and T. G. Theofanous, "On improving mass conservation of level set by reducing spatial discretization errors," *Int. J. Multiphase Flow,* vol. 31, pp. 1329-1336, 2005.

[86] M. Sussman and E. G. Puckett, "A coupled level set and volume-of-fluid method for computing 3D and axisymmetric incompressible two-phase flows," *J. Comput. Phys.,* vol. 162, pp. 301-337, 2000.

[87] Y. Q. Zu, Y. Y. Yan, S. Gedupudi, T. G. Karayiannis, and D. B. R. Kenning, "Confined bubble growth during flow boiling in a mini-/micro-channel of rectangular cross-section part II: Approximate 3-D numerical simulation," *Int. J. Therm. Sci.,* vol. 50, pp. 267-273, 2011.

[88] S. Gedupudi, Y. Q. Zu, T. G. Karayiannis, D. B. R. Kenning, and Y. Y. Yan, "Confined bubble growth during flow boiling in a mini/micro-channel of rectangular cross-section Part I: Experiments and 1-D modelling," *Int. J. Therm. Sci.,* vol. 50, pp. 250-266, 2011.

[89] M. S. Plesset and S. A. Zwick, "The growth of vapor bubbles in superheated liquids," *J. Appl. Phys.,* vol. 25, pp. 493-500, 1954.

[90] R. W. Schrage, *A Theoretical Study of Interphase Mass Transfer*. New York, U. S.: Columbia Univ. Press, 1953.

[91] W. M. Rohsenow and O. E. Dwyer, "Film condensation of liquid metals," presented at the 4th Int. Semin. Heat Mass Transfer Liq. Met., Trojir, Yugoslavia, 1973.

[92] I. Tanasawa, "Advances in condensation heat transfer," *Adv. Heat Transfer,* vol. 21, pp. 55-139, 1991.

[93] S. Zhou, X. Xu, and B. G. Sammakia, "Modeling of boiling flow in microchannels for nucleation characteristics and performance optimization," *Int. J. Heat Mass Transfer,* vol. 64, pp. 706-718, 2013.

[94] J. U. Brackbill, D. B. Kothe, and C. Zemach, "A continuum method for modeling surface tension," *J. Comput. Phys.,* vol. 100, pp. 335-354, 1992.

[95] H. J. Lee, E. A. Browne, Y. Peles, and M. K. Jensen, "The onset of nucleate boiling in a micro-channel subjected to a pulsed heat flux," in *Proc. ASME 2011 9th Int. Conf. Nanochannels, Microchannels, Minichannels*, 2011, pp. 55-62.

[96] L. Yin, L. Jia, P. Guan, and D. Liu, "Experimental investigation on bubble confinement and elongation in microchannel flow boiling," *Exp. Therm. Fluid Sci.,* vol. 54, pp. 290-296, 2014.

[97] S. V. Patankar, "A calculation procedure for two-dimensional elliptic situations," *Numer. Heat Transfer,* vol. 4, pp. 409-425, 1981.

[98] X. F. Peng, H. Y. Hu, and B. X. Wang, "Bubble formation of liquid boiling in microchannels," *Sci. China Ser. E Technol. Sci.,* vol. 41, pp. 404-410, 1998.

[99] R. K. Shah and A. L. London, *Laminar Flow Forced Convection in Ducts: A Source Book for Compact Heat Exchanger Analytical Data*. New York, San Francisco, U.S. London, UK: Academic Press, Inc., 1978.

[100] Y. Y. Hsu, "On the size range of active nucleation cavities on a heating surface," *J. Heat Transfer,* vol. 84, pp. 207-213, 1962.

[101] T. Sato and H. Matsumura, "On the conditions of incipient subcooled-boiling with forced convection," *Bull. JSME,* vol. 7, pp. 392-398, 1964.

[102] A. E. Bergles and W. M. Rohsenow, "The determination of forced-convection surface-boiling heat transfer," *J. Heat Transfer,* vol. 86, pp. 365-372, 1964.

[103] E. J. Davis and G. H. Anderson, "The incipience of nucleate boiling in forced convection flow," *Am. Inst. Chem. Eng. J.,* vol. 12, pp. 774-780, 1966.

[104] S. Kandlikar, V. Mizo, M. Cartwright, and E. Ikenze, "Bubble nucleation and growth characteristics in subcooled flow boiling of water," in *HTD-Vol.342, ASME Proc. 32nd Natl. Heat Transfer Conf., Vol. 4*, New York, US, 1997, pp. 11-18.

[105] G. P. Celata, M. Cumo, and A. Mariani, "Experimental evaluation of the onset of subcooled flow boiling at high liquid velocity and subcooling," *Int. J. Heat Mass Transfer,* vol. 40, pp. 2879-2885, 1997.

[106] Y.-Y. Hsu and R. W. Graham, *Transport Processes in Boiling and Two-Phase Systems*. Washington, U.S. London, U. K.: Hemisphere Publ. Corp., 1976.

[107] S. M. Ghiaasiaan and R. C. Chedester, "Boiling incipience in microchannels," *Int. J. Heat Mass Transfer,* vol. 45, pp. 4599-4606, 2002.

[108] S. G. Kandlikar, "Heat transfer mechanisms during flow boiling in microchannels," *J. Heat Transfer,* vol. 126, p. 8, 2004.

[109] L. Yin, L. Jia, P. Guan, and D. Liu, "Evaporating momentum force and shear force on meniscuses of elongated bubble in microchannel flow boiling," *J. Comput. Multiphase Flows,* vol. 23, pp. 160-168, 2014.

[110] L. Yin, L. Jia, and M. Xu, "Experimental investigation on bubble sliding during subcooled flow boiling in microchannel," *Exp. Therm. Fluid Sci.,* vol. 68, pp. 435-441, 2015.

[111] J. F. Klausner, R. Mei, D. M. Bernhard, and L. Z. Zeng, "Vapor bubble departure in forced convection boiling," *Int. J. Heat Mass Transfer,* vol. 36, pp. 651-662, 1993.

[112] S. G. Kandlikar, "A theoretical model to predict pool boiling CHF incorporating effects of contact angle and orientation," *J. Heat Transfer,* vol. 123, pp. 1071-1079, 2001.

[113] Y. Liaofei, J. Li, G. Peng, and L. Fuhao, "Evaporating momentum force and shear force on meniscuses of elongated bubble in microchannel flow boiling," *J. Therm. Sci.,* vol. 23, pp. 160-168, 2014.

[114] G. A. Bird, *Molecular Gas Dynamics and the Direct Simulation of Gas Flows, Volume 1*. Oxford: Clarendon Press, 1994.

[115] T. Ahmad, S. L. Plee, and J. P. Myers. (2011). *ANSYS FLUENT Theory Guide*.

[116] A. Koşar, C. J. Kuo, and Y. Peles, "Suppression of boiling flow oscillations in parallel microchannels by inlet restrictors," *J. Heat Transfer,* vol. 128, pp. 251-260, 2006.

[117]M. Knudsen, *The Kinetic Theory of Gases: Some Modern Aspects*. York, U. K.: Metheun Publ., 1934.

[118] Z. Yang, X. F. Peng, and P. Ye, "Numerical and experimental investigation of two phase flow during boiling in a coiled tube," *Int. J. Heat Mass Transfer,* vol. 51, pp. 1003-1016, 2008.

[119] J.-h. Wei, L.-m. Pan, D.-q. Chen, H. Zhang, J.-j. Xu, and Y.-p. Huang, "Numerical simulation of bubble behaviors in subcooled flow boiling under swing motion," *Nucl. Eng. Des.,* vol. 241, pp. 2898-2908, 2011.

[120] W. H. Lee, "A pressure iteration scheme for two-phase flow modeling," in *Multiphase Transp.: Fundam., React. Saf., Appl.: Proc. 2nd Multi-Phase Flow Heat Transfer Symp.,*, Miami Beach, US, 1980, pp. 407-432.

[121] H. L. Wu, X. F. Peng, P. Ye, and Y. E. Gong, "Simulation of refrigerant flow boiling in serpentine tubes," *Int. J. Heat Mass Transfer,* vol. 50, pp. 1186-1195, 2007.

[122] T. Ahmad, S. L. Plee, and J. P. Myers. (2011). *ANSYS FLUENT User Guide*.

[123] R. Cole, "Boiling nucleation," *Adv. Heat Transfer,* vol. 10, pp. 85-166, 1974.

[124] R. I. Issa, "Solution of the implicitly discretised fluid flow equations by operator-splitting," *J. Comput. Phys.,* vol. 62, pp. 40-65, 1986.

[125] T. J. Barth and D. C. Jespersen, "The design and application of upwind schemes on unstructured meshes," in *AIAA Pap. 89-0366 27th Aerospace Sciences Meeting*, Reno, US, 1989.

[126] W. K. Anderson and D. L. Bonhaus, "An implicit upwind algorithm for computing turbulent flows on unstructured grids," *Comput. Fluids,* vol. 23, pp. 1-21, 1994.

[127] S. V. Patankar, *Numerical Heat Transfer and Fluid Flow*. Washington, U.S. London, U. K. : Hemisphere Publ. Corp., 1980.

[128] L. Lin and A. P. Pisano, "Bubble forming on a micro line heater," *Micromech. Sensors, Actuators, and Syst.,* vol. 32, pp. 147-164, 1991.

[129] L. Lin, K. S. Udell, and A. P. Pisano, "Liquid-vapor phase transition and bubble formation in micro structures," *Therm. Sci. Eng.,* vol. 2, pp. 52-59, 1994.

[130] M. Magnini, B. Pulvirenti, and J. R. Thome, "Numerical investigation of the influence of leading and sequential bubbles on slug flow boiling within a microchannel," *Int. J. Therm. Sci.,* vol. 71, pp. 36-52, 2013.

[131] R. Séméria, "Analyse Fine de l'Ébullition à l'Échelle local [Well-defined analysis of boiling at local scale]," *Les Instabilités en Hydraulique et em Mécanique des Fluides, VIIIèmes Journées de l'Hydraulique, Société Hydrodynamique de France-Lille-France, Question Vc, Rapport [The Instabilities Hydraul. Fluid Mech., 8th Hydraul. Conf. Hydrodyn. Soc. Fr.-Lille-Fr., Vice-Chairman's Quest., Report],* pp. 1-7, 1964.

[132] W. T. Brown, "A study of flow surface boiling," Ph.D. thesis, Dept. Mech. Eng., Mass. Inst. Technol., Cambridge, Mass., 1967.

[133] H. Wang, X. F. Peng, B. X. Wang, and D. J. Lee, "Jet flow phenomena during nucleate boiling," *Int. J. Heat Mass Transfer,* vol. 45, pp. 1359-1363, 2002.

[134] H. Wang, X. F. Peng, B. X. Wang, and D. J. Lee, "Bubble sweeping and jet flows during nucleate boiling of subcooled liquids," *Int. J. Heat Mass Transfer,* vol. 46, pp. 863-869, 2003.

[135] J. G. Collier and J. R. Thome, *Convective Boiling and Condensation*, 3rd ed. New York, U. S.: Oxford Univ. Press, 1994.

[136] A. Nechayev. "On the mechanism of laminar-turbulent transition and the origin of the critical Reynolds number". *Cornel Univ. Libr.,* pp. 1-3, Nov. 26, 2013. [Online]. Available: https://arxiv.org/ftp/arxiv/papers/1311/1311.6764.pdf [Accessed Apr. 28, 2017].

[137] H. Schlichting, K. Gersten, E. Krause, H. Oertel, and K. Mayes, *Boundary-Layer Theory*, 9th ed. Berlin/Heidelberg, Germ.: Springer-Verlag, 2017.

[138] A. G. Fedorov and R. Viskanta, "Three-dimensional conjugate heat transfer in the microchannel heat sink for electronic packaging," *Int. J. Heat Mass Transfer,* vol. 43, pp. 399-415, 2000.

[139] Y. A. Çengel and A. Ghajar, *Heat and Mass Transfer (A Practical Approach, SI Version)*: McGraw-Hill Education, 2011.

[140] J. H. Kim, S. M. You, and J. Y. Pak, "Effects of heater size and working fluids on nucleate boiling heat transfer," *Int. J. Heat Mass Transfer,* vol. 49, pp. 122-131, 2006.

Appendix A Flow Chart of Numerical Algorithm

In the numerical study of flow boiling in micro-channels, numerical algorithm of PISO pressure-velocity coupling scheme associates with explicit time discretisation scheme of mass equation of vapour phase in transient flow is employed. The flow chart of the numerical algorithm is shown in Figure A.1 and outlined as follows:

1. Initialise first set of variables where $\alpha_l{}^{***} = \alpha_{l,init}$, $\alpha_v{}^{***} = \alpha_{v,init}$, $p^{***} = p_{init}$, $u^{***} = u_{init}$, $v^{***} = v_{init}$, $w^{***} = w_{init}$, $E^{***} = E_{init}$, $k^{***} = k_{init}$ and $\omega^{***} = \omega_{init}$.
2. A time step value was set.
3. The discretised mass equation of vapour phase was solved using initial values $\alpha_v{}^{***}$ to obtain the volume fraction of vapour α_v, followed by computing the volume fraction of liquid phase α_l. The vapour phase mass equation was solved once per time step.
4. The discretised momentum equations were solved using p^{***}, u^{***}, v^{***} and w^{***}.
5. First equation of pressure correction was solved to obtain first corrected pressure $p^{**\prime}$ using u^{***}, v^{***} and w^{***}. The first equation of pressure correction is derived from mass equations and momentum equations.
6. The $p^{**\prime}$, u^{***}, v^{***} and w^{***} were corrected using the first equation of pressure correction to obtain a second set of pressure field p^{**} and velocity field u^{**}, v^{**} and w^{**}.
7. The second pressure correction equation was solved to obtain second corrected pressure field $p^{*\prime}$.
8. The $p^{*\prime}$, u^{**}, v^{**} and w^{**} were corrected using the second pressure correction equation to obtain a third set of pressure field p^{*}, and velocity field u^{*}, v^{*} and w^{*}.
9. The discretised governing equations for energy, turbulence kinetic energy and specific dissipation rate were then solved using the initial values E^{***}, $k^{***}$and ω^{***} to obtain a first set of energy E^{*}, turbulence kinetic energy k^{*} and specific dissipation rate ω^{*}.
10. The calculations were repeated from the step 4 to solve discretised momentum equations by setting $p^{***} = p^{*}$, $u^{***} = u^{*}$, $v^{***} = v^{*}$, $w^{***} = w^{*}$, $E^{***} = E^{*}$, $k^{***} = k^{*}$and $\omega^{***} = \omega^{*}$ until the solution converges.
11. If the solutions are converged, repeat the calculations from step 2 to calculate solutions for the next time step by setting setting $p^{***} = p$, $u^{***} = u$, $v^{***} = v$, $w^{***} = w$, $E^{***} = E$, $k^{***} = k$ and $\omega^{***} = \omega$ until the time t reaches t_{max}.

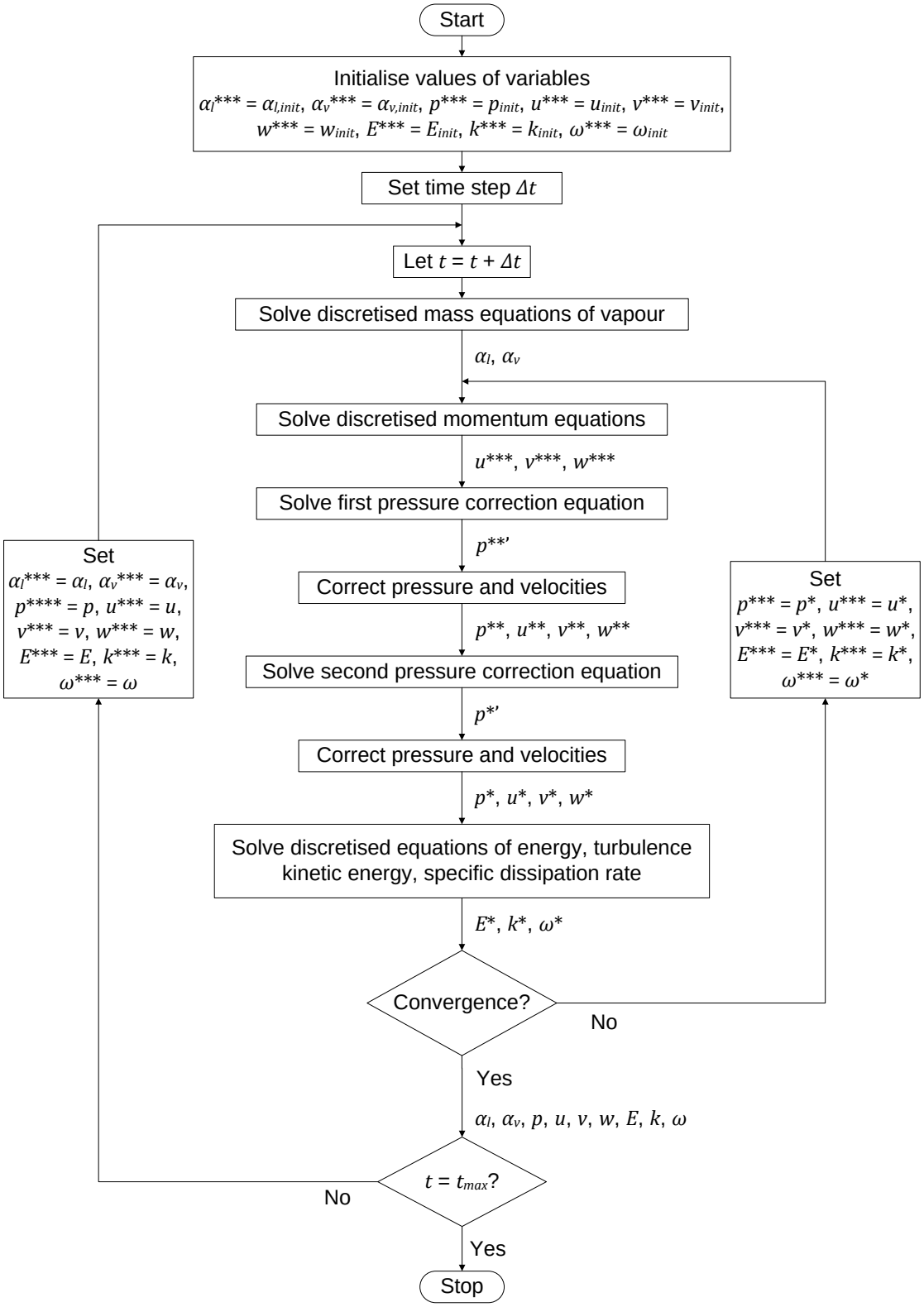


Figure A.1: PISO pressure velocity coupling scheme associated with explicit time discretisation scheme of mass equation of vapour phase